NASA CR-164835

NASA-CR-164835
1981 00 24206

A Reproduced Copy

OF

PROCEEDINGS OF THE INTERNATIONAL COLLOQUIUM ON DROPS AND BUBBLES

THEIR SCIENCE AND THE SYSTEMS THEY MODEL

California Institute of Technology
and
Jet Propulsion Laboratory

28-30 August, 1974

Volume II

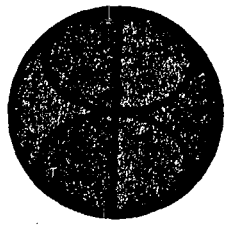

PROCEEDINGS
OF THE
INTERNATIONAL COLLOQUIUM
ON
DROPS AND BUBBLES

THEIR SCIENCE AND THE SYSTEMS THEY MODEL

California Institute of Technology
and
Jet Propulsion Laboratory

28-30 August, 1974

Volume II

Editors

D. J. COLLINS
M. S. PLESSET
M. M. SAFFREN

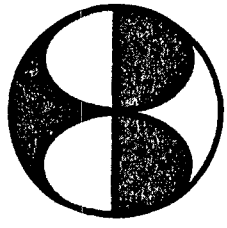

CHAIRMAN

M. S. Plesset —*Caltech*

STEERING COMMITTEE

M. M. Saffren
Chairman —*Jet Propulsion Lab.*

F. H. Busse —*UCLA*

J. R. Carruthers —*Bell Laboratories*

R. J. Donnelly —*University of Oregon*

D. D. Elleman —*Jet Propulsion Lab.*

D. W. Moore —*Imperial College-London*

M. Neiburger —*UCLA*

M. S. Plesset —*Caltech*

L. E. Scriven —*University of Minnesota*

EXECUTIVE SECRETARY

D. J. Collins

M/S 183-601

Jet Propulsion Laboratory

4800 Oak Grove Dr.

Pasadena, CA 91103

PREFACE

These Proceedings have been organized with papers given in the order in which they were presented in the Colloquium. Those papers representing contributions to the evening film sessions have been placed following the full length papers because of the somewhat different format involved. In several of these shorter papers are to be found some of the most stimulating presentations of the Colloquium, and the organizers are indeed grateful that the authors of these film discussions have been willing to participate by contributing what have in many cases been examples from unfinished and ongoing research.

The presentations of the Introductory Session have not been included in these Proceedings. In this Session, chaired by Dr. R. J. Mackin, Jr., Dr. W. H. Pickering greeted the participants, Dr. F. E. Goddard explained the Research and Advanced Developments Program at JPL, and Dr. M. M. Saffren gave the Introduction to the Colloquium.

The Editors

ACKNOWLEDGMENTS

In organizing and carrying out a colloquium of this scope and magnitude it is essential that myriad details be anticipated and attended to in order to ensure smooth functioning of colloquium activities which, besides the formal and informal sessions, included meals and transportation. The great effort required to accomplish this was borne by the members of the Steering Committee, and in particular by the Colloquium Chairman, Dr. Milton Plesset.

We specially thank Anne Shanahan who, as Colloquium Secretary, provided invaluable help in every phase of the preparation for the Colloquium, the activities of the Colloquium, and the preparation of these Proceedings; Nancy Hopkins for her capable assistance with local arrangements; Alex Irving for his support during the Colloquium in arranging for the facilities and equipment; and Carol Litchfield and Sandi Campbell for conducting tours and helping participants and their guests to feel at home in Pasádena.

We owe special gratitude to the Jet Propulsion Laboratory and the California Institute of Technology for their support of this Colloquium and for the use of the facilities. We also wish to thank the Space Technology Payloads Office of the Office of Aeronautics and Space Technology of NASA under Contract NAS 7-100 for supporting both the activities of the meeting and in part the publication of these Proceedings.

Without these people and organization--and we do not forget the participants themselves--this Colloquium could not have been the success that it was, both technically and as an international gathering of unusual warmth.

Dr. Melvin M. Saffren
Chairman, Steering Committee

TABLE OF CONTENTS

VOLUME I

TABLE OF CONTENTS

TABLE OF CONTENTS

VOLUME II

INTRODUCTION

Interest in the science of liquid drops and bubbles extends beyond those who work in fundamental fluid dynamics. Workers in meteorology, chemical engineering, mechanical engineering, and space processing have an evident and very practical concern with this science. Workers in nuclear physics and in astrophysics use liquid drops and bubbles as models for phenomena in atomic nuclei, and in self-gravitating astronomical systems.

This Colloquium provided an opportunity for workers in these various disciplines to come together, for the first time, to

- assess the present status of the science of liquid drops and bubbles in liquids
- forecast and help determine the future directions of this science
- determine the value to this science of forthcoming opportunities to perform experiments in a weightless environment.

One aim of the Colloquium was to make evident that what might appear at first sight to be a narrow and proscribed science with its best days behind it, was none of these things. A reader of these Proceedings can judge for himself how successfully this aim was met. An excellent technical summary of the Colloquium is provided by Dr. Scriven's paper on page xii.

A second aim was to help establish the future direction of the science of drops and bubbles by looking toward the proper balance of future work in theory, computation, laboratory experiment, and experiments in weightlessness. In retrospect this was too ambitious an aim to be met definitively by a single Colloquium; such a balance will probably emerge only after more conventions of this Colloquium have taken place.

Even so, the presentations do allow some general conclusions to be drawn. Almost without exception, theory is treated in linear approximation and applies to the equilibrium, or at best stationary state. While computation does indeed treat the non-linear dynamics of drops and bubbles it does so only when a high degree of symmetry significantly reduces the computational complexity. In laboratory experiments the fact that there are usually several complicated effects that are taking place simultaneously makes precise analysis difficult. Experiments in weightlessness are relatively new. However the several papers presented on the Skylab demonstrations hint at the potential for remarkable experiments that may allow effects simultaneously present in earth-based experiments to be disentangled.

Here I must confess to the personal prejudice that as this potential is slowly realized in the next few years, when what were demonstrations become carefully controlled experiments, more and more experimenters will be drawn to experiments in weightlessness, and what is learned will greatly stimulate both

theory and computation and even result in new experiments on earth. Presently, NASA KC 135 aircraft flying along a ballistic trajectory afford up to 25 seconds of weightlessness. Soon to be flown as part of the NASA Space Processing Program, sounding rockets will allow experiments times in weightlessness up to 10 minutes. Eventually, in 1980, the NASA Space Shuttle will provide 7 days of weightlessness, and in fact JPL is engaged in a project to result in an experiment module being made available on the Shuttle for drop dynamics experiments. It is expected that future conventions of this Colloquium will be under the auspices of this project which is itself part of the NASA Physics and Chemistry in Space Experiments Program.

Interdisciplinary meetings such as this one are notoriously high risk events. When successful, as this Colloquium was, the presentations stimulate specialist and non-specialist alike, provoking exciting discussions at sessions that spill over into corridors, and irrepressibly into the coffee and mealtime breaks. Hopefully the presentations as recorded in these Proceedings will be just as exciting to read as they were to hear.

Dr. Melvin M. Saffren
Chairman, Steering Committee

THE MOTION OF BUBBLES AND DROPS IN LIQUIDS

J. F. Harper
Department of Mathematics, Victoria University of Wellington, New Zealand

INTRODUCTION

The purpose for which I was honoured with an invitation to this Colloquium was that of pointing out some difficulties which have not been resolved, especially those which seem to provide opportunities for future useful work. It was not primarily that of reviewing well-known theories and the experiments which they explain. For a bubble or drop moving through a liquid under steady external forces, that has been done first by Levich (1), on whose work almost all later theory is based, and more recently in Refs. 2, 3, 4. Some defects have come to light in Ref. 2, which could usefully be mentioned here. Too little attention was paid to numerical work (5,6), to recent studies of raindrops (7,8) and to the stagnant-cap theory (see below), and there are some errors in the thermodynamic treatment of adsorption: temperature changes must be neglected in order to obtain equations (4.4) and (4.5) of Ref. 2, and the physical interpretation of Γ on the following page is too simple. A list of minor misprints will be provided on request.

INSTABILITY

The first difficulty and opportunity which I wish to mention is this. For many years now experimenters have disagreed on the criteria for stability of the steady rise of a gas bubble in a pure liquid. Let us define

$$M = g\eta^4/\rho\sigma^3 \ , \tag{1}$$

where g is the acceleration due to gravity, η is the dynamic viscosity of the liquid, ρ its density and σ its surface tension. Then some experimenters (9,10) find that bubbles of any size will rise stably in any liquid with $M > 10^{-8}$, while others (3) have observed instability at $M > 10^{-2}$ in circumstances quite similar to those of Ref. 10.

If $M < 10^{-8}$, it appears that marginal instability occurs when the Weber number

$$W = \rho U^2 d/\sigma \doteq 3 \ , \tag{2}$$

where U is the velocity and d is the equivalent spherical diameter of the bubble. The reason is well known: small changes in d then give rise to very large changes of shape and hence U, (2,11,12), and so steady-state theory predicts that quite different shapes and hence flows can almost co-exist for the same bubble. But what is not well understood is the type of motion which occurs when steady flow does become unstable (9,13). Experimental bubbles rise in either helices or plane zigzags, and there seems to be no way to tell which will occur in any given case. If anything, the present theoretical confusion is worse. Spiralling has been shown to persist if the motion is suitably started (13), but only if the bubble is also subject to the other instability as well, and the type of motion predicted for that case is not zigzagging but monotonic wandering away from a vertical path. It is unsatisfactory to have been left for seventeen years wondering, but not knowing, whether surface-active impurities are some way responsible (20).

THE WATER ANOMALY

Another phenomenon where the same suspicion arises might be called the "water anomaly". Provided that $W < 0.5$, bubbles are very nearly spherical, and their graphs of drag coefficient against Reynolds number follow the familiar universal curve for solid spheres if their surfaces are dirty, and a somewhat lower universal curve (14) if clean. But even the most carefully distilled water appears to behave in the same way as filtered (but undistilled) water, by following the solid-sphere curve if $R = Ud/\nu < 100$, where ν is the kinematic viscosity, and then gradually approaching the clean-surface one until $R = 500$, by which time distortion from a spherical shape has become important. If that is a real effect, (and I am indebted to Dr D W Moore for pointing out to me how strong the evidence in Ref. 14 is), it must mean that all so-called "clean" water has the same non-zero amount of the same surface-active impurity dissolved in it. The mystery is apparently deepened by the fact that a 13% alcohol solution in water behaves like a normal pure liquid (14).

The only obvious suggestion to make is that at least one of the natural chemical components in water exposed to the air is surface-active enough and abundant enough to act as the "impurity". Because a free water surface is always charged, and the electrical conductivity of water is notoriously about 10 times as high in the presence of ordinary air as when the carbon dioxide is carefully removed, we are led to consider water as a roughly 10^{-6} molar solution of H_3O^+ and HCO_3^-. The diffuse (Gouy-Chapman) double layer at the surface is then about 300 nm thick (15), and we can estimate the effect on the surface tension in order-of-magnitude terms as follows. Suppose that we take the potential difference across the double layer to be 0.1V, and then the energy in a capacitor with plates 300 nm apart and a water dielectric is about 10^{-5} J m^{-2}, which corresponds to a surface-tension difference of 10^{-2} mN m^{-1} between H_2O and the ionic solution.

That does not seem to be enough of a surface pressure to interfere with a bubble 1 mm in diameter rising at 0.2 m s^{-1}, but there is a magnifying mechanism for it. A rising bubble with a free surface is so efficient at sweeping any small amount of adsorbed impurity round to its rear stagnation point (16) that whenever the motion is visibly retarded, the surface must be totally clogged around that point, though it might well be effectively free and unpolluted over the forward part of the bubble. This is, of course, the "stagnant-cap" hypothesis (17). Now convective diffusion onto a freely moving surface is very much more efficient than off a surface at rest, and so the surfactant concentration at the rear stagnation point of a rising bubble will be many times its value at a stationary fluid surface in equilibrium. Detailed calculations are so far available only for a very small stagnant cap on a bubble rising at low Reynolds number (18), but magnification factors of 10 or 20 for the surface pressure seem entirely reasonable. That would explain how Davis and Acrivos (17) found it a good approximation to use in their theory the maximum possible surface pressure of which a given surfactant was capable, even if the bubble was rising in quite a dilute solution, and it would also bring up the electrical surface pressure for water to 0.1 or 0.2 mN m^{-1} at a rear stagnation point. Our only guide to the effect on a bubble is Moore's theorem (16) for the drag coefficient, i.e.

$$C_D = \frac{48}{R}\left\{1 - \frac{1}{2U\eta}\int_{-1}^{1} \mu\Pi(\mu)d\mu\right\} \quad , \qquad (3)$$

where μ is the cosine of the polar angle θ measured from the front stagnation point. This theorem holds when the flow is slightly perturbed

from irrotational, which is not accurately true here, but it seems that the surface pressure could perhaps suffice to explain the observed effects.

Obviously there is plenty of scope here for future work, both experimental on bubbles rising in water with the carbon dioxide removed (and with the conductivity simultaneously measured to check on it), and theoretical for a stagnant cap on a sphere at high Reynolds numbers, somewhat resembling Leal's (19) calculation for an analogous two-dimensional flow. The numerical work will not be easy: there are more independent dimensionless parameters than one would like, and even small Reynolds numbers gave some trouble (17).

LOW PÉCLET-NUMBER FLOW

Let us turn to a problem where the theoretical difficulties are quite minor. If a bubble or drop moves in an ideal surfactant solution at low Péclet number $P = Ud/D$ (and therefore low Reynolds number because $\nu >> D$ for all ordinary surfactants in all ordinary liquids), the motion and the distribution of surfactant are remarkably easy to find (2), even when diffusion through both bulk phases and along the surface is allowed for simultaneously. It would therefore seem to be a good system in which to try working out the effects of more complicated physical chemistry (such as the surfactant approaching the critical micelle concentration, or undergoing chemical reactions, possibly slowly enough to hold up its diffusive transfer), but for two objections. Low Péclet numbers are unusual in bubbles big enough to be visible with the naked eye, and even if there were some good means of observing tiny bubbles rising, the liquid would have to be extraordinarily pure for them to act as anything but small rigid spheres. The second difficulty is a challenge to a surface chemist, but the first could only be overcome in space. That is because U on earth is always between $gd^2/18\nu$ and $gd^2/12\nu$ (the Stokes and Hadamard-Rybczynski values), and so

$$gd^3/18\nu D < P < gd^3/12\nu D \qquad (4)$$

To get d up to 0.1 mm would require g to be reduced to a thousandth of the usual 9.8 m s^{-2}, and obviously greater reductions would allow for larger bubbles.

One reason why this Colloquium was called was "to determine the value to this science of forthcoming opportunities to perform experiments in a weightless environment". There seems to be no point in suggesting that any experiment be done in space if it is feasible on earth, but we seem to have here an experiment which is impossible on earth and which might tell us something important about surface chemistry in very dilute solutions. I shall be interested to learn whether the "rise" of small bubbles in a very highly purified liquid constitutes an experiment feasible in space.

REFERENCES

1. V G Levich, "Physicochemical Hydrodynamics", Prentice-Hall, Englewood Cliffs, N.J. (1962).
2. J F Harper, "The Motion of Bubbles and Drops through Liquids", Advances in Appl. Mech. 12, 59-129 (1972).
3. P P Wegener and J-Y Parlange, "Spherical Cap Bubbles", Ann. Rev. Fluid Mech. 5, 79-100 (1973).
4. J R Grace, "Shapes and Velocities of Bubbles rising in Infinite Media", Trans. Inst. Chem. Eng. 51, 116-120 (1973).
5. A E Hamielec, T W Hoffman and L L Ross, "Numerical Solution of the Navier-Stokes Equation for Flow past Spheres: Part I", AIChEJ 13, 212-219 (1967).

6. A E Hamielec, A I Johnson and W T Houghton, "Numerical Solution of the Navier-Stokes Equation for Flow past Spheres: Part II" , AIChEJ. 13, 220-224 (1967).
7. H R Pruppacher and K V Beard, "A Wind Tunnel Investigation of the Internal Circulation and Shape of Water Drops falling at Terminal Velocity in Air", Quart. J.R. Met. Soc. 96, 247-256 (1970).
8. B P Le Clair, A E Hamielec, H R Pruppacher and W D Hall, "A Theoretical and Experimental Study of the Internal Circulation in Water Drops falling at Terminal Velocity in Air", J. Atmos. Sci. 29, 728-740 (1972).
9. R A Hartunian and W R Sears, "On the Instability of small Gas Bubbles moving uniformly in various Liquids", J. Fluid Mech. 3, 27-17, (1957).
10. H Angelino, "Hydrodynamique des Grosses Bulles dans les Liquides Visqueux", Chem. Eng. Sci. 21, 541-550 (1966).
11. D W Moore, "The Velocity of Rise of Gas Bubbles in a Liquid of Small Viscosity", J. Fluid Mech. 23, 749-766 (1965).
12. M. El Sawi, "Distorted Gas Bubbles at Large Reynolds Number", J. Fluid Mech. 62, 163-183 (1974).
13. P G Saffman, "On the Rise of Small Air Bubbles in Water", J. Fluid Mech. 1, 249-275 (1956).
14. W L Haberman and R K Morton, "An Experimental Investigation of the Drag and Shape of Air Bubbles rising in various Liquids" , David Taylor Model Basin Rep. no. 802 (1953); "An Experimental Study of Bubbles moving in Liquids", Trans. Amer. Soc. Civil Eng. 121, 227-252 (1956).
15. D J Shaw, "Introduction to Colloid and Surface Chemistry", Butterworths, London. 2nd ed., (1970).
16. J F Harper, "On Spherical Bubbles rising slowly in dilute Surfactant Solutions", Q. J. Mech. appl. Math. 27, 87-100 (1974).
17. R E Davis and A Acrivos, "The Influence of Surfactants on the Creeping Motion of Small Bubbles", Chem. Eng. Sci. 21, 681-685 (1966).
18. J F Harper, "On Bubbles with small Immobile Adsorbed Films rising in Liquids at Low Reynolds Numbers", J. Fluid Mech. 58, 539-545 (1973).
19. L G Leal, "Steady Separated Flow in a Linearly Decelerated Free Stream", J. Fluid Mech. 59, 513-535 (1973).
20. H Tsuge and S Hibino, "Motion of Single Gas Bubbles rising in various Liquids" (in Japanese), Kagaku Kogaku 35(1), 65-71 (1971).

THE PENDANT DROP: THEORY AND EXPERIMENT

by A. A. Kovitz

Department of Mechanical Engineering and Astronautical Sciences
Northwestern University, Evanston, Illinois 60201

ABSTRACT

The spectrum of static, axisymmetric pendant drop shapes is studied, both experimentally and theoretically. Calculations, both numerical and analytical, based on the Young-Laplace equation, yield possible pendant drop shapes as a one-parameter (a non-dimensionalized pressure jump at the drop apex) family of curves. These results are interpreted in terms of varying contact circle radius and hydrostatic pressure in the contact circle cross-section, for any fixed value of interfacial tension and density difference across the interface. Experiments were conducted in which the above noted parameters were varied, and their relationship to the calculations evaluated.

The calculated family of solution curves is bounded by two envelopes; one gives the high pressure limit for existence of static drops; the other gives the low pressure limit. For given interfacial properties, and fixed contact circle radius, multiple solutions exist between these two pressure extremes.

Experiment shows that two pendant drops are observable for a given contact circle radius and pressure; one is statically stable; the other is statically metastable. With increasing pressure these two shapes approach each other; at a certain maximum pressure they coalesce into one pendant drop shape; any higher pressure results in dripping. It was also verified that drops suddenly break off when the low pressure limit is approached.

Static stability conclusions have recently been reported by a number of authors using energy methods; the direct experimental verification herein reported (except for some unpublished results to be noted), and the analytical results for high and low pressure drops appear to be new.

INTRODUCTION

A pendant drop is formed when the denser of two contiguous fluids is suspended below a closed, common curve of contact between the fluids and a fixed solid; implicit in this description is the supposition that the configuration is in static equilibrium under the influence of gravitational and surface tension forces. The axisymmetric case, which arises when the contact curve is a circle whose plane is perpendicular to the gravitational force, has received much attention both by early and recent investigators. The early work focused mainly on determination of the pendant drop shape, through solution of the governing Young-Laplace equation, and its use in measurement of surface tension. The most recent work is concerned with the static stability of pendant drops, primarily through application of variational techniques on the energy of the system.

This paper is also concerned with the static stability of pendant drops. Conclusions will be deduced from the family of drop shapes determined

numerically and analytically from the Young-Laplace equation rather than an energy approach. Certain results, for essentially low and high pressure in the contact circle cross-section, will be obtained analytically. Finally, these static stability conclusions will be shown to compare well with experiment.

Although the stability limits to be cited here have also been recognized in recent work using energy methods, they appear in a more compact and concise way through the interpretation of boundary envelopes to the pendant drop solution curves. Experiments focused on verifying these static stability limits, and the observation of certain multiple solutions, do not appear to be in the literature. However, many experiments on the breakaway volumes of pendant drops are reported, with the object of obtaining empirical equations useful in the drop-weight method for surface tension; Padday and Pitt (in a 1973 paper referred to later) give many references for these experiments.

No paper on pendant drops can fail to note the fundamental work of Young (1) and Laplace (2). These researchers established the general governing equation for interfacial surfaces and obtained solutions for limiting cases. Laplace (2), in particular, already recognized the ability of the interfacial equation to yield information on static stability.

The first comprehensive, and still useful, numerical treatment of the Young-Laplace equation is due to Bashforth and Adams (3). They published tables for drop shapes as a function of a "shape parameter", which is related to the apex pressure parameter to be used here. Lohnstein (4) obtained approximate results for the limiting volume of drops as a function of contact circle radius. These results were used in conjunction with a method for finding more accurate values of surface tension. Bakker (5) has summarized results up to 1928 for numerical computation of drop shapes and their practical application. More recently, Padday (6) and Princen (7) have given extensive and excellent reviews of the experimental and mathematical state of the art, up to 1968, for determination of interfacial shapes and surface tension.

Much current work on pendant drops concerns their static stability. Padday and Pitt (8) present a comprehensive study of the static stability of three types of axisymmetric interfaces, including pendant drops. Their results are based on an application of the energy method, using the extensive numerical results of Padday (9) to evaluate the first and second variations of the energy integral. Padday and Pitt (8) also note the appearance of bounding envelopes, and interpret them with respect to static stability. Their paper carefully classifies many types of stability phenomena, with detailed descriptions of meniscal behavior under a variety of constraints. Pitts (10) avoids the numerical approach of Ref. (8); in this way he is able to include more general perturbations in pendant drop shape; it is not clear that his stability boundaries differ from those of Padday and Pitt (8).

Related theoretical studies by Gillette and Dyson (11,12,13) consider the stability of liquid bridges, and disjoint capillary system, based on variational principles. Orr, Scriven, and Rivas (14) report on new results for liquid bridges (or pendular rings).

FORMULATION OF PROBLEM

Figure 1 is a schematic of the pendant drop with dimensional coordinate system. The basic Young-Laplace equation (see, for example, Refs. 6,7) relating the pressure difference across an interface to the interfacial curvature and interfacial tension is

$$\Delta p = p_+ - p_- = \sigma(1/R_1 + 1/R_2) \ , \qquad (1)$$

where p_+ and p_- are the local hydrostatic pressures on either side of the interface, R_1 and R_2 are the local principal radii of curvature of the interface, and σ is the interfacial tension. Let p_{c+} and p_{c-} be the pressures in the plane of the contact circle, inside and outside the drop, respectively; if ρ_+ and ρ_- are the corresponding fluid densities (with $\rho_+ > \rho_-$), and g the gravitational force per unit mass in the negative f direction, then

$$\Delta p = p_{c+} - p_{c-} + \rho g f_a - \rho g f \ , \qquad (2)$$

where $\rho \equiv \rho_+ - \rho_-$, f_a is the distance from the apex of the drop to its contact circle, and f is the distance from the apex to the plane where Δp is measured. Introduce the meniscus constant (a length)

$$k \equiv \sqrt{\sigma/\rho g} \ ,$$

and the non-dimensional lengths

$$x \equiv r/k \ , \quad y \equiv f/k \ ; \qquad (3)$$

these are identical to the variables used, among others, by Huh and Scriven (15), and Kovitz (16). It is convenient to introduce the non-dimensional pressure difference across the interface

$$-w \equiv \Delta p/\rho g k = G - y \ , \qquad (4)$$

where

$$G \equiv (p_{c+} - p_{c-} + \rho g f_a)/\rho g k \qquad (5)$$

is the non-dimensionalized pressure difference across the interface at the drop apex. It may be verified that

$$G = 2k/b = 2/\beta^{1/2} \ ,$$

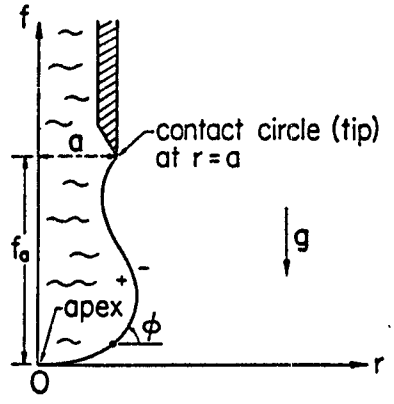

Fig. 1. Schematic of pendant drop showing dimensional coordinate system.

where b is the single radius of curvature at the drop apex, and β is the Bashforth and Adams "shape factor" used by many authors; see, for example, Refs. (3,6,7,8,9). Only positive values of G will be considered in this study; it will be seen (on Fig. 2) that this restricts the discussion to drops with apex below the contact circle plane.

The non-dimensionalized pressure difference at the contact circle cross-section is

$$-w_a = G - f_a/k = (p_{c+} - p_{c-})/\rho g k \quad . \tag{6}$$

In Ref. 8 the "hydrostatic pressure at the tip" is denoted by $\rho g Z_t = p_{c+} - p_{c-}$; since pressure varies linearly with vertical distance, Z_t/k is used there instead of y, as the dependent variable.

If R_1 and R_2 are written in terms of x, $y = G + w$, and φ (see Fig. 1) for the axisymmetric case, Eq. (1) becomes a pair of first-order ordinary differential equations for $w(\varphi)$ and $x(\varphi)$;

$$\begin{aligned} w' &= -\sin\varphi/(w + \sin\varphi/x) \quad , \\ x' &= -\cos\varphi/(w + \sin\varphi/x) \quad , \end{aligned} \tag{7}$$

with boundary conditions

$$w(0) = -G \quad , \quad x(0) = 0 \quad .$$

Development of Eqs. (7) is outlined in Refs. (15,16) with additional discussions in Refs. (2,6,7,10).

Equations (7) may be expressed as a single second-order ordinary differential equation for w(x);

$$w'' = \mp w\left(1 + w'^2\right)^{3/2} - w'\left(1 + w'^2\right) \Big/ x \quad , \tag{8}$$

where $\pm$ is to be used when $w' \gtrless 0$, respectively.

INTERPRETATION OF NUMERICAL SOLUTIONS

A standard Runge-Kutta finite difference technique was found adequate to solve the system, Eqs. (7). Further discussion on integration of the Young-Laplace equation may be found in the appendix to Ref. 10. The initial values $w(\varphi_1)$, $x(\varphi_1)$, for $0 < \varphi_1 \ll 1$, were obtained by series solution of Eqs. (7):

$$\begin{aligned} w(\varphi_1) &= -G + G^{-1}\varphi_1^2 + O\left(\varphi_1^4\right) \quad , \\ x(\varphi_1) &= 2G^{-1}\varphi_1 + O\left(\varphi_1^3\right) \end{aligned} \tag{9}$$

With φ_1 and G chosen, the numerical procedure yielded $w(\varphi{:}G)$, $x(\varphi{:}G)$; with $\varphi_1 = 10^{-6}$ the numerical results matched Eqs. (9) to five significant figures over a substantial range of $\varphi > \varphi_1$. This insured that the solution was

independent of φ_1, as long as $G \geq .25$. Solutions for small and large G will be discussed in a later section.

Results of the numerical solutions of Eqs. (7) are shown in Fig. 2. Each curve, $w(x;G)$, starts at $w(0;G) = -G$; shown in the figure are curves for integer values of $1 \leq G \leq 7$, as-well-as $G = 3.5, 2.5, 1.5, .50, .25$, and a segment of $G = 2.75$. The most striking feature of these integral curves is the appearance of envelopes which bound their undulating portions. Padday and Pitt (8) also notice one of these envelopes (see their Fig. 14), corresponding to $A_1B_1C_1E_1$ on Fig. 2. Comparison with their Fig. 14 shows sensible agreement with Fig. 2, with the possible exception of the neighborhood of E_1; it will be seen that the location of the envelope terminus E_1 in Fig. 2 is determined by an analytical solution of Eqs. (7) for small values of G, whereas Padday and Pitt (8) used a "fairing in" technique to obtain their envelope. Although Padday and Pitt (8) comment on the physical consequences (to be discussed below) implied by the envelope $A_2B_2C_2E_2$ in Fig. 2, they do not explicitly recognize its existence in the x,w-plane.

The reader is directed to Ref. 8 for an alternate and detailed description of the static stability phenomena to be described below. Padday and Pitt (8) identify pendant drops with tip coordinates on the $A_1B_1C_1E_1$ envelope as exhibiting "pressure-radius limited stability"; those with tip coordinates on the $A_2B_2C_2E_2$ envelope demonstrate "volume-radius limited stability". Pressure-radius limited drops become unstable with volume perturbation (for fixed tip pressure) at their stability limit; volume-radius limited drops become unstable with pressure perturbation (for fixed volume) at their stability limit. Most of the conclusions enunciated in Ref. 8 are in agreement with those to be discussed herein. However, there is a difference associated with the $A_2B_2C_2E_2$ envelope which will be noted when it is encountered.

The physical implications of Fig. 2 may be understood as follows: for a given value of the meniscus constant $k = \sqrt{\sigma/\rho g}$, and a given contact circle radius "a", the abscissa

$$x \equiv x_a = a/k \tag{10}$$

is determined; for a given pressure difference, $p_{c+} - p_{c-}$, in the contact circle cross-section

$$w \equiv w_a = -(p_{c+} - p_{c-})/\rho g k \tag{11}$$

is determined from Eq. (6). This specifies a point x_a, w_a on Fig. 2 through which may pass curves $G = \text{constant} > 0$; each of these curves (each with a different value of G), starting at $w(0;G) = -G$, and terminating at x_a, w_a, represents a static pendant drop configuration such that

$$y(x) = G + w(x) \quad . \tag{12}$$

It remains to discuss which of these curves represent stable drops (i.e., physically observable ones), and to note that for a given x_a there are values of w_a such that no values of G exist, or at most only one. Consider, for example, $x_a = .34$, $w_a = -3.86$; the two smallest values of G for this point

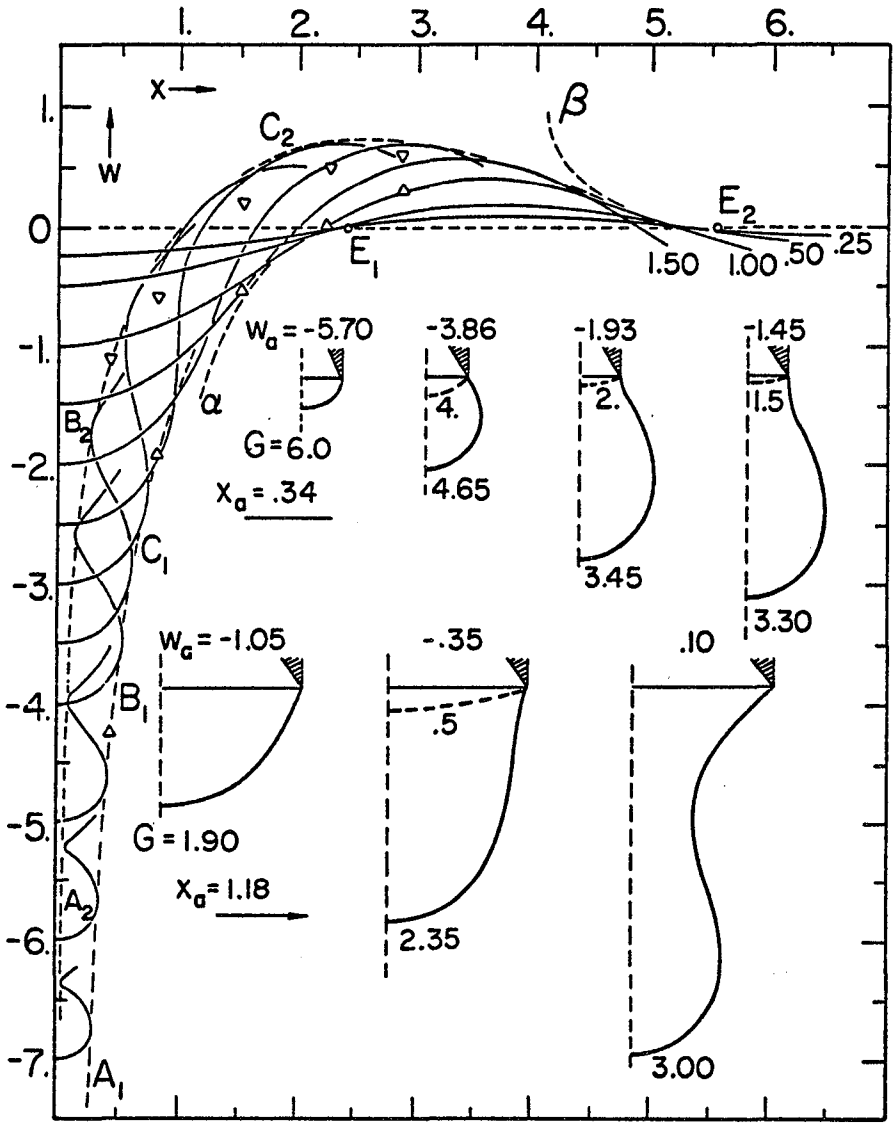

Fig. 2. Family of pendant drop profiles, and bounding envelopes, for the apex pressure parameter $G = -w(0;G)$. E_1 and E_2 (at x equal to the first two roots of $J_o(x) = 0$) are the termini of the high-pressure envelope ($A_1B_1C_1E_1$), and low-pressure envelope ($A_2B_2C_2E_2$), respectively. Envelope approximations αE_1 and βE_2 are given in Eq. (24); $A_1B_1C_1$ is given by Eq. (20). The data points (Δ,∇) correspond to the experimental data summarized in Table I. The sequence of profiles, for $x_a = .34$ and 1.18, respectively, show drop shapes from maximum to minimum tip pressure, with associated values of w_a and G.

are G = 4.00, 4.65. The drops corresponding to these specifications are shown on Fig. 2 as second from the left along the upper row of individually drawn pendant drops. Typically, the drop with the smallest G value (G = 4.0 in this case) does not touch the $A_1B_1C_1E_1$ envelope, while that with the next larger G value (G = 4.65 in this case) is tangent to this "outer" envelope.

With $x_a = .34$ the upper row of pendant drop shapes in Fig. 2 reflect the range of w_a values for which at least two values of G exist; at $w_a = -5.70$, $x_a = .34$ intersects the outer envelope; at this point only one value, G = 6.0, exists; for $|w_a| > 5.70$ no solutions exist. At the other extreme, $x_a = .34$ intersects the $A_2B_2C_2E_2$ (inner) envelope at $w_a = -1.45$ with G = 1.15, 3.30; for $0 < |w_a| < 1.45$ only one solution exists.

The second row of drop shapes in Fig. 2 illustrates, for $x_a = 1.18$, the same features of the solution. In this case the inner envelope limit occurs for $w_a = .10 > 0$, corresponding to $p_{c+} - p_{c-} < 0$, for which only one drop (G = 3.0) exists.

The physical implications of the above discussion for a given x_a (tip radius) are:

(a) at least two pendant drop shapes exist for each value of $-w_a$ (tip pressure) within a certain range of permissible values; experiment will verify that the drop corresponding to the smallest value of G (smallest pressure difference at the drop apex), for each permissible value of w_a, is stable (will occur naturally); experiment will also verify that its "conjugate" drop (that for the next largest value of G, but the same x_a, w_a) is metastable (can be observed experimentally, but under any perturbation it either contracts to the stable drop or elongates continuously until sudden break-off occurs);

(b) if $-w_a$ is greater than a critical value determined by intersection with the outer envelope no stable drop exists (dripping occurs);

(c) if $-w_a$ is less than another critical value determined by intersection with the inner envelope, the metastable drop does not exist; experiment will verify that this prediction corresponds to the sudden break-off of a quasistatically elongating (metastable) drop, with no constraints on volume or contact angle, whose sequence of shapes (for a given x_a) is closely approximated by the two rows of drops (solid curves) shown in Fig. 2.

It may be shown that, in general, a finite number (greater than 2) of G values exist for a given x_a, for each w_a within the permissible range delineated by the envelopes. However, all drop profiles for G greater than the two smallest values touch <u>both</u> envelopes before reaching x_a, w_a. These drops were never observable with the apparatus and experimental procedure to be subsequently described.

Finally, it should be noticed that

(a) stable drops exist for tip radii $E_1 < x_a < E_2$ only if the tip pressure $-w_a < 0$;

(b) no stable drops exist for $x_a > E_2$; this upper bound does not appear to be recognized in Ref. 8; therefore the "bath tap profile" shown there as Fig. 9 is questionable to this writer.

Both E_1 and E_2 are determined analytically in a later section.

ASYMPTOTIC SOLUTIONS FOR LARGE AND SMALL G

For large G (meaning large interfacial pressure differences at the drop apex) the apex curvature is large; this causes the linear pressure variation over the drop interior due to gravity to be small compared to the mean pressure within the drop; see Fig. 2. Thus gravity effects are small compared to the influence of interfacial tension; the drop shape is closely approximated by a spherical segment.

If G is small (meaning small interfacial pressure differences at the drop apex) the apex curvature is small; in this case the slope of the interfacial surface is everywhere small so that the drop shape is closely approximated by a linearized version of Eqs. (7).

Details of the solution to Eqs. (7) for large and small G will be given elsewhere. Both solutions are attainable as series expansions in terms of negative and positive powers of G for large and small G, respectively. These developments are in the spirit of the analysis given by Concus (17) for menisci internal to circular cylinders, and the solutions for rod-in-free-surface menisci in Ref. (16).

For large G:

$$w(\varphi;G) = -G + G^{-1}w_1(\varphi) + G^{-3}w_3(\varphi) + O(G^{-5}) \quad , \tag{13}$$

$$x(\varphi;G) = G^{-1}x_1(\varphi) + G^{-3}x_3(\varphi) + O(G^{-5}) \quad ; \tag{14}$$

where

$$x_1(\varphi) = 2\sin\varphi \quad , \tag{15}$$

$$x_3(\varphi) = 4[\sin^2\varphi + 2(\cos^3\varphi - 1)/3]/\sin\varphi \quad ; \tag{16}$$

$$w_1(\varphi) = 2(1-\cos\varphi) \quad , \tag{17}$$

$$w_3(\varphi) = (8/3)\{1/2 - 3\cos\varphi/2 + \cos^3\varphi - \ell n[(1+\cos\varphi)/2]\} \quad . \tag{18}$$

For small G:

$$w(x;G) = -GJ_o(x)$$

$$-G^3(\pi/4)\left\{\left[J_o(x) + x^{-1}J_1(x)\right]L_1(x) - \left[Y_o(x) + x^{-1}Y_1(x)\right]L_2(x)\right\} + O(G^5) \quad , \tag{19}$$

where $J_1(x)$, $Y_1(x)$ are Bessel functions of the first and second kind, respectively, and

$$L_1(x) \equiv \int_0^x zY_1(z)J_1^3(z)dz \quad ,$$

$$L_2(x) \equiv \int_0^x zJ_1^4(z)dz \quad .$$

The solution for large G exhibits the expected near spherical shape since

$$w \cong -G + 2G^{-1}(1-\cos\varphi) \quad , \quad x \cong 2G^{-1}\sin\varphi \quad ,$$

are parametric equations for a circle of radius $2G^{-1}$ with center at ($x = 0$, $w = -G + 2G^{-1}$). However, the representation given by Eqs. (13-18) does not admit an inflection point; therefore, it can describe the drop shape in the neighborhood of the outer envelope ($A_1B_1C_1$ in Fig. 2), but cannot be used to give the drop shape in the neighborhood of the inner envelope (A_2B_2 in Fig. 2).

The small G solution has as its leading term the solution to a linearized form of Eq. (8), namely,

$$w(x) = -GJ_o(x) \quad .$$

This solution was obtained by Rayleigh (18) for the case of nearly flat interfaces.

ENVELOPES OF SOLUTIONS

The large and small G pendant drop solutions, given in the previous section, may be used to obtain envelope curves. Analysis proceeds in the same way as in Ref. 16. The basic point is that an envelope curve is tangent to all members of the single parameter family of curves; there may be more than one envelope, which is the present case.

For large G, Eqs. (13-18) may be shown to require

$$G^2(\varphi) = x_1(\varphi)w_1'(\varphi)/x_1'(\varphi) - w_1(\varphi) - x_3'(\varphi)/x_1'(\varphi) \quad , \qquad (20)$$

on the envelope. Eq. (20), together with Eqs. (13-18) yield the envelope curve. This curve is shown as the dotted contour $A_1B_1C_1$ on Fig. 2. Within the scale of Fig. 2 one sees that the agreement with a possible "faired-in" envelope is excellent up to the neighborhood of point C_1.

For sufficiently large G, φ on the envelope approaches $\pi/2$. There an approximate solution for the outer envelope may be written as

$$w(x) \sim -2/x \quad , \qquad (21)$$

in the large G limit. This approximation can be used with no more than 5% error for $G \geq 8.0$; with $G \geq 15.0$ the error is within 0.1%.

The envelope for small G is obtained from Eq. (19). Define a function

$$f(x,w,G) = w + GJ_o(x) + G^3F(x) \quad , \tag{22}$$

where F(x) is the coefficient of G^3 in Eq. (19). On the envelope

$$\partial f(x,w,G)/\partial G = 0 \quad . \tag{23}$$

Eq. (23) yields

$$G^2(x) = -J_o(x)/3F(x) \quad , \tag{24}$$

on the envelope, for sufficiently small G; i.e., x must be such that G is small. Eqs. (19) and (23) allow the determination of the envelope curve w(x) for small G.

Numerical evaluation of Eq. (24) shows that in the neighborhood of the first zero of $J_o(x)$, i.e., for $x \leq x_o = 2.4048 \cdots$,

$$J_o(x) \geq 0 \quad , \quad F(x) < 0 \quad ;$$

therefore, real values of G exist for $x \leq x_o$. In the region $x_o \leq x \leq x_1$, where $x_1 = 5.5201 \cdots$ is the second zero of $J_o(x)$, $J_o(x) \leq 0$, and F(x) passes through zero and becomes positive. Therefore there is a second region in the neighborhood of $x \leq x_1$ where real values of G again exist. These two branches of Eq. (24) are plotted in Fig. 2 as the curves αE_1 and βE_2, respectively. It may be verified that these envelope curves possess zero slopes from the left and right at E_1 and E_2, respectively. The numerical curves for small G appear to agree very well with the analytical envelope segments αE_1 and βE_2. αE_1 is the small G portion of the outer envelope ($A_1B_1C_1$); βE_2 is the small G portion of the inner envelope ($A_2B_2C_2$).

These results indicate that for tip radii such that $E_1 < x_a < E_2$ no stable pendant drops can exist for positive tip pressures. Furthermore, when $x_a > E_2$ stable drops cannot exist, even when the tip pressure is negative. The $x_a < E_1$ bound was recognized explicitly by Pitts (10).

Any successful analysis for the inner envelope when G is large requires asymptotic drop solutions that admit inflection points. Only a limiting solution has been obtained using a crude integral approximation to the solution of Eqs. (7) in which an integrand is expressed through assuming the shape to be spherical. This yields for the x-coordinate of the inner envelope (with $\varphi \sim \pi/2$)

$$x \sim (16/3)G^{-3} \quad . \tag{25}$$

To this approximation the w-coordinate is simply $w \sim -G$.

This tentative result for the inner envelope in the limit of infinite G allows one to understand why pendant drops formed at very small tip radii have relatively large drop radii as they "drip off". The drop radius is approximated by the x-coordinate of the outer envelope, $x \sim -2/w \sim 2/G$ (from Eq. (21)); the tip radius is given by the x-coordinate of the inner envelope,

Eq. (25). Therefore, drop radius/tip radius $\sim 3G^2/8$, or

$$\text{drop radius} \sim [(3k^2/2)\cdot(\text{tip radius})]^{1/3} \tag{26}$$

as tip radius $\to 0$, $G \to \infty$. It would appear to be difficult to produce very small pendant drops simply by dripping from the end of a small tip; this is confirmed by experience.

EXPERIMENTAL PROCEDURE AND DATA REDUCTION

Experiments were conducted to test the validity of the theroetical conclusions. Pendant drops of a .1 normal $HC\ell$-H_2O solution in air were produced, photographed, and their relevant properties measured. The acidic aqueous solution (19) was used to minimize well-known surface aging effects (20), which may result in time dependent values of surface tension for an interval (order of minutes) after formation of a new surface. Direct observation of the stationary appearance of a newly formed drop (at least for the period of time necessary to take data) confirmed that surface aging did not introduce appreciable errors.

A schematic of the experimental apparatus is shown in Fig. 3; the caption relates the identifying letters to the system elements. All tubing is filled with the common liquid constituting the reservoirs and pendant drop.

Steps in a typical data taking event are as follows:

(a) with all stopcocks closed except ℓ_5, the vertical articulation is adjusted so that surfaces b and g communicate at a common level; the tip e (without drop) is lowered to touch g; this establishes the zero reading on the dial indicator f at which e (the contact circle location with known radius a) is at the same level as the "infinite reservoir b;

(b) the stopcocks are adjusted so that reservoir b and/or the micro-syringe c communicates, at the operator's discretion, with the tip;

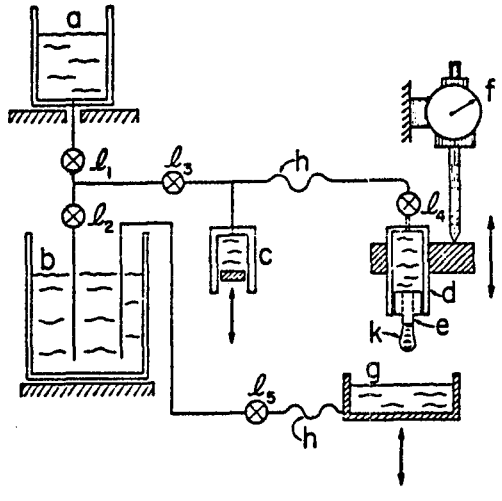

Fig. 3. Schematic of experimental apparatus: (a) filling reservoir; (b) tip-pressure reservoir; (c) micro-syringe device; (d) vertically articulated tip holder; (e) interchangeable tip; (f) dial indicator; (g) vertically articulated tip-level reservoir; (h) flexible constant-volume tubing; (k) pendant drop; ($\ell_{1,2,3,4,5}$) stop-cocks.

(c) the vertically articulated tip is moved relative to the reservoir b, and the micro-syringe is manipulated to produce a desired pendant drop;

(d) once a pendant drop has been produced which is stationary upon communicating e with b, the tip pressure $\Delta P \equiv (p_{c+} - p_{c-})/\rho g$ is read directly from the dial indicator (with .001 inch divisions);

(e) the stationary pendant drop is photographed.

To produce a drop at maximum ΔP, for a given tip radius a, requires the gradual lowering of e until it is no longer possible to observe a stationary drop when b communicates with e. Phenomena associated with drop development and break-off will be described in the next section; at this point assume that ΔP_{max} can be determined.

Before any comparisons between theory and experiment can be attempted it is necessary to know the meniscus constant $k \equiv \sqrt{\sigma/\rho g}$. This length may be determined from knowledge of ΔP_{max} and the contact circle radius, a. First, recognize that the contact point (x_a, w_a) corresponding to maximum contact circle pressure must lie on the $A_1B_1C_1E_1$ envelope in Fig. 2; second, observe that the ratio w/x = (pressure difference across the interface at f)/(radial distance of interface from axis of symmetry) must equal $\Delta P/a$ for $w = w_a$ and $x = x_a$. Thus, the locus of possible contact circle points in the x,w-plane for which ΔP and a are known must be on the straight line

$$w/x = -\Delta P/a \quad . \tag{27}$$

When $\Delta P = \Delta P_{max}$, the intersection of the straight line $w/x = -\Delta P_{max}/a$ with the envelope $A_1B_1C_1E_1$ gives the contact point for maximum pressure x_a, w_{a1}, say. Once x_a is so determined,

$$k = a/x_a \quad . \tag{28}$$

A test of the accuracy of the method is to compare the experimental drop shape at ΔP_{max} with that given by the numerical results. This prescription for finding k may be compared with that used in Ref. 16 for obtaining k in the case of rod-in-free-surface menisci.

The minimum pressure contact point, for the same x_a, should correspond to the intersection of $x = x_a$ with the envelope $A_2B_2C_2E_2$ of Fig. 2. This would determine x_a, w_{ae}, say, so that

$$\Delta P_{min,e} = -\rho g k w_{ae} \quad . \tag{29}$$

To produce a drop at minimum ΔP requires the gradual raising of tip e until a static-elongated drop can no longer be produced by manipulation of micro-syringe c and communication of e with b; in principal, this experimentally determined minimum pressure, as read by the dial indicator, should equal $\Delta P_{min,e}$ as given by Eq. (29).

An alternate procedure for determining $\Delta P_{min,e}$ is to close stopcock ℓ_3 (with ℓ_4 open, of course), and manipulate micro-syringe c to produce a sequence of static drops of increasing length. At a certain maximum length the drop suddenly breaks off. Since the system is static before break-off, the pressure in the contact circle cross-section just prior to break-off

should equal that predicted by Eq. (29). This may be tested by measuring the length f_{a2} of the drop just before break-off; then

$$y_{a2} = f_{a2}/k \quad . \tag{30}$$

With x_a the same as that for ΔP_{max}, numerical procedures, or Fig. 2, may be used to find the value of $G = G_2$ such that

$$y_{a2} = w(x_a;G_2) - w(0;G_2) \quad ;$$

then

$$w(x_a;G_2) \equiv w_{a2} = y_{a2} + w(0;G_2) \quad . \tag{31}$$

If $w_{a2} = w_{ae}$ then the drop broke off at the theoretical minimum pressure; in general, experiment has shown that $w_{a2} < w_{ae}$.

For ΔP such that $w_{a1} < w_a < w_{a2}$, for a fixed $x = x_a$, there are two observable pendant drops. The first with $f_a = f_{as}$, say, corresponding to the smallest value of G at x_a, w_a is stable to small disturbances; it is directly observable (with ΔP impressed upon the tip by communication between b and e, Fig. 3). The second drop with $f_a = f_{am}$, say, corresponds to the next largest G value; it is metastable, and must be produced by successive manipulation of c and ℓ_3 (with ℓ_2 and ℓ_4 open, and tip position fixed). The observer notes that if $f_a < f_{am}$, with ℓ_3 closed, then $f_a \rightarrow f_{as}$ after ℓ_3 is opened; on-the-other-hand, if $f_a > f_{am}$ for ℓ_3 closed, then f_a grows until the drop breaks off. When $f_a = f_{am}$ the drop length remains constant upon opening ℓ_3. This behavior is readily observed after some practice; a photograph of this stationary drop is obtained and used to compare its shape with that predicted by the appropriate G curve in Fig. 2.

Drops corresponding to larger values of G than the above noted smallest pair, for the same (x_a,w_a), were not observed.

EXPERIMENTAL RESULTS AND DROP BEHAVIOR

Photographs of pendant drop pairs, for a fixed x_a, and $w_{a1} < w_a < w_{a2}$ are shown in Fig. 4. In that case the tip radius was $\sim$ 1 mm, using distilled water in air. Passing from Fig. 4a to 4f corresponds to ΔP decreasing from slightly less than ΔP_{max} to slightly greater than ΔP_{min}; the darker profile belongs to the stable drop; the lighter profile to the metastable drop, as described in the previous section. The shapes correspond very closely to theory, with $k \cong 2.64$ mm (or $\sigma \cong 68$ dynes/cm), and $x_a \cong .38$; they may be compared with the first row of pendant drops, for $x_a = .34$, on Fig. 2. Published values of $\sigma \cong 72$ dynes/cm for water are considered correct under room temperature conditions; never-the-less, this value of 68 dynes/cm should not be disturbing because no special precautions were taken to insure surface or handling cleanliness; these experiments required internal consistency, not accuracy with respect to some external standard.

Production of maximum pressure drops requires some care. Even when tip e is set such that $\Delta P < \Delta P_{max}$ dripping can occur because, after break-off of

the elongating drop the new interface may be such that it forms an unstable drop which again grows and drips off. This dripping depends upon the pressure loss through the stopcocks and tubing between reservoir b and tip e as the emerging drop develops. The greater the pressure loss the less likely will the new interface form a drop which is "longer" than the metastable drop; if the new interface is "longer" than the metastable drop it will grow and drip; if it is "shorter" it will contract to the stable configuration and become stationary. One can always adjust the stopcocks so that the contraction, after break-off, is observed. As ΔP is increased (by moving tip e downward) the contraction-after-break-off motion diminishes; for $\Delta P = \Delta P_{max}$ contraction-after-break-off is not observable; the drop remains stationary, with intermittant dripping due to small disturbances or, possibly, surface aging effects.

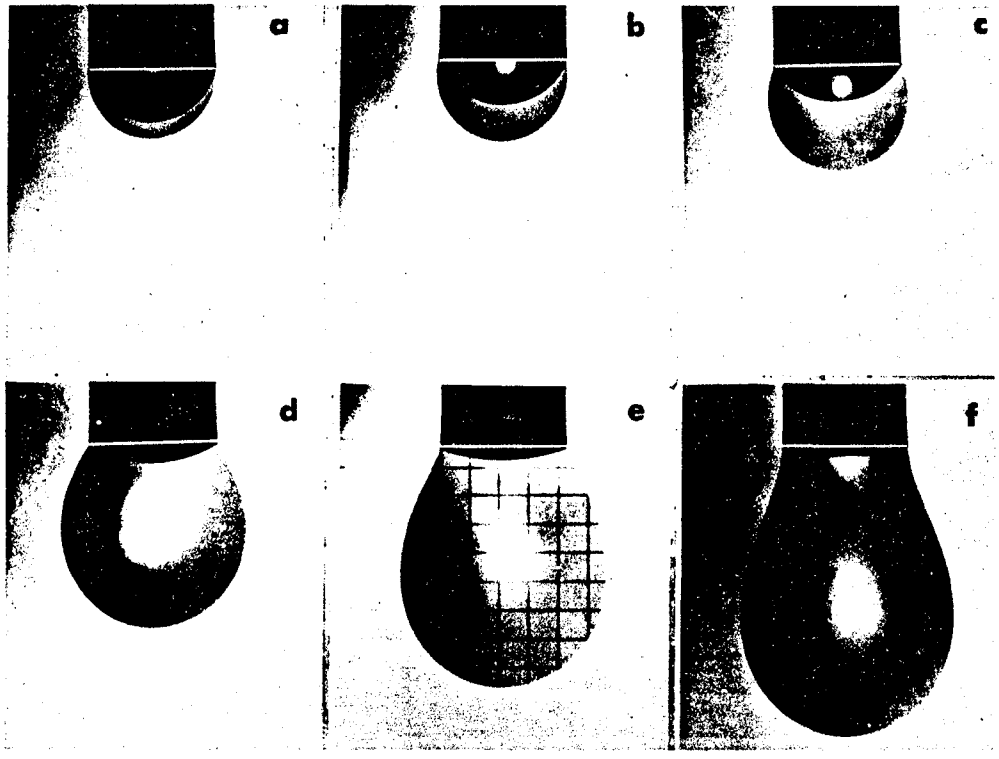

Fig. 4. Pendant drop pairs, showing the effect of decreasing pressure in the contact circle plane on the shape of stable (dark profile) and metastable (lighter profile)drops; distilled water in air. Contact circle radius, 1.05 mm; $x_a = 0.38$. Contact circle pressure in mm of H_2O: (a) 13.0; (b) 12.4; (c) 11.2; (d) 7.0; (e) 5.0; (f) 3.7. The superposed grid spacing in (e) is 0.5 mm. Temperature $\sim 80^{\circ}F$.

These ΔP_{max} drops are shown in Fig. 5 as the dark profiles; Table I summarizes the data for these drops.

Table I. Experimental data on pendant drops (.1N, HCℓ-H_2, aqueous solution in air at ~ 80°F), and results of data reduction using Fig. 2 and appropriate numerical solutions. Values of tip radius a, ΔP_{max} and a drop photograph (Fig. 5) are experimental; all other quantities are inferred from the numerical results using these inputs.

Drop No.	a(mm)	ΔP_{max} (mm H_2O)	x_a	w_a	G .	$\sqrt{\sigma/\rho g}$ (mm)	ΔP^{**}_{min} (mm H_2O)	$\Delta P^{\dagger}_{min,e}$ (mm H_2O)
1	1.05	10.9	.43	-4.22	4.55	2.5		
2	1.05		.43	-1.10	3.15	2.5	2.76	2.67
3	2.03	4.82	.82	-1.91	2.70	2.5		
4	2.03		.82	- .57	2.70	2.5	1.41	.62
5	4.04	1.37	1.55	- .53	1.50	2.6		
6	4.04		1.55	.20	2.25	2.6	- .51	-1.14
7	5.87	~ 0.	2.26	~ 0.	.85	2.6*		
8	5.87		2.26	.50	1.90	2.6*	-1.28	-1.71
9	7.46		2.87	.29	1.00	2.6*		
10	7.46		2.87	.62	1.75	2.6*	-2.38	-2.69

* Assumed values of the meniscus constant

** Experimentally inferred minimum tip pressure

† Theoretically predicted minimum tip pressure

Production of minimum pressure drops is relatively simple. The alternate procedure described in the previous section was used to obtain the photographs in Fig. 5 (the lighter profiles); again, the data for these drops are shown in Table I.

In Fig. 2 the triangular symbols correspond to the contact circle coordinates of the drops shown in Fig. 5. One sees that the ΔP_{max} points fall close to the $A_1B_1C_1E_1$ envelope; however, the ΔP_{min} points are all substantially below the $A_2B_2C_2E_2$ envelope, except for the smallest drop at $x_a = .43$; i.e., $\Delta P_{min} > \Delta P_{min,e}$ as given by Eq. (29). This seems reasonable since the force balance on smaller drops is dominated by surface tension forces; for larger drops inertia effects become important. It is believed that an experiment with better vibration control could result in closer agreement with the low pressure limit.

Padday and Pitt (8) exhibit in their Fig. 33 some experimental and theoretical results for critical and separating volumes of volume-radius limited pendant drops; i.e., those drops whose static stability limits are given by the present $A_2B_2C_2E_2$ envelope. Unpublished photographs by R. Picknett (1970) "of pendant drops just before rupture" are noted with apparently excellent agreement of the experimental parameters of his critical shapes with the theoretical results of Ref. 8.

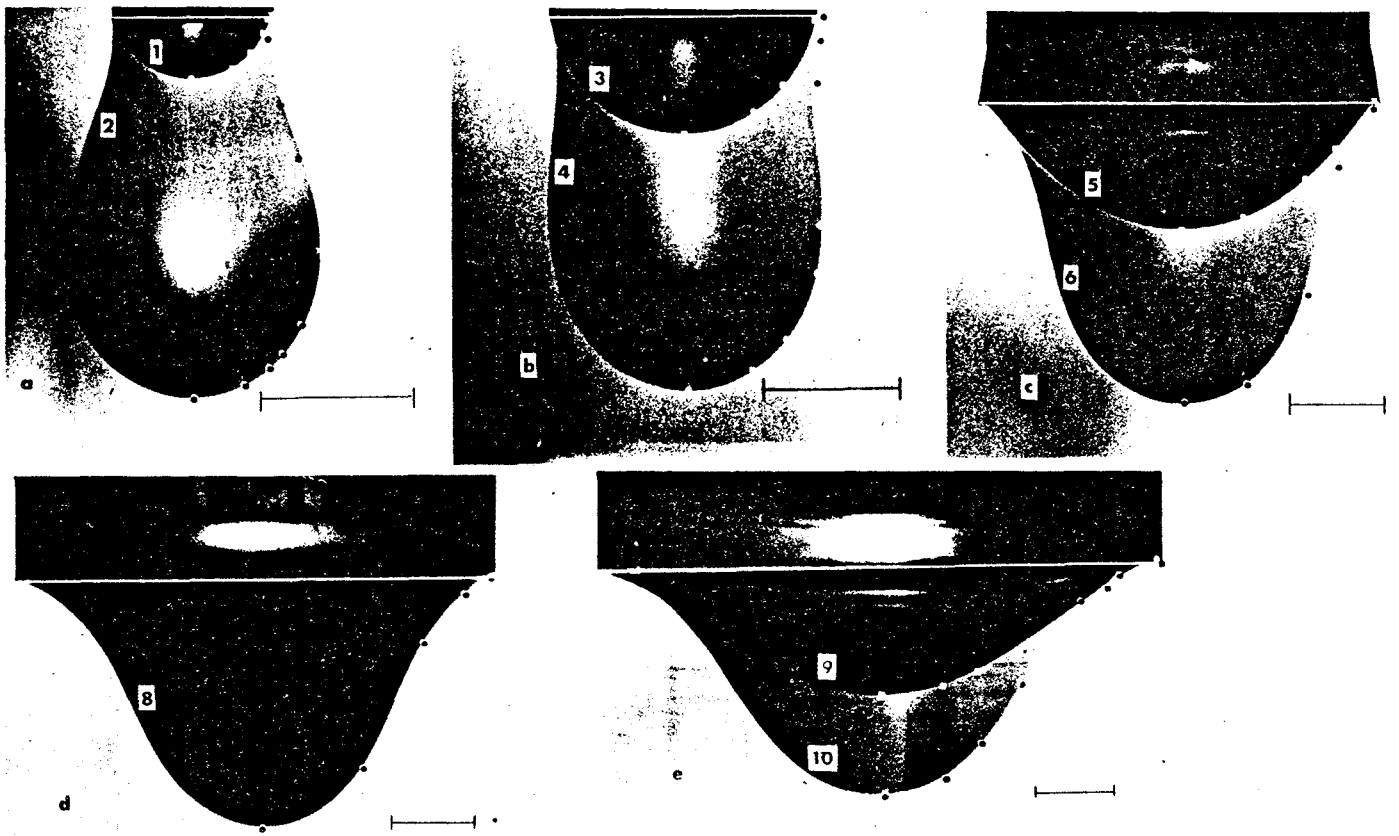

Fig. 5. Photographs of static pendant drops: 0.1 N, HCℓ-H_2O solution in air. Those with two surfaces superposed are double exposures of drops with a common contact circle. Numbers adjacent to the surfaces refer to Table I which summarizes the data for these drops. The symbols (circles and squares) give the applicable numerical results. Triangular symbols in Fig. 2 show the contact circle location of these drops in the x,w-plane. The scale mark in each photograph indicates 2 mm. Temperature ~ 80°F.

CONCLUSIONS AND RESULTS

Assuming that the meniscus constant k is known, the following conclusions may be listed.

(a) Certain limiting conditions for the production of pendant drops can be seen from the envelopes bounding solution curves for drop shapes.

(b) A "high-pressure" envelope gives the maximum pressure in the contact circle cross-section, with prescribed radius, for existence of static drops.

(c) There exists a "low-pressure" envelope which, for a prescribed contact circle radius, gives the minimum pressure for static pendant drops.

(d) An intermediate range of contact circle pressures exist, for a given tip radius, such that two observable pendant drops exist, one stable, the other metastable.

(e) For a certain range of contact circle radii only negative contact circle pressures will produce static pendant drops.

(f) There exists a maximum contact circle radius for existence of static pendant drops.

(g) Experiments reported herein are in good agreement with the foregoing remarks.

(h) Analytical solutions for the drop shape, in the form of series representations, were obtained for low and high pressure in the contact circle plane.

(i) These solutions allow the envelopes for high and low pressure to be analytically determined; in particular, envelope properties in the limits $G \to \infty$, and $G \to 0$ are explicitly displayed.

REFERENCES

1. T. Young, Phil. Trans. Roy. Soc. (London) 95, 65 (1805).
2. P. S. Laplace, "Méchanique Céleste, No. 4, Supplément au X^e Livre (1805); translation, Vol. 4, by N. Bowditch, Little and Brown, Boston (1839).
3. F. Bashforth and J. C. Adams, "An Attempt to Test the Theories of Capillary Action," Camb. Univ. Press, London/New York (1833).
4. T. Lohnstein, Ann. Phys. 22, 767 (1907).
5. G. Bakker, "Kappilarität," Handbuch der Exp. Phys. (ed. W. Wien and F. Harms), 6, Leipzig: Akademische Verlagsgesellschaft (1928).
6. J. F. Padday, "Surface and Colloid Science," (ed. E. Matijevic and F. R. Eirich), 1, pp. 39-149, Wiley (Interscience), New York (1969).
7. H. M. Princen, Ibid., 2, pp. 1-84.
8. J. F. Padday and A. J. Pitt, Phil. Trans. Roy. Soc. (London) 275, 489 (1973).
9. J. F. Padday, Phil. Trans. Roy. Soc. (London) 269, 265 (1971); for reference to tables see J. electroanal. Chem. 37, 313 (1972).
10. E. Pitts, J. Fluid Mech. 63, 487 (1974).
11. R. D. Gillette and D. C. Dyson, Arch. Rat. Mech. and Analysis, p. 150 (1974).

12. R. D. Gillette and D. C. Dyson, Chem. Eng. J. 3, 196 (1972).

13. R. D. Gillette and D. C. Dyson, Chem. Eng. 2, 44 (1971).

14. F. M. Orr, L. E. Scriven, and A. P. Rivas, Preprints, 48th National Colloid Symposium, Univ. of Texas, Austin, June (1974).

15. C. Huh and L. E. Scriven, J. Colloid and Interface Sci. 30, 323 (1969).

16. A. A. Kovitz, J. Colloid and Interface Sci. (to appear).

17. P. Concus, J. Fluid Mech. 34, 481 (1968).

18. Lord Rayleigh, Proc. Roy. Soc. (London) 92, 184 (1915).

19. Private communication.

20. J. J. Bikerman, "Physical Surfaces," Academic Press, New York/London (1970), p. 69.

ACKNOWLEDGEMENTS

The author's interest in this subject was initiated by Dr. Ralph E. Hise who, as a graduate student, studied the statics and dynamics of a liquid index (Ph.D. thesis, Northwestern University, 1968). It is also a pleasure to recognize many stimulating general discussions with Professors R. A. Burton, A. L. Kistler, and M. C. Yuen of the Department of Mechanical Engineering and Astronautical Sciences, Northwestern University.

ADDENDUM

During the Colloquium the author was made aware of the following publications concerning interfacial problems:

Finn, R., "Capillarity Phenomena," Uspechi Matem. Nauk, Petrovski Mem. Issue; to appear.

Pujado, P. R., Univ. of Minnesota, Ph.D. Thesis (1971).

Concus, P., and Finn, R., "On Capillary Free Surfaces in a Gravitational Field," Acta Math. 132, 207 (1974).

Hida, K. and Miura, H., "Shape of a Bubble or a Drop Attached to a Flat Plate Subject to a Weak Gravitational Force," Nippon Koku Uchu Gakkai-Shi 18, 433 (1970); in Japanese, with English abstract.

See also Hida, K. and Nakanishi, T., J. Phys. Soc. Japan 28, 1336 (1970).

ON THE PRODUCTION OF BUBBLES BY FOCUSED LASER LIGHT

W. Lauterborn and H. Bolle

Drittes Physikalisches Institut, Universität Göttingen

D-34 Göttingen, Federal Republic of Germany

ABSTRACT

The bubbles produced in liquids when giant pulses of a ruby laser are focused into it are studied by high speed photography with up to one million frames per second using a rotating mirror camera. In most of the experiments the light pulses are focused into distilled water by a single lens with low f/number to get only one single spherical bubble or a very limited number of bubbles. Bubble motion is evaluated from the frames with the aid of a digital computer using a graphic input device. Smoothed radius-time curves of different portions of the bubble wall are obtained by a sophisticated treatment of the data also allowing a reliable calculation of bubble wall velocities (except at the very instant of bubble collapse). Bubble production by laser light shows to be a very flexible method to investigate bubble dynamics. It is applicable to a broad variety of experimental configurations. An extensive study has been done so far on bubble dynamics near boundaries and to a lesser extent on bubble interaction and nonspherical bubbles. One of the numerical examples of the collapse of a spherical bubble near a plane solid boundary obtained by Plesset and Chapman (J. Fluid Mech. 47 (1971) 283) could be realized experimentally. Good agreement is found. Moreover, bubble history can be followed far beyond the validity of the theoretical model. Besides the well-known microjet formation towards the wall two new jetlike phenomena are observed which both may be given the name counterjet as these jets are directed away from the wall. Bubble interaction and the collapse of nonspherical bubbles usually lead to jetting phenomena, too. Almost symmetric bubble division into two parts with simultaneous jet development in opposite directions has been observed on collapse of a bubble being flattened by a bigger bubble in its vicinity. Presently the usefulness of holographic lenses to produce many-bubble configurations is investigated.

INTRODUCTION

Bubble dynamics is a basic problem in cavitation research. Its experimental investigation suffers from a lack of suitable bubble production methods. As a new approach to this problem, the bubbles formed when focussing giant pulses of a ruby laser into a liquid were studied. The advantages of this bubble production method are:

1. The location and the instant of production are precisely known. Thus, high-speed photography, the most powerful experimental method to study bubble dynamics, applies rather easily.
2. There are no disturbing objects - like electrodes when using underwater sparks - influencing bubble motion.
3. Spherical bubbles can be obtained. Thus a comparison with existing theory is possible.

The first results on bubble dynamics obtained by this new method look very promising.

APPARATUS

A schematic diagram of the most essential parts of the experimental setup is shown in Fig. 1. Giant pulses emitted by a Q-switched ruby laser with a beam

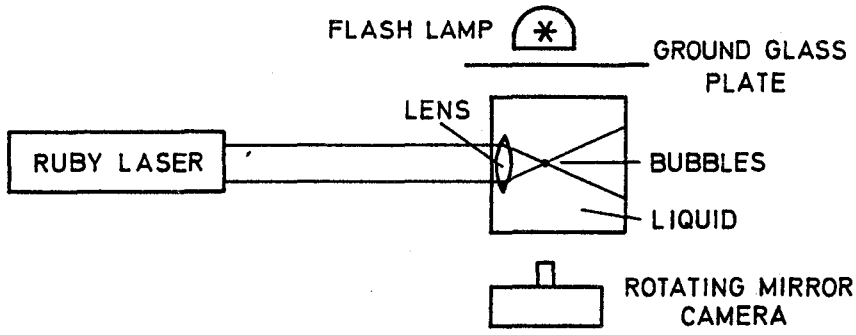

Fig. 1: Schematic diagram of the setup

cross section of about 1 cm, a duration of about 30 to 50 nsec and a total energy of about 0.1 to 1 Joule are focused into the liquid under investigation by a single lens with a focal length of 1.28 cm in air. The container used is a cube with an edge length of 10 cm. The bubbles produced in the vicinity of the focal point of the lens (in most cases submerged into the liquid) are diffusely illuminated by a flash lamp through a ground glass plate and photographed by a rotating mirror camera. Spherical bubbles then look black on a bright background with a bright central spot where the light passes the bubble undeflected. For the sake of clearness, the electronics needed for timing the different activities of the devices has been omitted in the diagram as well as some auxiliary equipment like a He-Ne laser used for alignment of the optical components and the photographic apparatus.

RESULTS

When a giant pulse of the ruby laser is focused into water, usually several points of breakdown occur, each being the center of a rapidly expanding bubble. The number of bubbles formed depends on the purity of the water, the light intensity and the effective numerical aperture of the lens used. The number of bubbles is decreased when the water is purified and increases with increasing light intensity and focal length of the lens used. The dependence on the purity of the water suggests that light absorbing impurities in the water act as nuclei for the bubble forming process. In the present investigation doubly distilled water with normal gas content (full access to the air, no degassing) is used in most cases. The chance to get only one single spherical bubble is then rather high. The dependence of the number of points of breakdown on the light intensity and the focal length of the lens is quite clear, as with increasing light intensity and focal length the liquid volume where the light intensity is sufficient to start a breakdown at an impurity becomes larger.

It was observed that when the centers of breakdown are very close to each other, the bubbles coalesce on growth and often form a spherical or almost spherical bubble. With a lens of "long" focal length (5 cm, say) and at a

sufficiently high light intensity (and total energy) oblong bubbles may develop from the string of points of breakdown either symmetric or unsymmetric with respect to the focal plane, but with a high degree of symmetry about the optical axis. These observations can be said to be a direct experimental proof of the stability of the spherical shape of a bubble during growth. When the centers of breakdown are not very close to each other, all kinds of distorted bubbles and linear bubble strings will occur. Up to now, the arrangement of these bubbles cannot be reproduced, but the pure observation of what may happen has led to new insights into bubble behavior upon interaction. Some examples will be given below. But our first aim was to produce single spherical bubbles to compare their motion with theoretical models and predictions as a first step to more complicated bubble systems.

In this paper we will mainly discuss the dynamics of a single spherical laser-produced bubble near a plane solid boundary. Besides the well-known microjet formation towards the solid boundary two new jetlike (or spikelike, as they seem to be on a smaller scale) phenomena were discovered. These jets or spikes are directed away from the wall (or, to be cautious, appear at the side of the bubble opposite to the wall). Therefore the name counterjet is suggested. A possible explanation for the occurrence of these jets is given below.

DYNAMICS OF A BUBBLE NEAR A PLANE SOLID BOUNDARY

Phenomena observed

A typical sequence of pictures of bubble growth, collapse and rebound taken at 75 000 frames per second is shown in Fig. 2. The solid boundary (brass plate) is to be seen dark in the lower part of each frame. It is somewhat unsharp because it extends far out of the depth of field of the photographic system. This is the main source of error in the evaluation of distance-time curves of the bubbles to evaluate their dynamics (especially speeds of different parts of the bubble wall). With a computer-aided sophisticated smoothing procedure described below this difficulty could be overcome. The bubble of Fig. 2 was produced at a distance of b = 4.5 mm from the solid boundary and reached a maximum radius of R_{max} = 1.1 mm. Thus the ratio b/R_{max}, important for a normalization, becomes 4.17. This is a rather large value, nevertheless a pronounced jet is produced towards the boundary on collapse by involution of the top of the bubble. It should be pointed out that the jet (of water) is directly visible as a fine dark line only in the bright central spot of the bubble after the first collapse. The conelike or funnel-shaped protrusion is a secondary effect produced by the jet through deformation of the lower bubble wall on impingement. The jet inside the protrusion is supposed to be much thinner (like the fine dark line in the bright central spot). Also it is believed that the velocity of the tip of the protrusion is not the velocity of the jet which will be higher. So we make a difference between a so-called "tip velocity" and a "true jet velocity". Up to now only the tip velocity could be measured (see below).

On second collapse the bubble starts as a deformed (nonspherical) bubble of a distinct shape: flattened at the top, elongated at the bottom and with a thin rod (or needle) of liquid connecting top and bottom. This very special configuration (but always obtained by an initially spherical bubble near a plane solid boundary) usually collapses with a formation of a jet in the opposite direction of the first jet. This jet is just to be seen in the last frame of Fig. 2, but its development can also be suggested by the flattening of the formerly elongated bottom of the bubble. Sometimes (it is believed in very symmetric and undisturbed situations) no such jet is observed, presumably because the rod of liquid of the first jet prevents its development. The explanation of this second jet formation runs as follows. A region of higher curvature of a

bubble wall collapses always faster than a part of a bubble wall with less curvature. This statement has been deduced from experiments with nonspherical bubbles (1) and is also supported by numerical calculations (2). The inward motion of such a faster collapsing part of a bubble wall is not arrested when it involutes due to the inertia of the liquid. Thus a jet is formed striking the opposite wall and again causing a protrusion which indicates the jet (see also (3)).

The preceding description of bubble dynamics near a plane solid boundary is valid in the majority of cases investigated. But quite often a somewhat different behavior of the bubble is observed as shown in Fig. 3. In Fig. 3 only part of the whole bubble motion is shown near first collapse. The framing rate in this case is 300 000 frames per second corresponding to a time interval between frames of 13.3 µsec. In the first frame it can be seen that the bubble is elongated with its long axis perpendicular to the solid boundary. Then the bubble top flattens and involutes, but after collapse a tiny jet (or spike) sticks out of the bubble in the opposite direction! The big jet towards the boundary develops on a much slower time scale. A possible explanation makes use of the above statement that higher curved parts of a bubble wall collapse faster than less curved parts. As a spherical bubble near a solid boundary becomes elongated perpendicular to the boundary, two areas of higher curvature develop which tend to collapse faster than the rest of the bubble (compare (2)). Obviously, there must be a competition between the higher curved lower part of the bubble tending to a higher collapse rate and the influence of the solid boundary tending to slow down the motion of the lower part of the bubble. It seems (because of the almost flat appearance of the bubble near final collapse) that the higher curvature takes over in the final stage of collapse and may thus be able to develop its own jet. It is believed that this jet can only appear when there is some dissymmetry present in the bubble motion so that the main jet downwards cannot swallow it or push it with it (because of its higher velocity and bigger dimensions). That this may be the case is indicated by the fact that always, when such a "counterjet" is observed, the main jet is grossly distorted and does not develop very well. The counterjet sticks considerably far out of the upper part of the bubble immediately after collapse. This is not due to its high velocity but because the bubble as a whole is suddenly driven to the wall during collapse. The often porcupine-like appearance of a bubble immediately after collapse (or on collapse) may be attributed to the striking of the two jets (or opposite parts of the bubble wall) leading to a splashing of liquid in all directions but preferably downwards, the direction of the higher velocity jet.

These explanations of the observed behavior of initially spherical bubbles near a plane solid boundary seem probable but must be confirmed by more experiments, especially with higher framing rates and higher resolution to confirm the mechanisms. The crucial part is the final stage of bubble collapse which is not easily accessible.

Evaluation of the Frames

As a vast number of films were taken of bubbles collapsing near solid boundaries, the evaluation of bubble motion from the films became a problem. Also, as the boundary appears unsharp on the frames the data (distance of different points of bubble wall from the boundary) may scatter considerably unless a very careful estimation of the grey scale the boundary exhibits is made. These problems were overcome with the aid of a computer and a graphic input device. The frames were projected onto the translucent plate of the input device and the coordinates (bubble wall and boundary) fed into the computer. These data (as indicated by the crosses in Fig. 4a) were intended to be low pass filtered

for smoothing, but because of the steep collapse of the bubble some precautions must be taken as to not filter out just this steep collapse. To get rid of the sharp edges in the distance-time curves (just for filtering) of the top and bottom curves of the bubbles (T and B in Fig. 4a) the sum (S = T + B) and difference (D = T - B) curves are calculated (Fig. 4b), the part of the difference curve after collapse is turned about (change of sign), and both sum and difference curves are continued symmetrically to get periodic curves without jumps (denoted S' and D' in Fig. 4c). These curves are then low pass filtered by Fourier transformation (FFT on the computer), weighting of the spectra (multiplication with a special function having low pass properties), and back transformation (again a FFT on the computer). The curves obtained are denoted S'_g and D'_g in Fig. 4d. These curves are then unscrambled to get the original, but smoothed, distance-time curves of the bubble as shown in Fig. 5a.

As from the smoothed curves in Fig. 5a derivates could be taken, the velocities of different points of the bubble wall could be calculated. They are plotted in Fig. 5b for three cases. Of course, the velocity-time curves could not be followed through the collapse for the top and bottom of the bubble as there is a very fast change of speed and the framing rate is too slow to follow the motion. The corresponding parts of the curves before and after collapse are therefore connected only by a straight dotted line.

In Fig. 5 T again denotes the top of the bubble and B the bottom (after collapse it is the tip of the protrusion). C is the center of the bubble (taken from the central bright spot of the bubble in the frames). The framing rate in this case is 250 000 frames per second and the ratio of the distance of the bubble (center) and the maximum radius 3.08. The time scale is arbitrarily set to zero at the beginning of the plot. The center curve shows that the bubble is driven towards the boundary during the final stage of collapse and the first stage of rebound with a maximum velocity of about 35 m/sec, attained apparently at the very point of collapse (Fig. 5b). The bubble develops a jet towards the boundary as can be seen in Fig. 5a from the asymmetry of the top and bottom curves after collapse with respect to the center curve. The tip velocity of the protrusion can be read from the lower diagram in Fig. 5. A maximum velocity of about 120 m/sec was calculated. As mentioned before, the true jet velocity is supposed to be higher than this tip velocity by an amount not yet known. But in any case the experiments show that even bubbles far away from boundaries (in this case $b/R_{max} \approx 3$) may develop a strong jet (when undisturbed). From these experiments it is concluded that a spherical collapse of a cavitation bubble down to the very point of collapse is highly unprobable in any real situation and that jet formation of a cavitation bubble on collapse is a normal process.

Comparison with Theory

Plesset and Chapman (4) have calculated the collapse of an empty, initially spherical cavity in the neighborhood of a solid boundary for two cases, i.e. $b/R_{max} = 1$ and 1.5. The case $b/R_{max} = 1.5$ could be realized experimentally and thus compared with these calculations. As the instants at which pictures are taken of the bubble do not coincide with the instants of the calculated curves, an interpolation of the experimentally determined bubble shape is done to fit the calculated curves. Additional difficulties arise from the fact that even at the framing rate applied of 300 000 frames per second the instant of collapse cannot be determined precisely and also from the calculations it is not quite clear what instant may be taken as the final collapse. (There seems to be no simple answer to this question.) Thus a more or less arbitrary estimate of the instant of collapse, where the experimental and theoretical curves were fitted in time, has been made and then the shape of the bubble was compared back in

time. The result is shown in Fig. 6. The open circles represent experimental data, the solid lines are taken from the calculations of Plesset and Chapman (4). The bubble has a maximum radius of R_{max} = 2.6 mm and was produced at a distance to the boundary of b = 3.9 mm, so that b/R_{max} = 1.5. At the framing rate of 300 000 frames per second not the total history of bubble motion could be followed because of the limited frame number of 80 of the rotating mirror camera used. Also the initial shape of the bubble is not truely spherical. But nevertheless the behavior of the bubble (involution of the top and jet formation towards the boundary) fits the theory almost quantitatively.

BUBBLE INTERACTION

As mentioned earlier, special precautions must be taken to get only one single spherical bubble. Usually a linear string of bubbles is produced. All other parameters being the same, by variation of the laser light intensity (or total energy) it is possible to get only two bubbles along the optical axis. Up to now the mode structure and stability of the ruby laser could not be sufficiently controlled to get reproducible two-bubble configurations, but since films are easily taken a wide variety of different two-bubble configurations could be studied. It was noted that jet formation is predominant in bubble interaction. When the two bubbles are produced far away from one another and are of almost equal size, both develop a jet towards the other bubble on collapse. When the two bubbles are very close to each other they coalesce on growth to form a spherical or almost spherical bubble. At an intermediate distance they flatten on growth on the facing sides and usually develop jets towards each other. An example with a smaller and a bigger bubble is shown in Fig. 7, taken at 75 000 frames per second. The smaller bubble shows a peculiar shape on collapse as the hemispherical bubbles observed by Benjamin and Ellis (5). Qualitatively, this shape can again be understood by the fact that parts of a bubble with higher curvature collapse faster than parts of less curvature. A pronounced jet, clearly visible in the bright central area of the bigger bubble, is formed by the smaller bubble. It penetrates the bigger bubble and sticks out at the opposite side. The collapse of the bigger bubble is markedly influenced by the collapse of the smaller bubble, it collapses strongly nonspherically with one side flattened.

A second very interesting example was obtained with one big and one very small bubble produced simultaneously at some distance (Fig. 8, 75 000 frames per second). The small bubble is highly flattened attaining a shape very similar to an oblate spheroid like the earth but with somewhat different curvatures at the north and south pole. It is believed that this shape is a result of both the strong shock wave emitted on bubble formation(6) and the geometrical interaction of both bubbles. On collapse the small bubble divides itself into two parts and develops two jets through each of these parts in opposite directions through the north and south pole. One jet penetrates the big bubble and leads to a division of the big bubble on collapse into two parts (not shown in Fig. 8). This behavior of the small bubble can again be understood by the fact that parts of higher curvature collapse faster than those of less curvature. The curvature of the small bubble in the direction towards the north and south pole at the equator is higher than at the poles. Thus the bubble constricts more rapidly along the equator and the inflowing water divides the bubble upon contact at its center. The water can be supposed to attain a high velocity and is apparently squeezed out in the direction of the north and south pole simultaneously because of the symmetry of the configuration. So two bubbles each with a jet in the opposite direction to the other are formed.

The collapse of a bubble of similar shape as in Fig. 8 was calculated by Chapman and Plesset (2) up to near collapse. Qualitatively the calculations could

be confirmed by this observation. Moreover, bubble history can be followed in the experiment beyond the point of collapse giving a more complete picture of bubble dynamics in this case.

ON THE PRODUCTION OF MANY-BUBBLE CONFIGURATIONS

Of most interest in cavitation bubble dynamics is the investigation of whole cavitation bubble fields where many bubbles are present at a time because this is what happens in reality. The multiple interactions may totally alter the dynamics observed with a single bubble or with two bubbles. To start some systematic experiments concerning these questions an extension of the method described is presently investigated. The idea is to use holographic lenses (i.e. lenses with multiple focal points in space) to get simultaneous breakdown in the liquid (and thus bubbles) at different points according to the lens used. The experimental setup will then remain simple as before.

Fortunately the question of the production of holographic lenses that will withstand the high light intensities needed has recently been studied and obviously been solved (7). In the technique described in (7) the holographic interference pattern is etched in chromium or quartz layers deposited on glass substrates. It is not a simple technique as it demands some very special equipment and very careful and precise work. But the knowledge that it will work will render it less difficult. The first step is to calculate the hologram, i.e. the interference pattern in some plane of the different points in space (later the focal points of the holographic lens) and a plane reference wave perpendicular to the plane. Upon illumination of the hologram with the plane reference wave, the points in space will be reproduced, and thus a lens with multiple focal points is obtained. Several digital holographic lenses have already been calculated on a computer, but not yet etched into quartz layers. An example is shown in Fig. 9, where a small portion of a calculated hologramm is shown in almost the size the electrostatic plotter produces it on paper. To plot the interference pattern only two grey scales (black and white) were used. This introduces higher diffraction orders, but also the efficiency of the first diffraction order is enhanced. The real drawback of having only two levels in the plot (or hologram) is the appearance of additional points in space near the original ones due to what may be called "cubic difference diffraction orders". This question has been studied by several authors the first being Friesem and Zelenka (8). The hologram part of which is shown in Fig. 9 focuses a plane wave into 27 points in four different planes. The points are arranged in such a way as to form the letter string "HOLO" with each letter in a different plane in space. Fig. 10 shows photographs of the point distribution in space obtained upon illumination of the hologram. The arrangement of the letters in different depths can easily be noticed.

We hope that with this method it will be possible to produce many-bubble configurations with some degree of repeatability so that their dynamics can be investigated.

FUTURE WORK

As the first results look very promising the investigations will go on with special emphasis on bubble interaction studies. As a sideline to these investigations a holographic apparatus is developed to store the bubble fields produced in a hologram (9). Then better conclusions on the bubble shapes and their relative location in space can be drawn. As up to now no suitable holographic apparatus exists capable of taking holograms at high framing rates (a holographic equivalent to the rotating mirror camera) first steps towards the con-

struction of such a device are undertaken.

ACKNOWLEDGEMENTS

The work on laser-produced bubbles reported here was supported by the Deutsche Forschungsgemeinschaft and the Fraunhofer-Gesellschaft. The experiments with the rotating mirror camera were done at the Institut für den Wissenschaftlichen Film in Göttingen.

REFERENCES

1. W. Lauterborn, "Kavitation durch Laserlicht", Acustica, in press.
2. R.B. Chapman and M.S. Plesset, "Nonlinear effects in the collapse of a nearly spherical cavity in a liquid", Trans. Amer. Soc. Mech. Eng., J. Basic Eng., Vol. 94 (1972), pp 142-146.
3. W. Lauterborn, "General and basic aspects of cavitation", in: L. Bjørnø (Ed.), Proc. 1973 Symp. Finite-Amplitude Wave Effects in Fluids, Copenhagen. IPC Science and Technology Press, Guildford (England) 1974, pp. 195-202.
4. M.S. Plesset and R.B. Chapman, "Collapse of an initially sperical vapor cavity in the neighborhood of a solid boundary", J. Fluid Mech., Vol. 47 (1971), pp. 283-290.
5. T.B. Benjamin and A.T. Ellis, "The collapse of cavitation bubbles and the pressures thereby produced against solid boundaries", Phil. Trans. Roy. Soc. London, A., Vol. 260 (1966), pp. 221-240.
6. W. Lauterborn, "High-speed photography of laser-induced breakdown in liquids", Appl. Phys. Letters, Vol. 21 (1972), pp. 27-29.
7. A. Engel, J. Steffen and G. Herziger, "Laser machining with modulated zone plates", Appl. Optics, Vol. 13 (1974), pp. 269-273.
8. A.A. Friesem and J.S. Zelenka, "Effects of film nonlinearities in holography", Appl. Optics, Vol. 6 (1967), pp. 1755-1759.
9. K. Hinsch, F. Bader and W. Lauterborn, "The dynamics of cavitation bubble fields studied by double-pulse holography", in: L. Bjørnø (Ed.), Proc. 1973 Symp. Finite-Amplitude Wave Effects in Fluids, Copenhagen. IPC Science and Technology Press, Guildford (England) 1974, pp. 240-244.

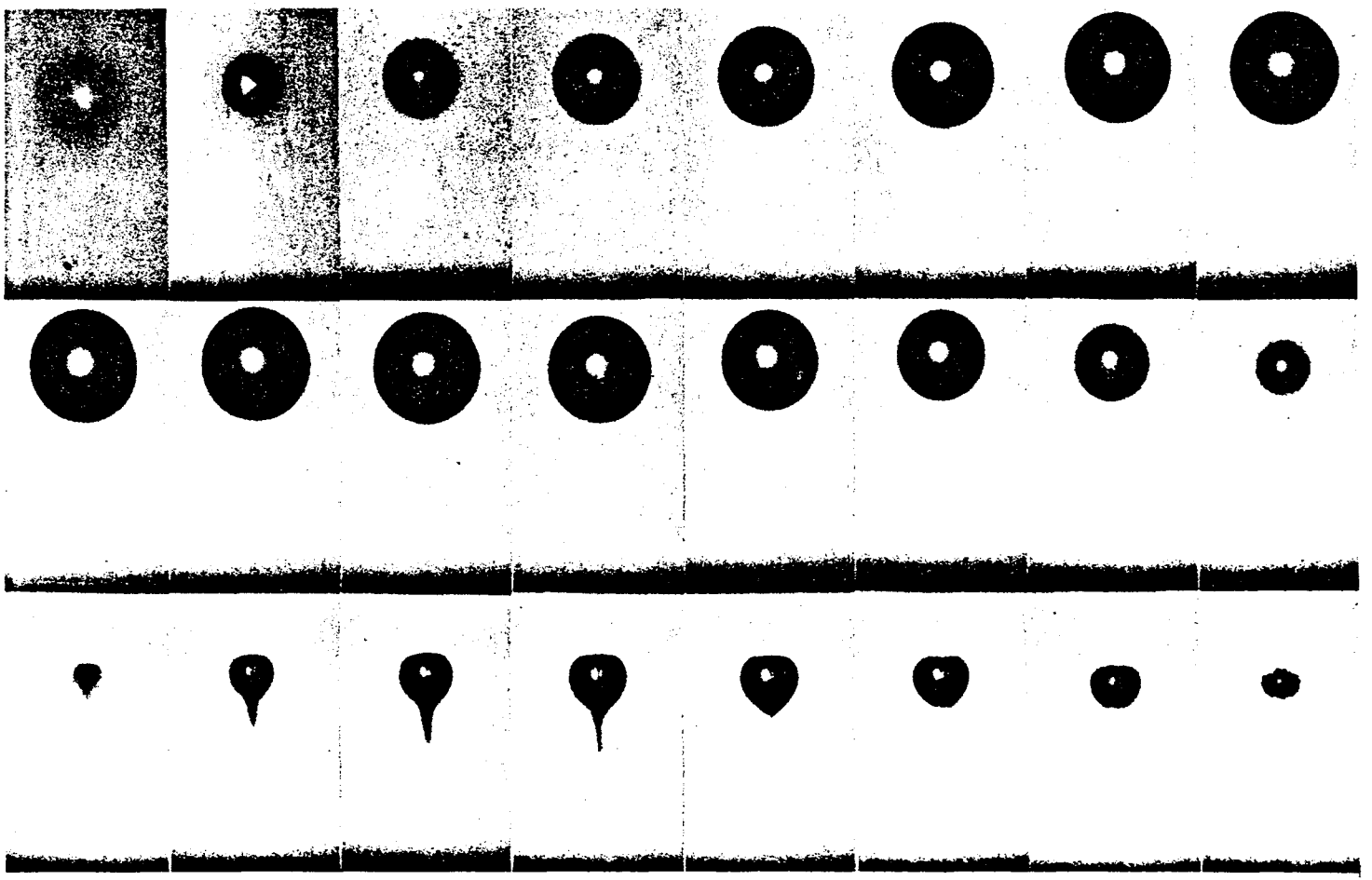

Fig. 2: Dynamics of a laser-produced spherical bubble near a solid boundary. Framing rate 75 000 frames per second, maximum bubble radius R_{max} = 1.1 mm, distance of bubble center from solid boundary b = 4.5 mm, b/R_{max} = 4.17, size of the individual frames 5.4 mm x 3.3 mm.

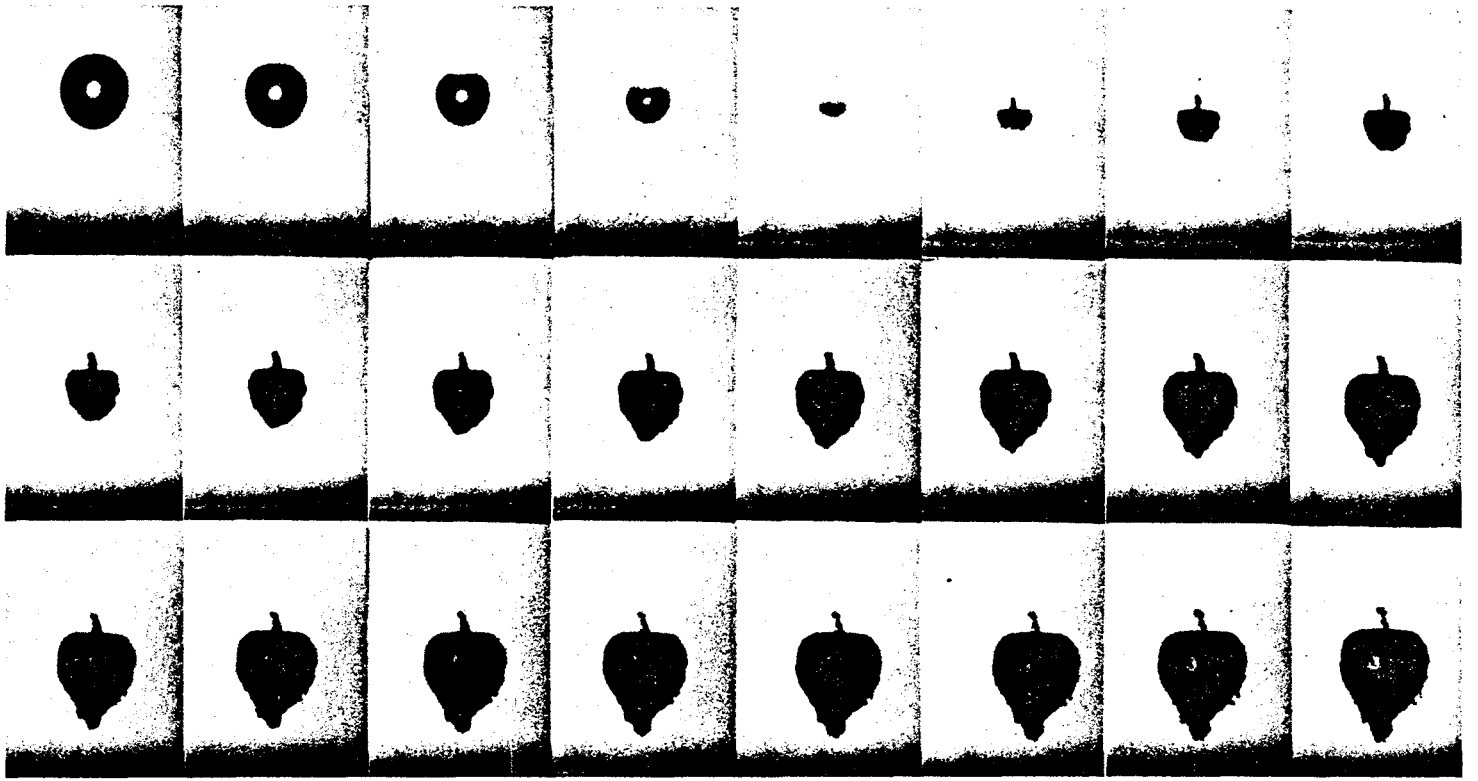

Fig. 3: Bubble collapse and rebound near a solid boundary. The framing rate is 300 000 frames per second, the size of the individual frames is 5.6 mm x 3.9 mm.

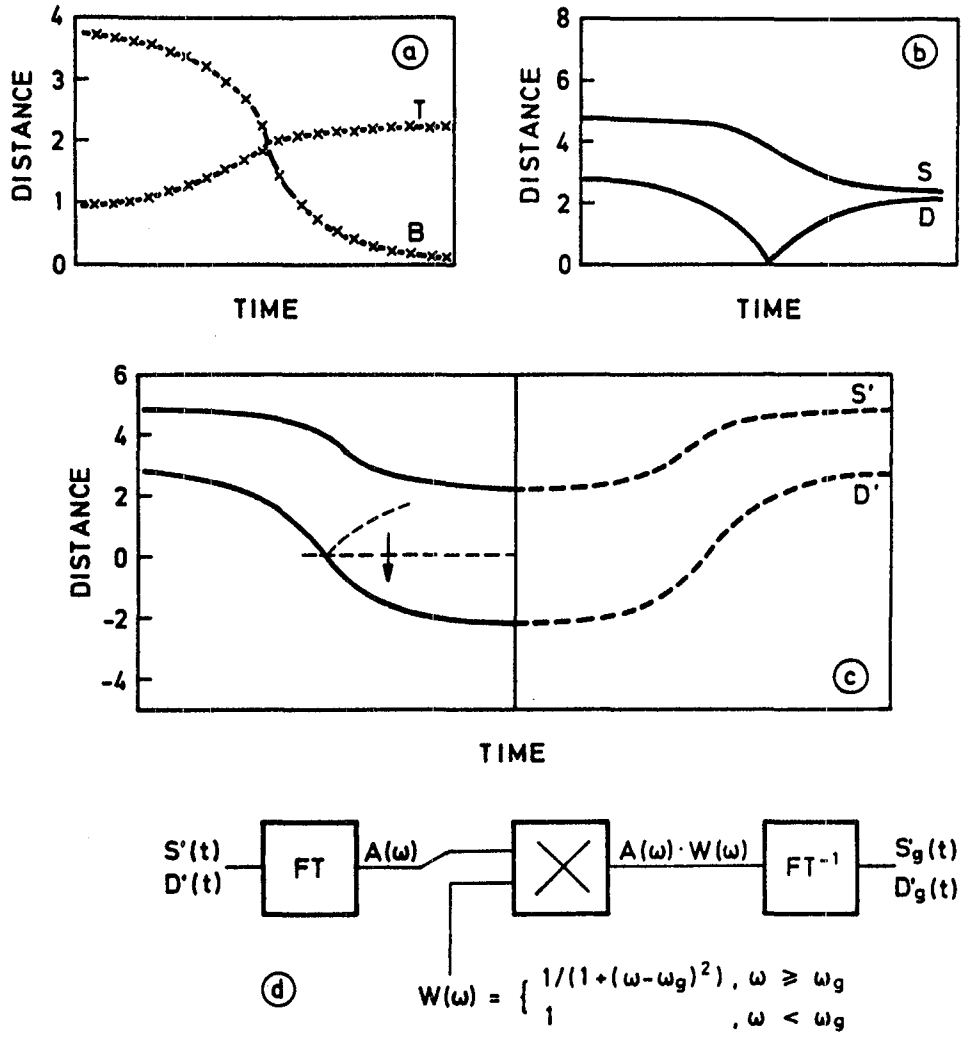

Fig. 4: Smoothing procedure applied to the distance-time curves of different points of the bubble wall taken directly from the frames.
a) Top (T) and bottom (B) curves of the bubble.
b) Sum (S = T + B) and difference curves (D = T - B).
c) Turn about of part of the difference curve and symmetric continuation of both sum and difference curve.
d) Smoothing of the curves by low pass filtering (Fourier transformation, weighting of the spectra, back transformation).

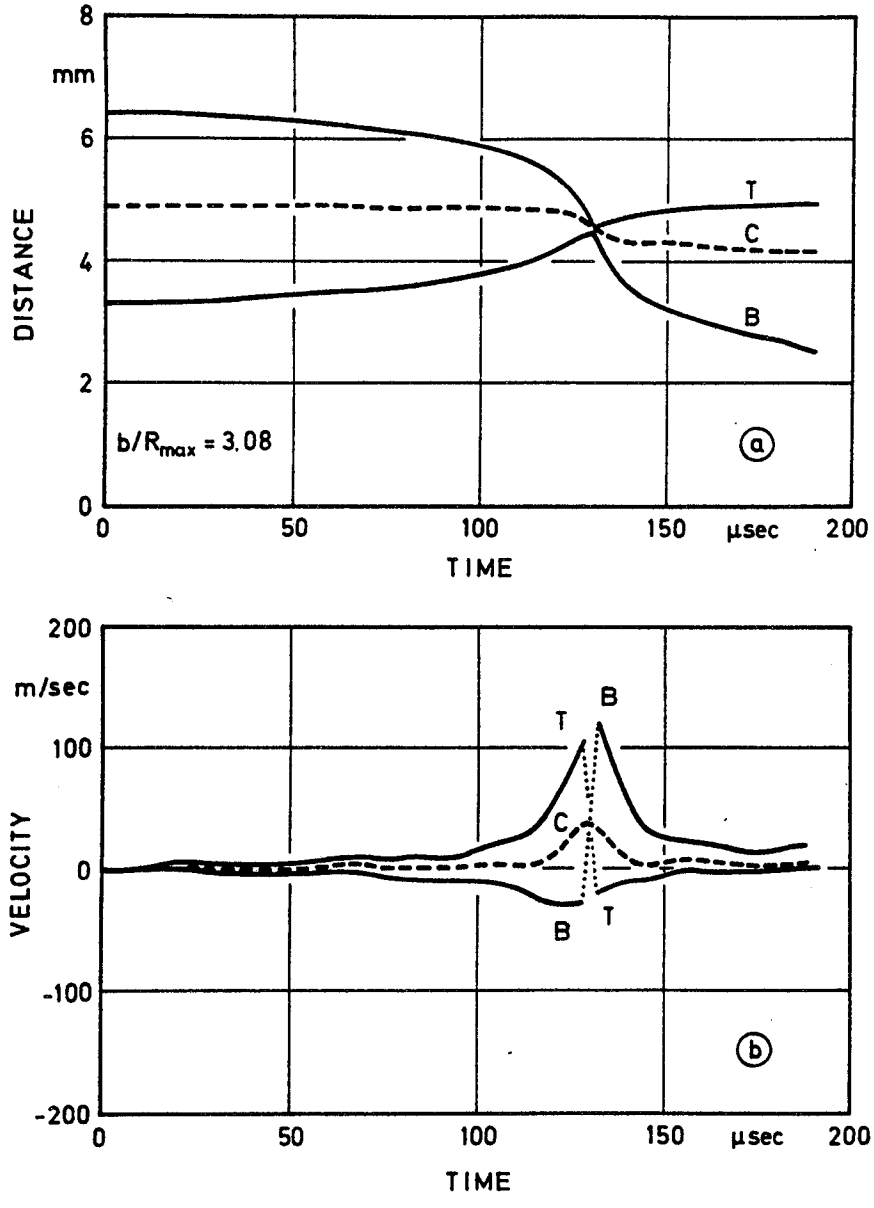

Fig. 5: Bubble collapse near a solid boundary evaluated from a film with a framing rate of 250 000 frames per second.
a) Distance from the boundary for different points of the bubble wall (T = top, C = center, B = bottom) versus time.
b) Velocity of the three points versus time.

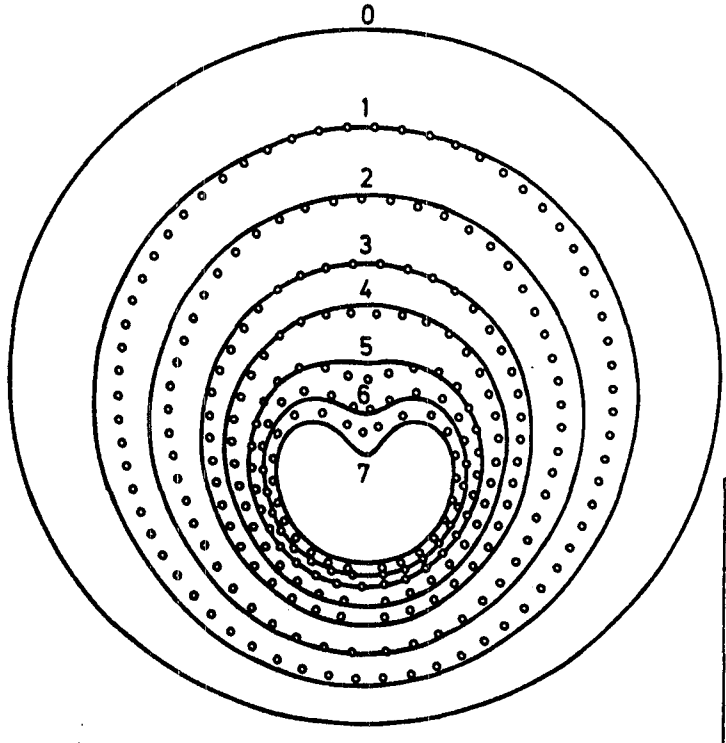

Curve	time $R_{max}\sqrt{\rho_0/\Delta p}$
0	0
1	0.725
2	0.875
3	0.961
4	0.991
5	1.016
6	1.028
7	1.036

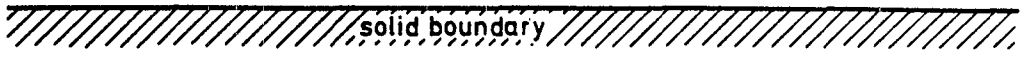

Fig. 6: Comparison of experimentally determined bubble form (open circles) on collapse of a spherical bubble near a plane solid boundary with interpolated theoretical curves taken from Plesset and Chapman (4) (solid curves). Framing rate 300 000 frames per second, maximum bubble radius R_{max} = 2.6 mm, distance of bubble from the solid boundary b = 3.9 mm, b/R_{max} = 1.5..

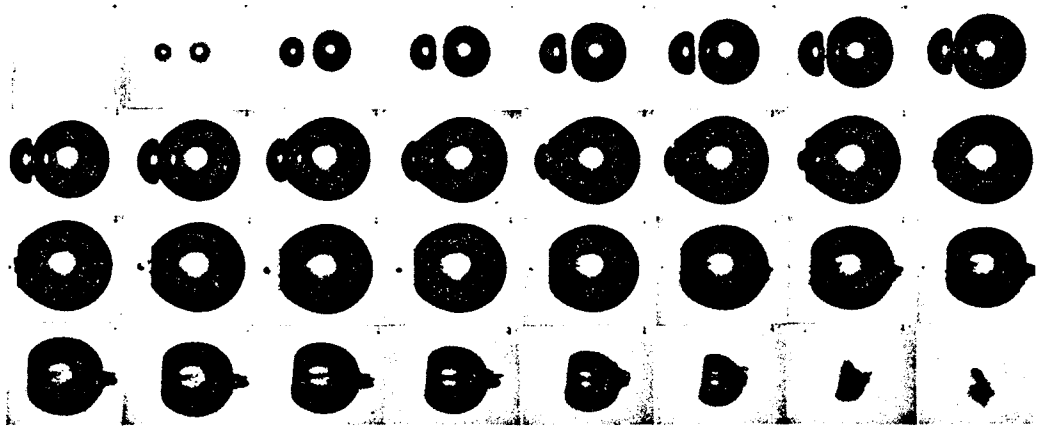

Fig. 7: Interaction of two bubbles produced at an intermediate distance. The framing rate is 75 000 frames per second, the size of the individual frames is 5 mm x 6 mm.

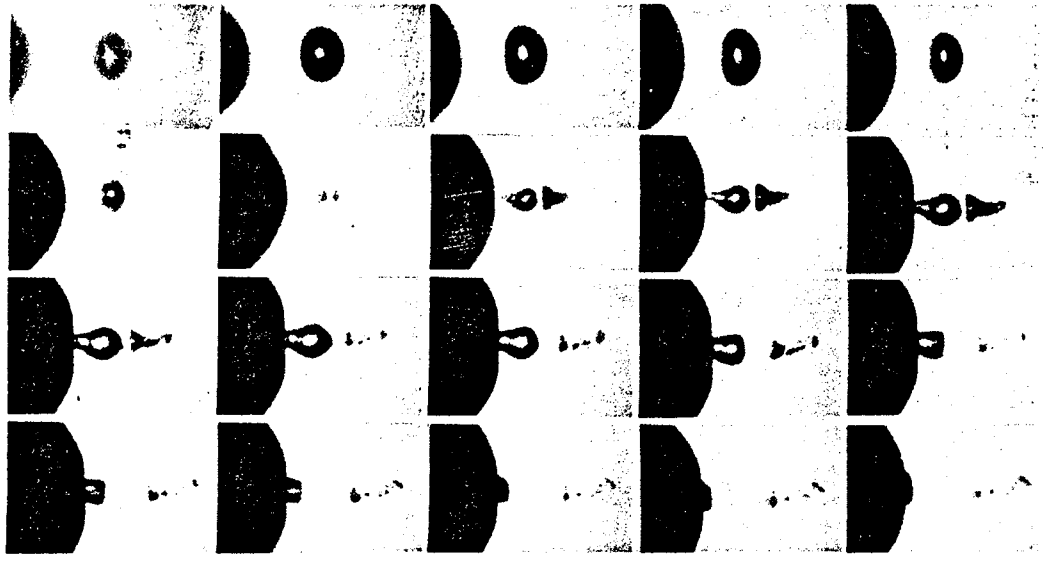

Fig. 8: Interaction of two bubbles, one being small compared to the other. The framing rate is 75 000 frames per second, the size of the individual frames is 2.25 mm x 3.5 mm.

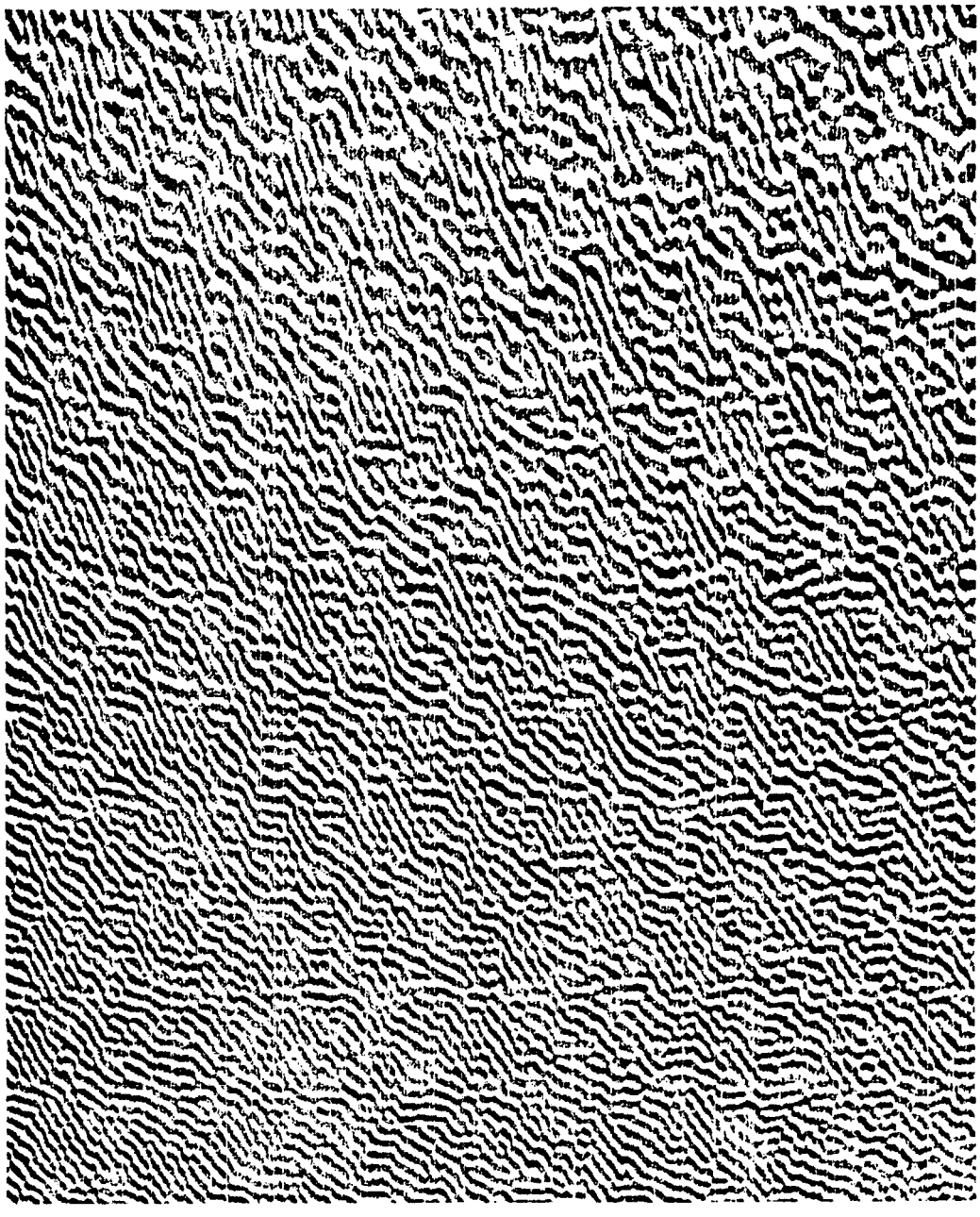

Fig. 9: Portion of a digital holographic lens (hologram) focusing a plane wave into 27 points in space, reproduced at almost the original size of the electrostatic plotter output. For application the plot is reduced in size. One edge of this plot would then have a length of about 5 mm.

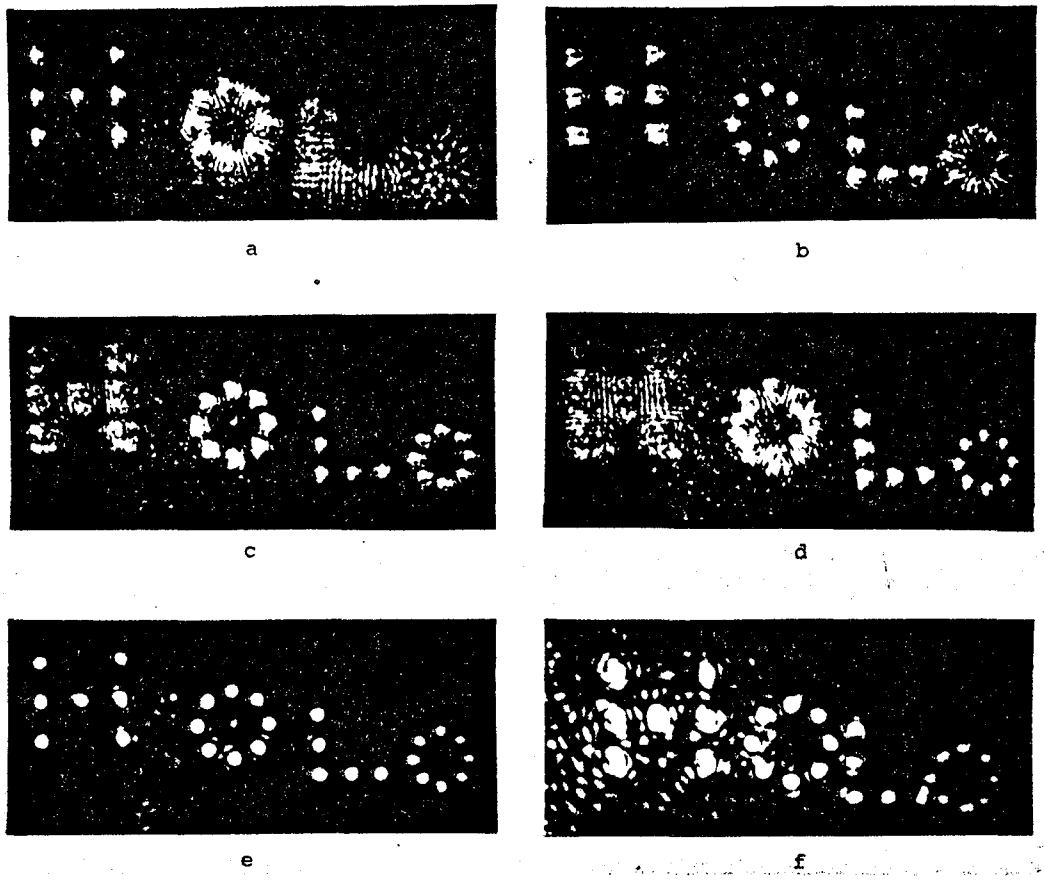

Fig. 10: Photographs of the focal point distribution of the holographic lens part of which is shown in Fig. 9.
a) - d) Small depth of field, the four different planes of the letters are approximately in focus,
e) large depth of field, viewpoint as in a) - d) (loss in resolution),
f) another aspect (looking from the left) at large depth of field.

SOME ASPECTS ON DYNAMICS OF NONSPHERICAL BUBBLES AND LIQUID DROPS

D. Y. Hsieh
Division of Applied Mathematics, Brown University, Providence, R.I.

ABSTRACT

The general formulation of the dynamical problem of nonspherical bubbles and liquid drops, or the problem of two ideal fluids separated by an interface is presented both in terms of Eulerian and Lagrangian coordinates. These formulations may also be expressed by a Hamiltonian variational principle which takes into account explicitly the surface energy of the interface between the two fluids. The general formulations are applied specifically to two classes of problems, i.e. the nonlinear oscillation of bubbles in an oscillating pressure field and the coalescence of two liquid drops or bubbles.

I. INTRODUCTION

This paper reports some of the recent progress in the study of the dynamics of nonspherical bubbles and liquid drops. To deal with some specific problems in this category, the straightforward way may be the numerical methods making extensive use of computers. For analytical approaches, the perturbation expansion based small deviation from spherical symmetry of the system have usually been adopted in the past. Recently, an approximate method based on the variational formulation seems to offer some promise for the study of this class of problems, and that is one aspect of the problem we shall report in this paper.

Most of the fluid dynamical problems are more conveniently treated in terms of Eulerian coordinates. It is also generally true for most studies on bubbles and liquid drops. However, there are certain situations in which the Eulerian coordinates are not adequate. In particular, the details of the process of break-up and coalescence are often lost in terms of the more convenient Eulerian coordinates. Therefore a parallel development in terms of Lagrangian coordinates is very helpful and sometimes even essential. The similarities and differences of the solutions in terms of Eulerian and Lagrangian coordinates, could furthermore offer some insight for further progresses.

Thus, in the following we shall first present the Eulerian and Lagrangian formulations of the problem as well as the corresponding variational principles. Then we shall use the Lagrangian formulation to solve the linear stability problem of a spherical bubble. Using this solution as a guide, we shall indicate how an approximate variational method can be developed to solve the problem of

nonlinear nonspherical motion of the bubble. Next we shall also use the Lagrangian formulation to treat the problem of the coalescence of two liquid drops, one large and one small. The approaches employed to deal with the bubble problem can of course be adapted to deal with the problem of the liquid drops and vice versa.

Another class of the problem is the oscillation of bubbles and liquid drops in an externally imposed oscillating pressure field. Here we present some of the recent results on the nonlinear oscillation of a spherical bubble in an external sinusoidal pressure field using the newly developed variational method. Ultimately, the variational method will be applied also to the problem of nonlinear oscillation of nonspherical bubbles. The present study can be considered as a preliminary step towards that goal.

II. Eulerian and Lagrangian Formulation and the Variational Principle.

Let $$F(x^1,x^2,x^3,t) = 0 \tag{1}$$

be a surface that divides the whole space into two regions G and G' each occupied by an ideal, compressible fluid. Then the governing equations in Eulerian form in G are[1]:

$$\rho_{,t} + (\rho v^i)_{,i} = 0 , \tag{2}$$

$$(\rho s)_{,t} + (\rho s v^i)_{,i} = 0 , \tag{3}$$

and

$$v_{i,t} + v^j v_{i,j} = -\frac{1}{\rho} p_{,i} , \quad i = 1,2,3, \tag{4}$$

where ρ is the density; s, the entropy; p, the pressure and v^i the ith contravariant component of the velocity of the fluid in G; and the general tensor notation has been adopted here. If we introduce the internal energy function $U(\rho,s)$, then we also have the following thermodynamic relations:

$$\frac{\partial U}{\partial \rho} = \frac{p}{\rho^2} , \tag{5}$$

and

$$\frac{\partial U}{\partial s} = T , \tag{6}$$

where T is the temperature.

An identical set of equations in primed variables can be similarly written down for the fluid in the region G'.

On the interface $F(x^1,x^2,x^3,t) = 0$, the kinematic and dynamic interfacial conditions are as follows:

$$F_{,t} + v^i F_{,i} = 0 , \tag{7}$$

$$F_{,t} + v'^i F_{,i} = 0 , \tag{8}$$

and

$$p-p' = \sigma\left(\frac{1}{r_1} + \frac{1}{r_2}\right) , \tag{9}$$

where σ is the coefficient of surface tension, and r_1 and r_2 are the two principal radii of curvature at the point of interest on F=0. They are taken to be positive if the centers of curvature lie on the side of G, and negative if otherwise.

To express the same problem in Lagrangian form, we introduce (X^1,X^2,X^3) as the generalized coordinates of a fluid particle at the initial moment. Thus the present coordinates of the particle, (x^1,x^2,x^3) are given by

$$x^i = x^i(X^1,X^2,X^3,\tau). \tag{10}$$

while the inverse relation is

$$X^i = X^i(x^1,x^2,x^3,t) , \tag{11}$$

and $t=\tau$.

Then the equations of conservation of mass, entropy and momentum are given respectively by:

$$\frac{\rho(X^1,X^2,X^3,0)}{\rho(X^1,X^2,X^3,\tau)} = \mathcal{J} , \tag{12}$$

$$s(X^1,X^2,X^3,\tau) = s_o(X^1,X^2,X^3) \tag{13}$$

$$\rho x^i{}_{;J}\ddot{x}_i = -p_{;J} \tag{14}$$

where

$$\mathcal{J} = \frac{[\det g_{km}]^{1/2}}{[\det g_{KM}]^{1/2}} \frac{\partial(x^1,x^2,x^3)}{\partial(X^1,X^2,X^3)} , \tag{15}$$

and $\dot{(\ )}$ denotes the material derivative with respect to time and $(\ )_{;J}$ denotes the total covariant derivative.[2]

The kinematic interfacial condition is expressed simply by the equation of initial interface:

$$F_o(X^1,X^2,X^3) = 0 \ , \tag{16}$$

while the dynamical interfacial condition is

$$p-p' = -2\sigma H \ , \tag{17}$$

where H is the mean curvature of the present interface and can be expressed in terms of surface tensors.[2]

The above Eulerian formulation as given by (2)-(9) can be shown[3] to be equivalent to the following variational problem: the flow field of the system and the motion of the interface are such that the functional

$$J = \int_{t_1}^{t_2} dt \int_V dV[\tfrac{1}{2}\rho v^2-\rho U] - \int_{t_1}^{t_2} dt \int_A \sigma dA \ , \tag{18}$$

is an extremum, subject to the constraint conditions (2), (3), and

$$(\rho\alpha)_{,t} + (\rho\alpha v^i)_{,i} = 0 \ , \tag{19}$$

where α can be interpreted as one of the Lagrangian coordinates of the fluid particles, A denotes the interface and $V = V_G+V_{G'}$ is volume of both regions G and G'.

To deal with regions that contain incompressible fluids or of uniform state, it is often more convenient to use another functional for variation[3]:

$$J = \int_{t_1}^{t_2} dt \int_V p(H,s)dV - \int_{t_1}^{t_2} dt \int_A \sigma dA \ , \tag{20}$$

where the pressure p is considered as a function of the enthalpy H and entropy s given by the usual thermodynamic relation

$$dp = \rho dH - \rho T ds, \tag{21}$$

with H explicitly prescribed as

$$H = -\phi_{,t} - s\psi_{,t} - \alpha\chi_{,t} - \frac{1}{2}(\phi_{,i} + s\psi_{,i} + \alpha\chi_{,i})^2 , \tag{22}$$

where χ is a variable conjugate to α, while the fluid particle velocity is interpreted as:

$$v_i = \phi_{,i} + s\psi_{,i} + \alpha\chi_{,i} . \tag{23}$$

The Lagrangian formulation as given by (12)-(17), on the other hand, can be shown[2] as equivalent to the following variational principle: the flow field of the system and the interfacial conditions are such that the functional

$$I = \int_{t_1}^{t_2} d\tau \int_V dX^1 dX^2 dX^3 [\det g_{KM}]^{1/2} [\tfrac{1}{2} \rho_o g_{ij} \dot{X}^i \dot{X}^j - \rho_o U] - \int_{t_1}^{t_2} d\tau \int_A \sigma\, a^{1/2} du^1 du^2 , \tag{24}$$

is an extremum subject to the conditions (12) and (13), where (u^1,u^2) are the surface coordinates for the interface, and a is a surface tensor.[2]

III. The Motion of a Nonspherical Bubble.

For the study of the nonspherical motion of a system, we often start with the study of the stability of the spherical motion of the system. For linear stability analysis, we usually perturb the interface from sphericity slightly. Mathematically, if the original Eulerian spherical interface is given by:

$$r = R(t) ,$$

now we usually take the interface as given by:

$$r = R(t) + \Sigma\, a_n^m(t) Y_n^m(\theta,\phi),$$

where Y_n^m's are spherical harmonics and $a_n^m(t)$'s are assumed to be small.

For bubbles in an incompressible, inviscid, thermally non-conducting fluid, the stability problem has been investigated fairly extensively. The linear stability of expanding and collapsing bubbles[4][5] as well as bubbles in oscillation[6][7] have all been studied in some detail. For collapsing bubbles, the nonlinear stability problem has also been treated numerically[8]

as well as by approximate analytical methods.[9][10] When the effect of compressibility and heat and mass transfer is included, the stability equations have also been derived.[10] On the other hand, deviations from spherical shape of a drop of incompressible fluid lead to surface waves[11][3] or even break-up of the drop.

In this section, we shall be mainly concerned with the non-spherical motion of a bubble in an incompressible fluid based on the Lagrangian formulation. Let us adopt the spherical polar coordinate systems for both the present and initial coordinates. Thus the system (r,θ,ϕ) will be identified with present general coordinates (x^1,x^2,x^3), while (R,Θ,Φ), with (X^1,X^2,X^3). With these identifications, if we consider the spherical motion, i.e.

$$\left.\begin{aligned} r &= r(R,\tau), \\ \theta &= \Theta, \\ \phi &= \Phi, \end{aligned}\right\} \tag{25}$$

and take the fluid in the region G as incompressible, we obtain from equation (12)-(17) in section II:[2]

$$r^3 = R^3+D^3(t)-D_o^3 , \tag{26}$$

and

$$D\ddot{D} + \frac{3}{2}\dot{D}^2 = \frac{1}{\rho}\left(p' - \frac{2\sigma}{D} - p_\infty\right) , \tag{27}$$

where p_∞ is the pressure in the liquid at infinity. The equation of bubble surface is

$$R = D_o \text{ , or } r = D(T) . \tag{28}$$

To treat nonspherical motion, let us write

$$\left.\begin{aligned} r &= F(R,\tau) + f(R,\Theta,\Phi,\tau) , \\ \theta &= \Theta + g(R,\Theta,\Phi,\tau) , \\ \phi &= \Phi + h(R,\Theta,\Phi,\tau) , \\ p &= p_o(R,\tau) + p_1(R,\Theta,\Phi,\tau) , \end{aligned}\right\} \tag{29}$$

where

$$F^3 = R^3+D^3-D_o^3 , \tag{30}$$

and $p_o(R,\tau)$ is the solution for pressure in the spherically symmetric case. Let us expand f and other functions in terms of spherical harmonics, e.g.

$$f(R,\Theta,\Phi,\tau) = \sum_{\ell,m} f_{\ell m}(R,\tau)\, Y_m^{\ell}(\Theta,\Phi) \ . \tag{31}$$

Now let

$$\frac{\partial}{\partial\tau}\left[F^2 f_{\ell m}\right] = \left(\frac{D}{F}\right)^{\ell} \frac{d}{d\tau}\left[D^2 a_{\ell m}(\tau)\right] \ . \tag{32}$$

Then, it can be shown that when the perturbations from spherical motion, f,g,h,p_1, are small, we can obtain the following linear stability equation:[2]

$$\ddot{a}_{\ell m} + \frac{3\dot{D}}{D}\dot{a}_{\ell m} - \left[\frac{(\ell-1)\ddot{D}}{D} - (\ell-1)(\ell+1)(\ell+2)\frac{\sigma}{\rho D^3}\right] a_{\ell m} = 0. \tag{33}$$

It may be noted that when $a_{\ell m}$ is small, the bubble surface is given in terms of Eulerian coordinates by:

$$r = D + \sum_{\ell,m} a_{\ell m}\, Y_m^{\ell}(\theta,\phi) \ ,$$

and the equation (33) is the same as that derived from the Eulerian formulation.[4] When $a_{\ell m}$ is not very small, as sometimes one wants to extrapolate the linear solution to the nonlinear region, the results obtained here will differ from the corresponding extrapolation.

To treat the nonlinear problem, the variational method is often useful when experience or other information could suggest good trial functions. Thus when spherical harmonics of higher degrees are expected to be not as important, we could take the added terms in (29), i.e. f,g,h and p_1, to contain only spherical harmonics of degree 2.

Based on this assumption, let us treat the problem of the axially symmetric collapse of a bubble with uniform internal pressure in an incompressible fluid as an example, and indicate how we approach this problem. For simplicity, we shall neglect the surface tension. Even with the angular dependence explicitly given by the spherical harmonics of degree 2, the functions f,g, and p_1 are functions of both R and τ. This is not desirable, since the resulting Euler equations would be coupled nonlinear partial differential equations. Using the solution of the linear stability problem as a guide, let us take the trial solution as:

$$\left.\begin{aligned} r &= F + \left(\frac{D}{F}\right)^4 a_2(\tau) P_2(\cos\theta) \ , \\ \theta &= \Theta - \frac{1}{3}\frac{D^4}{F^5} a_2(\tau) \frac{d}{d\theta} P_2(\cos\theta) \ , \\ \phi &= \Phi \ , \\ p &= p_o(R,\tau) + p_1(R,\tau) P_2(\cos\theta) \ , \end{aligned}\right\} \tag{34}$$

where

$$F(R,\tau) = [R^3 + D^3(\tau) - D_o^3]^{1/3} \ , \tag{35}$$

$$p_o(R,\tau) = p_\infty + \frac{\rho_o(D^2\ddot{D} + 2D\dot{D}^2)}{F} - \frac{\rho_o}{2}\frac{(D^2\dot{D})^2}{F^4} \ , \tag{36}$$

and

$$p_1(R,\tau) = \rho_o\{\frac{1}{3}\left[F^2\left(\frac{D^4 a_2}{F^5}\right)_\tau\right]_\tau - F_{\tau\tau} a_2\} \ . \tag{37}$$

For incompressible fluid, the internal energy term $(-\rho_o U)$ in the expression (24) should be replaced by $p\mathscr{J}$. Thus the volume integral will yield $\int p dV$ in the present volume of the fluid. For this problem with axial symmetry, as given by (15), we have

$$\mathscr{J} = \frac{r^2 \sin\theta}{R^2 \sin\Theta}\left(r_R \theta_\Theta - r_\Theta \theta_R\right) \ . \tag{38}$$

It is evident the term sin θ will cause difficulty in evaluating the integral (24) with respect to the variable Θ and R. It may be reasonable approximation for the purpose here to replace sin θ by sin Θ in (38), then in the integral (24), the integration with respect to R and Θ in (24) can be put in the form:

$$I = \int_{t_1}^{t_2} d\tau \, L(\ddot{D}(\tau), \dot{D}(\tau), D(\tau), \ddot{a}_2(\tau), \dot{a}_2(\tau), a_2(\tau); p_\infty, p', D_o) \ . \tag{39}$$

The variation of I with respect to D and a_2 will then lead to two ccupled nonlinear ordinary equations. The comparison of the solution of this approximate scheme with the corresponding solution from the Eulerian formulation[10] should be interesting.

IV. The Coalescence of Two Spherical Drops

It has been well established that the coalescence process plays an important role in the growth of raindrops especially in warm clouds.[12] Extensive theoretical and experimental research has been carried out for the study of coalescence efficiency, i.e. the fraction of the processes that lead to coalescence after two raindrops collide with each other.[13] Due to difficulty of the analysis and the general state of art in the study of the complete rainfall problem, it is understandable that there has not been much investigation of the detailed hydrodynamics of the coalescence process. However, it is certainly fascinating if we can follow the coalescence process in time especially in the vicinity of the point of coalescence, and see how the coalesced drop oscillates or how the drops separate again after collision.

To approach this problem, we shall limit our study to the coalescence of one large drop and one small drop. The initial configuration is taken to be two drops with radii D and d respectively just in touch with each other. (Fig. 1) Let us assume $d \ll D$, and take the larger drop stationary initially while the smaller drop as a whole has some initial velocity not necessarily perpendicular to the tangent plane of the drops at the contact point.

Since $d \ll D$, it can be argued that the free surface of the drops does not deviate much from the spherical shape $r = D$, or $r = R_o$, where

$$R_o = [D^3+d^3]^{1/3} , \tag{40}$$

is the radius of the coalesced drop if it is spherical. Thus, the linear theory of the stability of the spherical motion may be adequate for this study.

It is clear from the outset that the Eulerian formulation is not appropriate for this problem. Because the initial free surface can not be described by the form like:

$$r = R_o + \Sigma a_{\ell m} Y_m^{\ell}(\theta,\phi) ,$$

which implies that r is a single-valued function of θ and ϕ. To achieve the single-valueness of the free surface, the small drop could be replaced artifically by a small cap with same volume and free surface area as those of the original small drop. But then the initial contact would be a surface contact with finite area rather than the point contact, and the detailed dynamical process at the contact point would not be revealed.

Therefore we should try to approach this problem by use of the Lagrangian coordinates. We shall formulate the problem as if the motion of the system is some deviation from a single spherical drop of radius R_o. Let us define a fictitious initial state or reference state at some $\tau = \tau_i < 0$ for which the drops are described by

$$\begin{aligned} r &= R \ , \\ \theta &= \Theta \ , \\ \phi &= \Phi \ , \end{aligned} \tag{41}$$

with the free surface given by

$$r = R_o \ . \tag{42}$$

The general state of the system are given by

$$\begin{aligned} r &= R+f(R,\Theta,\Phi,\tau) \ , \\ \theta &= \Theta+g(R,\Theta,\Phi,\tau) \ , \\ \phi &= \Phi+h(R,\Theta,\Phi,\tau) \ . \end{aligned} \tag{43}$$

In particular, the real initial state at $\tau = 0$ as shown in figure 1 is given by

$$\begin{aligned} r(R,\Theta,\Phi,0) &= R+f(R,\Theta,\Phi,0) \ , \\ \phi(R,\Theta,\Phi,0) &= \Theta+g(R,\Theta,\Phi,0) \ , \\ \phi(R,\Theta,\Phi,0) &= \Phi+h(R,\Theta,\Phi,0) \ . \end{aligned} \tag{44}$$

The fictitious initial state can be chosen in many ways. Or in other words, the functions $f(R,\Theta,\Phi,0)$, $g(R,\Theta,\Phi,0)$ and $h(R,\Theta,\Phi,0)$ can be chosen in many ways. The only requirements is that the states at $\tau = \tau_i$ and $\tau = 0$ are kinematically connected, since we are dealing with drops of incompressible inviscid fluids. For compressible or viscous fluids, the situation will not be so simple.

One such solution is given by

$$r(R,\Theta,\Phi,0) = RH(D_1-R)+H(R-D_1)[H(\Theta_o(R)-\Theta)R_1+H(\Theta-\Theta_o(R))R_2] \ , \tag{45}$$

$$\begin{aligned} \cos[\theta(R,\Theta,\Phi,0)] = \cos\Theta H(D_1-R)+H(R-D_1)\{&H(\Theta_o(R)-\Theta)(D+d+R_3)/R_1 \\ &+ H(\Theta-\Theta_o(R))[R^2\cos\Theta+2(R-D_1)^2/D_1(2R-D_1)]\}, \end{aligned} \tag{46}$$

$$\phi(R,\Theta,\Phi,0) = \Phi \ , \tag{47}$$

where

$$D_1 = R_o - d, \quad R_1^2 = (D+d)^2 + (R-D_1)^2 + 2(D+d)R_3 ,$$

$$R_3 = [R^2 \cos\theta - D_1(2R-D_1)]/(R-D_1),$$

$$\cos\theta_o(R) = 1 - 2\left(1 - \frac{D_1}{R}\right)^2 ,$$

and H is the Heaviside function such that $H(x) = \begin{cases} 1 \\ 0 \end{cases}$, for $x \gtrless 0$.

The correspondence between the configurations of the state $\tau=\tau_1$ and $\tau=0$ is shown in Figures 1 and 2. The same coordinates describe the fluid inside the sphere $R < D_1$. For fluids in the spherical shell $D_1 < R < R_o$ in Fig. 2, those with $\theta < \theta_o(R)$ will occupy the small sphere in Fig. 1, and the surface $\theta = \theta_o(R)$ degenerates into a singular line; while those fluids with $\theta > \theta_o(R)$ will spread out to fill the entire spherical shell $D_1 < R < D$ in the large sphere of Fig. 1. When $d \ll D$, the state described by (45)-(47) can be put in the form (44) with f,g,h considered as small quantities.

It is easily verified that the state at $\tau=\tau_1$ as described by (2) and (3) satisfy the equations (12)-(17) in section II. Moreover the pressure inside the liquid drop is constant:

$$p = \frac{2\sigma}{R_o} , \tag{48}$$

if outside the liquid drop is assumed to be free space with zero pressure.

Now let us substitute (43) into (14) and (15), write

$$p = \frac{2\sigma}{R_o} + p_1(R,\theta,\phi,\tau) , \tag{49}$$

and keep only terms linear in f,g,h and p_1. We obtain

$$f_{\tau\tau} = -\frac{1}{\rho}(p_1)_R , \tag{50}$$

$$R^2 g_{\tau\tau} = -\frac{1}{\rho}(p_1)_\theta , \tag{51}$$

$$R^2 \sin^2\theta h_{\tau\tau} = -\frac{1}{\rho}(p_1)_\phi , \tag{52}$$

and

$$\frac{2f}{R} + f_R + \frac{1}{\sin\theta}(g \sin\theta)_\theta = 0 . \tag{53}$$

From equations (51) and (53), we obtain

$$R^2\left(\frac{2f}{R} + f_R\right)_{\tau\tau} - \frac{1}{\rho}\frac{1}{\sin\theta}\left[\sin\theta(p_1)_\theta\right]_\theta = 0 \ . \tag{54}$$

Let us now express f and p_1 in terms of spherical harmonics, thus

$$\begin{aligned} f(R,\theta,\Phi,\tau) &= \Sigma f_{\ell m}(R,\tau)Y_m^\ell(\theta,\Phi) \ , \\ p_1(R,\theta,\Phi,\tau) &= \Sigma p_{\ell m}(R,\tau)Y_m^\ell(\theta,\Phi) \ . \end{aligned} \tag{55}$$

Then the equation (54) becomes

$$\left[2Rf_{\ell m} + R^2(f_{\ell m})_R\right]_{\tau\tau} + \frac{1}{\rho}\ell(\ell+1)p_{\ell m} = 0 \ , \tag{56}$$

while (50) becomes

$$(f_{\ell m})_{\tau\tau} = -\frac{1}{\rho}(p_{\ell m})_R \ . \tag{57}$$

Equations (56) and (57) lead to

$$R^2(p_{\ell m})_{RR} + 2R(p_{\ell m})_R - \ell(\ell+1)p_{\ell m} = 0 \ . \tag{58}$$

Thus

$$p_{\ell m}(R,\tau) = A_{\ell m}(\tau)R^\ell + B_{\ell m}(\tau)/R^{\ell+1} \ . \tag{59}$$

As $p_{\ell m}$ is finite at R=0, and we obtain

$$p_{\ell m}(R,\tau) = A_{\ell m}(\tau)R^\ell \ . \tag{60}$$

For this linear theory, the boundary condition (17) leads to

$$p_{\ell m}(R_o,\tau) = \frac{\sigma(\ell+2)(\ell-1)f_{\ell m}(R_o,\tau)}{R_o^2} \ . \tag{61}$$

Thus

$$A_{\ell m}(\tau) = \frac{\sigma(\ell+2)(\ell-1)f_{\ell m}(R_o,\tau)}{R_o^{\ell+2}} \ . \tag{62}$$

Now the equation (57) becomes

$$(f_{\ell m})_{\tau\tau} = - \frac{\sigma \ell(\ell+2)(\ell-1) f_{\ell m}(R_o,\tau) R^{\ell-1}}{\rho R_o^{\ell+2}} \quad . \tag{63}$$

Let us denote $$\omega_\ell = [\frac{\sigma \ell(\ell+2)(\ell-1)}{\rho R_o^3}]^{1/2} \quad , \tag{64}$$

then the integration of (63) yields

$$f_{\ell m}(R,\tau) = - \omega_\ell^2 (\frac{R}{R_o})^{\ell-1} \int_o^\tau dt' \int_o^{t'} f_{\ell m}(R_o,t'') + \tau[\frac{\partial f_{\ell m}}{\partial \tau}(R,0)] + f_{\ell m}(R,0) \quad . \tag{65}$$

Let us denote

$$u_{\ell m}(\tau) = f_{\ell m}(R_o,\tau), \; \alpha_{\ell m} = f_{\ell m}(R_o,0), \; \beta_{\ell m} = \frac{\partial f_{\ell m}}{\partial \tau}(R_o,0). \tag{66}$$

Then after setting $R=R_o$ the equation (65) leads to

$$u_{\ell m}(\tau) = -\omega_\ell^2 \int_o^\tau (\tau - t) u_{\ell m}(t) dt + \alpha_{\ell m} + \beta_{\ell m} \tau \quad . \tag{67}$$

The last equation can be solved to obtain

$$u_{\ell m}(\tau) = \alpha_{\ell m} \cos \omega_\ell \tau + \frac{\beta_{\ell m}}{\omega_\ell} \sin \omega_\ell \tau \quad . \tag{68}$$

Thus we obtain from (65):

$$f_{\ell m}(R,\tau) = (\frac{R}{R_o})^{\ell-1} [\alpha_{\ell m} \cos \omega_\ell \tau + \frac{\beta_{\ell m}}{\omega_\ell} \sin \omega_\ell \tau] + [\frac{\partial f_{\ell m}}{\partial \tau}(R,0) - \beta_{\ell m} (\frac{R}{R_o})^{\ell-1}] \tau + [f_{\ell m}(R,0) - \alpha_{\ell m} (\frac{R}{R_o})^{\ell-1}]. \tag{69}$$

Now $f_{\ell m}(R,0)$ and $\frac{\partial f_{\ell m}}{\partial \tau}(R,0)$, hence also $\alpha_{\ell m}$ and $\beta_{\ell m}$ can be obtained from (45) and the initial impact velocity. Therefore $f_{\ell m}(R,\tau)$ is completely determined. The solution (69) is of course the general

solution of the problem of the linear stability of a spherical drop in Lagrangian form. The first term represents the oscillatory part of the motion with frequency ω_ℓ, and in the linear range, the last two terms will make no contribution to surface motion. Thus strictly speaking, the linear theory presented here can only apply to the coalescence of drops by normal impact. That $f_{\ell m}$ does not depend on the solutions and the initial condition of g and h is also an indication to this effect. To account for the oblique impact we need either a second order development beyond this linear analysis or a judicious extrapolation of the linear results. With the results of the linear theory available here, it is not very difficult to develop the second order theory. However, many interesting features of the coalescence process in the vicinity of contact point could already be revealed from the study of the coalescence by the normal impact.

V. Nonlinear Oscillation of Bubbles

We shall report here the recent results on the nonlinear oscillation of bubbles making use of the variational methods. The details of the variational methods as well as the specific application to bubble oscillation is presented elsewhere[14][15]. Let us consider the adiabatic oscillation of a spherical gas bubble in an incompressible fluid under an externally applied sinusoidal pressure field. The governing equation for the bubble radius R is:

$$R\ddot{R} + \frac{3}{2}\dot{R}^2 + \alpha R\dot{R} = \frac{p_a}{\rho}\left[\left(\frac{R_a}{R}\right)^{3\gamma} - 1\right] - \frac{2\sigma}{\rho}\left(\frac{1}{R} - \frac{1}{R_a}\right) + \frac{p_o}{\rho}\sin \omega t, \tag{70}$$

where γ is the ratio of specific heats; R_a, the equilibrium radius; α, a damping constant; and the last term represents the externally applied pressure field. The damping is introduced somewhat artifically. The damping due to the viscosity of liquid can be easily represented accurately. However it is more involved to incorporate the damping due to thermal dissipation and the viscosity of the gas.

Equation (70) is equivalent to the variational principle:

$$\Delta J + \Delta I = 0 , \tag{71}$$

where

$$J = \int_0^t dt\{R^3\dot{R}^2 + \frac{2}{(3-3\gamma)\rho} p_a R_a^{3\gamma} R^{3-3\gamma} - \frac{\sigma}{\rho} R^2 - \frac{2}{3\rho}(p_a - \frac{2\sigma}{\rho R_a})R^3 + \frac{2}{3} R^3 p_o \sin \omega t\} dt , \tag{72}$$

and $$\Delta I = -2\alpha \int_0^t dt\, R^3 \dot{R}\, \Delta R. \tag{73}$$

Now let us take

$$R = R_b + R_o \sin(\omega t+\delta_o) + R_1 \sin(p\omega t+\delta_1)\ . \tag{74}$$

In more refined treatment, we can let R_o, δ_o, R_1 and δ_1 all as slowly varying function of t. Here for simplicity, we shall assume that they are all real constants. $p \neq 1$ is taken to be real and positive. Thus we are looking for asymptotically periodic solutions.

Substitute (74) into (72) and (73), then for large t, the integrals can be approximately evaluated. The dominating terms are the secular terms multiplied by t. From the independent variation of ΔR_b, ΔR_o, $\Delta\delta_o$, ΔR_1, and $\Delta\delta_1$, we obtain a set of five algebraic equations to determine these five unknowns.

If we make further simplifying approximations that the surface tension be neglected and $R_b = R_a$, and the forcing amplitude is not very large so that we can neglect the 3rd and higher order small terms, then we obtain the following interesting results:[15]

For $p \neq \frac{1}{2}$, and $p \neq 2$, we obtain

$$R_1 = 0\ . \tag{75}$$

However for p = 1/2, it is found that there is another branch of the solution for which $R_1 \neq 0$. This branch is determined by the following relations:

$$(\omega^2-\omega_o^2)R_aR_o + \frac{p_o}{\rho}\cos\delta_o = -[\omega_s^2 \sin(2\delta_1-\delta_o) - \tfrac{3}{4}\alpha\omega\cos(2\delta_1-\delta_o)]R_1^2, \tag{76}$$

$$-\frac{p_o}{\rho}\sin\delta_o - \alpha\omega R_aR_o = [\omega_s^2\cos(2\delta_1-\delta_o) + \tfrac{3}{4}\alpha\omega\sin(2\delta_1-\delta_o)]R_1^2, \tag{77}$$

$$(\frac{\omega^2}{4} - \omega_o^2)R_a = -2\omega_s^2R_o\sin(2\delta_1-\delta_o) - \tfrac{3}{4}\alpha\omega R_o\cos(2\delta_1-\delta_o) - \frac{p_o}{\rho R_a}\sin 2\delta_1, \tag{78}$$

and

$$\tfrac{\alpha}{2}\omega R_a = -2\omega_s^2R_o\cos(2\delta_1-\delta_o) + \tfrac{3}{4}\alpha\omega R_o\sin(2\delta_1-\delta_o) - \frac{p_o}{\rho R_a}\cos 2\delta_1, \tag{79}$$

where $\omega_s^2 = \frac{9}{16}\omega^2 + \frac{3}{2}(\gamma-1)\omega_o^2$, $\omega_o^2 = \frac{3\gamma p_a}{\rho R_a^2}$.

From (76)-(79), we can solve for R_o, R_1, δ_o and δ_1. The details will be presented elsewhere.[15] They contain the information about the threshold amplitude p_o for such solution to exist, the amplitudes and phases of the fundamental and subharmonic modes of the oscillation.

If we carry out our analysis to include terms of the 3rd order small terms, we found that there is also another branch of the solution for which $R_1 \neq 0$ if $p = 1/3$. These subharmonic have also been found independently by Prosperetti.[16]

In principle, this variational technique can also be applied to the nonlinear oscillations of nonspherical bubbles. But there are still formidable practical problems to overcome. It may be remarked that the variational methods has been successfully applied to the study of collapse of a nonspherical bubble.[10] The approximate trial solution we take consists of the spherical mode and the spherical harmonic mode of degree 2. This is found to be a fairly good approximation. However, for the oscillation problem, it seems that higher spherical harmonics may be important and it is not clear that a single harmonic mode is adequate as a first approximation. Further study in this area is continuing.

1. D.Y. Hsieh, "Some analytical aspects of bubble dynamics", Trans. ASME, 87D, 991-1005 (1965).

2. D.Y. Hsieh, "Lagrangian formulation of bubble dynamics" To appear in Quart. Appl. Math.

3. D.Y. Hsieh, "Variantional methods and dynamics of nonspherical bubbles and liquid drops", Proc. 1973 Symposium on Finite Amplitude Wave Effects in Fluids, IPC Science and Tech. Press, Surrey, England (1974).

4. M.S. Plesset, "On the stability of fluid flows with spherical symmetry", J. Appl. Phys. 25, 96-98 (1954).

5. M.S. Plesset and T.P. Mitchell, "On the stability of the spherical shape of a vapor cavity in a liquid", Quart. Appl. Math., 8, 419-430 (1956).

6. D.Y. Hsieh and M.S. Plesset, "Theory of rectified diffusion of mass into gas bubbles", J. Acoust. Soc. Am. 33, 206-215 (1961).

7. D.Y. Hsieh, "On thresholds for surface waves and subharmonics of an oscillating bubble", To appear in J. Acoust. Soc. Am.

8. R.B. Chapman and M.S. Plesset, "Nonlinear effects in the collapse of a nearly spherical cavity in a liquid", Trans. ASME 94D, 142-146 (1972).

9. C.F. Naudé and A.T. Ellis, "On the mechanism of cavitation damage by nonhemispherical cavities collapsing in contact with a solid boundary", Trans. ASME 83D, 648 (1961).

10. D.Y. Hsieh, "On the dynamics of nonspherical bubbles", Trans. ASME 94D, 655-665 (1972).

11. H. Lamb, "Hydrodynamics", pp. 473-475, Dover Publications (1932).

12. H. Riehl, "Tropical Meteorology", McGraw-Hill, New York, 1945.

13. D.M. Whelpade and R. List, "The coalescence process in raindrop growth", J. Geophys. Res. 76, 2836-2856 (1971).

14. D.Y. Hsieh, "Variational methods and nonlinear forced oscillations", To be published.

15. D.Y. Hsieh, "Variational methods and nonlinear oscillation of bubbles", To be published.

16. A. Prosperetti, "Viscous and nonlinear effects in the oscillations of drops and bubbles", Ph.D. thesis, Calif. Institute of Technology, May 1974.

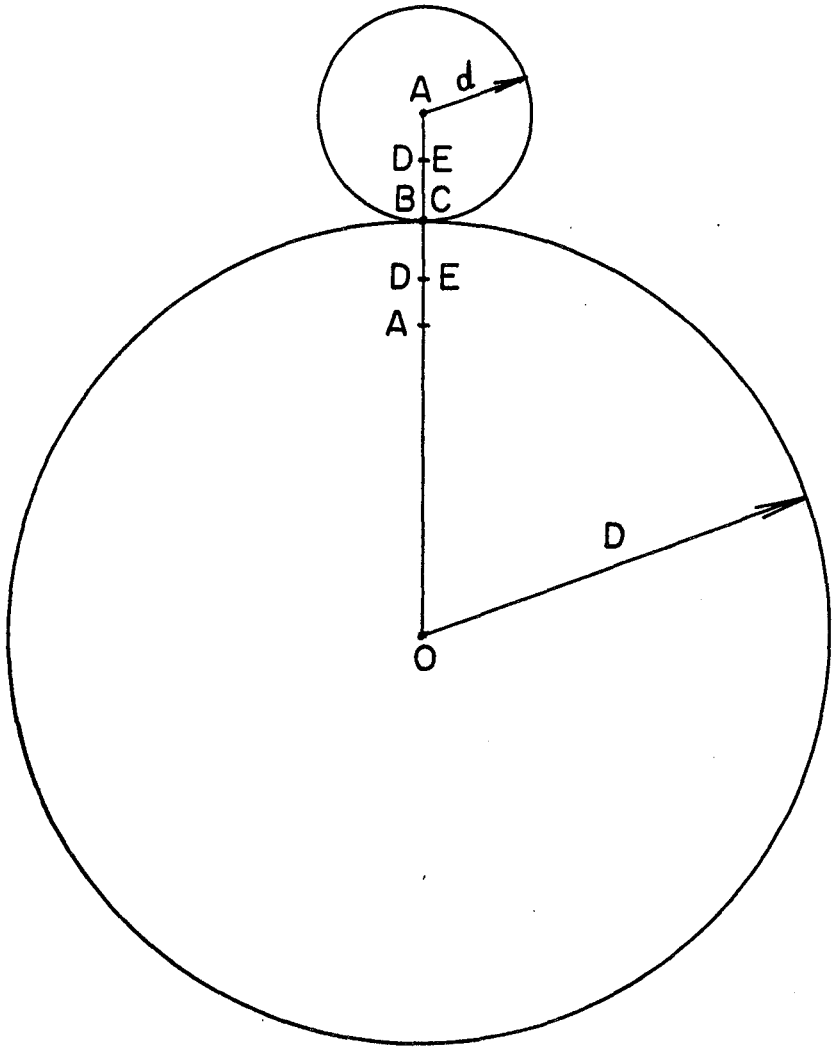

FIG.1. THE INITIAL CONFIGURATION OF DROPS

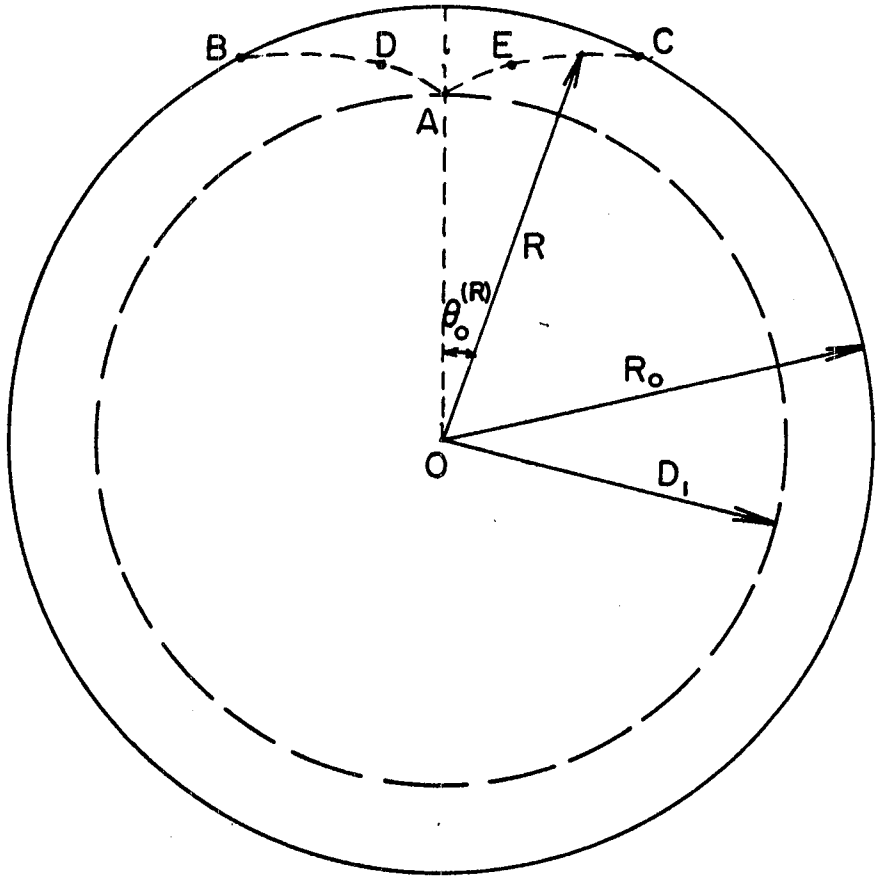

FIG. 2 THE REFERENCE CONFIGURATION OF DROPS

ON THE OSCILLATIONS OF DROPS AND BUBBLES IN VISCOUS LIQUIDS

Andrea Prosperetti‡
California Institute of Technology, Pasadena, California

INTRODUCTION

The normal-mode approach to problems of small-amplitude waves in fluids is a standard one and has been widely used in the past. The method consists in assuming an exponential time dependence of the type $\exp(-\sigma_n t)$ for all the dependent variables and in deriving a characteristics equation for the complex eigenfrequencies σ_n (see e.g. Ref. 1, Ch. X, XI). The solution to a particular initial-value problem is then obtained in the form of a series by a superposition of the various normal modes with appropriate coefficients.

In the presence of viscosity the equations governing the motion become parabolic, and the series in question is usually very slowly converging for small times. However, for free (damped) oscillations, the small-time behavior is of considerable interest for many important aspects, such as questions of stability, so that a different form of the solution is needed. It is the purpose of the present paper to analyze the problem from this point of view, elucidating the characteristics of the small-time behavior of the oscillations of drops and bubbles about the spherical shape.

For the case of a viscous liquid drop in a medium of negligible dynamical effects (vacuum, air) it is found that, if the motion is irrotational at the initial instant, the effective damping and frequency agree with those given by Lamb (Ref. 2, p. 640) and Rayleigh (Ref. 8) for small times. However, as time passes, the vorticity that is generated at the surface starts to diffuse inwards bringing about an increase in the effective damping. The normal-mode results of Chandrasekhar (Ref. 1, p. 675; Ref. 3) and Reid (Ref. 4) are recovered as $t \to \infty$. It is interesting to notice that the relaxation of the system towards the asymptotic regime is not exponential, but only algebraic with time. Another remarkable feature is that the asymptotic effective damping is smaller than the initial one.

‡ On leave of absence from Istituto di Fisica, Universitá Degli Studi, Milano, Italy.

Similarly, for the case of a bubble in an unbounded liquid, Lamb's irrotational results (Ref. 2, p. 641) are reproduced for small times, whereas the asymptotic solution coincides with that derived by Miller and Scriven (Ref. 5) in a normal mode framework.

PRELIMINARIES

We consider a nearly spherical free surface $\Sigma(t)$ separating two incompressible, viscous, immiscible fluids that fill the entire space. If body forces are negligible, the equilibrium configuration of Σ is maintained by surface tension and is that of a sphere; the pressures in the inner and outer regions are uniform, and they are related by:

$$p_1 - p_2 = \frac{2T}{R} \tag{1}$$

where T is the surface tension and R the equilibrium radius. The outer pressure p_2 will be taken as reference value and set to zero. In the following the subscripts 1 and 2 will be attached to all quantities pertaining to the inner and outer region respectively. When no subscript is indicated, reference can be made indifferently to either region.

When the equilibrium situation is slightly perturbed, the ensuing motion is governed by the (linearized) Navier-Stokes equations:

$$\vec{\nabla} \cdot \vec{U} = 0 \tag{2}$$

$$\rho \frac{\partial \vec{U}}{\partial t} = - \vec{\nabla} p - \mu \vec{\nabla} \times (\vec{\nabla} \times \vec{U}) \tag{3}$$

where $\vec{U}$ denotes velocity and ρ, μ are the density and viscosity of the fluids.

The surface Σ can be represented by a superposition of spherical harmonics. To first order in the perturbation of the spherical symmetry, however, the equations for the different modes are uncoupled so that we may consider a single one; in spherical coordinates we thus let:

$$\Sigma(t) : F(r, \theta, t) \equiv r - R - \epsilon a(t) P_n(\cos \theta) = 0, \tag{4}$$

where $0 < \epsilon << 1$, and P_n is a Legendre polynomial of degree $n \geq 2$. In writing Eq. (4) it has been assumed for simplicity that the surface maintains an axial symmetry; this restriction (which can be lifted by adopting the toroidal-poloidal formalism for the description of the velocity field, see Ref. 1, p. 622), has no consequence on the equation of motion for $a(t)$.

In the following developments only terms of first order in ϵ will be retained. To this approximation the outward unit normal $\vec{n}$ to Σ is given by the expression:

$$\vec{n} = \vec{e}_r - \epsilon \frac{a}{R} \frac{dP_n}{d\theta} \vec{e}_\theta , \tag{5}$$

where $\vec{e}_r$, $\vec{e}_\theta$ are unit vectors in the radial and azimuthal direction respectively. On the free surface the kinematical boundary conditions are (Ref. 6, pp. 60, 148):

$$\frac{\partial F}{\partial t} + (\vec{U} \cdot \vec{\nabla})F = 0 \tag{6}$$

$$\vec{U}_{t_1} = \vec{U}_{t_2} \tag{7}$$

where the subscript t denotes the tangential component of the velocity to the free surface. If one of the two fluids is inviscid, only the first condition applies. The dynamical boundary conditions stipulate that there should be no discontinuity in the tangential stresses:

$$\vec{n} \times [(\sigma_2 - \sigma_1)\vec{n}] = 0 , \tag{8}$$

and that the discontinuity in the normal stress should equal the surface tension T times the total curvature:

$$\vec{n} \cdot [(\sigma_2 - \sigma_1)\vec{n}] = T \vec{\nabla} \cdot \vec{n} . \tag{9}$$

In these equations the stress tensors σ_1 and σ_2 are evaluated on the inner and outer sides of Σ respectively. To the above boundary conditions the requirements of regularity at infinity and at the origin must be added.

It is convenient to separate out the effect of viscosity by writing:

$$\vec{U} = \vec{u} + \vec{v}$$

where $\vec{u}$ is the potential flow velocity of the inviscid case satisfying:

$$\vec{u} = \epsilon \vec{\nabla}\varphi \qquad \vec{\nabla} \cdot \vec{u} = 0 \tag{10a}$$

$$\frac{\partial F}{\partial t} + \vec{u} \cdot \vec{\nabla} F = 0 \tag{10b}$$

$$\vec{\nabla}\left(\epsilon \frac{\partial \varphi}{\partial t} + \frac{p^\circ}{\rho}\right) = 0 \tag{11}$$

From Eq. (3) one then deduces the following equations for $\vec{v}$:

$$\frac{\partial \vec{v}}{\partial t} = -\nu \vec{\nabla} \times (\vec{\nabla} \times \vec{v}) + \frac{1}{\rho} \vec{\nabla} p' \tag{12}$$

$$\vec{\nabla} \cdot \vec{v} = 0 \tag{13a}$$

$$\vec{v} \cdot \vec{\nabla} F = 0 \tag{13b}$$

where $\nu = \mu/\rho$ is the kinematic viscosity and the pressure has been split into two parts, $p = p^\circ + p'$. In order to satisfy (13a) identically, we introduce a stream function representation of the viscous flow field:

$$\vec{v} = \frac{\epsilon}{r^2 \sin\theta} \frac{\partial \psi}{\partial \theta} \vec{e}_r - \frac{\epsilon}{r \sin\theta} \frac{\partial \psi}{\partial r} \vec{e}_\theta \tag{14}$$

Results of the type of those obtained by Chandrasekhar, Reid, Miller and Scriven can now be derived by assuming an exponential time dependence of the various quantities.

SOLUTION OF THE FLUID MECHANICAL PROBLEM

The solution of the potential problem (10) can be taken from Lamb (Ref. 2, p. 121) or Plesset (Ref. 7) as:

$$\varphi_1 = \frac{1}{n} R^{-n+1} r^n \dot{a} P_n \tag{15}$$

$$\varphi_2 = -\frac{1}{n+1} R^{n+2} r^{-n-1} \dot{a} P_n \tag{16}$$

where dots denote time differentiation. Eq. (11) then determines the inviscid part of the pressure to be:

$$\frac{p_1^\circ}{\rho_1} = \frac{2T}{R\rho_1} - \frac{\epsilon}{n} R^{-n+1} r^n \ddot{a} P_n \tag{17}$$

$$\frac{p_2^\circ}{\rho_2} = \frac{\epsilon}{n+1} R^{n+2} r^{-n-1} \ddot{a} P_n \tag{18}$$

To solve for the viscous component of the flow we introduce the vorticity $\vec{\omega} = \epsilon \vec{\nabla} \times \vec{v}$, in terms of which Eq. (12) becomes:

$$\frac{\partial \vec{\omega}}{\partial t} = -\nu \vec{\nabla} \times (\vec{\nabla} \times \vec{\omega}) \tag{19}$$

The solution can be found by separation of variables as:

$$\vec{\omega} = \Omega(r,t)\ P_n^1(\cos\theta)\ \vec{e}_\varphi \tag{20}$$

where P_n^1 is an associated Legendre polynomial, $\vec{e}_\varphi = \vec{e}_r \times \vec{e}_\theta$, and $\Omega(r,t)$ is the solution of:

$$\frac{\partial \Omega}{\partial t} - \nu \frac{\partial^2 \Omega}{\partial r^2} - \frac{2\nu}{r} \frac{\partial \Omega}{\partial r} + n(n+1) \frac{\nu}{r^2} \Omega = 0 \tag{21}$$

The boundary conditions for this equation are that $\partial\Omega_1/\partial r$ vanish at the origin and Ω_2 at infinity, and that $\Omega_1(R,t)$, $\Omega_2(R,t)$ equal two functions

$\Omega_{01}(t)$, $\Omega_{02}(t)$ that will be determined by the conditions at the interface Σ[‡]. As initial condition we assume $\Omega(r,0)=f(r)$, with $f(r)$ a prescribed function. Eq. (21) can now be solved by taking its Laplace transform with respect to time. The solutions satisfying the appropriate initial and boundary conditions in the two regions are:

$$\tilde{\Omega}_1(r,p)=\left(\frac{R}{r}\right)^{\frac{1}{2}}\tilde{\Omega}_{01}(p)\,\frac{I_{n+\frac{1}{2}}(r(p/\nu)^{\frac{1}{2}})}{I_{n+\frac{1}{2}}(R(p/\nu)^{\frac{1}{2}})}$$

$$+\frac{1}{\nu r^{\frac{1}{2}}}\int_R^r \rho^{\frac{3}{2}} f(\rho)W(r,\rho;p)d\rho$$

$$+\frac{W(r,R;p)}{\nu r^{\frac{1}{2}}I_{n+\frac{1}{2}}(R(p/\nu)^{\frac{1}{2}})}\int_0^R \rho^{\frac{3}{2}}f(\rho)I_{n+\frac{1}{2}}(\rho(p/\nu)^{\frac{1}{2}})d\rho \qquad (22)$$

$$\tilde{\Omega}_2(r,p)=\left(\frac{R}{r}\right)^{\frac{1}{2}}\tilde{\Omega}_{02}(p)\,\frac{K_{n+\frac{1}{2}}(r(p/\nu)^{\frac{1}{2}})}{K_{n+\frac{1}{2}}(R(p/\nu)^{\frac{1}{2}})}$$

$$+\frac{1}{\nu r^{\frac{1}{2}}}\int_R^r \rho^{\frac{3}{2}} f(\rho)W(r,\rho;p)d\rho$$

$$+\frac{W(R,r;p)}{\nu r^{\frac{1}{2}}K_{n+\frac{1}{2}}(R(p/\nu)^{\frac{1}{2}})}\int_R^\infty \rho^{\frac{3}{2}}f(\rho)K_{n+\frac{1}{2}}(\rho(p/\nu)^{\frac{1}{2}})d\rho \qquad (23)$$

where the tilde denotes the Laplace transformed function, p is the transformed variable and:

$$W(r,\rho;p)=K_{n+\frac{1}{2}}(r(p/\nu)^{\frac{1}{2}})I_{n+\frac{1}{2}}(\rho(p/\nu)^{\frac{1}{2}})-K_{n+\frac{1}{2}}(\rho(p/\nu)^{\frac{1}{2}})I_{n+\frac{1}{2}}(r(p/\nu)^{\frac{1}{2}})$$

The stream function ψ is determined by integration of Eq. (14) to be:

$$\psi(r,\theta,t)=\frac{n(n+1)}{2n+1}\Psi(r,t)\left[P_{n-1}(\cos\theta)-P_{n+1}(\cos\theta)\right]$$

where:

$$\Psi(r,t)=\frac{r^{-n}}{2n+1}\left[c(t)-\int_R^r s^{n+2}\,\Omega(s,t)\,ds\right]$$

$$+\frac{r^{n+1}}{2n+1}\left[\int_R^r s^{-n+1}\,\Omega(s,t)\,ds-\frac{c(t)}{R^{2n+1}}\right] \qquad (24)$$

One of the integration constants has been eliminated with the aid of Eq. (13b) which requires:

[‡]In writing Eqs. (20), (21) the effect of the boundary condition (8) has been partially anticipated in that the separation constant has been set at $\nu n(n+1)$ instead of that at $\nu k(k+1)$, with k an integer to be determined.

$$\frac{\partial \psi}{\partial \theta}(R,\theta,t) = 0$$

and the other, c(t), is determined by the regularity requirements at the origin and at infinity:

$$c_1(t) = -\int_0^R s^{n+2}\Omega_1(s,t)ds \tag{25a}$$

$$c_2(t) = R^{2n+1}\int_R^\infty s^{-n+1}\Omega_2(s,t)ds \tag{25b}$$

Now the modification to the pressure introduced by viscosity can be computed from Eq. (12) with the result:

$$\frac{p_1'}{\rho} = (n+1)\nu_1\left(\frac{r}{R}\right)^n \Omega_{10}(t)P_n(\cos\theta)$$

$$\frac{p_2'}{\rho} = -n\nu_2\left(\frac{R}{r}\right)^{n+1}\Omega_{20}(t)P_n(\cos\theta)$$

In the following we shall restrict the analysis mainly to the case in which the initial vorticity distribution vanishes, f(r) = 0. This will happen for instance if the oscillations start from a position of perturbed equilibrium with zero initial velocity. In this case the Laplace transforms of c(t) have the following expressions:

$$\tilde{c}_1(p) = -R^{n+2}(\nu/p)^{\frac{1}{2}}\tilde{\Omega}_{01}(p)\frac{I_{n+\frac{3}{2}}(R(p/\nu)^{\frac{1}{2}})}{I_{n+\frac{1}{2}}(R(p/\nu)^{\frac{1}{2}})} \tag{26a}$$

$$\tilde{c}_2(p) = R^{n+2}(\nu/p)^{\frac{1}{2}}\tilde{\Omega}_{02}(p)\frac{K_{n-\frac{1}{2}}(R(p/\nu)^{\frac{1}{2}})}{K_{n+\frac{1}{2}}(R(p/\nu)^{\frac{1}{2}})}\,. \tag{26b}$$

THE EQUATION OF MOTION OF THE INTERFACE

We shall now apply the remaining boundary conditions and derive the equation of motion of the interface. From the continuity of the tangential velocity, Eq. (7), we get:

$$c_1 - c_2 = \frac{2n+1}{n(n+1)}R^{n+2}\dot{a} \tag{27}$$

The continuity of tangential stresses, Eq. (8) reduces to:

$$2R^{-n-3}(\mu_1 c_1 - \mu_2 c_2) + \mu_1\Omega_{01}(t) - \mu_2\Omega_{02}(t)$$

$$= \frac{2}{R}\left(\frac{n+2}{n+1}\mu_2 - \frac{n-1}{n}\mu_1\right)\dot{a} \tag{28}$$

These two equations determine $\Omega_{01}(t)$, $\Omega_{02}(t)$ in terms of a(t); the remaining boundary condition on the normal stresses, Eq. (9), plays then the role of a consistency condition and yields the following equation of motion for a(t):

$$\frac{(n+1)\rho_1+n\rho_2}{n(n+1)}\ddot{a} - 2(n-1)(n+2)\frac{\mu_2-\mu_1}{R^2}\dot{a} + (n-1)(n+2)\frac{T}{R^3}a$$

$$+ (n-1)(n+1)\frac{\mu_1}{R}\Omega_{01}(t) - n(n+2)\frac{\mu_2}{R}\Omega_{02}(t) = 0 \qquad (29)$$

The set of simultaneous equations (27), (28), (29) describes the motion of the interface. It is a system of three linear integro-differential equations, which can be solved for the Laplace-transformed functions. The final step of inversion of the transforms, however, does not appear to be possible without recourse to numerical methods. The following sections describe some approximate results.

THE OSCILLATIONS OF A VISCOUS LIQUID DROP IN AIR

We consider first the case in which the fluid occupying the outer region has negligible dynamical effects, so that is is appropriate to neglect μ_2, ρ_2 compared to μ_1, ρ_1. This would be the case, for example, for a liquid drop in a vacuum or in air. As was noted after Eq. (7), the condition of continuity of tangential velocity does not apply to this case, so that Eq. (27) should be neglected. Further, setting $\mu_2 = 0$, $\rho_2 = 0$ in Eqs. (28), (29) and dropping the subscript 1, we get:

$$2R^{-n-3}\,c\,(t) + \Omega_0(t) = -\frac{n-1}{n}\frac{2}{R}\dot{a} \qquad (30)$$

$$\ddot{a} + 2n(n-1)(n+2)\frac{\nu}{R^2}\dot{a} + n(n-1)(n+2)\frac{T}{\rho R^3}a$$

$$+ n(n-1)(n+1)\frac{\nu}{R}\Omega_0(t) = 0 \qquad (31)$$

The quantity $c(t)$ is given by Eq. (25a) or (26a). Observe first that by combination of (30), (31) one obtains:

$$\ddot{a} + 2(n-1)(2n+1)\frac{\nu}{R^2}\dot{a} + n(n-1)(n+2)\frac{T}{\rho R^3}a$$

$$+ 2n(n-1)(n+1)\nu R^{-n-4}\int_0^R s^{n+2}\Omega(s,t)\,ds = 0 \qquad (32)$$

If $\Omega(r,t)$ is so small that the last term is negligible, we can read directly from the equation the frequency ω_0 and the decay constant τ_d of the oscillations:

$$\omega_0^2 = n(n-1)(n+2)\frac{T}{\rho R^3}$$

$$\tau_d^{-1} = (n-1)(2n+1)\frac{\nu}{R^2}$$

The first of these equations is the result obtained by Rayleigh (Ref. 8) for the oscillations of an inviscid drop, the second coincides with the expression derived by Lamb (Ref. 2, p. 640) in the approximation of irrotational flow. To proceed further it is necessary to express Ω in terms of a. Taking the Laplace transform of (30) and using (26a) one deduces that:

$$\tilde{\Omega}_0(p) = -\frac{2}{R}\frac{n-1}{n}\tilde{a}(p)\left[1 - \frac{2}{q}\frac{I_{n+\frac{3}{2}}(q)}{I_{n+\frac{1}{2}}(q)}\right]^{-1} \tag{33}$$

where $q = R(p/\nu)^{\frac{1}{2}}$.‡ This equation shows the connection between the superficial vorticity and the velocity of deformation of the drop shape. Substitution into (32) and application of the convolution theorem for the Laplace transform yields:

$$\ddot{a} + 2\tau_d^{-1}\dot{a} + \omega_0^2 a + 2\beta_n\tau_d^{-1}\int_0^t Q(t-\tau)\dot{a}(\tau)\,d\tau = 0 \tag{34}$$

where

$$\beta_n = \frac{(n-1)(n+1)}{2n+1}$$

and $Q(t)$ is defined by its transform as:

$$\tilde{Q}(p) = \frac{2I_{n+\frac{3}{2}}(q)}{2I_{n+\frac{3}{2}}(q) - qI_{n+\frac{1}{2}}(q)}$$

On physical grounds one expects the solution of Eq. (34) to have the form of modulated oscillations; we therefore let:

$$a(t) = Ae^{-\sigma(t)t}$$

where A is a complex constant and $\sigma(t)$ a complex function of time. In order to bring out the relation to the irrotational oscillations it is also expedient to define a new dependent variable:

$$u(t) = \exp\{-[\sigma(t) - \sigma_0]t\} \tag{35}$$

‡It may be noted that the function $\mathcal{J}_\nu(q) = qI_{\nu-1}(q)/I_\nu(q)$ is a particular case of modified quotients of cylinder functions, which are treated in Ref. 9.

(where

$$\sigma_0 = \tau_d^{-1} \pm i\left(\omega_0^2 - \tau_d^{-2}\right)^{\frac{1}{2}} \tag{36}$$

is the complex frequency of the irrotational oscillations) so that:

$$a(t) = Ae^{-\sigma_0 t}u(t) \tag{37}$$

Without loss of generality we may also take $u(0) = 1$, $\dot{u}(0) = 0$. Substituting (37) into (34) and taking the Laplace transform we find:

$$\tilde{u}(p) = \frac{p + 2\left(\tau_d^{-1} - \sigma_0\right) + 2\beta_n \tau_d^{-1}\tilde{\Omega}(p-\sigma_0)}{p^2 + 2\left(\tau_d^{-1} - \sigma_0\right)p + 2\beta_n \tau_d^{-1}(p - \sigma_0)\tilde{\Omega}(p-\sigma_0)} \tag{38}$$

The inversion of this function appears to be a hopeless task analytically, and one must have recourse to numerical techniques for a full solution. Here we shall content ourselves with an approximate solution valid for small times and an investigation of the asymptotic properties for $t \to \infty$.

Upon expansion of (38) in series, term by term inversion, and comparison with (35) we deduce‡:

$$\frac{\sigma(t)}{\sigma_0} = 1 + (n-1)^2(n+1)\left\{\frac{32}{15\pi^{\frac{1}{2}}}\left(\frac{\nu t}{R^2}\right)^{\frac{3}{2}} - \frac{2}{3}(n-1)\left(\frac{\nu t}{R^2}\right)^2 + \frac{32}{105\pi^{\frac{1}{2}}}\left[5(\sigma_0 t)\left(\frac{\nu t}{R^2}\right)^{\frac{3}{2}} - (7n-4)(n+1)\left(\frac{\nu t}{R^2}\right)^{\frac{5}{2}}\right] + \ldots\right\} \tag{39}$$

Figure 1 is a plot of the first three terms of this equation for $2 \le n \le 5$. There are some features of this result which are worth noticing. The first and most apparent one is the fact that the damping factor of the system increases with time in the early stages of the motion. This characteristic is not surprising in view of the fact that the energy equation can be written in integrated form as (Ref. 2, p. 581):

$$\frac{\partial E}{\partial t} = -\mu\left\{\int_V \omega^2 dV + \int_S \vec{n}\cdot[(\vec{U}\cdot\vec{\nabla})\vec{U}]\, dS\right\} \tag{40}$$

where E is the total energy of the system, V its volume and S the surface bounding V. Only the second term of this equation is nonzero for an irrotational flow, and in our case it gives rise to the decay constant

‡It may be of some interest to note that if one requires that the first power of time occurring in (39) be as high as possible, one obtains an equation for σ_0 whose solution is given by (36).

τ_d^{-1} in the very first, approximately irrotational stages of the motion. The contribution of the first term, however, increases from zero as the vorticity generated at the surface (cf. Eq. 33) gradually diffuses into the drop, and brings about the increase in damping shown by Eq. (39). A remarkable characteristic of this increase is that, although it is due to a diffusive process, its time dependence is not $t^{\frac{1}{2}}$ but only $t^{\frac{3}{2}}$. This feature, on which the small-time accuracy of the irrotational results rests in practice, is produced by a cancellation between the lowest order contributions (i. e. those proportional to $t^{\frac{1}{2}}$ and t) of the convective and diffusive terms of Eq. (40).

To investigate the behavior of $a(t)$ for large values of time we let:

$$a(t) = Ae^{-\sigma_\infty t} v(t)$$

where σ_∞ is a constant to be determined in such a way that:

$$\lim_{t\to\infty} v(t) = \text{constant} \qquad (41)$$

The Laplace transform of $v(t)$ can be expanded near $p = 0$ with a result of the form:

$$\tilde{v}(p) \propto \frac{1}{B + Cp}$$

with B, C constants. To satisfy (41) we thus must require $B = 0$; this condition, written out in full, reads:

$$\sigma_\infty^2 - 2\tau_d^{-1}\sigma_\infty + \omega_0^2 + 2\beta_n \tau_d^{-1}\sigma_\infty \frac{2J_{n+\frac{3}{2}}(x)}{xJ_{n+\frac{1}{2}}(x) - 2J_{n+\frac{3}{2}}(x)} = 0 \qquad (42)$$

$$x = R(\sigma_\infty/\nu)^{\frac{1}{2}}$$

which coincides with the Chandrasekhar-Reid equation. It is therefore seen that the result of the normal mode analysis are recovered asymptotically as $t\to\infty$. It is interesting to note that in this limit the distribution of vorticity inside the droplet is an equilibrium distribution which satisfies Eq. (19) with a vanishing LHS. Indeed, from Eqs. (33), (22), (20) one obtains that, as $p\to 0$:

$$\tilde{\omega}(r, \theta, p) \sim -2\frac{n-1}{n}\frac{2n+3}{2n+1}\frac{r^n}{R^{n+1}}\tilde{a}P_n^1(\cos\theta) \qquad (43)$$

which is a solution of $\nabla^2\tilde{\omega} = 0$. It is easy to show that Eq. (42) holds also for an arbitrary initial vorticity distribution. We shall not attempt here to discuss in detail the differences between Eqs. (39) and (42). We shall restrict our attention to the case of initially critically damped oscillations,

$\omega_0 = \tau_d^{-1}$, for which the initial (irrotational) motion changes nature becoming aperiodic, i. e. to the case:

$$\omega_0 \frac{R^2}{\nu} = (n-1)(2n+1) \tag{44}$$

Chandrasekhar (Refs. 1, 3) gives a short table of the maximum values M of $\omega_0 R^2/\nu$ that give rise to aperiodic decay; values of $\omega_0 R^2/\nu$ greater than M would result in damped oscillations. The comparison with Eq. (44) is as follows:

n = 2	M = 3.630	$\omega_0 R^2/\nu = 5$
n = 3	M = 6.026	$\omega_0 R^2/\nu = 14$
n = 4	M = 8.457	$\omega_0 R^2/\nu = 27$

Therefore it is seen that, even if the motion is initially aperiodic, it changes nature at a certain time to become oscillatory. This circumstance suggests very strongly that in general the damping factor corresponding to Eq. (42) is smaller than that given by the irrotational approximation, but no general proof can be furnished for this conjecture. In view of our result (33), one would then conclude that the effective damping factor at first increases and then decreases with time.

THE OSCILLATIONS OF BUBBLES AND OF LIQUID DROPS IMMERSED IN ANOTHER LIQUID

The case in which it is the inner liquid to have negligible dynamical effects can be treated analogously to what was done in the preceding section. Setting $\mu_1 = 0$, $\rho_1 = 0$ and dropping the subscript 2, we obtain:

$$\ddot{a} - 2(n-1)(n+1)(n+2)\frac{\nu}{R^2}\dot{a} + (n-1)(n+1)(n+2)\frac{T}{\rho R^3}a$$

$$-n(n+1)(n+2)\frac{\nu}{R}\Omega_0(t) = 0 \tag{45}$$

$$\Omega_0(t) + 2R^{-n-3}c(t) = -\frac{2}{R}\frac{n+2}{n+1}\dot{a} \tag{46}$$

Again eliminating Ω_0, Eq. (45) becomes:

$$\ddot{a} + 2(n+2)(2n+1)\frac{\nu}{R^2}\dot{a} + (n-1)(n+1)(n+2)\frac{T}{\rho R^3}a$$

$$+ 2n(n+1)(n+2)\nu R^{n-3}\int_R^\infty s^{-n+1}\Omega(s,t)ds = 0 \tag{47}$$

from which the irrotational frequency and decay constant follow as:

$$\omega_0^2 = (n-1)(n+1)(n+2)\frac{T}{\rho R^3}$$

$$\tau_d^{-1} = (n+2)(2n+1)\frac{\nu}{R^2}$$

Both these results are given by Lamb (Ref. 2, pp. 475, 640). The surface vorticity and velocity of deformation are found to be connected by:

$$\tilde{\Omega}_0(p) = -\frac{2}{R}\frac{n+2}{n+1}\tilde{a}\left[1+\frac{2}{q}\frac{K_{n-\frac{1}{2}}(q)}{K_{n+\frac{1}{2}}(q)}\right]^{-1}$$

$$q = R(p/\nu)^{\frac{1}{2}}$$

and the final equation for a(t) is obtained in the same form as Eq. (34), in which the kernel is now given by:

$$\tilde{Q}(p) = -\frac{2K_{n-\frac{1}{2}}(q)}{qK_{n+\frac{1}{2}}(q)+2K_{n-\frac{1}{2}}(q)}$$

The small-time behavior of the modulated frequency $\sigma(t)$ is found in the same way as was done before, with the result:

$$\frac{\sigma(t)}{\sigma_0} = 1+n(n+2)^2\left\{\frac{32}{15\pi^{\frac{1}{2}}}\left(\frac{\nu t}{R^2}\right)^{\frac{3}{2}}-\frac{2}{3}(n+2)\left(\frac{\nu t}{R^2}\right)^2\right.$$

$$\left.+\frac{32}{105\pi^{\frac{1}{2}}}\left[5(\sigma_0 t)\left(\frac{\nu t}{R^2}\right)^{\frac{3}{2}}-6n(n+2)\left(\frac{\nu t}{R^2}\right)^{\frac{5}{2}}\right]+\ldots.\right\} \qquad (48)$$

The similarity between this result and Eq. (39) is apparent.

For the large-time solution the same procedure applied before yields in this case the characteristic equation:

$$\sigma_\infty^2-2\tau_d^{-1}\sigma_\infty+\omega_0^2+2\beta_n\tau_d^{-1}\sigma_\infty\frac{2H^{(1)}_{n-\frac{1}{2}}(x)}{xH^{(1)}_{n+\frac{1}{2}}(x)+2H^{(1)}_{n-\frac{1}{2}}(x)} = 0 \qquad (49)$$

$$x = \left(\sigma_\infty R^2/\nu\right)^{\frac{1}{2}}$$

$$\beta_n = n(n+2)/(2n+1)$$

After some simplifying mathematical manipulations, the result obtained by Miller and Scriven by means of a normal mode analysis (Ref. 5) can be brought to the form of Eq. (49). Again there is a striking similarity between this result for the bubble and that obtained before for the drop, Eq. (42).

For the case in which both fluids have non-negligible dynamical effects (drop in liquid), the analysis is more complicated and also, for certain aspects, qualitatively different. Physically this comes about because the two fluids are now coupled through the no-slip boundary condition at the interface so that Eq. (27) must be used. In this case one finds that:

$$\tilde{\Omega}_{01}(p) = \frac{\tilde{a}}{nR}\left\{2(n-1)(\mu_2-\mu_1)C_n(q_2) - \frac{2n+1}{n+1}\mu_2\right\}\Delta^{-1}(q_1,q_2)$$

$$\tilde{\Omega}_{02}(p) = \frac{\tilde{a}}{(n+1)R}\left\{2(n+2)(\mu_1-\mu_2)\mathcal{T}_n(q_1) - \frac{2n+1}{n}\mu_1\right\}\Delta^{-1}(q_1,q_2)$$

$$\Delta(q_1,q_2) = \mu_1 C_n(q_2)[1-2\mathcal{T}_n(q_1)] + \mu_2\mathcal{T}_n(q_1)[1+2C_n(q_2)]$$

$$q_i = R(p/\nu_i)^{\frac{1}{2}} \qquad \mathcal{T}_n = I_{n+\frac{3}{2}}/q_1 I_{n+\frac{1}{2}} \qquad C_n = K_{n-\frac{1}{2}}/q_2 K_{n+\frac{1}{2}}$$

The equation of motion can now be written as:

$$\frac{(n+1)\rho_1+n\rho_2}{n(n+1)}\ddot{a} + \int_0^t Q(t-\tau)\dot{a}(\tau)\,d\tau + (n-1)(n+2)\frac{T}{R^3}a = 0 \qquad (50)$$

where:

$$\tilde{Q}(p) = \frac{\Delta^{-1}}{R^2}\left\{2\frac{n+2}{n+1}(2n+1)\mu_2(\mu_2-\mu_1)\mathcal{T}_n(q_1) - \frac{n-1}{n}(2n+1)\mu_1(\mu_2-\mu_1)C_n(q_2)2\right.$$

$$\left. - 4(n-1)(n+2)(\mu_2-\mu_1)^2\mathcal{T}_n(q_1)C_n(q_2) + \frac{(2n+1)^2}{n(n+1)}\mu_1\mu_2\right\}$$

It should be noticed that, although the irrotational frequency of oscillation can be read from Eq. (50) to be:

$$\omega_0^2 = \frac{(n-1)n(n+1)(n+2)}{(n+1)\rho_1+n\rho_2}\frac{T}{R^3}$$

(cf. Lamb, Ref. 2, p. 475), it is not possible to put (50) in a form analogous to (32) or (47). Nevertheless the irrotational decay constant can be determined by the method explained in the footnote on page 9 to be:

$$\tau_d^{-1} = \frac{1}{2R^2}\frac{2n+1}{(n+1)\rho_1+n\rho_2}\frac{1}{(\mu_2\sqrt{\nu_1}+\mu_1\sqrt{\nu_2})^2}$$

$$\times\left\{(\mu_2-\mu_1)\left[2(n+2)n\mu_2^2\nu_1+(2n+1)\mu_1\mu_2\sqrt{\nu_1\nu_2}-2(n-1)(n+1)\mu_1^2\nu_2\right]\right.$$

$$\left.+\frac{(2n+1)n(n+1)(\rho_1-\rho_2)^2\mu_1^2\mu_2^2}{\rho_1\rho_2[(n+1)\rho_1+n\rho_2]}\right\}$$

It can be verified that this expression reduces to the ones for the isolated drop and bubble when μ_2 or μ_1 vanish. The first time-dependent term in the equation for $\sigma(t)$ is also in this case of order $t^{\frac{3}{2}}$.

A more complete analysis will be published elsewhere.

ACKNOWLEDGMENTS

It is a pleasure to thank Professor Milton S. Plesset for the many illuminating discussions on the content of this work and for his warm encouragement. A conversation with Professor Derek W. Moore is also gratefully acknowledged.

REFERENCES

1. S. Chandrasekhar, Hydrodynamic and Hydromagnetic Stability, Clarendon Press (1961).
2. H. Lamb, Hydrodynamics, 6th Ed., Cambridge University Press (1932); Dover Reprint (1945).
3. S. Chandrasekhar, "The Oscillations of a Viscous Liquid Globe," Proc. London Math. Soc. 9, 141-149 (1959).
4. W. H. Reid, "The Oscillations of a Viscous Liquid Drop," Quart. Appl. Math. 18, 86-89 (1960).
5. C. A. Miller and L. E. Scriven, "The Oscillations of a Fluid Droplet Immersed in Another Liquid," J. Fluid Mech. 32, 417-435 (1968).
6. G. K. Batchelor, An Introduction to Fluid Dynamics, Cambridge University Press (1967).
7. M. S. Plesset, "On the Stability of Fluid Flows With Spherical Symmetry," J. Appl. Phys. 25, 96-98 (1954).
8. Lord Rayleigh, The Theory of Sound, 2nd Ed., Art. 364, Macmillan (1894); Dover reprint (1945).
9. M. Onoe, Tables of Modified Quotients of Bessel Functions of the First Kind for Real and Imaginary Arguments, Columbia University Press (1958).

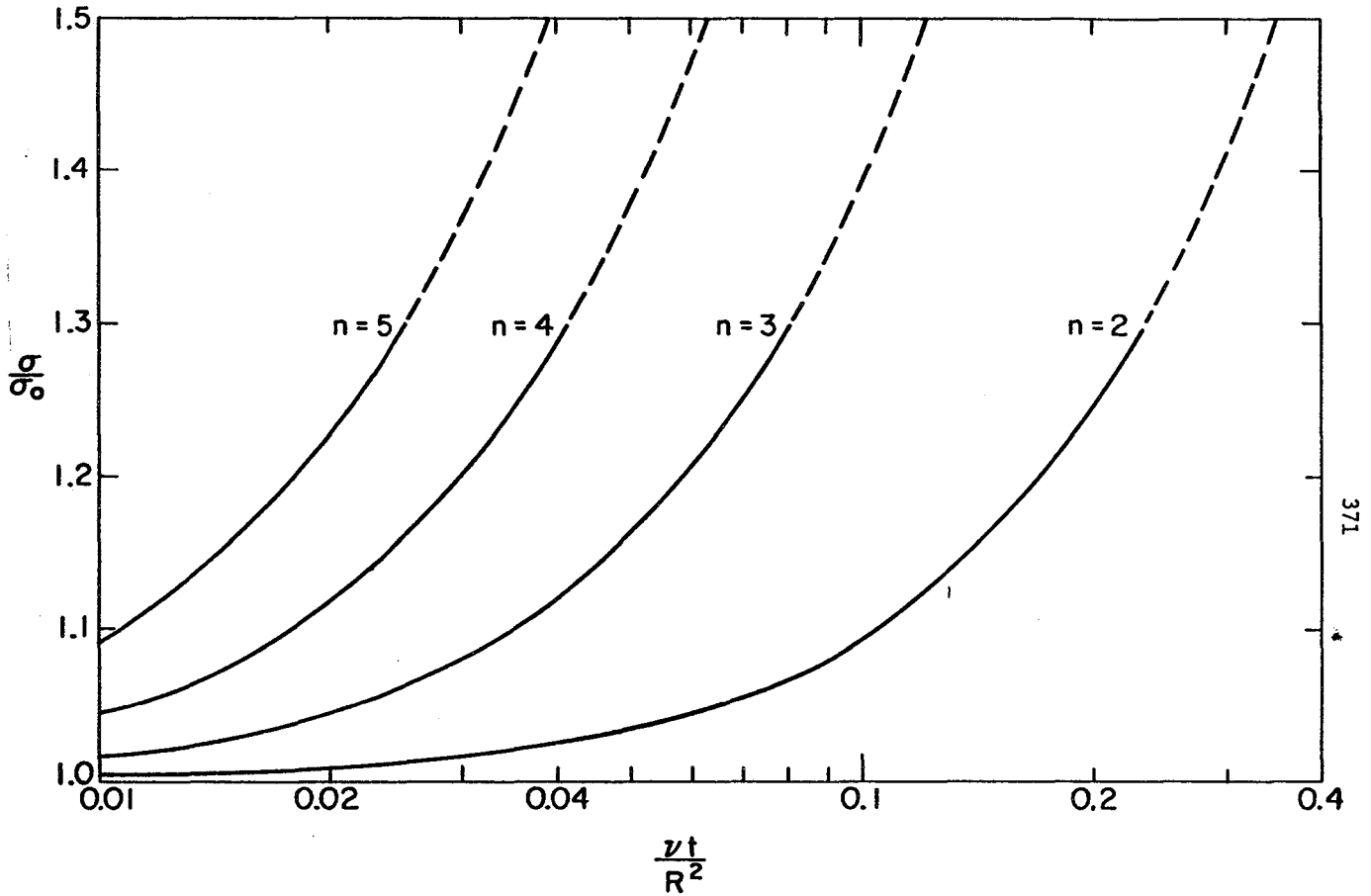

Fig. 1. Small-time behavior of the complex frequency $\sigma(t)/\sigma_0$ for the case of a drop oscillating in vacuum (only the terms in the first line of Eq. (39) have been used to construct the curves).

NON-LINEAR EFFECTS ON DROPLET DEFORMATION

P.G. Simpkins*
Department of Aeronautics and Astronautics
Southampton University, England

1. INTRODUCTION

When a liquid droplet moves through an ambient fluid a natural oscillation is set up between the aerodynamic forces tending to distort the drop, and the surface tension forces seeking to restore the shape to the profile with minimum surface energy. A large amount of experimental evidence has established that when the Weber number exceeds a value of order unity, large deformations from the spherical profile occur and ultimately the droplet ruptures. During the deformation process the droplet develops from a disc-like shape into a canopy which resembles either a parachute or a parasol. Photographs of such highly distorted drops have been taken by Lane and Green[7], Hanson, Domich and Adams[8], Wolfe[9] and the author[10] for a variety of liquids from water to mercury. Figures (1) and (2) illustrate the two types of behaviour that occur for Weber numbers greater than unity and are typical of pictures recorded by numerous experimenters. Table 1 summarizes the observations made of the response characteristics, and illustrates the uncertainty in predicting the behaviour. Whereas the author's data suggests the bag response occurs at Weber numbers below those for which the parasol is generated, the observations of others do not always support this contention. It should be emphasized that these response characteristics are the result of aerodynamic forces and that the droplet is not unstable in a rigourous sense, i.e. the distortion does not grow exponentially in time. An instability of the windward surface does occur when the induced acceleration of the droplet becomes very large. The resulting Taylor instability has been the subject of a recent paper by Harper, Grube and Chang.[11]

Although the occurrence of the large deformation and break-up phenomenon is now experimentally well-established, attempts to predict the incipient conditions have been limited to semi-empirical approaches. One of the earliest estimates of the critical Weber number We_c was given by Hinze[3] who considered the two cases of large and small liquid viscosity. For the purpose of the discussion We_c is taken to be that value at which the droplet ruptures. For small viscosity fluids, Hinze compared the linear theory expressions for the surface displacement at the stagnation point to a series of experimental observations. By these comparisons he deduced that $6 < We_c < 10$ depending on the initial conditions applied to the drop. Such estimates however can at best be only subjective since as Hinze himself notes the critical deformation, which leads to the breaking up of a droplet, has a value far exceeding that tolerable by linear assumptions. In a more basic approach Gordon[2] equated the energy required to displace a cylindrical section from a droplet exposed to an external flow. To do this Gordon estimated the aerodynamic, viscous

and surface tension forces and combined these with the inertial effects to obtain an expression for time-dependent surface displacement. As a result, a value of $We_c = 8$ was predicted. Golovin[4(a)] examined the case in which the external flow about the drop was assumed to be potential but the internal liquid motion had finite vorticity. To make this connection Golovin argued that the internal rotational motion is driven by viscous forces in the liquid near the interface. By equating the internal dynamic pressure gradient to that in the external potential flow he deduced the normal modes for the surface vibration of the above model, and a critical value of $We_c \simeq 2.5$. In a subsequent paper Golovin[4(b)] examined the problem assuming a potential flow in the droplet interior. In that case, he deduced a value of $We_c = 2.2$. In both Hinze[3] and Golovin's[4] work the predictions for We_c are based on linear theory and whereas Gordon's[2] energy method implicitly relies on the assumption that viscous effects may be represented as a Poiseuille flow. None of the above approaches has accounted for the interaction which occurs between the droplet and the external flow as the distortion grows.

Recently, calculations of the higher-order approximations to the equations of motion have been performed by Harper, Simpkins and Grube[5] in which the coupling between the droplet distortion and the pressure distribution exerted by the external flow on the drop are taken into account. This paper will briefly review the nature of the droplet response in the vicinity of the critical Weber number. In Section 2 the linear theory will be described for the limiting cases of $We < 1$ and $We >> 1$. These limits show the droplet response to be vibratory and algebraic functions of time, respectively. Subsequently, in Section 3, the method of improving the estimate for the transition point between the two response characteristics is described. In Section 4 the general three-dimensional response case is discussed and the occurrence of degenerate oscillations is noted.

2. REVIEW OF THE LINEAR THEORY

The vibrational response of a liquid droplet about a spheroidal shape was originally established by Rayleigh[1] from a linear analysis. The shape of the droplet can be represented in spherical co-ordinates (r, θ, ϕ) as

$$\eta = 1 + \sum_{n=o} a_n P_n(\cos\theta) \qquad (1)$$

where $\eta = r/R$, P_n is the n^{th} order Legendre function of the

first kind, R is the radius of the unperturbed sphere, and the coefficients a_n are functions of time. Rayleigh's results, obtained from energy principles, showed that $a_n = b_n \cos w_n t$ and that the non-dimensional eigen-frequencies w_n are given in terms of a modified Weber number by

$$w_n^2 = n(n-1)(n+2)/We^* . \tag{2}$$

The Weber number We, which is a measure of the dynamic pressure force compared to the surface tension, restoring force, is expressed as

$$We = \rho \frac{U_\infty^2 R}{\sigma} = \varepsilon We^* \tag{3}$$

where $\varepsilon = \rho/\hat{\rho}$ is the ratio of the gas-liquid density ratio, U_∞ is the external airstream velocity and σ is the surface tension.

More generalized treatments of the droplet response problem have been given by Landau and Lifshitz[12] and by Harper, Grube and Chang[11]. The former authors have shown that for each of the axi-symmetric modes there are (2n + 1) oscillations, i.e. the frequencies are degenerate. This aspect will be discussed further in Section 4. The results of Harper, Grube and Chang on the other hand gave an explicit result for the axi-symmetric response of a vibrating droplet, which is

$$\eta(\theta,t) = 1 + \varepsilon \sum_{n=o} \frac{n(2n+1)}{4w_n^2} C_n P_n(\cos\theta)\left[\cos w_n t - 1\right] + O(\varepsilon^2) \tag{4}$$

The coefficients C_n in equation (4) are determined from the external pressure distribution on the droplet.

An important change in the response characteristics is observed when $\cos w_n t$ is expanded for $w_n t \ll 1$. In that circumstance the surface displacement is found to be

$$\eta(\theta,t) \simeq 1 + \varepsilon \sum_{n=o} \frac{1}{8} n(2n+1) C_n P_n(\cos\theta) t^2 + O(\varepsilon^2) \tag{5}$$

i.e. the droplet now executes an irreversible distortion which is algebraic in time. This limiting procedure, $w_n t \ll 1$, is strictly not one which implies $t \to 0$ but more realistically

that We → ∞. Therefore, it may be stated that in the absence of surface tension the droplet response to an external flow-field is one of continuous distortion; a conclusion which is implicit in Rayleigh's original result.

To illustrate the linearized response characteristics consider an external potential flow associated with a rigid sphere, for which the pressure distribution is given by

$$P_e(\theta) = 1 - (^9/_4)\sin^2\theta \qquad (6)$$

The droplet response to such an external field has been established by a number of authors as

$$\eta(\theta,t) = 1 + \frac{3}{4}\,\varepsilon\, P_2(\cos\theta)t^2 + O(\varepsilon^2). \qquad (7)$$

This characteristic is shown in Figure (3) from which it is observed that the axial thickness decreases to zero when the normalized time t = 32.7. If instead the external flow is considered to be one in which flow separation occurs, then the predicted droplet response is altered significantly. Hinze[3] used a pressure distribution of the form

$$P_e(\theta) = 1 - (^9/_4)\sin^2\theta \qquad 0 < \theta < {}^{\pi}/_3$$

$$= \text{const} \qquad {}^{\pi}/_3 < \theta < \pi$$

as a means of estimating a value for the critical Weber number. More recently the pressure distributions on a rigid sphere recorded by Maxworthy[13] have been synthesized by an eighty term series and used to calculate the transient response of a droplet. Results taken from these calculations are given in Figure (4). For small times the predicted response is in good agreement with experimental shock tube studies, however for values of t > 15 say the predictions are less realistic. This result is not unexpected since as the droplet distortion grows the external flow about it is modified. Thus, the applied pressure distribution changes and the assumption that it is similar to that on a rigid sphere is no longer valid. It is this non-linear coupling which will be discussed in the next section. A comparison between the two linear models described above and data taken from a bag-type response is given in Figure (5) where the ordinate $(^b/_a)$ is the ratio of the minor to major axes. The data support the conclusion that for t < 15 the predicted response is good a representation of the behaviour. However, the predictions suggest a rate of distortion greater than that observed.

3. NON-LINEAR EFFECTS

The previous section illustrated how, between the limits of We << 1 and We → ∞, the droplet response changes from a vibratory characteristic to one which is monatonically deforming in time. A question that therefore naturally arises is, can an estimate be made of the value of the Weber number at which the vibrational response ceases and the continuous distortion begins? We use this aforementioned criterion as a definition for the critical Weber number, We_c. Other investigators, as has been previously noted, have based their estimates of We_c on when the droplet ruptures.

In examining the higher-order terms of the equation of motion Harper, Simpkins and Grube[5] have considered the droplet as a non-linear oscillator for which the forcing term represents the external air flow. The non-linearity in the problem causes a change in the modal frequencies which, when evaluated, allows a revised estimate of the surface displacement to be made. To reduce the algebra to manageable proportions the external flowfield is considered to be the potential flow given by equation (6) for which $P_e(\theta) \sim P_2(\cos\theta)$. In the higher-order approximation a regular perturbation in ε is not uniformly valid because of the appearance of secular terms of the form $t \sin w_2 t$. These secular terms arise because the linear response to an external potential flow has a displacement $\eta(\theta,t) \sim P_2(\cos\theta)$. Thus, when in the higher-order approximation a forcing function proportional to $P_2(\cos\theta)$ is introduced it excites a $P_2(\cos\theta)$ mode at exactly the fundamental frequency giving rise to a resonant condition. The PLK co-ordinate stretching technique[6] has been used to render the estimated response uniformly valid and the correction to the eigen-frequency is found to be

$$\alpha = \left(1 - \frac{We}{3.85}\right) \tag{8}$$

so that to first-order, the surface displacement now becomes

$$\eta(\theta,t) = 1 + \frac{3}{2}\,\varepsilon\, P_2(\cos\theta)\left\{\frac{\cos\alpha w_2 t - 1}{w_2^2}\right\} + O(\varepsilon^2) \tag{9}$$

The result for the corrected eigen-frequency, equation (8), shows that when $\alpha \simeq 1$, i.e. We << 1, the effect of the non-linear interaction is to reduce the frequency below that of the fundamental. In the limit $\alpha \to 0$ with t bounded it is noted that the droplet will begin to deform continuously as the Weber number approaches the critical value We ≃ 3.85. Thus the higher-order analysis yields an estimate for the commencement of the distortion when We ~ O(1) rather than the linear result

of We → ∞. The reduced frequency αw_2 which develops as a result of non-linear effects is shown in Figure (6) as a function of We.

Because of the non-linear interaction between the distorted droplet and the external potential flowfield the second-order correction to the surface displacement is found to be of the form

$$\eta^{(2)}(\theta,t) \sim \varepsilon^2 \left\{ P_2(\cos\theta)\left[K_1 \frac{\cos\alpha w_2 t}{w_2} + K_2 \frac{\cos 2\alpha w_2 t}{w_2}\right] + P_3(\cos\theta) K_3 \left[\frac{\sin\alpha w_3 t}{w_3} - \frac{\sin\alpha w_2 t}{w_2}\right] + P_4(\cos\theta)\left[\begin{array}{l}\text{terms in } \cos\alpha w_4 t,\ \cos\alpha w_2 t \\ \text{and higher harmonics}\end{array}\right]\right\} \qquad (10)$$

where the K's are constants to be evaluated. Two interesting features therefore emerge from the high-order analysis. Firstly, an anti-symmetric term, i.e. the P_3 mode, is found in the surface displacement in response to an external pressure distribution which was initially symmetric. Secondly, as We increases through We_c the sign of α changes. This sign change affects only the anti-symmetric $P_3(\cos\theta)$ mode because the symmetric modes only contain terms in $\cos\alpha w_n t$ and their higher harmonics. Consequently as We passes through the critical value the droplet response changes. In the potential flow model under discussion it would in effect appear as though the freestream direction had been reversed.

4. DISCUSSION

It is of interest to consider briefly the more general treatment of the response described by Landau and Liftshitz[12]. Let the deformed surface be described in terms of the spherical harmonic functions $Y_{nm}(\theta,\phi)$ as

$$r = R + \varepsilon e^{-iw_n t} Y_{nm}(\theta,\phi) \qquad (11)$$

where

$$Y_{mn}(\theta,\phi) = e^{im\phi} P_n^m(\cos\theta) \qquad (12)$$

and $P_n^m(\theta)$ are associated Legendre functions of the first kind. Then for each mode n of the eigen-frequency w_n there are (2n + 1) different oscillations corresponding to m = 0, ± 1, ± 2 ..... $\pm n$. The oscillations are therefore degenerate, since at any particular eigen-frequency there is more than one oscillation which satisfies the first-order equations of motion. Since both $\pm m$ give rise to the same oscillation there are, however, only (n + 1) independent oscillations. Thus, for the fundamental n = 2 mode, there are three independent oscillations, (i) the axi-symmetric P_2-mode, (ii) an anti-symmetric P_2^1-mode and (iii) a symmetric P_2^2-mode. The latter three-dimensional modes are tabulated in standard texts[14,15] and shown in Figure (7). The P_2^1-mode gives rise to a transverse oscillation which wavers about an axis through the poles in the manner shown in Figure (7). Since the nodal line is a great circle through $\phi = \pi/2$ zero displacement occurs when $\theta = \ell\pi/2$. The P_2^2 modal response is more complicated since the nodal lines are in planes normal to the equator through $\phi = \pm\pi/4$. The projected profile in the equatorial plane therefore resembles an ellipse whose major axis oscillates between two normal directions parallel and perpendicular to the freestream velocity vector. The occurrance of this P_2^2 mode is of interest since it illustrates that the droplet can seek to become distorted in a direction parallel to the freestream.

When the non-linear effects are taken into account it is found that even for just a P_2-mode in the external flow, the droplet response is excited not only in the w_2 eigen-frequency, but also in w_3 and w_4. Thus additional degenerate oscillations occur each associated with the higher-order eigen-frequencies. Of the modes established by the non-linearity, those associated with the P_3^3 and P_4^4-modes are of most germane to this discussion. These modes, whose characteristics are similar to P_2^2, intensify the droplets inclination to become extended in the vicinity of the stagnation point. At the same time the region over which this extension occurs becomes more restricted in θ as the number of nodes increases with m. Whether the occurrance of the degenerate oscillations is the reason for the two types of response observed beyond the critical Weber can only be conjecture at this time. It is however noteworthy that both the bag and the parasol responses have been recorded by different experimenters at approximately the same Weber numbers.

5. CONCLUSIONS

The following remarks summarize the principle points of this paper.

(i) Solutions of the second-order equations of motion show that for an external potential flow the fundamental

eigen-frequency is reduced by an amount $[1 - (We/3.85)]$ as a result of the non-linear interaction between the droplet and the freestream.

(ii) The non-linear analysis suggests that the transition from the vibratory to the algebraic response occurs at about $We_c \simeq 3.85$.

(iii) The appearance of higher-order modes in the predicted surface displacement introduces a number of degenerate oscillations each associated with a particular eigen-frequency. Specific modes of some of these degeneracies have the effect of causing the stagnation point on the droplet to become elongated. These degenerate modes may give rise to the observed effects beyond We_c where two types of response occur whose characteristics resemble (a) a bag, and (b) a parasol.

6. ACKNOWLEDGMENTS

I wish to thank Dr. E.Y. Harper for helpful discussions during the preparation of this paper.

Figure (1) is published by permission of the Controller of Her Majesty's Stationery Office.

REFERENCES

1. Lord Rayleigh, (1879). "On the Capilliary Phenomena of Jets". Proc. Roy.Soc. 29, 71.

2. Gordon, G.D. (1959). "Mechanism and Speed of Breakup of Drops". J.Appl.Phys. 30, 1759.

3. Hinze, J.O. (1949). "Critical Speeds and Sizes of Liquid Globules". Appl.Sci.Res. A1, 263.

4. Golovin, A.M. (1964)a. "The Theory of the Vibration and Breakdown of Droplets in a Gas Stream in the Presence of Rotational Motion inside the Drops". Bull (Izv) Akad. Sci. Nauk. Geophys. USSR, 7, 1084.

   Golovin, A.M. (1964)b. "On the Theory of Oscillations and Fractioning of a Drop in a Gas Stream with a Potential Movement within the Drop". Bull (Izv) Akad. Sci. Nauk. Geophys. USSR 8, 1269.

5. Harper, E.Y., Simpkins, P.G. and Grube, G.W. (1974). "Non-Linear Droplet Response to External Pressure Distributions". To be published.

6. Nayfeh, A.H. (1973). "Perturbation Methods". Wiley-Interscience.

7. Lane, W.R. and Green, H.L. (1956), in "Surveys in Mechanics" pp.162-215, edit. Batchelor and Davies, Cambridge Univ. Press.

8. Hanson, A.R., Domich, E.G. and Adams, H.S. (1963). "Shock Tube Investigation of the Break-up of Drops in Air Blasts". Phys. Fluids, 6, 1070.

9. Wolfe, H.E. (1966). "Photographic Study of the Breakup of Liquid Drops". J.SMPTE. 75, 738.

10. Simpkins, P.G. (1971). "Non-Linear Response of Deforming Drops". Nature Phys. Sci. 233, 31.

11. Harper, E.Y., Grube, G.W. and Chang, I. Dec.(1972). "On the Breakup of Accelerating Liquid Drops". J.Fluid Mech., 52, 565.

12. Landau, L.D. and Lifshitz, E.M. (1959). "Fluid Mechanics" Addison-Wesley Co. Inc. Reading, Mass.

13. Maxworthy, T. (1969). "Experiments on the Flow Around a Sphere at High Reynolds Numbers". J.App.Mech., 36, 598.

14. Jahnke, E. and Emde, F. (1945). "Tables of Functions" Dover Pubs. New York.

15. Hobson, E.W. (1931). "The Theory of Spherical and Ellipsoidal Harmonics". Cambridge Univ. Press.

16. Bukhman, S. (1954). "Experimental Investigation of the Disintegration of Drops". Vestnik AN Kazakhskoy SSR, 11.

17. Margarvey, R.H. and Taylor, B.W. (1956). "Free Fall Breakup of Large Drops". J.Appl.Phys. 27, 1129.

Authors	Liquid	Response	We	Experiment
Bukhman[16]	Water	Bag	2.3±0.4	Steady air jet
	Ethyl alcohol	"	"	" " "
	Glycerin	"	"	" " "
	Methyl benzene	"	"	" " "
Hanson et al[8]	Water	Bag	3.6-6.8	Shock Tube
	Silicon Oil	"	6.5-10.5	" "
Lane	Water	Bag	11	Wind Tunnel
Lane & Green[7]	Water	Bag	5.2	Wind Tunnel
Margaivey & Taylor[17]	Water	Bag	6.0-6.2	Free Fall
Simpkins[10]	Water	Bag	10-17	Shock Tube
Wolfe[9]	Water	Bag	3.8	Shock Tube
Hanson et al[8]	Water	Parasol	6.8-9.3	Shock Tube
	Silicon Oil	Parasol	7-10.4	" "
Simpkins[10]	Water	Parasol	30-45	Shock Tube
Wolfe[9]	Mercury	Parasol	4.3	Shock Tube

TABLE 1

Observations of Large Deformation Characteristics

and their Corresponding Weber Numbers

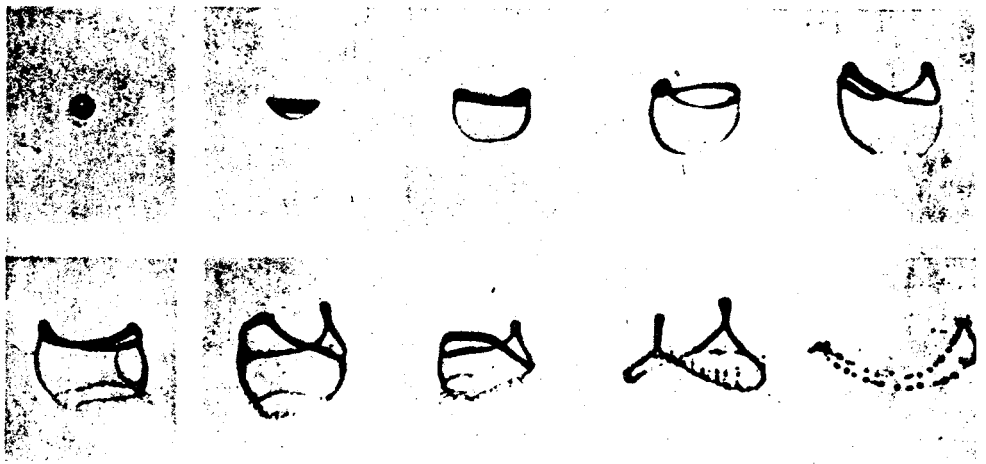

FIG. 1. DEVELOPMENT OF THE BAG-TYPE RESPONSE AT We = 11 (FROM LANE & GREEN)

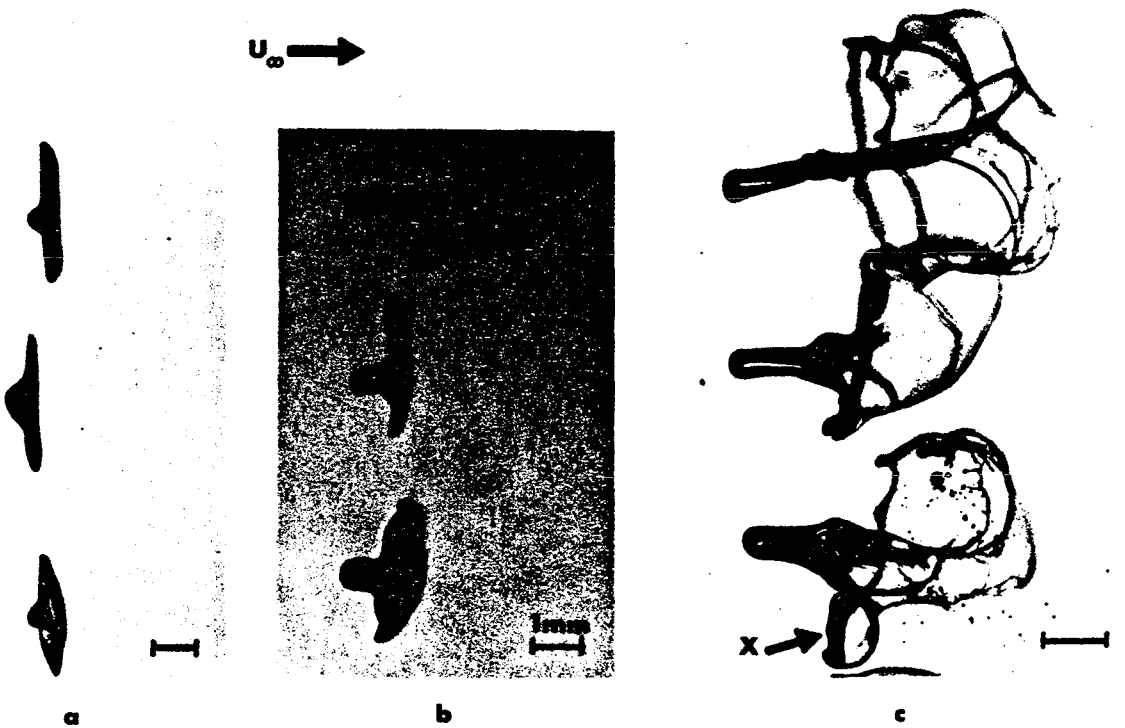

FIG 2

DEVELOPMENT OF THE UMBRELLA RESPONSE AT We = 32.5;
(a) 969 μs, (b) 1528 μs, (c) 1662 μs.

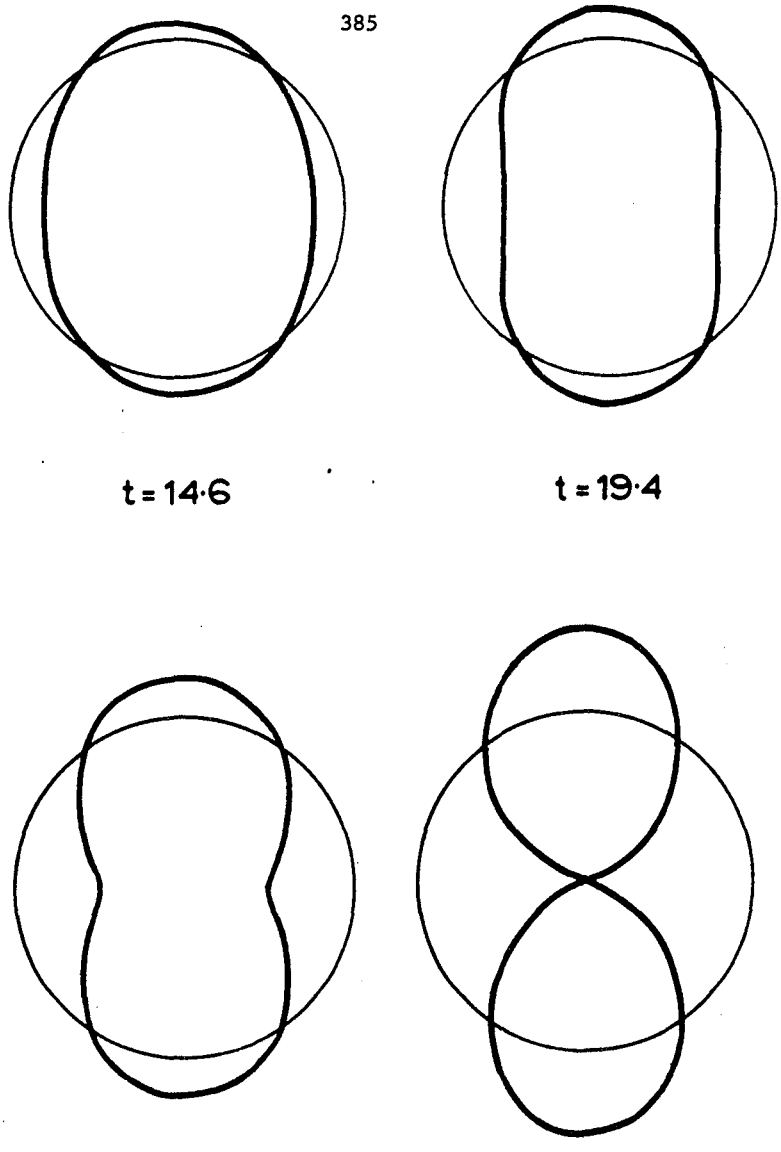

$$\eta(\mu) = 1 - \frac{3}{4} P_2(\mu) \epsilon t^2$$

LINEAR RESPONSE TO AN EXTERNAL POTENTIAL FLOW

FIG. 3.

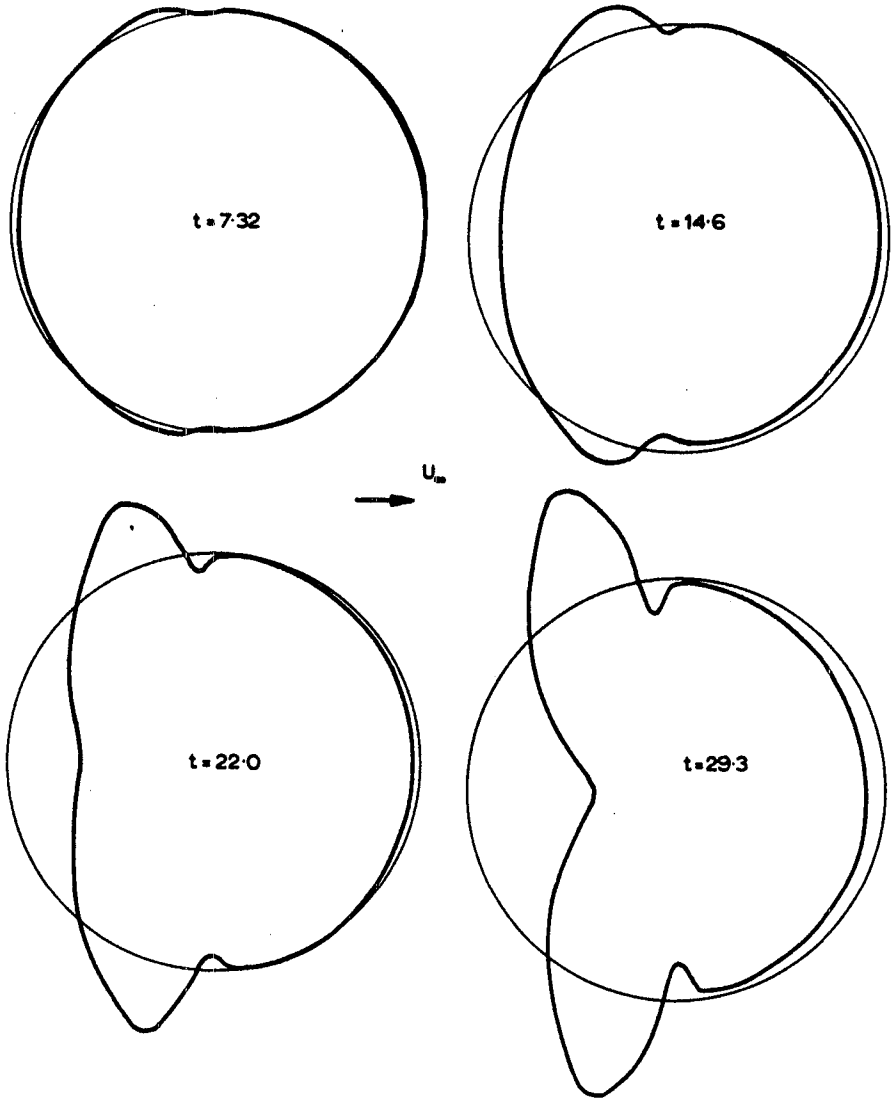

DYNAMIC RESPONSE TO THE PRESSURE DISTRIBUTION ON A RIGID SPHERE, $Re = 2 \times 10^5$

FIG. 4.

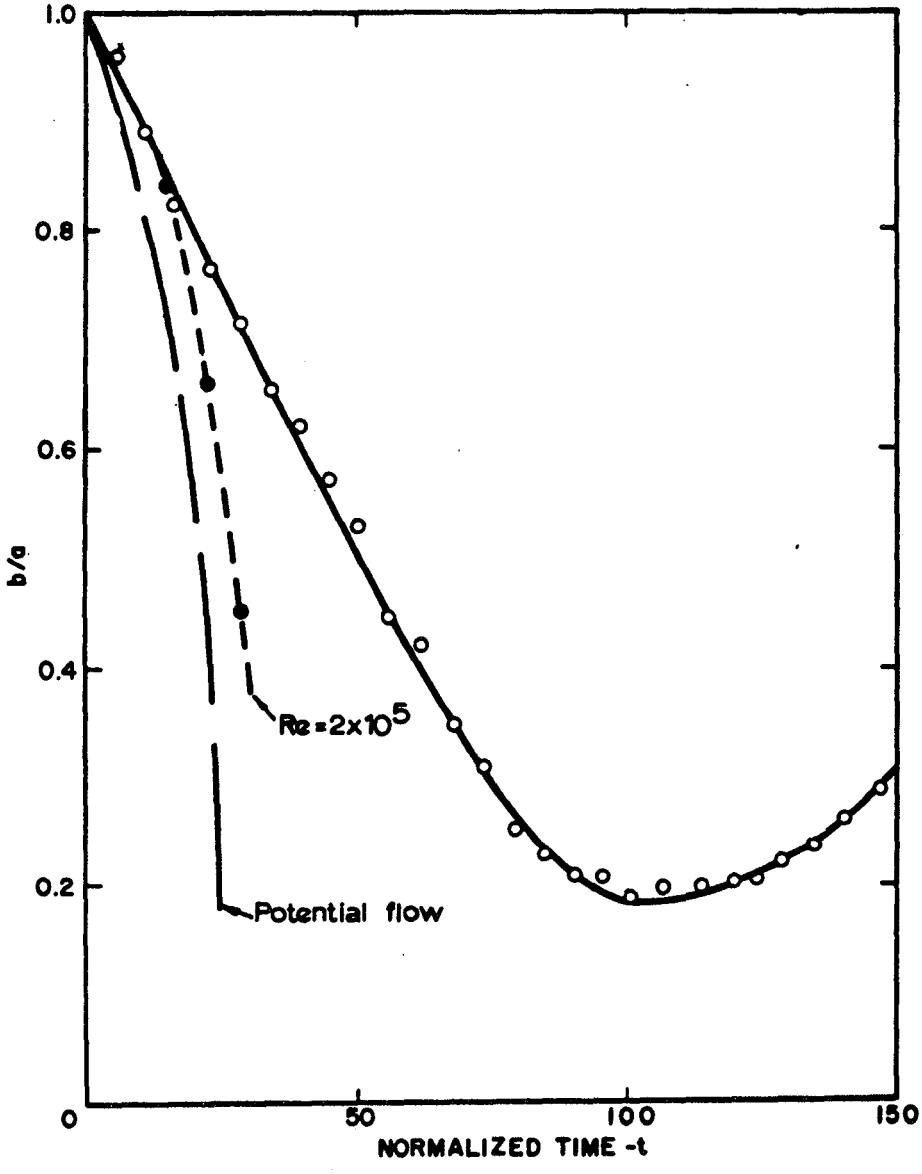

DISTORTION OF A 1mm DROP DURING THE INITIAL PHASE OF A BAG-TYPE BREAK UP

FIGURE 5.

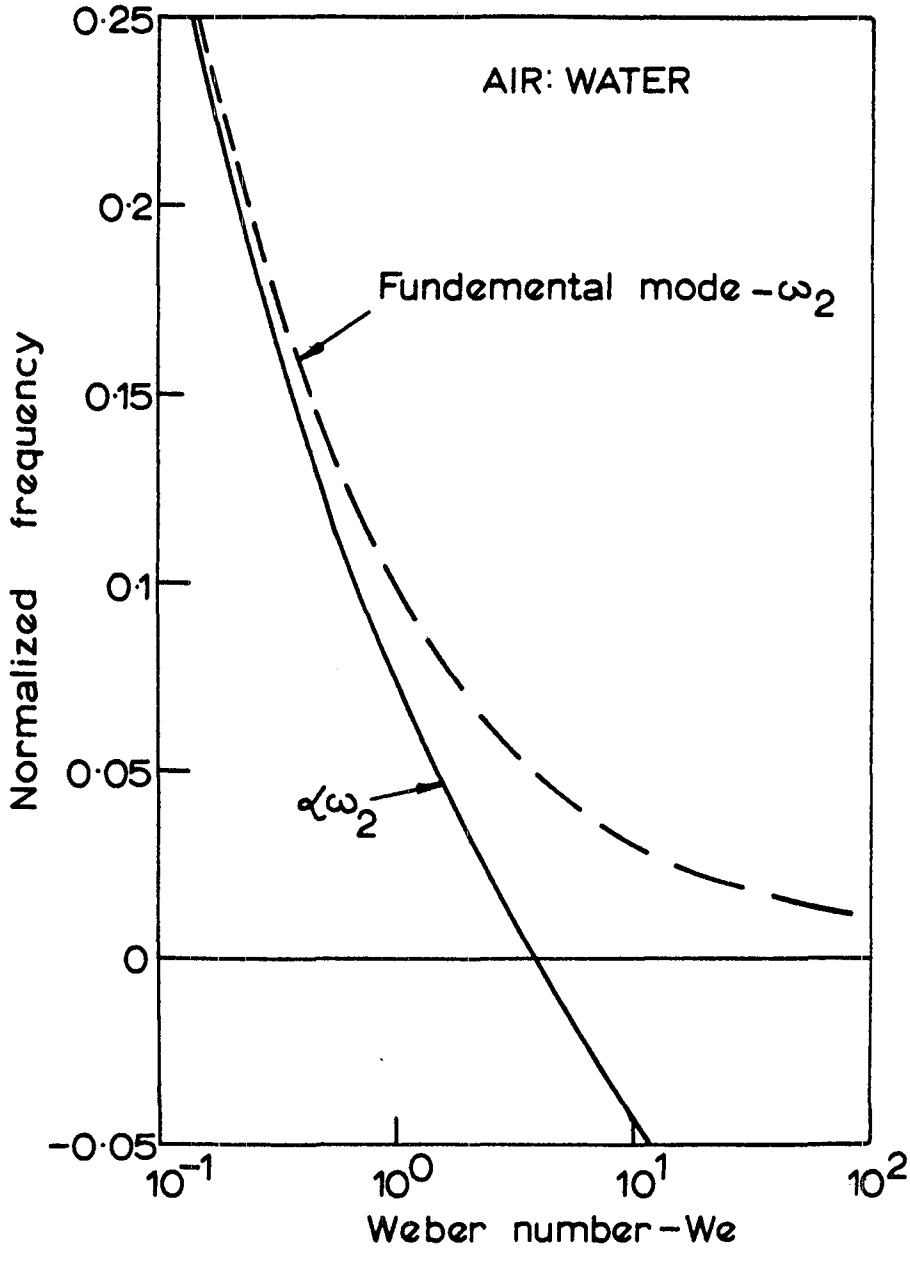

REDUCED FREQUENCY DUE TO NON-LINEAR EFFECTS.

FIG. 6.

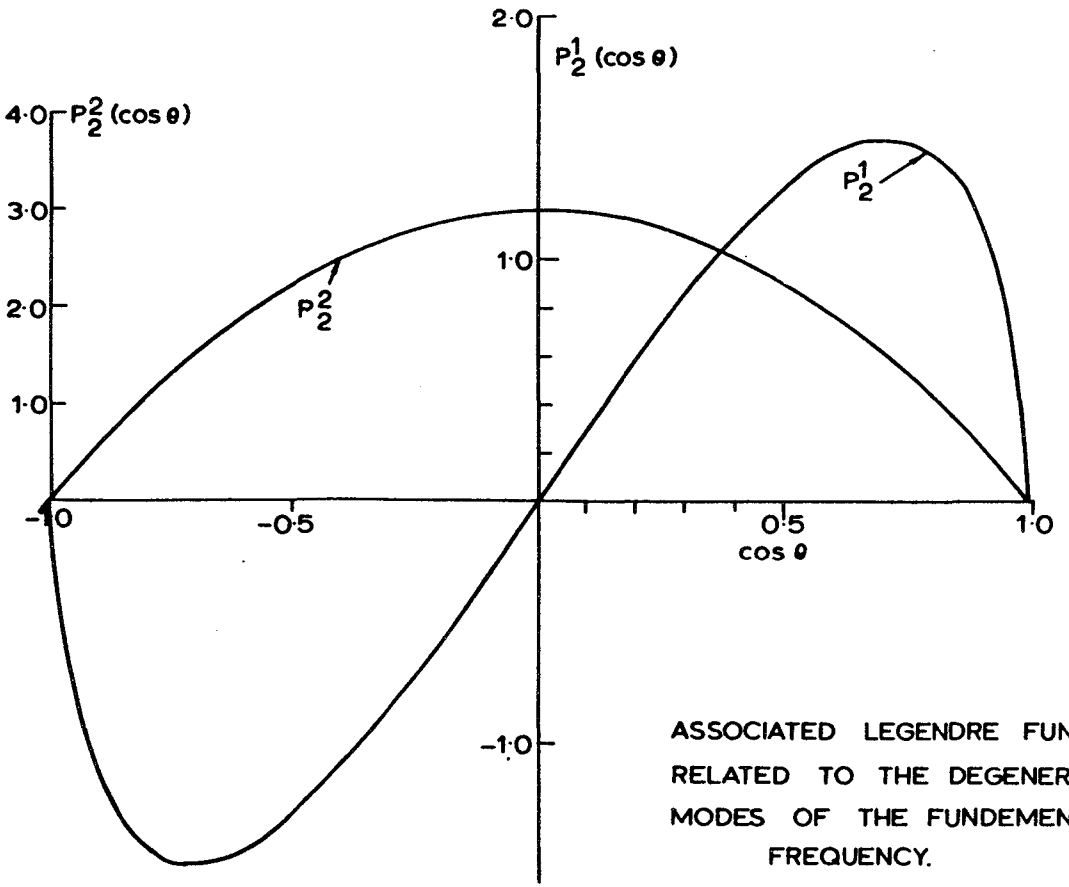

ASSOCIATED LEGENDRE FUNCTIONS RELATED TO THE DEGENERATE MODES OF THE FUNDEMENTAL FREQUENCY.

FIG. 7.

DEFORMATION AND BURST OF SINGLE DROPS IN A VISCOUS FLUID*

Andreas Acrivos
Stanford University, Stanford, California 94305

ABSTRACT

The motion of small drops in a viscous fluid is considered theoretically and experimentally. Two cases are examined in some detail: drops moving steadily in a quiescent fluid, and neutrally buoyant drops freely suspended in a linear shear field. Theoretical expressions are presented for the shapes of these drops, and these are compared with the available experimental data. The conditions under which bursting of drops is expected to occur, plus the application of the basic data involving single drops to the interpretation and prediction of the dispersion performance of static mixers, are also discussed.

INTRODUCTION

Flow phenomena, which involve the motion of drops and bubbles in viscous liquids, are known to occur frequently in nature and to play an important role in many processes of physical interest. Familiar examples, taken from different branches of engineering, include: agitation induced by bubble motion, the removal of carbon monoxide in Open Hearth Steelmaking, mass transfer from a dispersed liquid phase into another as in liquid-liquid extraction, lift pumps, the flow of emulsions whose non-Newtonian characteristics are often very striking, the dispersion and mixing of one viscous fluid into another, and many more. Although these systems are, in general, much too complicated of course to permit their quantitative theoretical description, many of their basic features can be modeled, sometimes to a surprisingly accurate extent, by considering the detailed behavior of the individual drops in the two-phase mixture. Thus, for example, the efficiency of a liquid-liquid extraction contacting device is closely related to the rise velocity of the liquid drops comprising the dispersed phase, while the dispersion performance and power requirements of static mixers are strongly affected by the breakup characteristics of single drops in a shear field. Thus, the flow past single drops and bubbles is a subject not only of considerable academic interest but also of potential practical applicability to many diverse processes in engineering and science.

* Work supported in part by the National Science Foundation.

In what follows, we shall review briefly some of the more important theoretical and experimental results pertaining to two areas of the above field: (a) drops moving steadily in a quiescent fluid; and, (b) neutrally buoyant drops freely suspended in a linear shear flow. Only the case of laminar motion will be considered.

THE RISE VELOCITY OF BUOYANT DROPS

Harper [1] has already presented an excellent and detailed review of this subject, and hence we shall restrict our discussion to some of the highlights.

The basic relation which determines the terminal velocity of a single drop is the simple force balance

$$\text{drag} = \frac{4\pi}{3} a^3 g (\rho - \rho') \tag{1}$$

where a is the known equivalent radius of the drop, g is the gravitational constant, and ρ and ρ', are the densities of, respectively, the continuous and the dispersed phase. Thus, in contrast to many of the classical problems in fluid mechanics, the drag is given while the velocity of translation of the body is the unknown. Of course, this is not the main complicating feature; rather it is the fact that the shape of the drop cannot be specified a priori, but needs to be obtained as part of the overall solution.

The problem to be solved can, therefore, be stated as follows: One seeks a solution to the appropriate Navier-Stokes equation, in the region both inside and outside the drop, which leads to finite velocities everywhere and which satisfies the boundary conditions:

i) At infinity, $u_i \rightarrow U\delta_{i3}$ (2)

ii) On the surface of the drop:

a) $$u_i n_i = 0, \quad u_i = u_i' \tag{3}$$

b) $$(\sigma_{ij} - \sigma_{ij}') n_j = \gamma n_i \, \partial n_k / \partial x_k \tag{4}$$

where x_i is a position vector with origin at the center of mass of the drop, δ_{i3} is a unit vector parallel to the gravitational acceleration, u_i is the velocity vector, U is the unknown terminal drop velocity, n_i is the unit outer normal to the surface of the drop, σ_{ij} is the stress tensor and γ is the interfacial tension. All primed symbols refer to quantities within the drop. Also, we shall limit our discussion to systems with clean interfaces; i.e. we shall not consider the effects of surface active agents which are known to play an important role in some cases when the drop is small [1, 2].

In spite of the rather simplified nature of the problem as stated above, an exact solution cannot be obtained in general except through laborious time-consuming finite-difference numerical computations. It is instructive, therefore, to examine some special cases.

To this end, let us consider the case of a gas bubble rising in a Newtonian liquid. Here $\rho' << \rho$ and $\mu' << \mu$, with μ being the viscosity. Hence, the independent parameters of the system reduce to the following six: U, a, g, ρ, μ and γ, which can be combined into the three independent dimensionless groups

$$R \equiv a\rho U/\mu, \quad W \equiv a\rho U^2/\gamma, \quad M \equiv g\mu^4/\rho\gamma^3$$

where R is the familiar Reynolds number and W is the Weber number. It should be noted that, of these groups, only M depends exclusively on the properties of the liquid medium, while R and W depend on both the size and the velocity of the bubble. In fact, since γ and ρ do not vary greatly from one system to another, M is effectively proportional to μ^4.

In some respects, in the case of rising bubbles, the use of R and W is somewhat awkward at times because, in contrast to most of the classical problems in hydrodynamics, U and a are not independent entities since, for a given bubble size, the rise velocity must adjust itself so as to maintain the proper balance between the buoyancy force and the drag acting on the bubble. Thus, U is seen to depend on a as well as on the physical properties of the system.

Particularly simple expressions for the rise velocity U exist when the equivalent radius a is either very small or large. In the former case, typically for $a < 10^{-2}$ cm., the bubble is spherical, owing to the small value of W, and inertia effects are negligible because $R << 1$. Thus, by solving the creeping flow equations one obtains the well-known result, first derived by Hadamard and by Riabouchinsky [1, 3].

$$U = a^2 g\rho/3\mu \quad . \tag{5}$$

At the other extreme, i.e. when a typically exceeds 1 cm., the Reynolds number is large and the surface tension forces negligible. Then, as first shown by Davies and G. I. Taylor [1, 3], the bubble assumes the shape of a "spherical cap" and its rise velocity is given by

$$U = 1.02\sqrt{ga} \quad . \tag{6}$$

The subject of spherical cap bubbles has recently been reviewed by Wegener and Parlange [4]. As shown by Haberman and Morton [5], among others, (5) and (6) are in very good agreement with experimental data provided that, as mentioned earlier, the bubble surface is clean.

In contrast to the simple asymptotic expressions (5) and (6), the U vs. a curve in the intermediate regime is somewhat more complicated and assumes one of two possible shapes depending on whether M is large or small. Two such representative curves are shown in figure 1.

Large values of M ($M > 10^{-3}$) typically correspond to very viscous liquids. Consequently, when a becomes sufficiently large for the bubble to deform, the Reynolds number is still small enough for an analysis based on the creeping flow solution to apply. Thus, as shown by T. D. Taylor and Acrivos

[6], an expression for the deformation of the bubble can be obtained, when both R and W are small, by means of a perturbation solution of the Navier-Stokes equations. Actually, since the appropriate creeping flow solution automatically satisfies the normal stress balance in (4), the deformation here results from the effects of inertia forces; but since, as is well known, the creeping flow solution does not lead to a uniformly valid approximation of the flow far from the bubble, the analysis cannot proceed via a regular perturbation. Rather it requires that the method of matched asymptotic expansions be employed for this purpose. The resulting expression for the bubble shape including the additional two terms recently obtained by Brignell [7] is

$$\frac{r}{a} = 1 - \frac{5W}{24} P_2(\cos\theta) - \frac{5W^2}{56R} P_3(\cos\theta) + WR \left\{\frac{1}{16} P_2(\cos\theta) - \frac{1}{1400} P_3(\cos\theta)\right\}$$

$$- \frac{WR^2}{24} (\ell n\, R)\, P_2(\cos\theta) + \ldots \qquad (7)$$

where P_2 and P_3 are the appropriate Legendre polynomials and θ is the azimuthal angle measured from the downstream direction. Thus, as can easily be seen from (7), the bubble first deforms into an oblate spheroid and then, following a further increase in $\underline{a}$, into a shape approaching that of a spherical cap. In fact, it is a simple matter to demonstrate experimentally that the transition from a spherical bubble to a spherical cap is a gradual one and that the corresponding shape of the U vs. $\underline{a}$ curve for liquids with larger values of M is, typically, as shown in figure 1 for mineral oil. Hayashi and Matunobu [8] have experimentally verified the Taylor-Acrivos [6] expression for the deformation of drops as well as bubbles when R and W are small, while Wellek, Agrawal and Shelland [9] have reported that this expression seems to hold for substantially larger values of $\underline{a}$, and, therefore, of R and W, than would be expected on the basis of the theory.

A very different state of affairs is encountered, however, when M is small, i.e. less than approximately 10^{-10}. Low values of M are, of course, indicative of low viscosity liquids and hence it is quite possible that small (and, therefore, spherical) bubbles can rise fast enough for the Reynolds number to be large. To a good approximation then, the vorticity is confined to a thin boundary-layer at the bubble surface plus in a narrow axisymmetric wake, and the flow outside this region is effectively inviscid. Moreover, as Levich [2] was the first to recognize, the rate of mechanical energy dissipation in the liquid can be determined, at sufficiently large R, from the irrotational flow alone, and, therefore, an expression for the drag can be obtained without a detailed analysis of the boundary-layer. Levich's result is

$$U = a^2 g\rho / 9\mu \quad , \qquad (8)$$

which is identical to (5), the corresponding creeping flow expression, except for a numerical factor. By considering the dissipation in the boundary-layer and in the wake, Moore [10] corrected (8) for the effects of a finite Reynolds number and showed that, to a first approximation

$$U = \frac{a^2 g\rho}{9\mu} \left[1 + 1.6\, R^{-1/2} + O(R^{-5/6})\right] . \qquad (9)$$

The most remarkable thing about the corresponding U vs. $\underline{a}$ curve, such as the one shown in figure 1 for turpentine, is the appearance of a local maximum

in the rise velocity when $\underline{a}$ is still quite small. For a while, it was believed that this resulted from the presence of instabilities at the gas-liquid interface, which have been observed experimentally [11] and predicted theoretically [12] to occur at values of W between 3 and 4. Moore [13] has shown, however, that this instability is probably not the main cause for the existence of this velocity maximum, but rather the fact that beyond a certain radius $\underline{a}$ the bubble rapidly begins to deform into an approximately oblate spheroidal shape, the drag of which increases with $\underline{a}$ faster than a^3, the corresponding rate of increase of the buoyancy force. Moore's [13] analysis, later refined by El Sawi [14], consists of an irrotational inviscid solution for the flow external to the bubble approximately satisfying the normal stress balance at the gas-liquid interface, which, as seen in figure 1, is in excellent agreement with the experimental points in the region where the local maximum rise velocity occurs. This theory also predicts the existence there of a maximum Weber number above which the symmetric shape is impossible. It is of interest to note that this maximum value of W, approximately equal to 1.6, is almost exactly the same as that of the critical Weber number obtained by Hartunian and Sears [12] for the onset of instability.

The discussion presented above has been primarily limited to bubbles. The case of a liquid drop rising in another fluid with which it is immiscible is not very different although, of course, the presence of viscous effects within the drop complicates both the analysis as well as the interpretation of the experimental results. For example, the extension of (9) to drops of low but finite viscosity requires a complicated analysis of the motion within the discrete phase [15] which has not been extended, as yet, to non-spherical systems. Also, drop shapes have been reported which have not been observed in the case of bubbles, e.g. spherical drops deforming into prolate spheroids [8]. Thus, the subject appears to be in need of further study.

DROPS FREELY SUSPENDED IN A LINEAR SHEAR FIELD

This case differs from that discussed earlier in that the drops are now neutrally buoyant, i.e. force-free and couple-free, in a linear shear field. Thus, relative to a set of axes that move with the center of the drop, we have, in lieu of (2), that:

$$\text{At infinity,} \qquad u_i \to e_{ij} x_j + \frac{1}{2} \epsilon_{ijk} \omega_j x_k \ , \tag{10}$$

where ω_i and e_{ij} denote, respectively, the vorticity and rate of strain tensor of the undisturbed shear flow.

G. I. Taylor [16] was the first to study this problem both theoretically and experimentally for the case of creeping flow. He showed that, for the simple shear flow

$$u_i = G x_2 \delta_{i3} \qquad \text{at infinity,} \tag{11}$$

and for $k \equiv \gamma / \mu Ga \gg 1$ and $\lambda \equiv \mu'/\mu = O(1)$, the drop would deform into an ellipsoid with semi-axes a(1-D), a, a(1+D), where

$$D = \frac{19\lambda + 16}{16\lambda + 16} k^{-1} . \qquad (12)$$

Taylor showed moreover that, under these conditions, $\alpha = \pi/4$ where α is the angle between the major axis of the ellipsoid and the 2-axis. He also considered the case of a very viscous drop, i.e. $\lambda >> 1$ and $k = O(1)$, for which he found that, again for the simple shear flow (11)

$$D = \frac{5}{4\lambda} \quad \text{and} \quad \alpha = \frac{\pi}{2} . \qquad (13)$$

In his analysis, Taylor solved the creeping flow equations for a spherical drop and then obtained (12) and (13) from the normal stress component of (4). Thus, this case is, in at least one respect, simpler than the corresponding problem of the distortion of a rising drop discussed earlier, in that an expression for the deformation can be obtained here without the need to consider inertial effects.

Cox [17] placed Taylor's theory on a more systematic basis. He examined the general problem of a drop in both steady and unsteady linear shear flow for all circumstances in which the drop deformation is small, and presented a scheme for extending the analysis to higher order in k^{-1} or λ^{-1}. For the simple shear flow (11), Cox found that, at steady-state,

$$D = \frac{5(19\lambda + 16)}{4(\lambda+1)\sqrt{(20k)^2+(19\lambda)^2}} , \qquad \alpha = \frac{\pi}{4} + \frac{1}{2}\tan^{-1}(19\lambda/20k) , \qquad (14)$$

which reduces to (12) and (13) under the appropriate conditions.

A number of very significant experimental studies have also appeared which have extended the range of Taylor's earlier measurements. Due to experimental limitations, all these have been performed either in the simple shear flow (11)--which can easily be generated in a Couette device--or the hyperbolic flow

$$\omega_i \equiv 0, \quad e_{ij} = G\{\delta_{i1}\delta_{j1} - \delta_{i2}\delta_{j2}\} \qquad (15)$$

of Taylor's four-roller apparatus. Of particular interest are the experiments of Rumscheidt and Mason [18], who studied the deformation and breakup of liquid droplets, of Torza, Cox and Mason [19], who examined the influence of time effects, and of Grace [20] who conducted a thorough experimental investigation of the phenomena associated with deformation and burst over the record-breaking range of λ's from 10^{-6} to 10^{3}. All these studies have yielded some extremely interesting results. First of all, they have confirmed Taylor's and Cox's analyses for small deformation; they have also shown that, under certain conditions, drops can deform, seemingly indefinitely, with an increase in the strength G of the shear rate and end up as filaments, whereas, under another set of circumstances, they will deform only to a moderate extent and then burst. This is illustrated in figure 2, where the experimentally determined value of the parameter k^{-1} required for burst is

plotted vs. λ for both simple shear and hyperbolic flow, and in figure 3 which depicts the corresponding value at breakup of ℓ/a with ℓ being the half-length of the drop.

Knowledge of the conditions for breakup would be extremely useful in many practical situations. For example, it would allow one to estimate the rheological properties of an emulsion which are known to be sensitive functions of the average size of the droplets comprising the discrete phase. Also, as shown by Grace [20], the basic data regarding the behavior of single drops in shear fields can be used successfully to predict the dispersion performance and the power requirements of a class of static mixers. In this context, it is undoubtedly useful to know that, as shown in figure 2, an irrotational shear field is more efficient, for the purposes of mixing two immiscible viscous fluids, than a corresponding simple shear, and that, for $\lambda > 4$, it would be very difficult if not impossible to mix two fluids in a Couette device, no matter how large the strength of the impressed shear. Evidently then there is a pressing need for a theory which would explain and quantitatively predict the phenomenon of burst.

Although such a general theory is not yet available, a promising start in this direction has recently been made by Barthès-Biesel and Acrivos [21] and by Buckmaster [22, 23]. The first authors succeeded, after much labor, in obtaining an additional term $O(k^{-2})$ in the solution of Cox [17] and showed that this truncated series could model the experimental results of [18], [19] and [20] often to a surprising degree of accuracy. This is illustrated in figure 4 which shows, according to the analysis by [21], that beyond a certain value of k^{-1}, no steady shape can exist for that particular set of conditions (the upper branch of the theoretical curve was found to be unstable to small disturbances [21]). Curves, similar to those of figure 4 were also computed for a variety of flows and values of λ [21, 24], all of which tend to suggest that the breakup of a droplet freely suspended in a shear field results not from an instability, but rather from the absence of a steady-state solution to the appropriate system of equations beyond a certain critical value of k^{-1}. The analysis of [21] is still rather incomplete, of course, in that it consists basically of a two-term expansion about a droplet whose shape is assumed to differ slightly from that of a sphere. Consequently, it cannot describe elongated drops and, indeed, its predictions have been found, at times, to be inaccurate and, on occasion, erroneous [21]. Nevertheless, it is believed that Barthès-Biesel and Acrivos' theory correctly models the essential physical aspects of the phenomenon even though it is still in need of considerable improvement for the purpose of yielding reliable quantitative predictions.

In contrast to [21], Buckmaster's analysis concerns a slender droplet, the shape of which he determined using the techniques of slender-body theory [22, 23]. Buckmaster's results are therefore exact, in an asymptotic sense, for very slender droplets, although unfortunately they are limited, at present, to the case of axisymmetric flows where comparison with experiments is not possible at this time. Nevertheless, both the results and the approach are valuable and interesting.

In his first paper[22], Buckmaster considered an inviscid bubble and

showed that its shape was given by

$$r(z) = \frac{\gamma}{G\mu} \frac{1}{4n} \left[1 - \left(\frac{z}{\ell}\right)^{2n}\right] \tag{16}$$

where z is the distance along the axis of symmetry from the center of the bubble and n is an unknown integer. Thus, Buckmaster obtained a family of solutions although he reasoned that the one corresponding to n = 1 was probably the most realistic. This was confirmed by Youngren [25] who expressed the solution of the appropriate creeping flow equations in terms of an integral involving a distribution of singularities along the surface of the bubble, the strength of which he then determined through a numerical solution of the appropriate integral equation while, simultaneously, adjusting the shape so as to satisfy the normal stress balance. Youngren's numerical results are shown in figure 5 and are seen to conform to (16) with n = 1 even when the slenderness ratio $\gamma/4G\mu\ell$ is far from small. This observation increases of course the potential usefulness of slender-body theories when applied to such problems.

Buckmaster [23] also considered the corresponding problem for a drop having a small but finite viscosity and showed that

$$r(z) = \frac{\gamma}{8G\mu} \left[1 + \left(1 - \frac{64}{K^2}\right)^{1/2}\right] \left(1 - \left(\frac{z}{\ell}\right)^2\right) \tag{17}$$

where

$$K \equiv \frac{\gamma}{G\mu\ell} \lambda^{-1/2} .$$

Evidently, since a solution exists only if $K \geq 8$, the condition K = 8 yields a criterion for burst which is qualitatively similar to that of [21] in the sense that breakup has been associated with the absence of a steady state solution when $G\mu a/\gamma$ exceeds a certain critical value.

This then appears to be the state of affairs regarding this interesting and important problem. Clearly, a more general and comprehensive theory would be desirable, and it is hoped that the analysis which, up to now, appears to have been limited to creeping flows, could also be extended to cases of finite or even large shear Reynolds numbers, $G\rho a^2/\mu$. Experiments at higher Reynolds numbers would also be welcome.

REFERENCES

1. J. F. Harper, "The Motion of Bubbles and Drops Through Liquids," Adv. Appl. Mech. 12, 59 (1972).
2. V. G. Levich, "Physiochemical Hydrodynamics," Prentice-Hall, Englewood Cliffs (1962).
3. G. K. Batchelor, "An Introduction to Fluid Dynamics," Cambridge University Press (1967).

4. P. P. Wegener and J.-Y. Parlange, "Spherical Cap Bubbles," Ann. Rev. Fluid Mech. 5, 79 (1973).
5. W. L. Haberman and R. K. Morton, "An Experimental Investigation of the Drag and Shape of Air Bubbles Rising in Various Liquids," David Taylor Model Basin Rep. No. 802 (1953).
6. T. D. Taylor and A. Acrivos, "On the Deformation and Drag of a Falling Viscous Drop at Low Reynolds Number," J. Fluid Mech. 18, 466 (1964).
7. A. S. Brignell, "The Deformation of a Liquid Drop at Small Reynolds Number," Quart. Journ. Mech. Appl. Math. 26, 99 (1973).
8. S. Hayashi and Y. Matunobu, "Experimental Study of a Deformed Drop Moving Through Viscous Media," J. Phys. Soc. Japan 22, 905 (1967).
9. R. M. Wellek, A. K. Agrawal and A. H. P. Skelland, "Shape of Liquid Drops Moving in Liquid Media," A. I. Ch. E. Journ. 12, 854 (1966).
10. D. W. Moore, "The Boundary Layer on a Spherical Gas Bubble," J. Fluid Mech. 16, 161 (1963).
11. S. Winnikow and B. T. Chao, "Droplet Motion in Purified Systems," Phys. Fluids 9, 50 (1966).
12. R. A. Hartunian and W. R. Sears, "On the Instability of Small Gas Bubbles Moving Uniformly in Various Liquids," J. Fluid Mech. 3, 27 (1957).
13. D. W. Moore, "The Velocity of Rise of Distorted Gas Bubbles in a Liquid of Small Viscosity," J. Fluid Mech. 23, 749 (1965).
14. M. El Sawi, "Distorted Gas Bubbles at Large Reynolds Number," J. Fluid Mech. 62, 163 (1974).
15. J. F. Harper and D. W. Moore, "The Motion of a Spherical Liquid Drop at High Reynolds Number," J. Fluid Mech. 32, 367 (1968).
16. G. I. Taylor, "The Viscosity of a Fluid Containing Small Drops of Another Fluid," Proc. Roy. Soc. A, 138, 41 (1932); "The Formation of Emulsions in Definable Fields of Flow," Proc. Roy. Soc. A, 146, 501 (1934).
17. R. G. Cox, "The Deformation of a Drop in a General Time-Dependent Fluid Flow," J. Fluid Mech. 37, 601 (1969).
18. F. D. Rumscheidt and S. G. Mason, "Particle Motion in Sheared Suspensions. XII. Deformation and Burst of Fluid Drops in Shear and Hyperbolic Flows," J. Coll. Sci. 16, 238 (1961).
19. S. Torza, R. G. Cox and S. G. Mason, "Particle Motions in Sheared Suspensions. XXVII. Transient and Steady Deformation and Burst of Liquid Drops," J. Coll. Interface Sci. 38, 395 (1972).
20. H. P. Grace, "Dispersion Phenomena in High Viscosity Immiscible Fluid Systems and Application of Static Mixers as Dispersion Devices in Such Systems," Engng. Foundation 3rd Res. Conf. on Mixing, Andover, New Hampshire (1971).

21. D. Barthès-Biesel and A. Acrivos, "Deformation and Burst of a Liquid Droplet Freely Suspended in a Linear Shear Field," J. Fluid Mech. 61, 1 (1973).
22. J. D. Buckmaster, "Pointed Bubbles in Slow Viscous Flow," J. Fluid Mech. 55, 385 (1972).
23. J. D. Buckmaster, "The Bursting of Pointed Drops in Slow Viscous Flow," J. Appl. Mech. E, 40, 18 (1973).
24. D. Barthès-Biesel, Ph. D. Dissertation, Stanford University (1972).
25. G. K. Youngren, To be published.

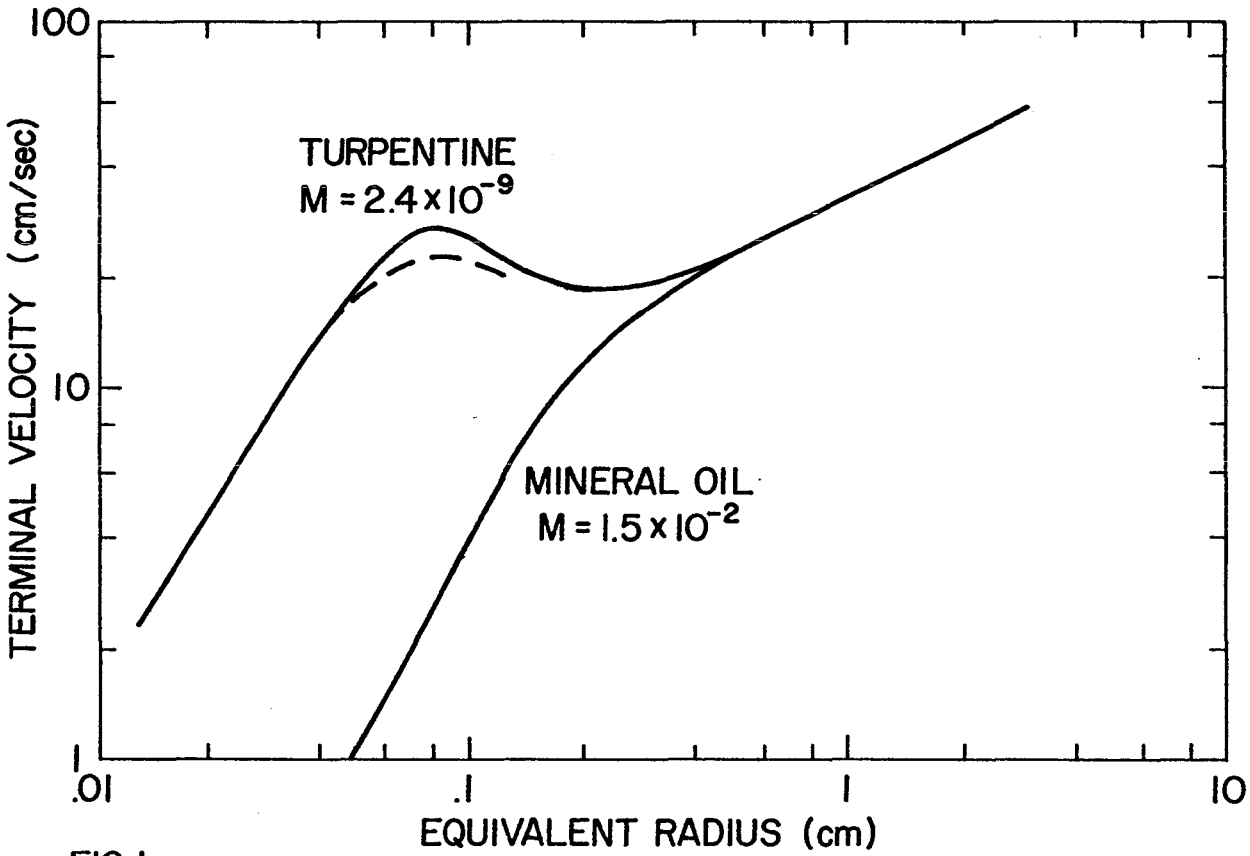

FIG 1

TERMINAL VELOCITY FOR A HIGH M AND A LOW M LIQUID;
— — MOORE'S THEORY [13]; —— SMOOTHED EXPERIMENTAL DATA.

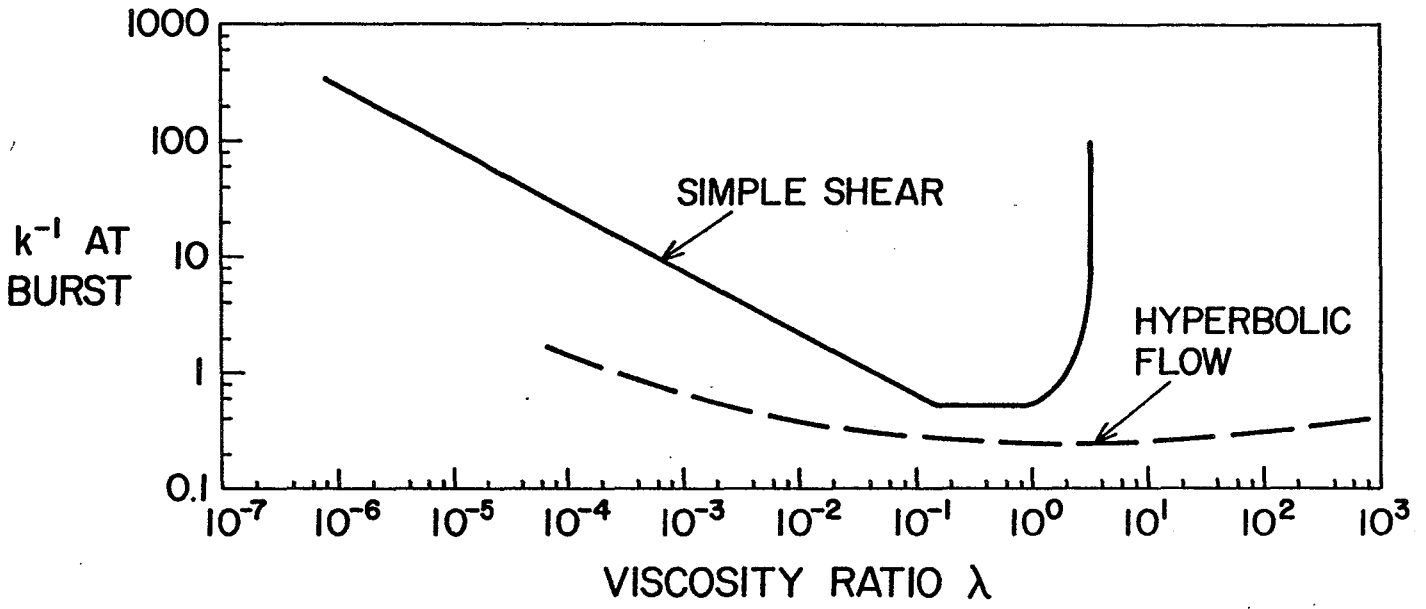

FIG 2
COMPARISON OF CRITICAL SHEAR GRADIENT REQUIRED FOR DROP BREAKUP IN SIMPLE SHEAR AND IN HYPERBOLIC FLOW [20].

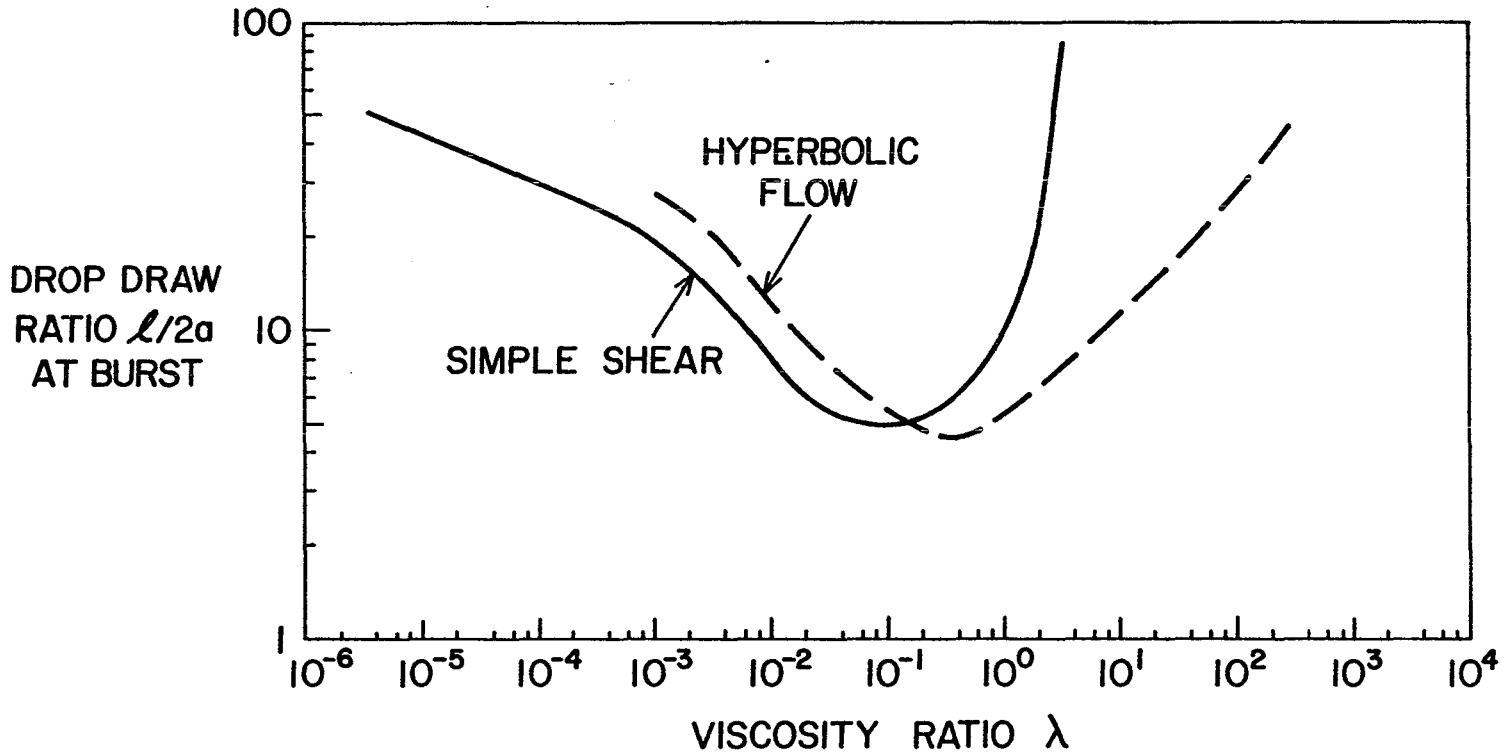

FIG 3
COMPARISON OF CRITICAL DRAW RATIO FOR DROP BREAKUP IN SIMPLE SHEAR AND IN HYPERBOLIC FLOW [20].

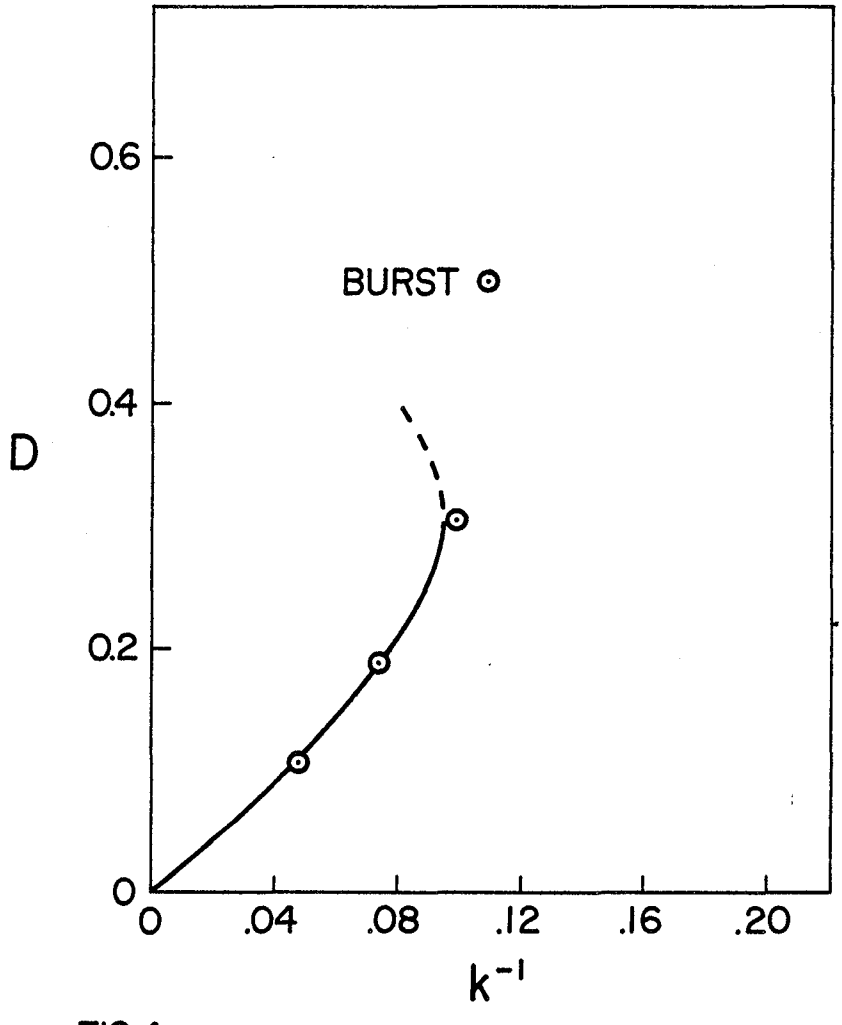

FIG 4
DEFORMATION OF A DROP ($\lambda = 6$) IN HYPERBOLIC FLOW; ⊙ EXPERIMENTS [18]; — THEORY [21]; - - - UNSTABLE STATE

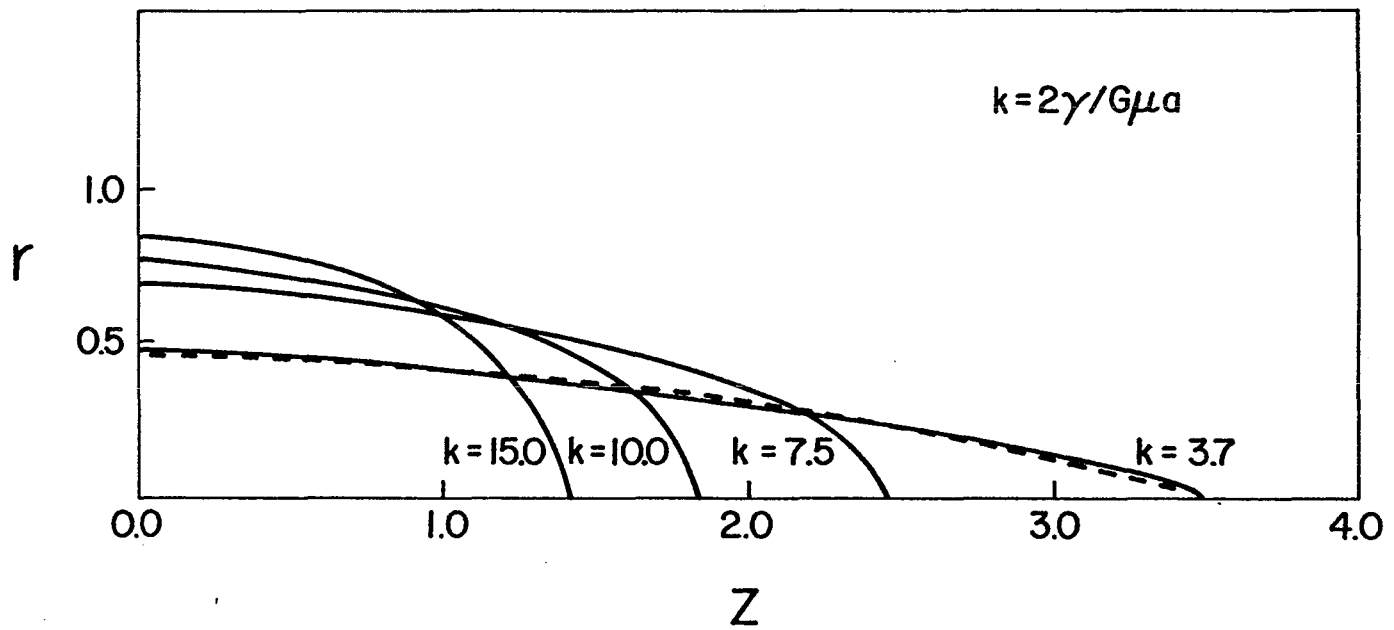

FIG 5
A BUBBLE IN AN AXISYMMETRIC FLOW; —— NUMERICAL SOLUTION [25]; - - - SLENDER BODY THEORY WITH n=1 [22].

PRESSURE WAVES IN BUBBLY LIQUIDS

L. van Wijngaarden
California Institute of Technology*

ABSTRACT

A bubbly liquid is a compressible fluid and therefore any compression wave of finite amplitude will tend to steepen. There are various mechanisms, which oppose this. Discussed are three of these: 1) Dispersion, caused by volume oscillations of the bubbles; 2)Dissipation of thermal and viscous nature; 3) Relaxation caused by relative motion between bubbles and liquid. Depending on which of these dominate, the structure of the shock wave takes a different form. Examples, taken from systematic experiments are shown. A brief account is given of the theoretical considerations, which enable to explain the observed shock wave forms.

In this talk I would like to review some of the features of pressure waves in bubbly liquids, as they appeared during research by Dr.L.Noordzij and myself in recent years. Details may be found in the references cited at the end. For convenience we restrict ourselves here to spherical bubbles with radius R, locally, and initial radius R_0.The fluid phase has constant density ρ_f, the gas in the bubbles however is compressible. The mixture has, when the number density of the bubbles is n, a density

$$\rho = \rho_f (1-\beta) , \tag{1}$$

where β is the concentration of the gas by volume,

$$\beta = \frac{4}{3} \pi n R^3 . \tag{2}$$

When a pressure wave passes through the mixture the bubbles execute volume oscillations. Free volume oscillations have, under adiabatic circumstances, the frequency

$$\omega_B = \left(\frac{3\gamma p}{\rho_f R^2} \right)^{\frac{1}{2}} , \tag{3}$$

where γ is the ratio between specific heats of the gas. At frequencies much lower than ω_B, the pressure inside the bubbles equals the local pressure p in the fluid and when in addition the bubbles move locally whith the fluid, the velocity of propagation of sound waves is, for small β, given by

$$c_o = \left(\frac{\gamma p}{\rho_f \beta} \right)^{\frac{1}{2}} \tag{4}$$

*Permanent address:
Technische Hogeschool Twente, Enschede, The Netherlands.

For very small bubbles, radius $\sim 10^{-5}$m, the changes in pressure are isothermal, and c_o is $\gamma^{-\frac{1}{2}}$ times the value of (4).
At frequencies comparable with ω_B the pressure in the gas no longer equals the pressure in the bubbles due to the inertia of the fluid accelerated or decelerated in radial direction as the bubbles execute volume oscillations. As a result dispersion occurs and the waves travel with a speed less than c_o, the difference with c_o becoming larger when the frequency approaches ω_B.
Damping of these pressure waves is provided by several dissipative effects, the main one being thermal conduction from the gas into the fluid. For waves of finite amplitude the above mentioned items provide interesting phenomena. Just as in ordinary gas dynamics compression waves are steepened because in a compressed part of the wave the speed of sound is larger than in an expanded part. Dispersion tends to spread the wave because high wave number parts of the wave travel slower than low wave number parts. The two opposing effects may balance in waves of permantent form, analogous to cnoidal waves on water of finite depth [1]. No shock waves are possible without the additional help of some dissipation. Including this by a logarithmic decrement δ of linear waves, we find (see e.g. [2]) for the pressure disturbance $\tilde{p}=(p-p_o)/p_o$ in a wave that travels in x-direction,

$$\frac{\partial \tilde{p}}{\partial t} + c_o \frac{\partial \tilde{p}}{\partial x} + c_o \tilde{p} \frac{\partial \tilde{p}}{\partial x} + \tfrac{1}{2} \frac{c_o^3}{\omega_B^2} \frac{\partial^3 \tilde{p}}{\partial x^3} - \tfrac{1}{2} \frac{\delta c_o^2}{\omega_B} \frac{\partial^2 \tilde{p}}{\partial x^2} = o. \qquad (5)$$

It is understood that the wave is of moderate amplitude and (5) constitutes an approximation of one order beyond the linear (acoustic) approximation. In equation (5) the third term on the left hand side represents the nonlinear steepening, the fourth and fifth terms represent dispersion and dissipation, respectively. Equation (5) has stationary solutions in the form of an undular bore, that is a steep rise of the pressure in front followed by oscillations about the equilibrium pressure at the backside. These type of pressure waves were found indeed in experiments reported in [3]. An example is shown in Figure 1.

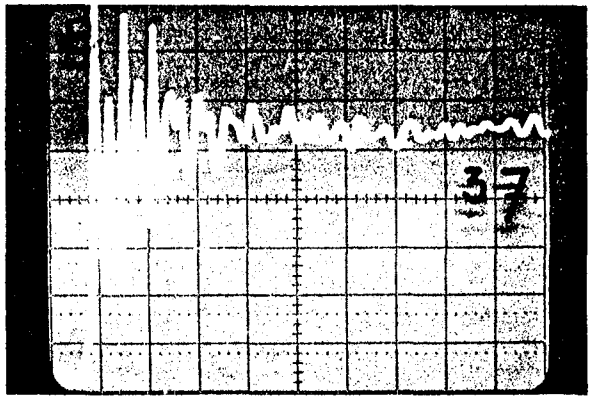

Figure 1. Shock wave of undular bore type (A shock) $p_1/p_o=1.79$, $\beta_o=3.21\%$, $R_o=1.33\times10^{-3}$m, U=66m/s, $d_A=3.3\times10^{-2}$m

These experiments were carried out in a shock tube of about 1 meter length with air bubbles of about 1 mm radius in a aqueous solution of glycerine. The thickness of the wave, for further reference denoted with d_A, follows from balancing the nonlinear and the dispersion term in (5) and is

$$d_A \simeq \frac{R_o}{\left\{\beta_o (p_1/p_o - 1)\right\}^{\frac{1}{2}}} . \tag{6}$$

When p_o is the pressure in front and p_1 the pressure at the backside of the wave, we can also calculate the speed of propagation of this shock wave. The result is

$$\frac{U^2}{c_o^2} = \frac{1}{\gamma} \frac{p_1/p_o - 1}{1-(p_o/p_1)^{\frac{1}{\gamma}}} , \tag{7}$$

for adiabatic bubbles, and

$$\frac{U^2}{c_o^2} = \gamma^{-1} \frac{p_1}{p_o} , \tag{8}$$

under isothermal conditions.
Figure 2, taken from [3], shows good agreement with (7), in accordance with the expectation that at a typical frequency U/d_A the penetration depth of heat is small with respect to R_o.

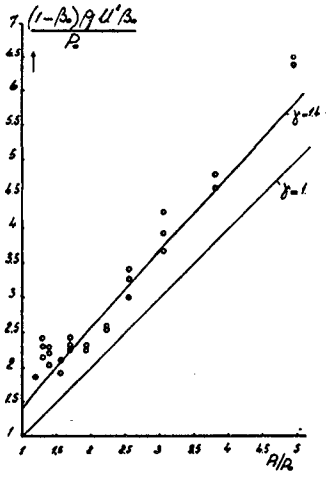

Figure 2: Speed of A shocks. o: experiments. ——Theory, for adiabatic and isothermal bubbles respectively.

After the experiments of [3] were carried out, we built a longer shock tube, as depicted in Figure 3 and observed that shock waves, initially (in part A) of the form of Figure 4a,just described, took a different form lower in the tube either of the form B shown in Figure 4b or of the form C in Figure 4c.

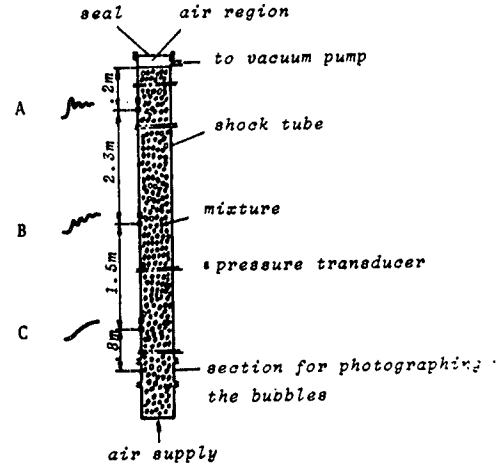

Figure 3: Experimental setup.

Figure 4: This Figure illustrates the different shock structures observed in the laboratory.

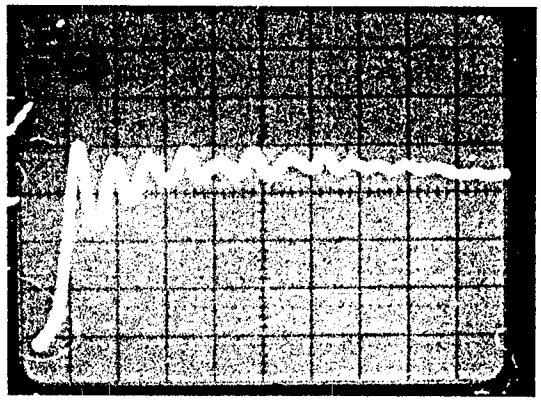

a) A shock.

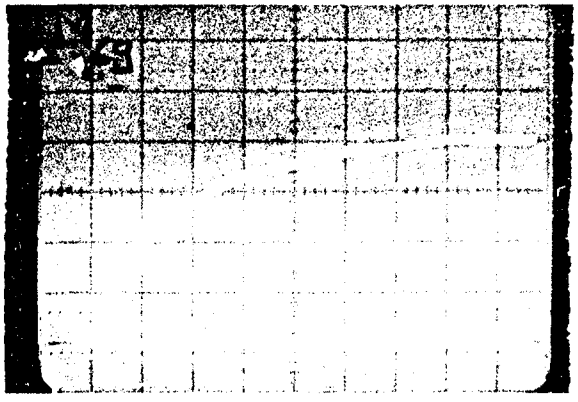

b) B shock.

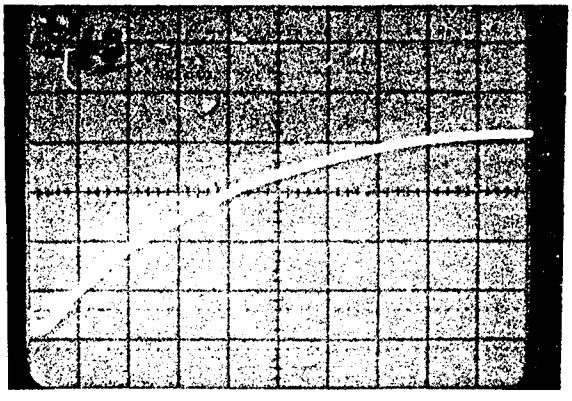

c) C shock.

The remainder of this talk is on this gradual change of A shocks into B or C shocks and is a very condensed version of [4], which is shortly to appear. The clue to the understanding of the change in shock structure is provided by looking at the relative motion of the bubbles with respect to the fluid. When a fluid containing bubbles is instantaneously accelerated to a velocity u, the bubbles acquire a velocity 3u, approximately. In the absence of viscosity the bubbles continue to move at this velocity. When the fluid is viscous the bubbles are gradually slowed down to the fluid velocity. The time this process takes depends on the magnitude of the viscous force and on the virtual mass of the bubbles. For spherical bubbles the virtual mass is $\frac{1}{2}\rho_f$ times the bubble volume and, adopting the Levich model for the flow around the bubble, the viscous resistance is $12\pi\mu R$ times the relative velocity ; μ is the dynamic viscosity of the fluid.

The relaxation time τ then is

$$\tau = \frac{R^2 \rho_f}{18\mu} \quad . \tag{9}$$

For deformed bubbles both the virtual mass and the resistance increase severely with the deformation but, surprisingly enough, τ remains virtually unchanged for not too large deformation[4]. When a pressure wave in the form of a step function enters the mixture at t=o, the mixture reacts for times $t \ll \tau$ as if the fluid were inviscid. The bubbles are free to move relative to the fluid and the velocity of sound is not as given by (4) but is

$$c_f^2 = c_o^2 \quad (1+2\beta_o) \quad . \tag{10}$$

The sound velocities c_o^2 and c_f^2 may be compared with the equilibrium and frozen sound speeds in chemically reacting gas flows. In part A of the shock tube of Figure 3 viscosity does not yet resist relative motion and the shock is of the undular bore type, however with c_f in stead of c_o. The expression for the speed of the shock wave is

$$\frac{U^2}{c_o^2} = \frac{1}{\gamma} \frac{p_1/p_o - 1}{1-(p_o/p_1)^{\frac{1}{\gamma}}} \left\{ 1+\beta_o \left(1+ \frac{p_o}{p_1}\right)^{\frac{1}{\gamma}} \right\}, \tag{11}$$

but the effect of β_o, (as compared with (7)), is too small to be measurable at values of β_o of a few percent.
For times t comparable with τ or, in terms of distance, at distances along the tube of order $c_f\tau$, viscous forces tending to decrease the relative velocity become important. They have a diffusive action on the wave with a diffusion coefficient $\tau(c_f^2 - c_o^2)$. This diffusion resists nonlinear steepening and may, at low enough pressure ratios, even completely balance the nonlinear steepening. When this happens, the profile of the wave is smooth. The wavelets in the front of the wave can at maximum travel with the speed c_f. The speed of the wave is given by (7), whence by expanding (7) for small values of $p_1/p_o - 1$, we find for the threshold of these smooth waves

$$\frac{p_1}{p_o} = 1 + \frac{4\gamma\beta_o}{\gamma+1} \quad . \tag{12}$$

Indeed for values of p_1/p_o satisfying (12), completely smooth waves, C waves, were found in the lower section of the shock tube. An example is shown in Figure 5. The thickness of these waves is much larger than d_A. We find

$$d_C \approx U\tau \quad , \tag{13}$$

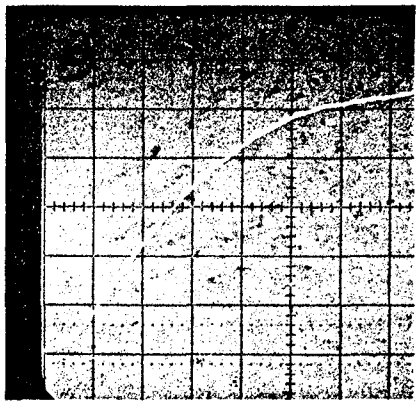

Figure 5. An example of a C shock. $p_1/p_o=1.07$, $\beta_o=4.17\%$, $R_o=1.15\times10^{-3}$m, U=65 m/s, d_c=2,1 m, $1+4\beta_o\gamma/\gamma+1=1.1$.

which is in our experiments, with $U\approx10^2$ m/s and $\tau\approx10^{-2}$s, of the order of magnitude of 1 m, whereas d_A is typically of order 10^{-2}m. There remain to consider the type of shock waves shown in Figure 4b which we denote with B shocks. They can be explained as follows: when the distance along the tube is comparable with or larger than $U\tau$, diffusion is active but no smooth profile is possible when p_1/p_o exceeds the value given in (12). Therefore the shock has a thin front, of order d_A, of the A type. At this front the pressure rises to a value in between p_o and p. We denote this pressure with p^*. The remainder of the pressure increase takes place over a distance of order $U\tau$ over which nonlinear steepening is, as in C shocks, in balance with diffusion by relaxation. The value of p^* is found by observing that the thin front shock must obey equation (11), with p^* in place of p_1, whereas the whole wave obeys equation (7). Equating the righthand sides of these equations, with p^* in stead of p_1 in (11), gives for the quantity

$$F = \frac{p^*-p_o}{p_1-p_o} \quad , \tag{14}$$

the expression

$$F = 1-\beta_o \frac{1+(p_o/p_1)^{\frac{1}{\gamma}}}{1-\frac{U^2}{c_o^2}(p_o/p_1)^{\frac{\gamma+1}{\gamma}}} \quad . \tag{15}$$

Qualitatively the form of the B shocks may therefore be interpreted as a thin front governed by the balance between nonlinear steepening and dispersion followed by a much thicker region where steepening is resisted by relaxation.

In figure 6 an example of a B shock is given. Quantitatively a check on the theory is possible by comparing the experimental data for F with the theoretical result (15). This is done in Figure 7.

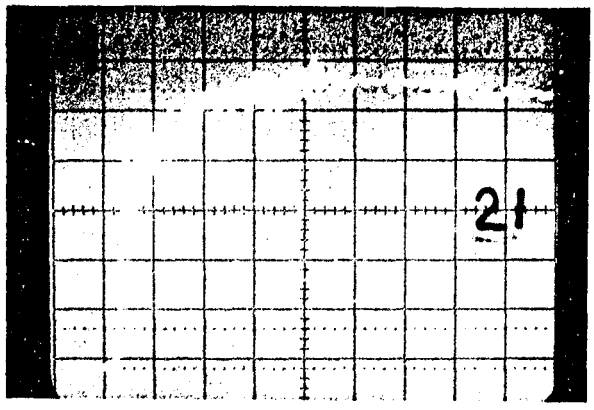

Figure 6. Pressure recording of a B shock. p_1/p_o= 1.81, β_o= 1.17%, R_o= 1.07×10^{-3}m, U=108 m/s, d_A= 4.3×10^{-2}m, d_B=0.54 m Fexp=0.61.

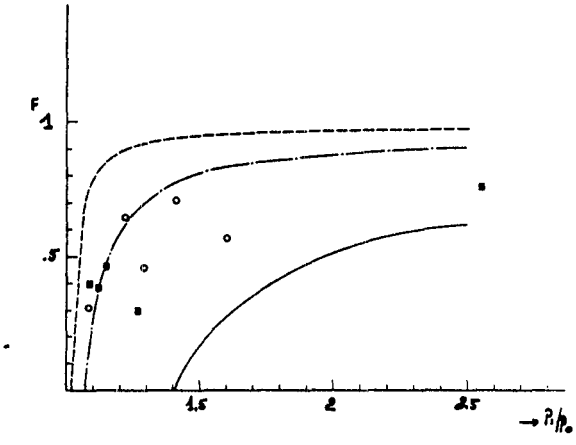

Figure 7. The quantity F (equation 14) as a function of p_1/p_o with β_o as parameter.
- - - - - - - - theory; o exp, β_o= o.87 x 10_2^{-2}
-.-.-.-.-.-.-. " ; ■ exp, β_o= 3.1 x 10^{-2}
The solid line gives for comparison the values for F when thermal relaxation were dominant.

The broken lines correspond to constant values of β_o. The solid line indicates the behaviour of F when relaxation of thermal nature were the dominant process. In that case the equilibrium and frozen speeds are $c_o\gamma^{-\frac{1}{2}}$ and c_o. Smooth profiles would occur below the pressure ratio

$$\frac{p_1}{p_o} = \gamma. \qquad (16)$$

Figure 7 shows that thermal relaxation cannot be ruled out in our experiments, but the fact that we found no C shocks in the range of pressure ratios between γ and $1+4\gamma\beta_o/1+\gamma$ indicates the predominance of relaxation associated with relative motion.

1	Wijngaarden, L van	J.Fluid Mech. 33,465,1968
2	id.	Ann.Rev.Fluid Mech. 4,369,1972
3	id.	Progr.Heat and Mass Transfer 6,637,1972
4	Noordzij L, Wijngaarden L,van	J.Fluid Mech. to appear.

MODELS OF SPHERICAL-CAP BUBBLES

R. Collins

Department of Mechanical Engineering, University College London.

INTRODUCTION

From the close correspondence between their theory and experiments which had related bubble velocity with apparent radius of curvature, Davies & Taylor (see Ref. 1 & 2) concluded that the flow near the front of a real spherical-cap bubble must be very close indeed to the irrotational flow near the front of a complete sphere of the same curvature,as they had assumed in their theory. They expressed some surprise at this result of their work. In fact the equation derived from their assumption about the flow agreed better with the experimental measurements of bubble velocity than did an equation of similar form derived from measurements of the pressure distribution on a solid model of the bubble cap, which had been obtained in a wind tunnel at high Reynolds number. Although their assumption works so well, it does not give the required constancy of pressure on the bubble cap except in the immediate vicinity of the stagnation point,where the static pressure is constant to a first approximation, that is as far as terms of order θ^2, θ being an angular coordinate with origin situated at the centre of curvature of the cap. Some time later, Rippin (Ref. 3 & 4) investigated the possibility of improving the pressure distribution and he followed Moore's suggestion (Ref.5) for an inviscid model of the flow rather like a Helmholtz free-streamline flow in which an infinite open wake of stagnant fluid followed the bubble. The numerical solution which he found did give a virtually constant pressure over the bubble cap, but agreement with experiment, as far as the relationship between bubble velocity and curvature was concerned, was essentially destroyed since the velocities predicted were almost 30% too high. This curious situation in which a model satisfying the constant pressure requirement only approximately was apparently superior to a model in which that condition was approached as closely as practicable prompted the work reported in Ref. 6. The procedure adopted there was to apply a small perturbation to the flow assumed by Davies & Taylor so as to improve the pressure distribution. This contrasts with the gross perturbation implied in adopting the infinite open-wake model. It was found with this small perturbation that the pressure condition could be satisfied as far as terms of order θ^4 near to the stagnation point thus producing a second approximation, and the slight adjustment in velocity given by the theory gave a result in excellent agreement with experiment. It was shown also that the relationship between bubble velocity and the radius of curvature at its stagnation point was uniquely defined by the acceleration of liquid along the bubble surface at the stagnation point and Batchelor (Ref. 7) has pointed out that, at the high Reynolds numbers relevant to this problem, the result is exact.

In work unknown to the author at the time of writing Ref. 6, Temperley & Chambers (Ref. 8) had also tried to improve the pressure distribution given by Davies & Taylor's approach by incorporating a sink term into their velocity potential and also by considering a source alone, but although they were able to satisfy the constant pressure condition to a

second approximation with the first of these approaches, they acknowledged that the relationship between velocity and curvature which resulted from their work was in poorer agreement with experiment than was Davies & Taylor's result. More recently, Harper (Ref. 9) has shown that an alternative closed model can also produce a second approximation which agrees with experiment but he saw the fact that his model required a flattened sphere while Ref. 6 produced an elongated sphere as a deficiency of this approach. He subsequently concluded that infinite, open, stagnant-wake models did give useful approximations to the flow field over the front part of the bubble and,in a similar vein,Wegener & Parlange (Ref. 10) stated that results from such models agreed fairly well with experiments when the wake is turbulent. The purpose of this paper is to consider these views in the light of evidence available.

COMPARISON BETWEEN THEORY AND EXPERIMENT

Using a system of spherical polar coordinates whose origin is located at the centre of curvature of the bubble boundary at its stagnation point, S, the velocity,U,of a large gas bubble moving with high values of Reynolds and Weber numbers has been shown (Ref. 6) to be given by the equation

$$U/(ga)^{\frac{1}{2}} = 1/(dh/d\theta)_s . \qquad (1)$$

Here g is the acceleration due to gravity and a the radius of curvature of the bubble boundary at S, while $h(\theta)$ describes the variation in the magnitude of the liquid velocity on the bubble boundary through the relation $q = Uh(\theta)$. As anticipated on dimensional grounds, the bubble Froude number is constant. In attempting to predict this Froude number the primary objective is to formulate a model whose geometry provides a proper description of the flow over the bubble cap so that the quantity $(dh/d\theta)_s$ may be accurately determined. (The suffix indicates that the derivative is to be evaluated at S.) If a model produces an incorrect value, it may be inferred that it gives an inadequate description of the flow in that region. The standard for comparison here is of course the experimental evidence which is expressed in terms of an apparent radius of curvature, $\bar{a}$, rather than a. A relationship between $\bar{a}$ and a is readily determined for any model (Ref. 6, 9) and, as the name for this class of bubbles suggests, $\bar{a}/a$ does not differ greatly from unity. The combined experimental results of Davies & Taylor, who measured bubble velocities in nitrobenzene, and of Rosenberg who used water (Ref. 11), show that

$$U/(g\bar{a})^{\frac{1}{2}} = 0.65 . \qquad (2)$$

The table overleaf shows values of this Froude number given by the various models previously described. The column labelled "Difference" shows the percentage departure from the experimental value in equation (2). What seems apparent from this table is that there is very little evidence to support the contentions that open, infinite wake models provide useful approximations to the flow over the front of the bubble or that they give results which agree fairly well with experiment.

Theoretical models

Authors	Dates	$U/(\bar{g}a)^{\frac{1}{2}}$	Difference	Geometry
Davies & Taylor	'44& '50	0.666	2.5%	sphere
Temperley & Chambers	'45	0.54 0.82	17% 26%	approximate cardioid open, infinite wake
Rippin	'59	0.84	29%	open, infinite wake
Collins	'66	0.652	0.3%	perturbed sphere
Harper	'72	0.643	1%	oblate spheroid

Harper emphasised the superficial differences between the perturbed sphere used in Ref. 6 and his own oblate spheroid Further consideration of these two shapes does reveal, however, that they have a more important similarity. Two influences on the flow in the vicinity of the stagnation point S may be identified. The first is the effect of the gross features of the complete flow at that point, that is whether the boundary shape employed is open or closed, the second is the effect of the local changes in curvature in the boundary. Clearly, the modified shapes are introduced in both cases in order to change the curvature, for constant curvature has been seen not to produce a constant pressure. If the local distribution of the radius of curvature,ω, in the vicinity of the stagnation point is evaluated for both these second approximations then it is found that for the perturbed sphere

$$\omega = a(1 - 0.94\theta^2 \ldots\ldots\ldots), \qquad (3)$$

while for Harper's oblate spheroid

$$\omega = a(1 - 0.5\theta^2 \ldots\ldots\ldots), \qquad (4)$$

where a is again the radius of curvature at S. Thus, in addition to both models being closed, both show that in order to produce a flatter pressure distribution the radius of curvature of the boundary should decrease along the bubble surface moving away from the stagnation point. It may be observed that the only known exact solution to the two-dimensional form of this free-boundary problem which satisfies the constant pressure requirement at all points on a cycloid also shows the same dependence of ω on θ (Ref. 12). Following Davies & Taylor's interpretation of their own close agreement with experiment, it is concluded that the flow near the front of spherical-cap bubbles must be very close to the irrotational flow near

the front of an approximately spherical closed body whose radius of curvature in the region of the stagnation point varies as $1 - k\theta^2$. It is stressed here that this conclusion does not say that the real flow is irrotational everywhere outside the closed boundary as some critics of this approach have implied. We turn now to the evidence concerning the gross features of the flow patterns associated with spherical-cap bubbles in order to see whether this can explain why closed wake models are so successful.

FLOW VISUALIZATION EXPERIMENTS

Spherical-cap bubbles are conventionally classified as those bubbles which rise with velocities independent of the properties of the liquids in which they are blown (Ref. 11,13). Haberman & Morton (Ref. 13) related bubble velocity with the equivalent spherical radius, r_e, through the equation

$$U = 1.02\ (gr_e)^{\frac{1}{2}}, \qquad (5)$$

and they also showed that the parameter which determines the attainment of the spherical-cap class in a liquid of density, ρ, and surface tension, σ, is the Weber number

$$We = \rho U^2 2r_e/\sigma\ . \qquad (6)$$

In Haberman & Morton's wordsthis should exceed "about 20", the lack of precision arising because there is no abrupt transition to spherical-cap behaviour. In fact a more stringent assessment of figure 21 in Haberman & Morton's paper indicates that complete independence of liquid properties would imply a somewhat higher value, but their value will be used for the moment recognising that it is optimistically low. Combination of these results shows that in order to form a spherical-cap bubble in a given liquid the minimum volume of gas required is

$$V_o = 125(\sigma/g\rho)^{3/2}. \qquad (7)$$

In the table below the values of V_o appropriate to two liquids of interest, water and nitrobenzene, are compared with the volumes of gas actually employed by various other investigators (Ref. 2, 11, 14, 15, 16) to generate what they regarded as spherical-cap bubbles in these liquids. It may be observed that in all investigations except Maxworthy's, the volumes employed exceeded the minimum required.

Minimum Volumes V_o

Liquid	V_o (ml)	Volumes Employed (ml)	Authors
Nitrobenzene	0.9	1.48 to 33.8	Davies & Taylor
Water	2.5	4.4 to 200	Davies & Taylor
		4.8 to 125	Rosenberg
		> 7.2	Slaughter
		4.5 to 40	Davenport et al
		1.5 and 2.5	Maxworthy

Maxworthy's 1.5 ml bubble is certainly too small and the ambiguous status of the 2.5 ml bubble may be resolved by reference to other investigators' criteria which serve to confirm that Haberman & Morton's criterion is set too low. For example, Rosenberg concluded that a minimum volume of 2.85 ml was required in water but he also stated that for transition to spherical-cap form to be complete, a minimum of 4.2 ml was necessary, and in those experiments where he actually measured cap curvature he used values in excess of 4.8 ml. Davenport, Richardson & Bradshaw (Ref. 15) quoted a minimum of 4.5 ml while Slaughter (Ref. 14) placed the end of the preceding ellipsoidal class of bubbles at 5.6 ml and found agreement with equation (5) at volumes above 7.2 ml. Slaughter also found that bubbles with volumes between 1.5 ml and 5.6 ml rocked regularly from side to side and he regarded them as falling in a transitional regime. Similarly, Rosenberg described bubbles whose volumes ranged from 0.7 ml and 2.9 ml as in transition with irregular shapes which fluctuated continuously. Maxworthy's finding that both a 1.5 ml and 2.5 ml bubble exhibit a turbulent amorphous wake stretching far downstream is entirely consistent with these statements for the rocking motion is most likely to be associated with periodicity in the wake. It is clear, however, that since the bubbles employed were not large enough to fall into that class, Maxworthy's evidence is inadmissible in a discussion of spherical-cap bubbles. The reviews by Harper (Ref. 9) and Wegener & Parlange (Ref. 10) have, however, quoted it without criticism. As far as the turbulent nature of the wake is concerned, it is not necessary to perform additional experiments to demonstrate this since it is already evident from Davies & Taylor's photographs and from their calculations of energy dissipation (Ref. 1 & 2). Batchelor has also argued (Ref. 7) that the fact that the velocity of a spherical-cap bubble is independent of liquid properties implies that the energy dissipation process in the wake must be turbulent. The question to be decided, however, is whether there is a structure to the flow in the wake on a scale larger than the scale of the turbulence.

Indirect evidence of structure in the wake of spherical-cap bubbles already existed before the flow visualization experiments reported here were performed. Davies & Taylor's photographs had shown a region of turbulence directly behind a spherical-cap bubble in nitrobenzene, 'two-dimensional' versions of these bubbles formed between plane parallel plates exhibited a double vortex immediately behind the bubble (Ref. 6), and Temperley & Chambers (Ref. 8) recorded that their experiments in water agreed with Davies & Taylor's because they had observed clouds of small bubbles following each large one. The bubble volumes used in the experiments with water presently reported ranged from approximately 40 ml to 90 ml so as to ensure that the bubbles were unequivocally of the spherical-cap class. These observations were noted in 1966 (Ref. 6), they were reported informally at a Euromech Colloquium in 1968 (Ref. 17) and one of the still photographs was published by Batchelor in 1967 (Ref. 7). In Wegener & Parlange's review article which was particularly concerned with visualization of wakes, this evidence was not considered.

The tank and method of bubble generation have been described elsewhere (Ref. 18). In some experiments, small satellite bubbles which occurred naturally during the generation process were used for flow visualization as in Temperley & Chambers' experiments. In others, tablets of a proprietary soluble aspirin ("Aspro") were used to provide white tracer particles. These were either introduced into the bubble path in a plane or column above the bubble generator, or they were allowed to form a cloud of material just above the point of generation. The advantage of using this material as a tracer was that a little time after the passage of one bubble the particles had dissolved thus leaving the tank clear for the next experiment. Dispersal of insoluble solid material or diffusion of dye between bubble and tank wall, in contrast, tends to obscure the detail which of interest.

The flow pattern seen naturally depends on the frame of reference of the observer. Cine film of the motion (Ref. 19, shown during presentation and available on loan on request) taken with camera fixed reveals the presence of a toroidal vortex behind the bubble accompanying a region whose boundary is roughly the spherical surface which continues the bubble cap. With still photographs this feature may be inferred using short time-exposures while panning the camera with the bubble as in the example in figure 1. Behind this bubble, whose volume is approximately 40 ml, are some secondary bubbles contained in a cloud of tracer material which has been transported upwards from the region just above the generator where it had been introduced. Some tracer material was introduced also into the flow outside the cap/vortex boundary in this case. Photographs obtained with camera fixed confirm the nature of the flow pattern although they require a little more interpretation because the bubble moves past the camera during the time-exposure and thus does not appear clearly on the print.

In figure 2, the brightest patch to the upper left of centre is due to light reflection from the left-hand side of the bubble which, in this instance also, had a volume of approximately 40 ml. The streaks below and to the right of this patch are from tracer particles in the closed region of the wake and the fact that the vertical dimensions of patch and streaks are of the same order implies that they move together through the

liquid. Tracer particles were also introduced outside this region in this case and the flow pattern observed there bears a striking resemblance to that of the irrotational dipole which is shown on the right-hand side of figure 3. An irrotational dipole gives the instantaneous streamline pattern to be expected from the motion of a sphere in an inviscid liquid, but the real liquid of course has viscosity and the real flow cannot be irrotational. The approximately spherical surface presented by the bubble cap and the primary closed part of the wake is the source of vorticity in these flows (which in figures 1 & 2 have Reynolds numbers of $O(10^4)$), so that the interpretation of the real pattern of figure 2 is that it closely resembles the pattern which one would expect to be produced by the movement of a sphere on which boundary layer separation was absent or delayed until close to the rear stagnation point. In figure 2, a band of turbulence is discernable behind the closed region. This secondary wake is taken to be produced by the confluence of the boundary layer at the rear stagnation point of the primary closed part.

Figure 4 shows the model of wake structure which emerged from these experiments (Ref. 19 ,20 ; the boundary layer thickness on the cap is exaggerated in this figure). It is unlike that envisaged in Rippin's work where the boundary layer was taken to separate from the bubble rim to produce an infinitely long open stagnant wake of liquid which moved with the bubble. The instantaneous streamline pattern for such a model is sketched on the left-hand side of figure 3, but since this pattern has not been observed, it is concluded that the model does not provide an acceptable description of the real flow. This is why it is unable to produce an accurate value for Froude number as shown in the earlier table. By the same token, figure 4 provides an explanation of the success of closed models for the system of bubble and primary wake does offer an approximately spherical boundary to the flow.

On solid spheres the pressure distribution over the forward region is known to be similar to that given by irrotational flow theory even in the condition when the boundary layer is laminar and separates before the maximum transverse dimension is reached. Boundary layers on free surfaces are less prone to separate in adverse pressure gradients than their counterparts on rigid surfaces (Ref. 7), so that in the bubble problem where the boundary layer has this different character and does not appear to separate from the surface of the primary wake, correspondence between irrotational flow theory and the flow over the forward part of the bubble is likely to be excellent. Closed models of the turbulent wake of spherical-cap bubbles thus have a rationale. As with other boundary layer approaches, the logical first approximation to the flow shown in figure 4 is the irrotational flow past the closed boundary. An understanding of boundary layer behaviour leads one to expect that flow to provide a very good description of the real flow in the region of prime interest, that is near to the front stagnation point, but leads also to the recognition that it will be inadequate to describe the details of the real flow over the rear part where the boundary layer thickens in the adverse pressure gradient. In order to remove an apparent misconception which was raised in Maxworthy's paper and is echoed by Wegener and Parlange it is stressed again that use of a closed model for the flow over the cap does not imply a belief that the real flow is irrotational everywhere outside the closed boundary.

Although Wegener & Parlange recognised the existence of a closed structure in the wake for large bubbles whose wakes were laminar (and whose velocities are thus dependent on liquid properties) their view was essentially that once transition to turbulence occurs, the wake becomes amorphous. Their method of flow visualization was a schlieren technique which certainly does reveal the extent of the turbulence but is not particularly suitable for revealing flow patterns since the paths of individual particles of fluid are not readily identified. The main features of their figure 5 showing turbulence behind spherical-cap bubbles in water are not inconsistent with figure 4 here, in particular the curvature of the edge of the turbulent region immediately below the bubble which continues the cap curvature implies order in the flow there, consistent with a primary wake vortex. In fact Wegener & Parlange record in a footnote that they have observed satellite bubbles to recirculate in this region and, as in the present experiments and in Temperley & Chambers' observations, this implies the existence of a mass of liquid in that region moving with the bubbles. The 'edge' of the turbulence in the secondary part of the wake is of course not a streamline in the flow, and the photographs do not demonstrate the existence of a wake of the Helmholtz type.

CONCLUSION

Closed wake models accurately describe the flow near the front of spherical-cap bubbles giving results in good agreement with experiment because they take into account the geometry of the real flow.

REFERENCES

1. Taylor, G.I. & Davies, R.M. "The Rate of Rise of Large Volumes of Gas in Water", (1944). Reprinted in :Underwater Explosion Research, vol II, p.415, Office of Naval Research, USA (1950).
2. Davies, R.M. & Taylor, G.I. "The Mechanics of Large Bubbles Rising through Extended Liquids and Through Liquids in Tubes", Proc. Roy. Soc. A 200, 315 (1950).
3. Rippin, D.W.T. "The Rise of Gas Bubbles in Liquids", Ph.D. Dissertation, Cambridge (1959).
4. Rippin, D.W.T. & Davidson, J.F. "Free Streamline Theory for a Large Gas Bubble in a Liquid", Chem. Engng. Sci. 22, 217 (1967).
5. Moore, D.W. "The Rise of a Gas Bubble in a Viscous Liquid", J. Fluid Mech. 6, 113 (1959).
6. Collins, R. "A Second Approximation for the Velocity of a Large Gas Bubble Rising in an Infinite Liquid", J. Fluid Mech. 25, 469 (1966).
7. Batchelor, G.K. "An Introduction to Fluid Dynamics", Cambridge University Press (1967).
8. Temperley, H.N.V. & Chambers, Ll.G. "The Rate of Rise of Large Volumes of Gas in Water", (1945) Reprinted in: Underwater Explosion Research, Vol. II, p.437. Office of Naval Research, USA (1950).

9. Harper, J.F. "The Motion of Bubbles and Drops through Liquids", Advances in Applied Mechanics, ed. Chia-Shun Yih. Academic Press, N.Y., 12, 59 (1972).

10. Wegener, P.P. & Parlange, J-Y. "Spherical-Cap Bubbles", Annual Reviews of Fluid Dynamics, ed. M.Van Dyke, W.G. Vincenti & J.V. Wehausen, Annual Reviews Inc. 5, 79 (1973).

11. Rosenberg, B. "The Drag and Shape of Air Bubbles Moving in Liquids." David Taylor Model Basin, Rep. 727 (1950).

12. Collins, R. "The Cycloidal-Cap Bubble: A neglected solution in the Theory of Large Plane Gas Bubbles in Liquids", Chem. Engng Sci. 22, 89 (1967).

13. Haberman, W.L. & Morton, R.K. "An Experimental Investigation of the Drag and Shape of Air Bubbles Rising through Viscous Liquids", David Taylor Model Basin, Rep. 802 (1953).

14. Slaughter, I. "The Motion of Gas Bubbles Rising Singly and in Streams through Liquids", Ph.D. Thesis, University of Newcastle-upon-Tyne (1967).

15. Davenport, W.G., Richardson, F.D. & Bradshaw, A.V. "Spherical Cap Bubbles in Low Density Liquids", Chem. Engng Sci. 22, 1221 (1967).

16. Maxworthy, T. "A Note on the Existence of Wakes Behind Large Rising Bubbles, J. Fluid Mech. 27, 367 (1967).

17. Collins, R. "Wake Structure of a Spherical-Cap Bubble", paper given at 7th Euromech Colloquium, Grenoble, (1968).

18. Collins, R. "The Effect of a Containing Cylindrical Boundary on the Velocity of a Large Gas Bubble in a Liquid", J. Fluid Mech. 28,97 (1967).

19. Collins, R. "Spherical-Cap Bubble Wakes", Cine Film, Department of Mechanical Engineering, University College London, (1967).

20. Collins, R. "Gas Bubbles in Liquids and in Fluidized Beds", Ph.D. Thesis, University of London (1968).

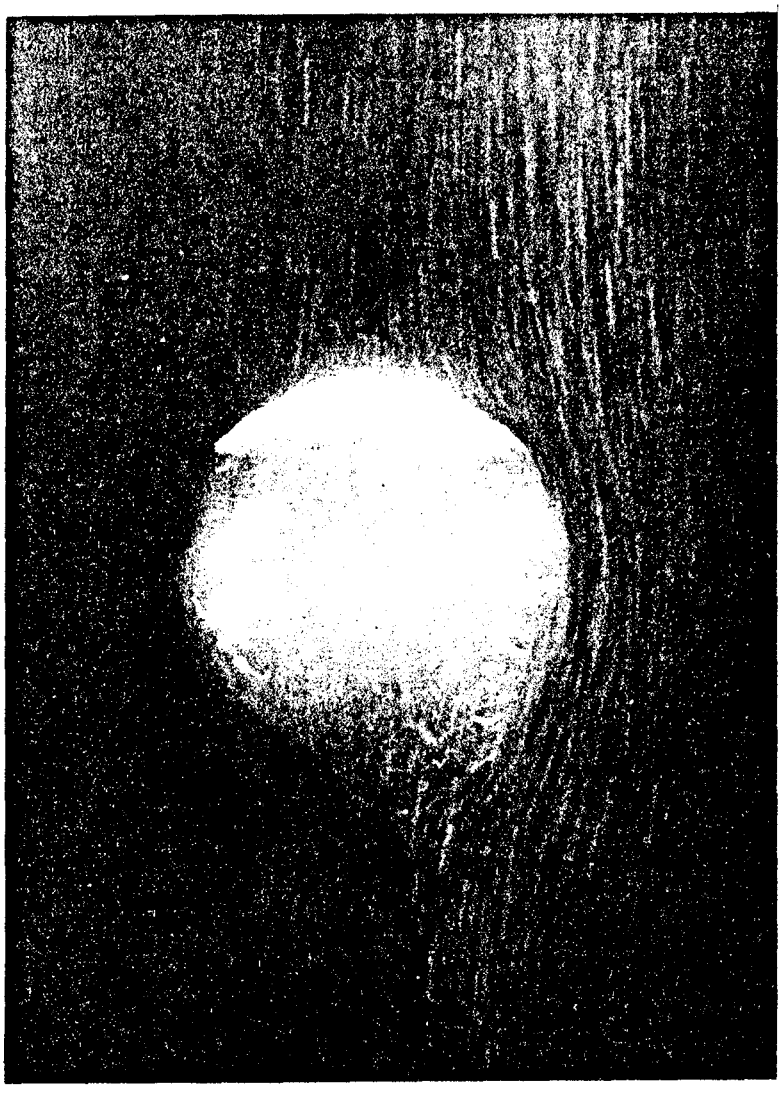

Figure 1. Streamlines relative to a 40 ml bubble

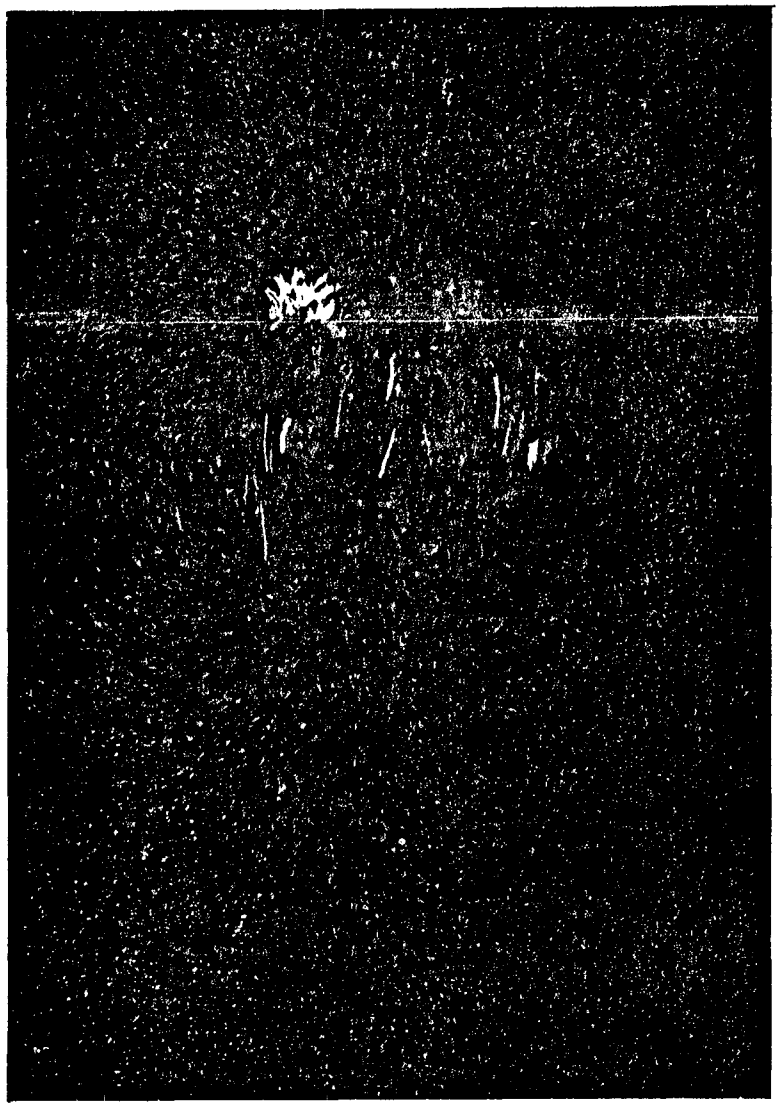

Figure 2. Instantaneous streamlines, 40 ml bubble

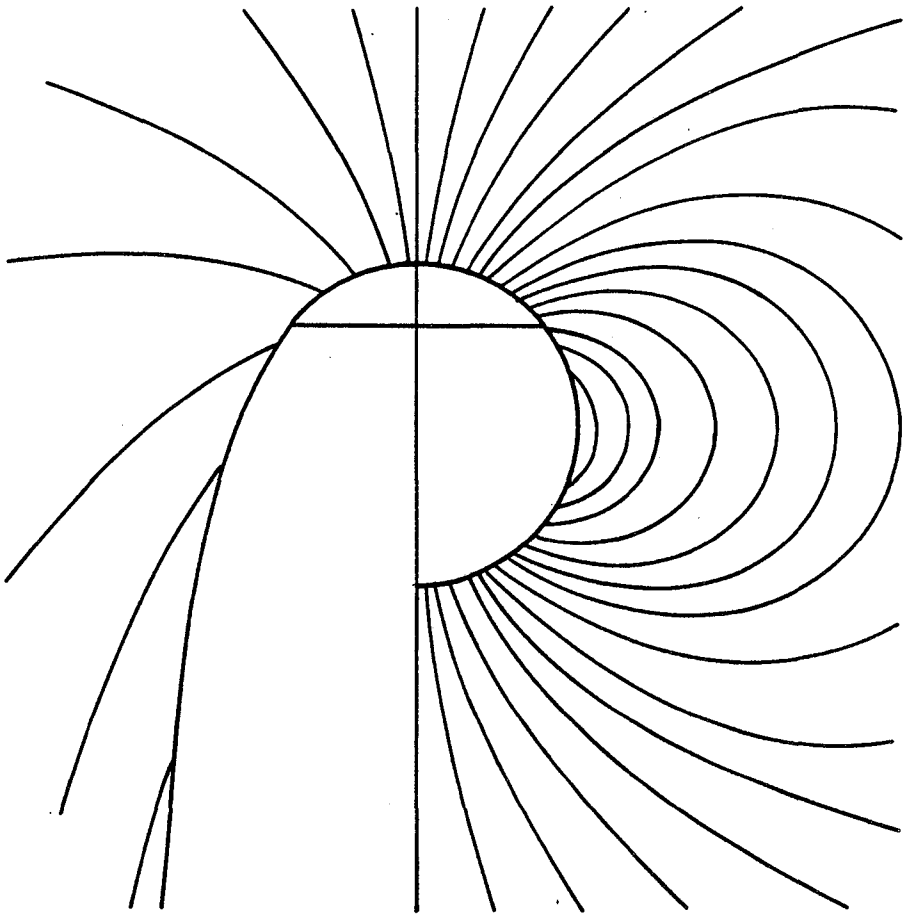

infinite open wake irrotational dipole

Figure 3. Instantaneous streamline patterns

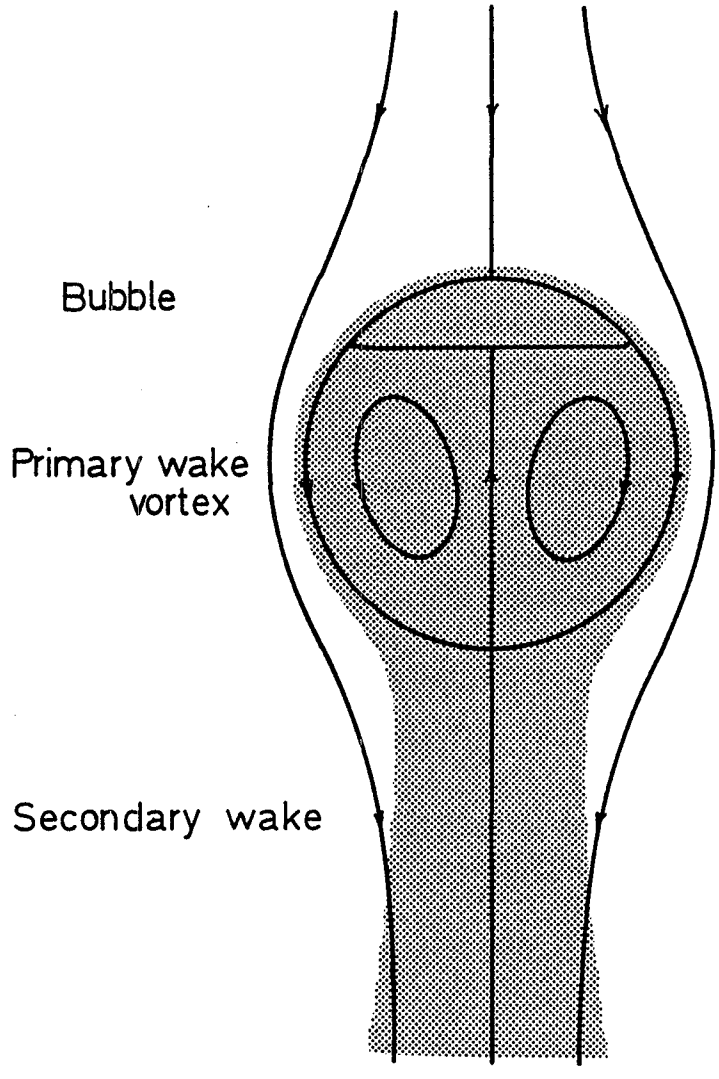

Figure 4. Wake structure inferred from experiment

THE APPLICATION OF DROPS AND BUBBLES TO FLUID FLOW MEASUREMENTS

E.F.C. Somerscales
Rensselaer Polytechnic Institute

This paper is concerned with the characteristics of drops and bubbles when used as flow tracers for the quantitative study of fluid velocity. Particular attention is paid to the practical aspects of assessing and choosing bubbles and drops for flow measurement. Both laminar and turbulent flow situations are considered. The determination of the dynamic characteristics of bubbles and drops is discussed together with the physical properties required for such a determination. The effect of extraneous force fields, particularly gravity, is reviewed. The theoretical and practical aspects of introducing bubbles and drops into the fluid are considered. The paper concludes with a discussion of the types of bubbles and drops, their selection and a review of previous applications.

Manuscript was not available from the author at the time the proceedings were submitted to the printer.

A Review of

THE DYNAMICS OF BUBBLES AND DROPS IN A VISCOELASTIC FLUID

E. Zana and L. G. Leal
Chemical Engineering, California Institute of Technology

I. INTRODUCTION

Some of the most important processes in the chemical industry involve the motion and dissolution of gas bubbles and drops in viscoelastic suspending fluids. Nevertheless, relatively few investigations have been undertaken to date which consider these problems either experimentally or theoretically. In this paper we briefly review recent research progress. The paper is split into two parts. In the first, we recap the rheological behavior of a viscoelastic fluid in general viscometric or elongational flows. In the second part, we describe recent observations and/or predictions for several diverse types of bubble or drop motion, concentrating on those effects which appear to us to be primarily due to the non-Newtonian rheological properties of the suspending fluid. Although most of the macromolecules which are commonly used to produce viscoelastic solutions are also moderately strong surfactants, we will not be specifically concerned with the related interfacial or surface effects. In addition, the many papers which describe theoretical calculations of bubbles or drops in power-law type non-Newtonian fluids will not be considered here.

II. RHEOLOGICAL PHENOMENA IN VISCOELASTIC FLUIDS

In general, the features characterizing most realistic viscoelastic fluids may be summarized[†] as a nonlinear relationship between stress and bulk deformation rate (specifically, the symmetric rate of strain tensor) and a memory for past configurations which diminishes on a time scale λ. The stress at a particular point in space thus depends not only on the instantaneous deformation rate, but on the history of deformation of the fluid element which occupies that point. In steady viscometric flows (i.e. shear flows), these features lead to a decrease in the effective viscosity with increasing shear rate and the existence of non-isotropic normal stress contributions which correspond to an extra flow-induced tension or compression in the fluid.[††]

Although these effects are well-known, they constitute only a portion of the picture for most problems in bubble and drop dynamics where the local fluid

[†] with apologies to any rheologists in the audience

[††] A fluid whose only non-Newtonian characteristic is a shear-thinning viscosity will be called purely-viscous. The power-law model is the most common description of such a fluid.

motion near the bubble or drop is almost always unsteady in either a Lagrangian or Eulerian sense. When the flow is not steady, the mechanical behavior of the fluid depends strongly on the time scale of change in the flow, T, compared with the intrinsic scale λ of the fluid's memory. Provided $T \gg \lambda$, the material response will be closely similar to that in steady flow. However, when T and λ are of comparable magnitude, the fluid microstructure lags behind the imposed deformation and the stress both increases relative to that in a purely-viscous fluid and shows a phase lag relative to the deformation. For example, in rapid start-up of a viscometric flow (or rapid increase in deformation rate from one steady value to another), there is a characteristic overshoot of stress which approaches the steady-state value in an oscillatory fashion with a period of the order λ. Similarly, if a steady flow is suddenly stopped, the stress does not return instantaneously to its rest value, as it would in a purely-viscous fluid, but rather relaxes on a time scale which is again related to λ. In addition, if the driving force for motion is suddenly removed, there is generally a macroscopic recoil in which the motion may actually reverse itself before vanishing at long times.

Further, of significance to many problems of bubble or droplet motion is the material behavior in non-viscometric flows, particularly the so-called uniaxial extensional deformations which are characterized by the elongational viscosity. The elongational viscosity is found to increase with increase of λ and to also increase rapidly with deformation rate (in direct contrast to the shear viscosity) even in very dilute polymeric solutions where the viscometric behavior is indistinguishable from a Newtonian fluid. It has, in fact, sometimes been suggested that the elongational viscosity becomes effectively infinite at some critical rate of elongation. Of course, such an effect cannot be observed experimentally. What happens instead is that the local rate of extension in the fluid is rapidly decreased most often by internal re-adjustment of the flow patterns. An example is the well-known converging flow from a large tank into a small channel.[1] In that case, instead of following the wall contours, which would produce some particular rate of extension for a given flow rate, the fluid which enters the small channel is restricted upstream to a narrow conical area, leaving a slowly recirculating toroidal eddy filling the region between the walls and the cone. In this way the resulting fluid motion exhibits a much reduced extension rate and correspondingly smaller stresses in the converging region of the flow. This type of internal flow adjustment is characteristic of uniaxial elongational motions due to the large variations in stress which accompany a change in the rate of extension.

Finally, it is relevant to remark briefly on the existence of constitutive models which incorporate the effects described above. In particular, one may ask whether the possibility exists for realistic theoretical calculations of bubble and drop motion in viscoelastic fluids. Unfortunately, the prospects are not good at present. The difficulties are two-fold. First, and foremost, is the lack of realistic constitutive models. Of the very large number of constitutive relations which have been proposed, none has yet been found to be quantitatively satisfactory even for simple viscometric (shear) flows, where extensive experimental data exists.[2] Furthermore, even if one is willing to accept qualitatively correct viscometric behavior, there is no *a priori* reason to expect equally good performance in nonviscometric flows such as those associated with the motion of bubbles or drops, and no extensive rheological studies of nonviscometric flows have yet been carried out. The second difficulty with any theoretical analysis is due to the basic nonlinearity of viscoelastic fluid behavior. In addition to the familiar non-linear inertia terms in the equations of motion, there are additional nonlinearities associated with the constitutive model. Only in the limit of dynamically and rheologically slow flow† do the equations become linear, and then the material is limited to nearly-Newtonian behavior.

Thus, if we are to improve our knowledge and understanding of the motion of drops or bubbles in a viscoelastic fluid, we must rely primarily upon experimental evidence, coupled with a qualitative application of general rheological principles rather than detailed theoretical analysis.

III. VISCOELASTIC CONTRIBUTIONS TO BUBBLE AND DROP DYNAMICS

A. Translation of Gas Bubbles through a Quiescent Fluid

The aspect of bubble and drop dynamics which has received the most attention in the literature is the buoyancy driven motion through a quiescent fluid. In addition to its fundamental importance, this problem is of considerable practical interest in the chemical engineering literature because of its relationship to residence-time and mass transfer rates in gas/liquid contact operations.

1. General Characteristics

In figure 1 we have plotted terminal velocity, U, as a function of bubble volume, V, for the typical case of a 1% solution of Separan AP30‡ in water. Also shown are data for glass spheres of various volumes, and instantaneous values

† Flows in which $T \gg \lambda$ and $UL/\nu \ll 1$.

‡ Typical rheological data for this system may be found in references 2 and 11.

of U versus V for a dissolving CO_2 bubble. Finally, we have superposed a series of photographs of the nondissolving bubbles, which are intended to illustrate typical bubble shapes in a viscoelastic liquid. The first extensive investigation of bubble shape seems to have been that of Philippoff,[3] but subsequently a number of investigators have reported relevant experimental observations. The present photographs are from Zana.[4] In the Newtonian case the bubble is spherical for small sizes, and is then deformed by the effects of fluid inertia through oblate spheroidal shapes to the well-known spherical-cap at larger bubble volumes. However, in the viscoelastic case the initial deformation is generally dominated by elastic contributions which produce a prolate ellipsoid, followed by an inverted tear-drop shape. As inertia effects increase, the prolate tear-drop is deformed into an oblate spheroid with a trailing cusp and finally into a modified spherical-cap. The terminal velocity data also show several distinct regimes. For the smallest bubble sizes in which the effective Reynolds number is very small and elastic effects modest, the data for the non-dissolving bubble is in essential agreement with that for the rigid glass spheres. However, at $r_e \sim 0.29$ cm, there is an abrupt transition from this Stokes-like regime to a new regime which shows essentially the same initial slope ($\partial \log U/\partial \log V$), but in which the terminal velocities are very considerably increased. Finally, there is a gradual transition region where the bubble approaches a spherical-cap shape and ($\partial \log U/\partial \log V$) approaches 1/6 after wall-corrections have been applied, as originally predicted by Davies and Taylor[5] for a Newtonian fluid.

A measure of the importance of fluid elasticity in an unsteady flow is the largeness of the ratio of the intrinsic memory relaxation time λ and the time scale of change of the flow R/U in which R is the characteristic length scale of the bubble in the direction of motion. This ratio, as well as the corresponding Reynolds number is tabulated for the data of figure 1 in table 1 which is appended to the figure. In the limit as bubble volume $V \to 0$ or $V \to \infty$, it may be shown that $\lambda/(R/U) \to 0$. However, clearly in the range $r_e = 0.15$ to $r_e = 1.5$ for which we have data, the ratio of time scales is not small and elasticity should have a noticeable influence, especially for the smaller sizes where it is not moderated significantly by inertia.

For $r_e < 0.15$, the slope ($d\log U/d\log V$) must approach the Newtonian creeping flow value of 2/3 as bubble volume is decreased. However, in the range of figure 1, the measured slope is greater than either the creeping flow value or the value $(1 + n)/3n$, which is calculated using a power-law constitutive model.[6] A comparison of the power-law parameter n obtained from measurements of viscosity in simple

shear flow with that inferred from the measured slope ($\partial \log U / \partial \log V$) is shown in table 2 for several Separan AP30/water/glycerine solutions. Since the power-law model only includes purely-viscous effects, this comparison provides strong evidence for the importance of the fluid elasticity in the motion of small bubbles, at least for moderate polymer concentrations. A further indication of significant elastic effects in the motion of small bubbles may be seen in the prolate shapes of figure 1. We have noted previously that viscoelastic flows often adopt a detailed pattern which minimizes the elastic component of the stress. In motion of a rigid body, this can only be accomplished by increasing the length of the region fore and aft in which the flow is significantly influenced by the body. Such an effect is indeed observed[7,8] in flow past rigid spheres and cylinders. In the case of bubbles (or drops), a similar effect can also be achieved by deformation of shape to an elongated (or prolate) form, and this fact suggests one possible explanation of the prolate spheroidal and tear-drop shapes which are actually observed.

The terminal velocity adopted at steady state is that value which gives an exact balance between the rate of working by buoyancy forces, FU, and the rate of energy dissipation in the fluid. The latter is effected by viscoelasticity in two distinct ways[6]; first, through changes in the velocity field and, second, by the elastic stress contribution to the dissipation rate. For large bubbles, in which the inertia terms dominate both viscous and elastic terms in the equations of motion, the velocity fields are essentially the same in Newtonian and non-Newtonian fluids so that the main effect is through the dissipation mechanism.[8] Although relatively minor, especially in the spherical-cap regime, experiments in a series of increasingly viscoelastic fluids[4] do show a systematic decrease in terminal velocity at a fixed volume, implying, as expected intuitively, that the elastic contribution to the rate of energy dissipation must be positive. Thus, in general, the viscoelastic effects on "dissipation" and of changes in the velocity field toward a smoother or elongated configuration are at least partially cancelling in their influence on terminal velocity for a given volume. For smaller bubbles, in which the inertia terms are negligible, the influence of viscoelasticity on bubble motion may still be small if the flow is "visco-elastically slow" in the sense $R/U \gg \lambda$. More frequently, viscoelasticity is important for small bubbles (or drops) as evidenced in figure 1 and table 1.

2. The Velocity Transition Phenomenon

Of all of the viscoelastic effects exhibited in figure 1, the most intriguing and potentially important is the large and discontinuous transition in terminal velocity at $r_e \sim 0.29$ cm. The existence of such a transition was first reported by Astarita and Apuzzo,[9] who found a six-fold increase in bubble velocity at the transition point for a 0.5% solution of the commercial J-100 polymer. Similar results have more recently been reported by Calderbank, Johnson and Loudon[10] in 1% Polyox solutions and by Leal, Skoog and Acrivos[11] in solutions of the commercial coagulation polymer Separan AP30. A steep but not abrupt increase in velocity has also been observed in the case of liquid drops moving through viscoelastic liquids[12,13,14,15] and for gas bubbles which are dissolving† (see figure 1).

Kintner et al.[15] proposed that the increase in velocity for drops is the result of a transition in the conditions at the drop interface from a no-slip to a freely-circulating regime (equivalent to the well-known transition from the Stokes to Hadamard regimes in Newtonian liquids) coupled with a change of shape corresponding to a decrease in frontal area. In the case of gas bubbles, however, Astarita and Apuzzo[9] showed experimentally that the frontal area actually increased during the velocity transition. As a result, it was speculated that the velocity increase was solely a result of the transition in surface conditions, with viscoelasticity hypothesized as being responsible for the abruptness of the transition. Further, it was implied that the magnitude of the velocity transition could be largely accounted for by considering only the purely-viscous, shear thinning viscosity, ignoring elastic and normal stress contributions.

A partial test of Astarita's proposal was reported several years ago by Leal, Skoog and Acrivos.[11] Careful experimental measurement showed that, a) the bubble velocities for volumes less than the critical volume are precisely equal to those measured for equal volume glass spheres provided suitable density corrections are utilized; b) no terminal velocity transition occurs for the

† The significance of this observation remains unclear to us at the present time.

glass spheres. The relevant data are reproduced in figure 1. Hence, strong indirect evidence was found to confirm the change in interfacial conditions as the cause of the observed velocity transition. The effect of shear dependent viscosity, in the absence of viscoelastic effects, was also studied by employing an empirical (curve-fit) purely-viscous fluid model to numerically calculate the terminal velocities on non-circulating, partially circulating, and fully circulating spherical bubbles at the measured critical volume. It was found that the presence of shear-dependent viscosity alone could only account for about 30% of the magnitude of the measured velocity transition. Hence, it was surmised that better agreement between theory and observation could only be achieved by taking account of viscoelastic effects in the fluid. Of perhaps greater significance however was the subsequent conclusion, based on simple qualitative arguments, that a relatively small additional viscoelastic contribution to the force balance on the bubble would be sufficient to account for the much larger measured velocity increases. The conditions required to produce a consistent result are that the drag be reduced in both the pre-transition and post-transition regimes, but with the effect being somewhat greater in the latter case.

As an initial test of the viability of this proposal, it was desired to determine whether elastic effects, in the absence of shear-dependent viscosity, would contribute to the particle drag in a qualitatively consistent manner. In order to investigate this question, Zana[4] utilized "slow-flow" asymptotic solutions, based on the 6-constant Oldroyd[16] fluid model, to compare the viscoelastic contributions to the drag on a rigid no-slip sphere and on a freely circulating spherical bubble. The rigid sphere result was taken from the solution of Leslie.[17] The solution for the case of a spherical bubble was obtained by Zana.[4] An equivalent, independent solution for the stream-function field was published independently by Wagner and Slattery.[18] However, Wagner and Slattery's analysis appears to contain a number of algebraic and/or printing errors. In the limit corresponding to a shear-independent viscosity, the drag on a spherical bubble was found by Zana to be

$$D_{bubble} = 2\pi\eta_o U_b a\{2 - 0.066(1 - \alpha)(30 + \alpha)\varepsilon^2 + \ldots\}$$

where η_o is the viscosity, U_b the bubble velocity and a the bubble radius. The parameter ε is the ratio of the intrinsic relaxation time λ_1 from the Oldroyd model, to the convective time scale a/U_b and is assumed to be small in accord with the "slow-flow" approximation. The parameter α is the ratio of

retardation and relaxation times λ_2/λ_1 and satisfies

$$0 \leq \alpha \equiv \frac{\lambda_2}{\lambda_1} \leq 1$$

with the Newtonian limit being $\alpha = 1$. The corresponding expression for the drag on a rigid sphere is[17]

$$D_{sphere} = 2\pi\eta_o U_s a\{3 - 0.016(1 - \alpha)(3 - \alpha)\varepsilon^2\} .$$

Hence, comparing the two expressions, it may be seen that the purely elastic contribution to the drag causes a decrease in both cases at $O(\varepsilon^2)$, but that the effect is much more pronounced for the bubble than for the rigid sphere. Thus, the "slow flow" viscoelastic approximation offers strong preliminary evidence to support the original hypothesis of Leal, Skoog and Acrivos.[11]

In addition, we have recently carried out an extensive flow visualization study for gas bubbles in solutions of Separan AP30 in water and water/glycerine, as an independent attempt to assess the importance of viscoelastic contributions to the velocity transition phenomena. Centerplane streakline photographs were obtained for bubbles which were slightly smaller and for bubbles which were slightly larger than the transition volume. Also obtained were streamlines for rigid particles, which were machined to the same shape as the bubbles, in Sep AP30/water and in mineral oil (Newtonian) at the same nominal Reynolds numbers. The main evidence of elastic influence was a somewhat stronger upstream influence of the bubbles on the flow in the Sep AP30 solutions, as compared with that for the geometrically similar rigid particles in mineral oil. Significantly, the degree of upstream influence for the bubble also appeared to be enhanced after transition, thus supporting the "requirement" of larger viscoelastic contributions in the post-transition regime.

B. Deformation and Break-up of Drops in Shear and Extensional Flows

A problem of considerable practical importance in the chemical processing industry is the dispersion or emulsification of one liquid phase in another. Insight into this highly complex phenomena may be obtained by studying the deformation and break-up of a single liquid drop subjected either to shear or extensional flow of an ambient fluid. When either the drop, or the suspending fluid (or both) is non-Newtonian, experimental observation has shown that the deformation and break-up processes can be fundamentally changed from the more

familiar phenomena in a Newtonian system.

The theory of deformation and alignment of Newtonian drops subjected to simple shearing motion of a second Newtonian fluid was initiated by Taylor[19] and taken to higher levels of approximation by Chaffey, Brenner and Mason,[20] and by Cox.[21] Here, we concentrate on the case of Newtonian or viscoelastic drops in a non-Newtonian suspending fluid, where the deviations from predicted Newtonian behavior are greatest.†

1. Deformation

The majority of experiments have been reported for Newtonian drops subjected to simple shearing motion of a non-Newtonian suspending fluid. When the ambient fluid is purely-viscous,[24] the drop becomes increasingly deformed with increase of shear-rate, but does so less rapidly than predicted by the Newtonian theory. On the other hand, the droplet orientation for a given degree of shape deformation appears qualitatively similar to the Newtonian case, and for small degrees of deformation, the major axis of the drop is aligned at 45° to the flow. In contrast, the degree of alignment for a viscoelastic suspending fluid[22] is much greater, and shows an apparent small deformation limit of only 29° from the flow direction. In addition, although the observed modes of deformation are similar to the Newtonian and purely-viscous cases, it has been shown experimentally[25] that the degree of deformation does not always increase monotonically with shear-rate, but for small drops exhibits a maximum at some intermediate value.

Relatively few studies have been carried out of bubble or droplet deformation in non-viscometric flow, other than the deformation in simple translation which was described earlier. The only other work of which we are aware is the Ph.D. thesis of W. K. Lee[26] which is concerned in part with deformation and breakup of viscoelastic drops in extensional flow fields of a Newtonian suspending fluid. The results of Lee show the deformation to be the same as for Newtonian drops with a viscosity equal to the zero shear viscosity of the non-Newtonian fluid.

It is important to note that all of the studies referred to above were carried out without any attempt to systematically vary or measure the interfacial properties between the drop and surrounding fluid. A recent experimental study by Bartram[27] provides one example which illustrates the danger in generalizing such results. Bartram studied the deformation of a viscoelastic

† Experiments relevant to non-Newtonian drops in a Newtonian suspending fluid have been reported by Gauthier, Goldsmith and Mason[22] and by Tavgaç.[23]

fluid with zero or near zero interfacial tension and relatively large internal viscosity. In this case the initially spherical drop first elongated in the direction of the vorticity axis, then exhibited a simultaneous rocking motion reminiscent of Jeffery orbits for a rigid spheroid in a Newtonian fluid,[28] finally buckling and breaking up as the elongation was continued. This rather astonishing mode of deformation (and break-up) is quite unlike any of the previous observations described above, and clearly emphasizes the difficulty of analyzing experimental results when all of the relevant dimensional parameters have not been determined or varied in a systematic fashion.

2. Break-up

The most comprehensive investigations of drop break-up in non-Newtonian systems are due to Flumerfelt[25] and his students.[23,26] Results for simple shear flow have been reported by Tavgaç[23] for viscoelastic drops in Newtonian fluids, and by Flumerfelt[25] and Tavgaç[23] for Newtonian drops in a viscoelastic suspending fluid. Dimensional analysis shows that the critical shear-rate for break-up in a given viscoelastic fluid must depend on the internal to external viscosity ratio, and on the relative magnitude of the relaxation time for the fluid, λ, compared to the time scale $\dot{\gamma}_c^{-1}$ of the shearing motion. Available experimental data for Newtonian systems has shown the critical shear rate for break-up, $\dot{\gamma}_c$, to be unique for each fluid system. In contrast, however, the extensive studies in viscoelastic fluids cited above all suggest that $\dot{\gamma}_c$ increases linearly with $\lambda\dot{\gamma}_c$ for fixed and moderate values of the viscosity ratio and $\lambda\dot{\gamma}_c$ greater than 1. Thus, in non-dimensionalized form, it is found

$$\left(\frac{\eta' D}{\sigma}\right)\dot{\gamma}_c \sim c_1(\lambda\dot{\gamma}_c) + c_2$$

where η' and σ are the viscosity and interfacial tension, and D the equivalent diameter of the drop. An extremely important and obvious implication of this relationship is that break-up can occur for a given fluid system only if

$$D > \left(\frac{\lambda\sigma}{\eta'}\right)c_1$$

i.e. there exists a critical drop-size below which break-up cannot occur for viscoelastic systems. This result is in sharp contrast with the Newtonian case where, within certain limits of the viscosity ratio, drops of any size may be broken by application of sufficiently high shear rates, and strongly suggests the difficulty of achieving very fine dispersions in viscoelastic systems.

Another result of considerable importance is the influence of transient effects on drop break-up in viscoelastic systems. Both Tavgac[23] and Flumerfelt[25] used rapid start-up of simple shear flow as a test case. For fully Newtonian systems, or for viscoelastic drops in a Newtonian fluid, the break-up under transient conditions does not differ significantly from that observed in steady flow. However, for Newtonian drops in a viscoelastic fluid, the critical shear-rate for break-up is sharply decreased in the start-up flow relative to its value in steady shear.

Finally, results similar to those of Flumerfelt and Tavgac were also obtained by Lee[26] for break-up in a uniaxial extensional flow. That is, for a fixed and moderate value of the viscosity ratio, the critical extension rate for break-up increases linearly as the time scale of the flow is decreased relative to the relaxation time of the fluid. Thus, for a fixed fluid system, break-up can occur only for drops larger than some critical volume.

In summary, we may note that the effect of viscoelasticity, in all cases, is to increase the required flow-rate for break-up. For small drops, where elastic effects are most significant, break-up is apparently prevented altogether in a sufficiently viscoelastic fluid (large λ). These effects may possibly reflect an increasing degree of "smoothing" of the disturbance flow as the fluid motion adjusts, in the manner described earlier, to avoid large elastic stress contributions. However, no detailed theoretical investigation of the break-up phenomena has yet been attempted, and there is no experimental evidence available of the detailed velocity fields in the vicinity of a drop which could be used to test this hypothesis. The decrease in critical shear-rate during a start-up flow,is almost certainly a result of the characteristic large overshoot of stress which occurs under such circumstances (see section II) although again no direct experimental or theoretical support exists for this assertion. In view of the practical importance of dispersion processes, it is to be hoped that further investigations will be carried out which will elucidate the mechanisms of deformation and break-up in viscoelastic fluids.

C. Lateral Migration of Deformable Drops in Poiseuille and Couette Flows

The change in bulk flow properties which may be attributed to the suspended drops of an emulsion depend critically on the concentration distribution in the flow apparatus. It has been observed that drops in a Newtonian system tend to migrate across the streamlines of a bulk (undisturbed) flow in such a manner as to produce a cross-stream variation of droplet concentrations, even at very low particle Reynolds numbers.[28] In Poiseuille flow, migration is toward the tube

centerline, while in Couette flow two-way migration occurs toward an equilibrium position which is midway between the cylinders. In both cases, the phenomena has been explained as resulting from deformation of the drop and its interaction with the walls.

Mason and co-workers[24,29] have shown experimentally that the phenomenon are altered significantly when the suspending fluid is non-Newtonian. Distinctly different results are obtained depending upon whether the fluid is fully viscoelastic or purely-viscous. In Couette flow,[24] the equilibrium position is moved closer to the inner cylinder for the purely-viscous case, but closer to the outer cylinder for a viscoelastic fluid. In Poiseuille flow,[29] drops in a viscoelastic fluid migrate toward the tube axis as in the Newtonian case, but at a much greater rate. Drops in a purely-viscous fluid, however, exhibit <u>two-way migration</u> toward an equilibrium position which lies between the centerline and tube wall.

Qualitatively, these results can be understood by considering Mason's further experiments with rigid spheres in the same flow systems.[24,29] These show migration in the direction of lowest shear-rate when the ambient fluid is viscoelastic, but migration in the opposite direction for a purely viscous suspending fluid. Recently, Ho and Leal[30] have obtained the former result analytically for a viscoelastic fluid in the slow flow limit, and have shown that the major effect arises because of induced normal stresses in the disturbance flow near the particle. Qualitatively then, it would appear that the migration of deformable drops can be accounted for by assuming a superposition of the migration effects due to particle deformability with those due to the non-Newtonian rheology. Of course, it is evident that this conceptual procedure takes no account of the coupled non-Newtonian deformation effects, and a more definitive understanding of the phenomena awaits further theoretical and experimental study.

D. <u>Oscillations and Collapse of Gas Bubbles Due to Acoustic and Impulsive Pressure Variations, and Due to Mass Transfer</u>.

The variation of bubble volume with time due to pressure variations in the ambient fluid, or to dissolution of the bubble by mass transfer is of both practical and theoretical interest in connection with problems of flow-induced (or acoustical) cavitation, and of gas-liquid contact mass-transfer operations. Interestingly, however, with the exception of mass-transfer measurements for a translating bubble,[4,10] very little experimental information of relevance is available. Furthermore, unlike all of the previous examples, the motion induced in the fluid by the changing bubble volume is a <u>pure</u> elongational deformation.

Although this extensional motion is generally coupled with a buoyancy-driven translation, we consider here the limiting case in which the characteristic velocity of translation is small and neglected compared with the characteristic radial velocity induced by the changing volume.

1. Pressure-induced Volume Variations

The motion of a void or an insoluble gas bubble induced by a sudden pressure surge, or by application of acoustic pressure variations has been studied theoretically by Fogler and Goddard[31,32] using a linear viscoelastic constitutive model.

In the absence of elastic effects, a void will generally collapse to zero radius when subjected to a sudden pressure surge, while an insoluble gas bubble will generally always rebound short of actual collapse as a result of the sharp increase in internal pressure. The response in a viscoelastic fluid depends upon the magnitude of the intrinsic relaxation time of the fluid compared with the classical Rayleigh collapse time for the bubble or void. When the relaxation time exceeds the Rayleigh collapse time, the elastic response of the fluid can significantly retard the collapse of a void and produce a prolonged oscillatory approach to the final collapse. Indeed, for $\lambda \to \infty$ and viscosity $\mu \to 0$, Fogler and Goddard's[31] analysis for a void shows either indefinite oscillation about an equilibrium radius, or complete collapse on the first cycle, depending on the magnitude of the imposed pressure increase. For finite μ, the oscillation is damped in time, while for finite λ, the void ultimately collapses, but the process is delayed for several cycles with a final collapse time which depends on λ. In all cases, the period of oscillation is essentially the Rayleigh collapse time for the system. Insoluble gas bubbles, in fluids with large λ, decrease from their initial radius to a new equilibrium radius via a similar oscillatory cycle which shows an amplitude dependent both on the intrinsic relaxation time λ and the elastic modulus of the linear viscoelastic model.[32] A minimum amplitude of oscillation is found for values of λ close to the Reyleigh collapse time.

In an oscillatory pressure field (such as that induced by acoustic waves), the motion of a gas bubble is systematically damped by a decrease in the time scale of oscillation relative to λ, and with increase of the elastic modulus.

2. Bubble Collapse Due to Dissolution

The related problem of bubble collapse due to dissolution of the gas into the surrounding liquid differs qualitatively from the pressure-induced motions which we have just discussed. Most important is the fact that the mass-transfer process which drives the collapse, and the collapse-induced fluid motion are

intimately coupled. In a recent investigation, Zana and Leal[33] have used an Oldroyd-type constitutive model[16] to study the dynamics of bubble collapse by dissolution assuming that the bubble and the suspending fluid are initially motionless. As in previous examples, it was found that the elasticity of the fluid played a significant role only when the natural collapse time was comparable to the intrinsic relaxation time λ.

A plot of bubble radius as a function of time is shown in figure 2 for three different values of λ. It may be noted, first of all, that the curves cross each other at a dimensionless time of approximately 0.4. Thus, an increase in λ actually produces an increased rate of bubble collapse during the initial stages of the collapse process, but then acts to retard the bubble motion for the remainder of the bubble's lifetime. The fluid flow induced by collapse of a spherical stationary bubble is an unsteady uniaxial extension. Therefore, one would expect the elastic influence on the collapse process to be a direct consequence of its influence on the elongational viscosity $\bar{\eta}$. We have noted earlier that $\bar{\eta}$ is an increasing function of the rate of elongation for fixed λ and steady flow, and is also increasing for increasing λ. Thus, one would expect the bubble to collapse more slowly as λ is increased, provided changes in the induced flow occur sufficiently slowly. This is precisely what is observed for times $t \geq 0.1$. Clearly, the enhanced collapse rate with increased λ for $t < 0.1$ cannot be explained in terms of the <u>increase</u> in steady-state elongational viscosity. However, it can be simply understood in a qualitative sense by considering the transients associated with stress growth. Recall that this is a start-up problem, i.e. initially the bubble is stationary and there is no fluid motion. Therefore, when the bubble boundary is set in motion at $t = 0$ by mass-transfer, there is a transient period of stress growth with an approximate time scale of the order of the intrinsic (stress) relaxation time, λ. During this period, the instantaneous resistance to motion is less than it would be at steady-state in the same fluid with the same elongation rate $\dot{e}$ and consequently the collapse rate overshoots its corresponding steady-state value. Ultimately, as the stresses build up, they too overshoot causing the elongation rate to decrease until it finally approaches a slowly varying state in which the steady elongational viscosity is effective in governing the collapse rate. We note that a similar overshoot of the rate of change of cavity volume was also reported by Street[34] for cavity <u>growth</u> in a viscoelastic liquid in spite of the fact that the fluid dynamics of Street's problem is fundamentally different from the present collapse problem—the bubble growth induces a biaxial extensional flow, whereas the

collapse produces a uniaxial extension.

Finally, it should be remarked that the stress-overshoot is closely related to the oscillatory motion predicted by Fogler and Goddard[32] in a cavity subjected to a sudden pressure surge. A more detailed account of the work described here may be found in Zana and Leal,[33] and in Zana.[4]

References

1. Metzner, A. B., Uebler, E. A. and Fong, C. F., AIChE J., 15, 750 (1969)
2. Spriggs, T. W., Huppler, J. D. and Bird, R. B., Trans. Soc. Rheol., 10, 191 (1966)
3. Phillipoff, W., Rubber Chem. & Tech., 10, 76 (1937)
4. Zana, E., Ph.D. Dissertation, California Institute of Technology (1975)
5. Davies, R. M. and Taylor, G. I., Proc. Roy. Soc. A200, 375 (1950)
6. Astarita, G., I & EC Fund., 5, 548 (1966)
7. Ultman, J. S. and Denn, M. M., Chem. Eng. J., 2, 81 (1971)
8. Zana, E. and Leal, L. G., To appear in Rheologica Acta (1975)
9. Astarita, G. and Apuzzo, G., AIChE J., 11, 815 (1965)
10. Calderbank, Johnson and Loudan, Chem. Eng. Sci., 25, 235 (1970)
11. Leal, L. G., Skoog, J. and Acrivos, A., Can. J. Chem. Eng., 49, 569 (1971)
12. Barnett, S. M., Humphrey, A. E. and Litt, M., AIChE J., 12, 253 (1966)
13. Garner, F. H., Mathus, K. B. and Jensen, V. G., Nature, 180, 331 (1957)
14. Warshay, F. H., Bogusz, E., Johnson, M. and Kintner, R. C., Can. J. Chem. Eng., 37, 29 (1959)
15. Fararouri, A. and Kintner, R. C., Trans. Soc. Rheol., 5, 369 (1961)
16. Oldroyd, J. G., Proc. Roy. Soc., A245, 278 (1958)
17. Leslie, F. M., Quart. J. Mech. and Appl. Math., 14, 36 (1961)
18. Wagner, M. G., Slattery, J. C., AIChE J., 17, 1193 (1971)
19. Taylor, G. I., Proc. Roy. Soc., A138, 41 (1932)
20. Chaffey, C. E., Brenner, H., and Mason, S. G., Rheol. Acta, 4, 64 (1965)
21. Cox, R. G., J. Fluid Mech., 37, 601 (1969)
22. Gauthier, F., Goldsmith, H. L. and Mason, S. G., Rheol. Acta, 10, 344 (1971)
23. Tavgaç, T., Ph.D. Thesis, University of Houston (1972)
24. Karnis, A. and Mason, S. G., Trans. Soc. Rheol., 10, 571 (1967)
25. Flumerfelt, R. W., I & EC Fund., 11, 312 (1972)
26. Lee, W. K., Ph.D. Thesis, University of Houston (1972)
27. Bartram, E., M.S. Thesis, McGill University (1973)

28. Goldsmith, H. L. and Mason, S. G., in Rheology (ed. Eirich), vol. 4 (1967)
29. Gauthier, F., Goldsmith, H. L. and Mason, S. G., Trans. Soc. Rheol., 15 297 (1971)
30. Ho, B. and Leal, L. G., to appear in J. Fluid Mech. (1976)
31. Fogler, H. S. and Goddard, J. D., Phys. Fluids, 13, 1135 (1970)
32. Fogler, H. S. and Goddard, J. D., J. Appl. Phys., 42, 259 (1971)
33. Zana, E., and Leal, L. G., I & EC Fund., 14, 175 (1975)
34. Street, J. R., Trans. Soc. Rheol., 12, 103 (1968)

Acknowledgement

The preparation of this paper was supported, in part, by a grant from the National Science Foundation, GK35468.

Table 1

r_e	$\lambda/(R/U)$	Ur_e/ν
0.15	0.36	1.8×10^{-4}
0.2	0.55	7.5×10^{-4}
0.3-	0.85	7.8×10^{-3}
0.3+	1.4	9.3×10^{-2}
0.4	2.0	0.43
0.5	2.2	1.3
0.6	2.1	3.6
0.7	2.1	4.6
0.8	1.9	5.9
1.0	2.3	5.7
1.5	2.1	7.8
2.0	1.9	8.3

Table 2

Solution	n(terminal velocity measurement)	n(viscosity @ 0.5 sec^{-1})
0.523% AP30 - 45.6% water - 53.9% glycerine	0.26 ± 0.02	0.45 ± 0.05
1% AP30 - water	0.48 ± 0.02	0.68 ± 0.07
0.5% AP30 - water	0.72 ± 0.05	0.77 ± 0.11
0.1% AP30 - water	0.80 ± 0.10	0.85 ± 0.14

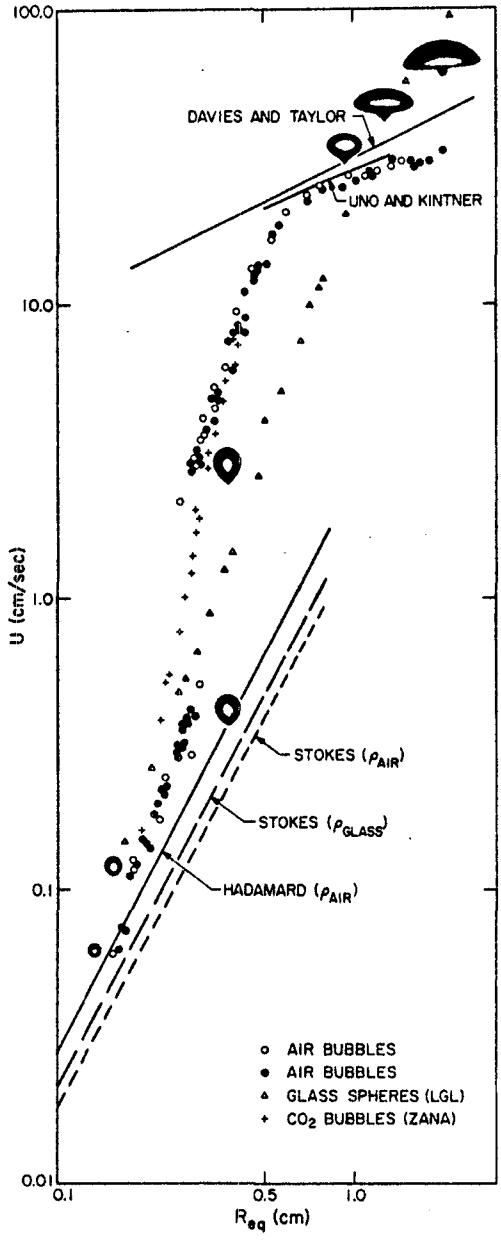

Figure 1: Terminal velocity and bubble shape as a function of equivalent radius for gas bubbles in a viscoelastic liquid: The Stokes and Hadamard lines are calculated for a Newtonian fluid with viscosity equal to that of the test fluid at zero shear-rate. The test fluid is 1% Separan AP30 in water.

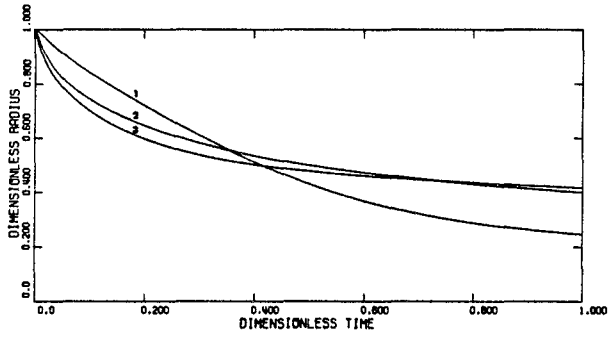

Figure 2: The effect of the memory relaxation time λ on the rate of dissolution of a gas bubble in a viscoelastic fluid: case 1, $\lambda = 0.1$; case 2, $\lambda = 0.5$; case 3, $\lambda = 1.0$ (from reference 33).

"A STUDY OF THE DEFORMATION AND BREAKUP OF ACCELERATING WATER DROPLETS"

James M. Reichman
University of California, Lawrence Livermore Laboratory, Livermore, California
and
Samuel Temkin
Rutgers University, New Brunswick, New Jersey

ABSTRACT

An experimental study of the deformation and breakup of water droplets induced by weak shock waves was conducted in a horizontal shock tube. Droplets with diameters between 350 μm to 750 μm were allowed to fall through the tube and were exposed to the lateral flow created by a shock wave. The shock strengths chosen resulted in droplet deformation leading to either oscillation or breakup. The droplet deformation and breakup were recorded using high speed photographic techniques capable of interframe times as short as 10 μs.

The Weber number range studied was between 2 and 8. In this range breakup occurred by the "bag" type mode. The deformation leading to this type of breakup was studied in detail and the process was divided into four stages. Each stage is described in terms of the physical changes of the shape of the droplet and a description of the flow causing the deformation is presented. The deformation leading to breakup was compared to the deformation leading to oscillation. The comparison of the two types of deformation resulted in the establishment of a breakup criteria based on a critical droplet thickness, where the critical thickness is defined as the deformed droplet width which, when measured, can predict if a droplet will either break up or oscillate.

A simple model was developed which predicts the lowest velocity that will cause a droplet to break up. The model was based on the experimentally observed critical thickness. The critical velocities predicted by the model were found to be within the experimental accuracy of existing data.

Introduction

In physical processes droplets are frequently subjected to a suddenly imposed flow field which has been initiated by the passage of a shock front. The manner in which the droplets respond to the dynamic forces of the flow field is often of importance to the process involved. For example, in a combustor the response of the fuel droplets to the detonation shock is of importance.[1] If droplet breakup occurs, better fuel atomization is achieved and higher combustion efficiencies are realized. When a space vehicle traveling at supersonic speeds enters a cloud the impaction of droplets on the nose cone can severely damage the vehicle.[2, 3] However, when the droplets enter the region behind the bow shock, breakup is possible and damage can be avoided. In a cloud, if a large droplet is shattered by a thunderclap it will produce several micron sized droplets which may result in an increased rate

of coalesence in the cloud. The above examples point to the need of understanding the mechanism of droplet breakup. By understanding what causes the breakup of a droplet, it may be possible to accurately model breakup and to predict when it will occur. To understand this phenomena it is necessary to conduct experimental studies which yield an accurate time history of deformation leading to either oscillation or breakup.

The type of response exhibited by a droplet when acted upon by an imposed flow field depends on the ratio of the dynamic forces trying to deform the surface to the surface tension force which resists deformation from a spherical shape. The ratio of these two forces is defined as the Weber number, $We = \rho_l Uo^2 R / \sigma$, and is used to characterize the droplet response to a flow field. In the above expression, ρ_l is the fluid density, Uo the flow velocity, R the droplet radius, and σ the surface tension. When We is small, of the order of 0.1 or less, the droplet will remain spherical. For Weber numbers above 0.1, but below a critical value, the droplet oscillates. The upper value for this range is called the critical Weber number, We_c, and defines the upper limit for which droplet breakup will not occur. Above this Weber number, the droplet will breakup, first by the "bag" type of breakup and then, as the Weber number increases, by the shattering type of breakup.

Droplet breakup has been studied previously with the objective of predicting the critical velocity for breakup, predicting breakup time, or determining the mechanism of droplet shattering. Lane,[4] and Hanson, Domich, and Adams[5] have studied breakup and presented experimental correlations for the lowest critical breakup velocity around a droplet. The lowest critical breakup velocity is that which causes the "bag" type mode of breakup. The breakup velocities, U_c, for droplets of the same liquid are represented by the relationship $U_c^2 D$ = constant in which D is the droplet diameter. The results of the two studies differ, with Lane obtaining consistently lower critical velocities than those found by Hanson, et al. The reason for this discrepancy will be discussed later.

Various studies of droplet shattering have been conducted. Taylor[6] studied the breakup of droplets due to shock waves and the breakup of droplets accelerating in a uniform flow field.

Engel[7] studied the response of droplets to a flow, where the Weber number was sufficiently high to shatter the droplet. Engel described the change in shape of a droplet as it shattered and divided the changes into stages. Engel found that the droplets flatten, then reach a plateau where the flattening ceases and then the droplet shatters. The plateau is attributed to surface tension acting against further flattening.

Simpkins and Bales[8] examined the droplet breakup for various Weber numbers. For $7 < We < 50$ they found droplet breakup occurred by the "bag" type mode. At higher Weber numbers droplet shattering occurred. Shattering was attributed to Taylor instabilities growing along the droplet surface rather than boundary layer stripping.

Waldman, Reinecke, and Glen[9] studied droplet shattering by means of x-ray photography. In this manner, they could see inside the droplet mist and determine when the droplet had disintegrated. From these experiments they obtained a droplet breakup time for various Weber numbers.

Analysis of droplet breakup and deformation have also been made. Hinze[10] developed a linear model based on the dynamic pressure exceeding the surface tension at the stagnation point by a factor, determined experimentally. His model allows only small variations from the spherical droplet shape. Gordon[11] developed a model to predict breakup time for a droplet breaking in the "bag" type mode. From this model he predicts a droplet diameter for a given velocity, below which breakup will not occur. Harper, Gruber and Chang[12] have developed a theory based on perturbation methods. Their model predicts that for high Weber number situations the droplet surface is susceptible to instabilities. When the growth rate of the instabilities is much faster than the aerodynamic deformation the instabilities cause the droplet to shatter. The instabilities are assumed to be Taylor instabilities. The agreement, between the theories and experiment in all the above studies is, however, not good.

From previous work, it can be seen that detailed information concerning the mechanisms of the "bag" type breakup is lacking. No studies of the change of the droplet shape similar to that of Engel, for shattering, have been made. Furthermore, the critical point, when it is certain that a droplet will breakup, has not been determined. The objective of this study was to characterize droplet deformation leading to breakup and to establish the necessary shape condition to determine if a droplet will oscillate or breakup. Based on this criterion, a simple model was developed which appears to correctly predict the critical velocity for breakup.

Experiment

(i) Apparatus

A shock tube was used to create the desired uniform flow conditions. The tube was constructed of seamless aluminum tubing having an inside diameter of 6.35 cm. The shock tube consisted of four sections: a 183 cm driver section; a 170 cm section located upstream of the test section; a 35.6 cm interchangeable test section; and a 173 cm section downstream of the test section. The test section had a viewing port and light window to permit direct light illumination located 180° apart. Both the viewing port and the light window were covered with thin glass. The test section was designed to permit a stream of droplets to fall unimpeded through the center of the test section. The shock tube was supported by means of steel rails and rigidly held in place by U-bolts. The mounting system assured accurate alignment of the shock tube and a minimum transfer of vibration along the tube wall. The shock tube is shown schematically in Figure 1.

The diaphragms used to create the shock waves were of 0.019 mm thick cellophane. The cellophane was supplied by FMC Corporation, American Viscose Division. The diaphragm was held between two concentric circular pieces of aluminum which could then be fitted over the shock tube. The holder caused the cellophane to be stretched uniformly resulting in uniform rupture of the diaphragm even at pressure differences as low as 1.25 psia. The diaphragm was ruptured by a needle located in the driven section of the shock tube. Positioning of the needle in the low pressure side eliminated the problem involved in sealing the opening for the needle.

The shock propagation velocity was measured by two time-of-arrival pressure transducers and associated electronic equipment shown schematically

in Figure 1. The transducers, Atlantic Research type LD-15, were located at equal distances upstream and downstream of the test section and were separated by a distance of 74.4 cm. The pulse produced by each transducer was amplified by a Hewlett Packard type 465A amplifier. The amplified signals were then fed into the start and stop gates of a Hewlett Packard 550 MHz Timer/Counter Model # 5327A where the time interval between the two transducers was recorded to an accuracy of ± 1 μs. The rise time of each transducer was 1 μs assuring accurate triggering of the timer upon the arrival of the shock front at each transducer.

The droplets were produced in a continuous uniform stream by means of an oscillating capillary device. Jet perturbation was achieved by means of flow oscillation. Suitable flow perturbation was achieved by means of an immersible pump powered by an audio oscillator. The pump (Edmund Scientific Company, Catalog # 60,307) was driven by a Hewlett Packard Audio Oscillator Model #200AB. The droplets were uniform in size, equally spaced, and had a velocity component only in the vertical direction.

The liquid jet was produced by forcing the liquid through a capillary tube with compressed air. The droplet diameters produced ranged between 350 μm to 750 μm for water. The driving pressure for all jets was that necessary to produce an approximately 1.5 cm long laminar portion in an undisturbed jet.

(ii) Photography

In order to study deformation, a series of backlighted pictures taken at 10 μs intervals were needed so that an almost continuous history of the change of the droplet shape could be obtained. This time interval corresponds to a framing rate of 10^5 pictures per second if a high speed cinephotographic technique was used. This rate far exceeded the speeds attainable with equipment available to us. An alternate approach was to take a single picture per test by means of a continuous delay single flash system. If the shock strengths were identical and droplet diameter the same then an equivalent framing rate of 10^5 fps could be achieved. A schematic of the system is shown in Figure 1.

A General Radio type 1541 Multiflash Generator functions as a continuous delay unit when it is used to produce a single flash. The unit is capable of producing a single flash after a preset time delay which can be controlled by means of the flash interval control. The delay after the initial triggering can vary from 10 μs to 1.6 seconds in steps of approximately 5 μs or larger. With this unit providing both the delay system and flash triggering system, the proper time interval for each deformation picture was conveniently obtained. The illumination for the pictures was supplied by a General Radio Strobotac type 1538A. Flash duration was 0.8 μs measured at 1/3 peak intensity. The short flash duration minimized blurring for each picture.

The multiflash unit was triggered by the amplified pulse of a pressure transducer located 0.6 cm upstream of the initial droplet position. The transducer signal was amplified by Hewlett Packard Type 465A amplifier. The amplified transducer pulse represented an approximately 30 μs delay after the shock front reached the droplet. The value of the flash delay was recorded by means of a Hewlett Packard Timer-Counter Model # 5327A. The delay was measured from the time of arrival of the shock front at the pressure transducer to the time when the stroboscope received its triggering pulse. The time interval was measured to within ± 1 μs of the actual delay.

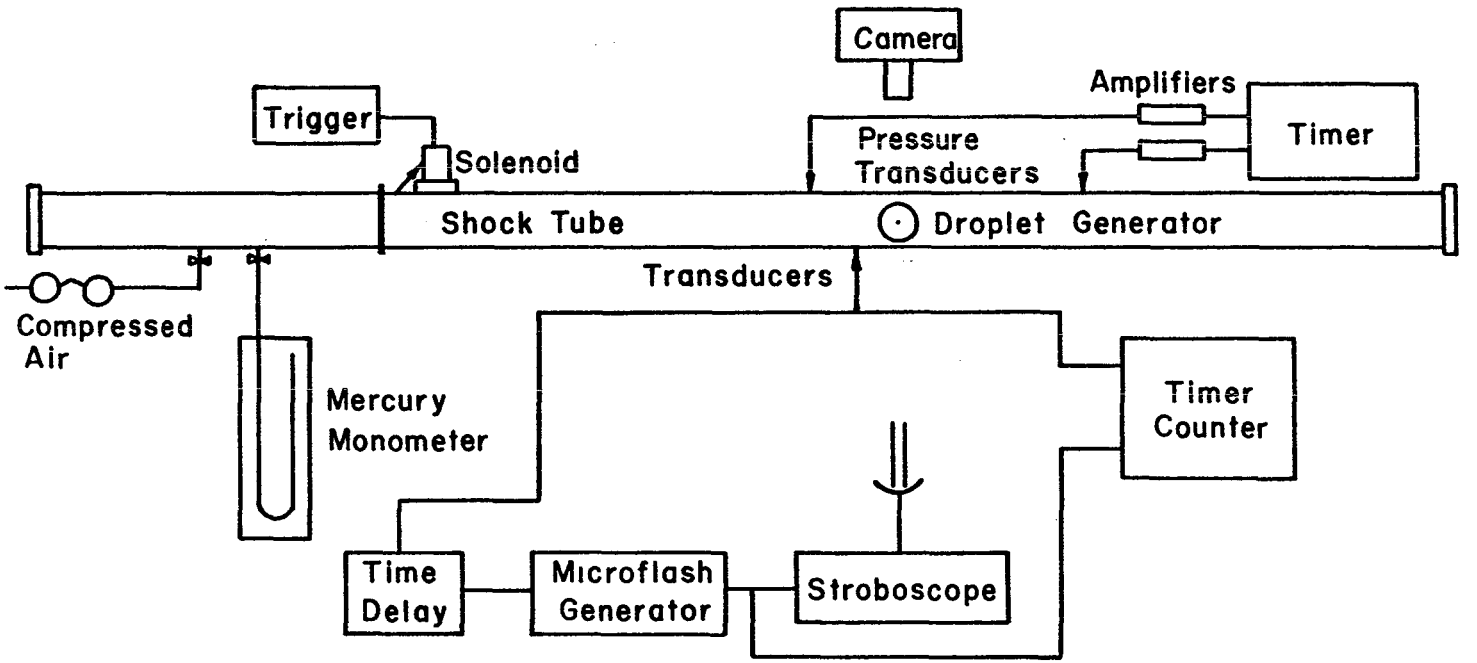

Figure 1.
Experimental Apparatus

Results and Discussion

Observations were made of the response of droplets to various strength shocks. The droplets studied were both breaking and oscillating drops. Of principal concern in this study was the change in shape of the droplets due to the shock-induced flow field. Therefore, the droplets were studied independent of displacement. Several series of pictures were obtained for various combinations of droplet diameter and shock-induced flow velocity. A typical series of deformation pictures for a breaking droplet are shown in Figures 2-4. The droplet shapes in these pictures are assumed to be axisymmetric because of the nearly axisymmetric flow field about each droplet. The following measurements and discussions refer to a meridian plane of the droplet.

The negatives for each series of pictures were examined with an optical comparator using a 10X magnification. In this manner, the change of shape of a droplet from that of a sphere could be measured. The front and rear of the droplet did not deform in a similar way. However, for uniformity, measurements were made of the deformed droplet height, a, and the deformed droplet width, b. Some results of the deformation measurements are shown in Figure 5. In these figures the droplet height, a, normalized with the diameter, D, is plotted versus real time for several series of pictures.

From examination of the deformation pictures and from the results of the measurements, it was possible to arrive at some conclusions about droplet deformation particularly, deformation leading to "bag" type breakup. With the understanding obtained from the deformation curves, it was possible to examine the deformation pictures and to establish four stages of breakup as well as a breakup criteria.

Each set of curves presented in Figure 5 represent the deformation of equally sized droplets subjected to various flow velocities. It is seen in Figure 5 that when U_o = 2640 cm/sec, the 710 μm diameter droplets do not breakup, but begin to oscillate. This curve will be discussed later; the concern of this discussion is the deformation leading to "bag" type breakup.

As a general description, one can simply say a droplet flattens, becomes hollow, and then bags outward. This would, however, oversimplify droplet breakup. From examination of various series of droplet breakup pictures, it was possible to describe breakup in a more accurate manner. Droplet breakup was divided into four stages, and each stage was described in physical terms. The end of the fourth stage was reached when the bag, formed by the droplet, was broken. The time, after the passage of the shock wave, for the droplet to reach this point is defined as the breakup time. The four stages of breakup are described below. In all cases, the flow is from left to right. The flow is the result of the passage of a shock wave and is, therefore, similar to the flow about a sphere set impulsively into uniform motion. Dennis and Walker[13] and others have shown that separation occurs almost immediately after the start of impulsive motion. All of our photographic observations were made at times when the flow had already become separated about the back of the droplets.

Stage 1 is characterized by the immediate flattening of the rear of the drop as in Figure 2 when t = 54 μs. The flat portion continues to grow until it reaches approximately one half of the initial droplet diameter. While the back of the drop is flattening, the front surface remains spherical. However, its

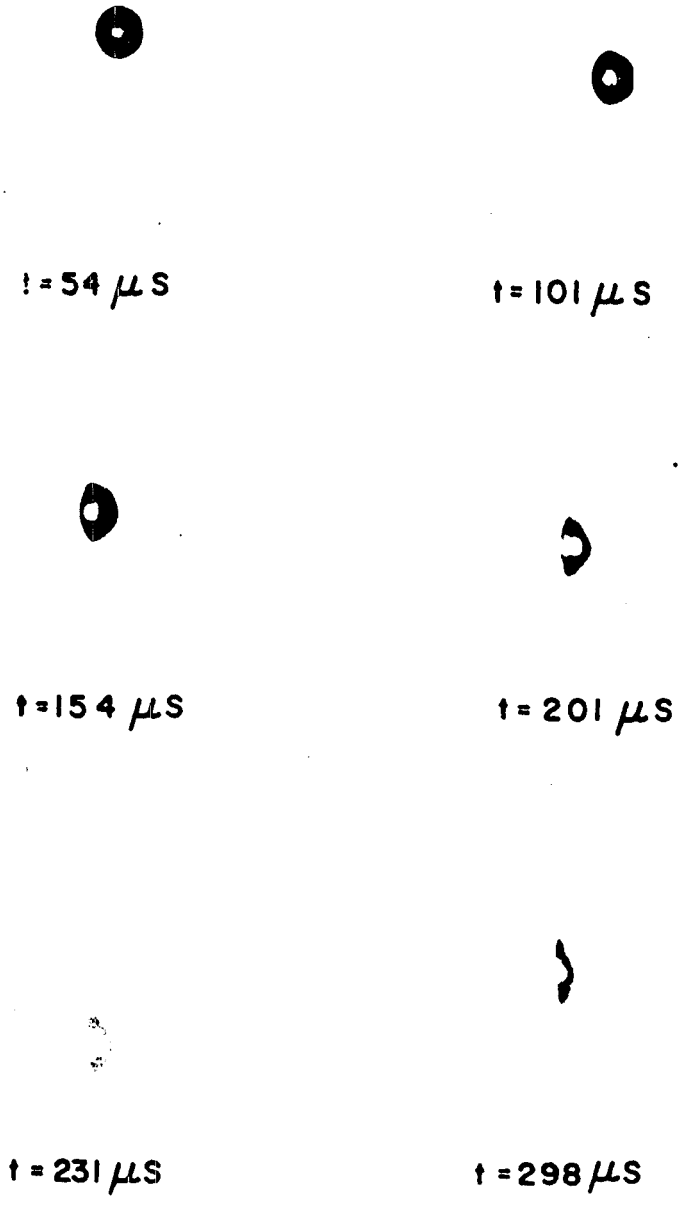

Figure 2.
Droplet Deformation Leading to
Breakup t = 54μs to t = 298μs

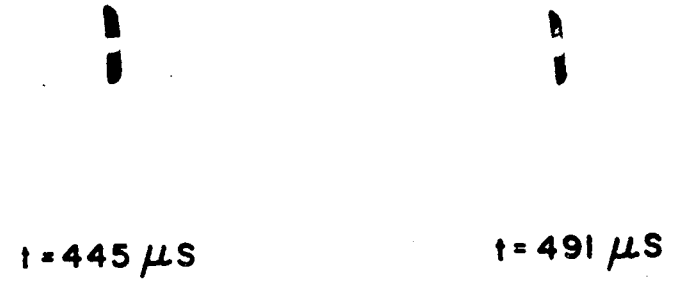

Figure 3.
Droplet Deformation Leading to
Breakup t = 34μs to t = 643μs

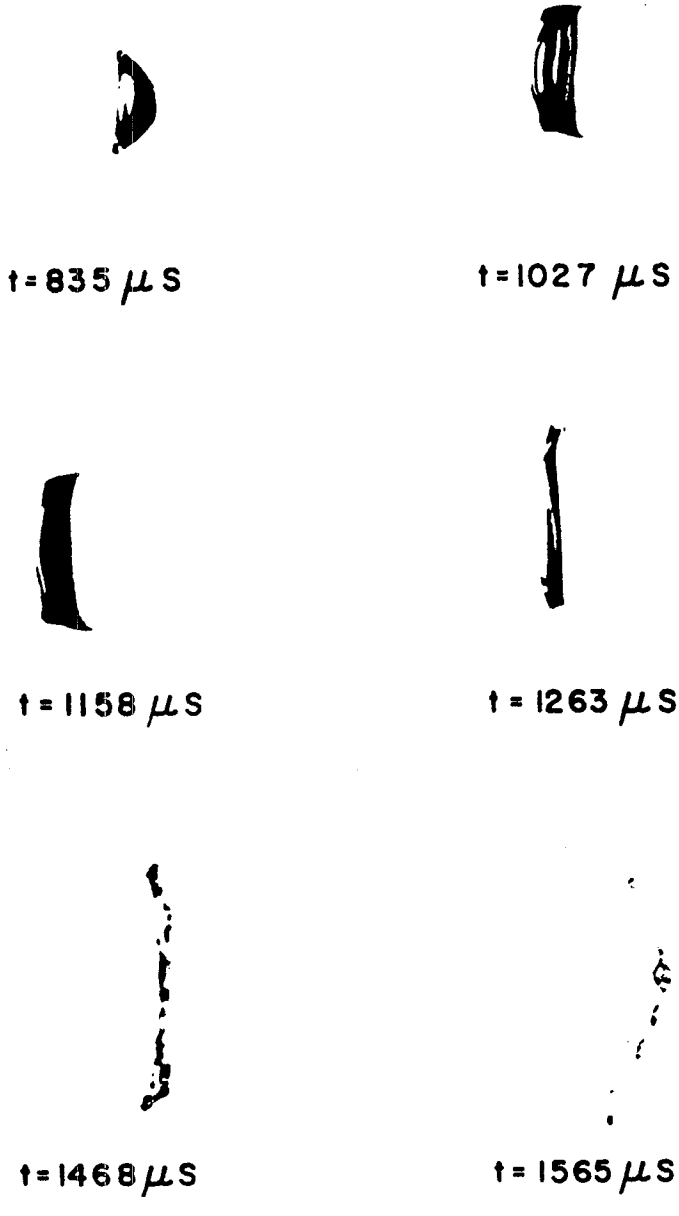

Figure 4.
Droplet Deformation Leading to
Breakup t = 835μs to t = 1565μs

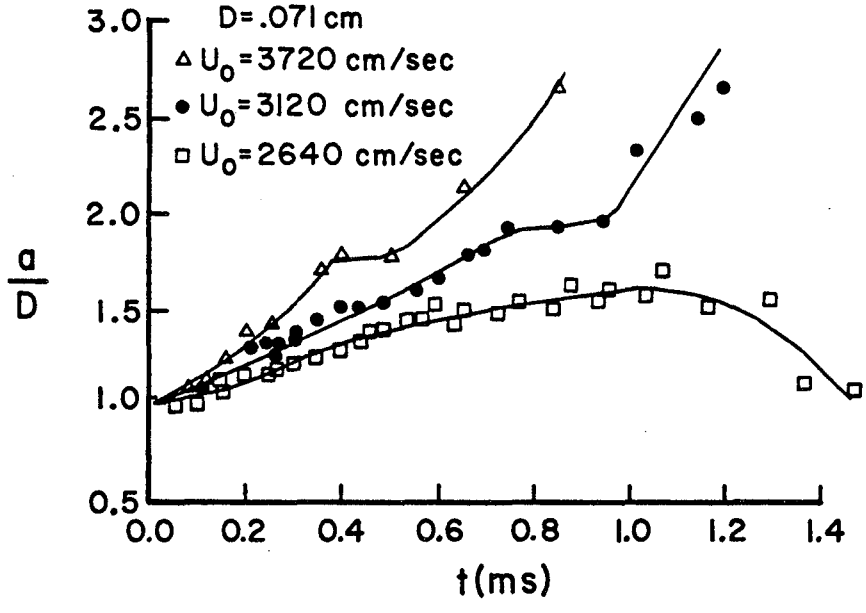

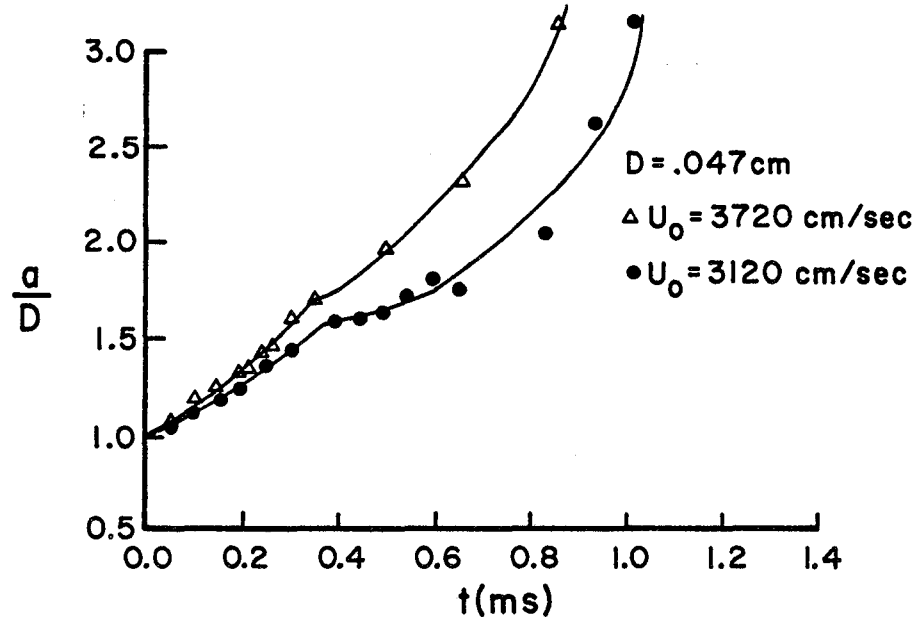

Figure 5.
Droplet Deformation Curves

radius of curvature increases. The end of this stage is reached when the sides of the droplet become straight. Stage 1 lasts approximately 10 % of the total breakup time. The overall effect of this stage is a general flattening of the droplet.

During Stage 1, the shock-induced flow cannot follow the droplet shape and separates from the droplet. The separated flow region is a low pressure region at the rear of the droplet and the flow velocity in this region is principally in the opposite direction of the main flow. However, the shock wave initially imparts an acceleration of about 10^8 cm/sec^2 to the droplet. The acceleration is opposed by the droplet mass which results in a pressure gradient in the droplet with the highest pressure in the front. The pressure at the rear of the droplet approximately equals the pressure in the separation region. To adjust to this situation, the liquid at the separation region must have an infinite radius of curvature or, it becomes flat. As time progresses, the flat portion grows upward from the rear stagnation point. The flattening of the drop is principally controlled by surface tension forces while the sole effect of the dynamic force is to increase the radius of curvature of the front surface.

The onset of the second stage of deformation is characterized by the appearance of a ridge at the top of the front surface, separating the front from the sides. The ridge continues to grow in height and as it grows it has the effect of increasing the radius of curvature of the front surface. As the ridge of the droplet becomes higher, the front surface becomes flat except for a small spherical region about the stagnation point. While the front surface is changing shape, the rear portion of the droplet loses its flatness and gives the appearance of being drawn toward the front surface. At the end of this stage, the rear portion of the droplet becomes flat over its entire height. The end of Stage 2 of the deformation process occurs when the droplet appears to have deformed by being "squeezed" symmetrically by the flow field. Stage 2 lasts approximately 20 % of the total breakup time. The overall effect of Stage 2 is to flatten the droplet to its minimum thickness. This stage corresponds to t = 154 μm to t = 395 μs in Figures 2 and 3.

In the second deformation stage, the droplet is more directly reacting to the flow field about the droplet than during the first stage. During this stage, the recirculating flow behind the droplet begins to bring mass from the back of the drop towards the front. At the same time, the flow about the front surface brings mass to the top and bottom of the front causing the front surface to assume a larger radius of curvature. This movement of mass from the front and rear of the droplet causes the ridge to form and to grow in height. As the ridge continues to grow, the recirculated flow possesses a larger velocity component in the negative x direction than the velocity in the positive x direction possessed by the incoming flow which is moving almost vertically along the front surface. This flow situation causes the ridge to be pushed into the direction of the flow resulting in the front surface becoming flat except for a spherical region about the stagnation point. Finally, the ridge is forced forward, and the front of the droplet appears flat.

Stage 3 corresponds to the flat portion of the curve in Figure 5. During this stage of deformation, the droplet goes through no noticeable external changes, all changes are internal. In this stage, the droplet appears to have a flat front. This results from the ridge formed during Stage 2 being forced forward. During this stage the region around the spherical portion of the droplet

becomes deeper and a greater percentage of the droplet mass becomes located at the spherical area about the stagnation point and at the edge of the flattened droplet. At the end of this stage, the rear surface of the droplet begins to move outward. Stage 3 represents approximately 12% to 15% of the droplet breakup time. The overall effect of Stage 3 is to transform an almost disk-like droplet into a hollow bowl with a hemispherical lump of mass located at the center.

The third stage of deformation is a stage of internal deformation of the droplet. Once the flow causes the ridge to be pushed out past the front surface it becomes inevitable from observation that the droplet will ultimately breakup. When the external flow approaches the spherical region at the stagnation point, the flow moves around the sphere and is then deflected upward by the solid rear surface. The flow, however, cannot move around the droplet rim formed from the ridge and must bend into the direction of U_o. This results in a circular flow region between the center sphere of mass and the rim of the droplet. The circular flow pattern scours mass from the back internal surface of the droplet until the back surface becomes so weak it begins to move in the direction of U_o. The dynamic force then causes the onset of bagging.

Stage 4 is the bagging deformation stage of the drop. This stage begins when the rear surface of the droplet moves in the direction of U_o. The initial movement of the rear surface gives the drop a lenticular shape with the flat portion facing the flow. The rear of the droplet quickly moves outward giving the droplet the appearance of a bag with a heavy rim. In the center of the bag a stem may appear. The stem is the result of the mass at the center of the drop being so large that it cannot move at the same speed as the bag. As the bag moves outward, the mass is stretched giving the appearance of a stem. Droplet rupture occurs on the bag surface, breaking it into small droplets which are swept along with the flow. The stem and rim breakup into droplets at a later time. Stage 4 represents approximately 50% of the total breakup time.

In Stage 4, the rear surface of the droplet has become weakened in the region about the spherical mass at the stagnation point. The aerodynamic force causes the rear region to move in the direction of flow while the heavy rim remains relatively still. As the rear of the drop is forced outward, the rear surface becomes weaker and as a result the bag moves faster and becomes stretched. The bag surface when stretched becomes susceptible to instabilities and breaks. The rim and stem are also broken by flow induced instabilities at a time after breakup.

The four stages discussed above describe droplet deformation leading to "bag" type breakup. By comparing the deformation of a breaking droplet to the deformation leading to droplet oscillation, it was possible to establish a criteria to determine if breakup occurs. The deformation of an oscillating droplet is shown in Figure 5 and corresponds to U_o = 2640 cm/sec. This particular oscillating droplet is subjected to a flow velocity approximately corresponding to the critical velocity for a 710 μm droplet. Oscillating droplets were found to deform in a manner similar to that described for a breaking droplet in Stage 1 and 2. However, once the droplet reaches its minimum thickness, b, corresponding to the maximum value of a/D, it rebounds and approaches a spherical shape, then overshoots this shape until it reaches a minimum value of a/D. The droplet then oscillates about its original spherical

shape. From our observations on both types of deformation, it was shown that the minimum thickness, b, of the droplet is the first clearly noticeable difference between a breaking and oscillating droplet and can, therefore, be used as the basis of a breakup criterion.

In Figure 5, the oscillating droplet reaches a maximum value of a/D equal to 1.6. This corresponds to a droplet subjected to a flow velocity just below the critical velocity. For the breaking droplets represented in Figure 5, the droplet thickness, b, corresponding to the flat portion of the curve, is less than the value corresponding to b for the oscillating droplet. In Figure 5, the curve corresponding to U_o = 3120 cm/sec for the 470 μm droplet represents a droplet subjected to a flow velocity just above the critical velocity. From this curve, it is seen that the minimum thickness of the droplet, corresponding to the flat portion of the curve, is a/D equal to 1.6. It was, therefore, determined that if a water droplet attains a thickness corresponding to a height to diameter ratio of about 1.6 or greater, the droplet will breakup. Using this criteria, it would not be necessary to follow droplet deformation through to breakup rather the value of a/D reached in the second stage of deformation can be used to determine if breakup occurs. The concept of a critical droplet thickness corresponding a/D was used to develop a model that can predict breakup for a droplet of a given liquid. This model is presented in the next section.

Breakup Model

When a droplet is deformed by a uniform flow field, caused by a shock wave, the front and rear deformation is not symmetric. However, when a bursting or oscillating droplet is deformed, it reaches a stage of deformation when the droplet appears to have been symmetrically deformed. At this stage, a nonbursting droplet will start to regain its spherical shape due to surface tension, while the front surface of the bursting droplet will continue inward and eventually the droplet will breakup by the "bag" type mode. By studying droplets of a given liquid both above and below the critical value of velocity for breakup for various droplet diameters a critical thickness can be determined for the droplet. If the droplet is compressed to a smaller thickness than the critical thickness it will breakup, but if it has a larger thickness it will oscillate. Therefore, by artificially "squeezing" a droplet to the critical thickness and at a time t = 0 imposing a uniform flow over the droplet we can, by examining forces on the fluid at the stagnation point of the droplet, determine whether the flow velocity is sufficient to cause breakup. If the flow velocity is less than the critical velocity, the surface tension force will push the front surface outward. If the flow velocity is greater than the critical velocity, the flow will push the front surface inward, and this would imply the droplet will breakup.

The model considers a droplet in a uniform flow field that has been deformed from its spherical shape. The droplet is assumed to have been deformed as an oblate spheroid with the axis of symmetry parallel to the flow. A cross section of the model is shown in Figure 6. The distance $Ro\xi$ is the amount of squeeze imparted to the droplet initially. By examining an element of fluid at the stagnation point and determining its motion due to the forces acting on the element a critical velocity for breakup is determined.

Consider the fluid in the vicinity of the forward stagnation point. It is assumed that some of the fluid will move as a solid body in response to the applied forces. It is further assumed that the pressure in the drop, acting on

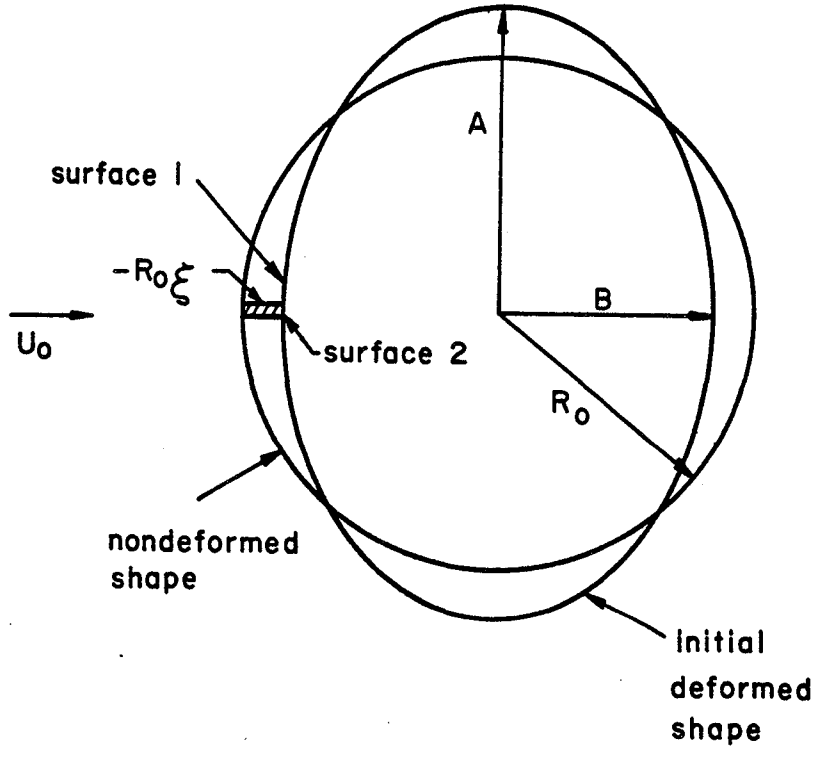

BREAKUP MODEL

Figure 6.
Droplet Breakup Model

surface 2 (see Figure 6) is the order of the internal pressure of a spherical droplet at rest, or

$$P_2 = P_o + \frac{2\sigma}{R_o}, \qquad 1$$

where P_2 = the internal pressure of the droplet.

The external pressure distribution on the front surface is equal to that about a sphere of radius, R. By limiting the surface of interest to an infinitesimal height about the stagnation point the external pressure simplifies to

$$P_e = P_o + \tfrac{1}{2}\rho_1 U_o^2, \qquad 2$$

where U_o is the free stream velocity and ρ_1 is the density of the gas. With the result of Equation 2, the pressure on the external surface 1 is given by

$$P_1 = P_e + \frac{2\sigma}{R_1},$$

where $R_1 = R_o^3 / B^2$.

Making use of Equation 2 we find the pressure difference on our infinitesimal element about the stagnation point to be

$$\Delta P = P_1 - P_2 = \tfrac{1}{2}\rho_1 U_o^2 + \frac{2\sigma}{R_o}\left(\frac{B^2}{R_o^2} - 1\right) \qquad 3$$

Equation 3 gives the pressure difference on the element in the X-direction. The pressure acting on the element in the Y-direction is considered to be zero, since the height of the element is considered to remain constant.

Integration of the equation of motion of a fluid in a particle fixed coordinate system in the X-direction yields

$$\rho_2 \frac{dU}{dt} V = -A\Delta P - \frac{d^2 x\, d}{d t^2} V \qquad 4$$

where V = ABc, is the volume of fluid assumed to move as a solid body, A is the surface area and Bc is its length. The other quantities appearing in Equation 4 are $B = R_o(1 + \xi)$, $U = dB/dt$ = velocity of volumetric element of fluid and $R_o \xi$ = change of distance from the center of droplet to the front surface due to deformation. Substitution into Equation 4 gives

$$\frac{d^2\xi}{dt^2} = -\tfrac{1}{2}\left(\frac{\rho_1}{\rho_2}\right)\frac{U_o^2}{CR_o^2}(1 + \xi) - \frac{2\sigma}{CR_o^3\rho_2}\left(\frac{(1+\xi)^2 - 1}{1+\xi}\right) - \frac{U_o^2}{\rho_2 R_o^3} K. \qquad 5$$

In Equation 5, the experimental results obtained by Simpkins and Bales[8] and the present study are used, which indicates that initially the particle displacement can be approximated by

$$X_d = K U_o^2 t^2 / R_o,$$

where $K \approx 10^{-4}$.

Equation 5 can be solved numerically by means of a fourth-order Runga-Kutta formula modified by Gill. The equation carries one constant, C, which must be evaluated by other means. If Equation 5 is solved for the case of a stationary drop, by making U_o equal to zero, and the resulting equation linearized it is found that

$$\frac{d^2\xi}{dt^2} = -\left(\frac{4\sigma}{CR_o^3\rho_2}\right)\xi. \qquad 6$$

This equation represents the harmonic vibrations for the drop. If C = .5 the circular frequency equals that of the frequency of the lowest mode of vibration of a spherical droplet.

An examination of the effect of the constant C in the solution of equation 6 showed that it principally effected the period of oscillation of the drop, not the amplitude of oscillation which change by less than 5% when C was varied from .125 to .75. The value of C = .5 was therefore adopted so that the model represents the vibration of a drop when U_o goes to zero. Equation 5 can now be solved once the initial conditions are established.

Our model, as stated previously, is based on a critical value of ξ. This initial value we shall call ξ_c. As stated when time t = 0 the droplet has the thickness $\xi = \xi_c$ and as the velocity field is imposed the front surface will respond accordingly. When the velocity is equal to the critical velocity the front surface does not move therefore the slope at this point, ξ', is equal to zero. To further restrict the zero slope criteria we impose the condition that ξ' remains zero or $\xi'' = 0$. Applying this second condition to equation 5 and combining terms equation 5 becomes

$$U_c^2 = -\frac{2\sigma}{R_o}\left(\frac{(1+\xi_c)^2 - 1}{\frac{1}{2}\rho_1 + (1+\xi_c)K}\right) \qquad 7$$

where U_c and ξ_c are the critical velocities and displacements. Examination of the denominator in Equation 7 shows the second term to be approximately an order of magnitude smaller than the first term and is neglected. Equation 7 can then be transformed into

$$U_c^2 D = \frac{8\sigma}{\rho_1}\left|\xi_c\right|\left(2 - \left|\xi_c\right|\right) \qquad 8$$

where ξ_c must always be negative.

Equation 8 can be used to determine the critical velocities for droplets of different fluids, if ξ_c is known. Our experiments have shown that ξ_c is the same for a wide range of diameters of droplets if the fluid is the same. The time to reach this value will be different owing to the change in period due to the change in size but the value reached will be the same. The critical thickness need only be found once for each fluid under consideration.

In our experiments the critical value of $\left|\xi_c\right|$ was found to be .56. Substitution into equation 8 yields

$$U_c^2 D = 3.92 \times 10^5$$

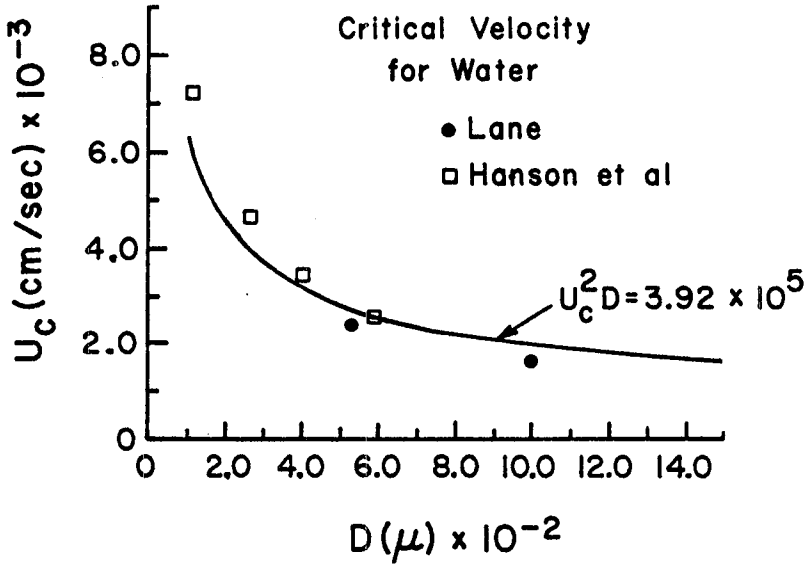

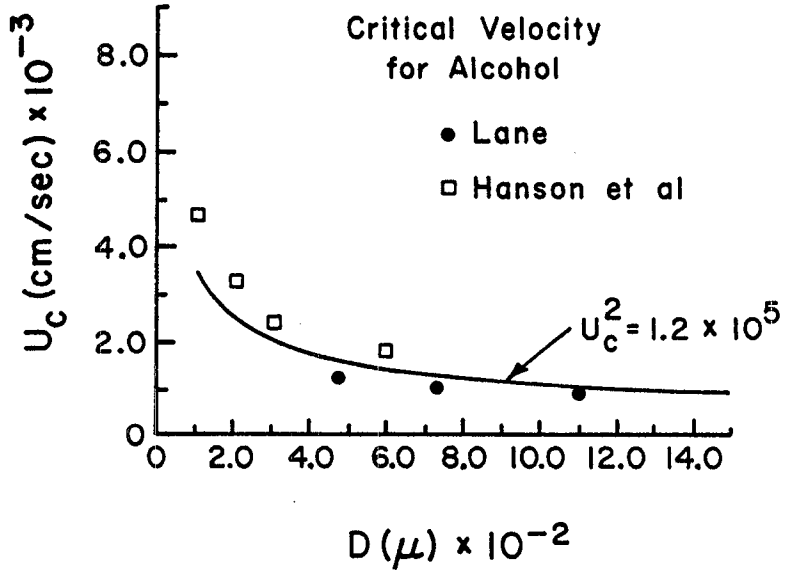

Figure 7.
Critical Breakup Velocity for
Water and Alcohol

for a water drop in air. The units of U_c and D are in the cgs system. This equation is plotted in Figure 7. Along with this curve are some experimental points obtained by Lane and Hanson et al. It can be seen that the curve fits the data points as well as the experimental relationships determined in the above studies.

By using the value of ξ_c for water and applying it to alcohol, Equation 8 will yield the curve plotted in Figure 7. Also shown there are the experimental data of Lane and Hanson [5] et al.

Examination of Figure 7 shows that our curves more closely approximate the data found by Lane [4]. This discrepancy may be related to the manner Hanson et al [5] supported their drops. The drops were supported by acoustic radiation pressure which was never turned off. The ratio of the acoustic radiation pressure to the dynamic pressure is of the order 10^{-2} [14]. The acoustic pressure can therefore, not be ignored when examining the pressure at the edges of the droplet. This could have resulted in an additional cohesive force on the drop which then required a larger velocity to cause droplet breakup.

Conclusions

Observations of the deformation of oscillating and breaking droplets caused by the flow field associated with a shock wave are summarized below.

1. The deformation leading to breakup by the "bag" type mode of breakup can be divided into four basic stages of deformation: Stage 1, surface tension controls the droplet shape; Stage 2, the flow around the droplet causes it to change shape eventually giving the droplet the appearance of being "squeezed"; Stage 3, the droplet goes through internal changes which cause it to become hollow; Stage 4, the flow pushes the rear of the hollowed droplet outward causing it to form a bag and then burst.

2. An oscillating and a breaking droplet will be initially deformed in a similar manner. However, the breaking droplet will be compressed to a greater extent. This observation leads to a breakup criterion based on a critical value of a/D which can be related to a critical droplet thickness, b.

3. Using the critical thickness as a criterion for breakup, a model was developed which predicts the critical breakup velocity for any given droplet. The critical thickness found for water was substituted into the model and predicted the relationship $U_c^2 D = 3.92 \times 10^5$ for water. Using the same critical thickness for alcohol droplets the model predicts $U_c^2 D = 1.2 \times 10^5$. Both expressions agree closely with existing experimental data.

Acknowledgments: This work was supported in part by the National Science Foundation under grant NSF GK-4007.

BIBLIOGRAPHY

1. Ranger, A.A. and Nicholls, J.A., "Atomization of Liquid Droplets in a Convective Gas Stream," International Journal of Heat and Mass Transfer, Volume 15, 1203 (1972).

2. Simpkins, P.G., "On the Distortion and Breakup of Suddenly Accelerated Droplets," AIAA Paper No. 71-325, 12th Annual Structures, Structural Dynamics and Material Conference, (1971).

3. Aeschliman, D.P., "An Experimental Study of the Response of Water Droplets to Flows Behind Plane Shock Waves," SCRR, 710 540 (1971).

4. Lane, W.R., "Shatter of Drops in Streams of Air," Industrial and Engineering Chemistry, Volume 43, 1312, (1951).

5. Hanson, A.R., Domich, E.G., and Adams, H.S., "Shock Tube Investigation of the Breakup of Drops by Air Blasts," The Physics of Fluids, Volume 6, 1070 (1963).

6. Taylor, G.I., Scientific Papers, Volume 3, 457, Cambridge University Press.

7. Engle, O.G., "Fragmentation of Waterdrops in the Zone Behind an Air Shock," Journal of Research of the National Bureau of Standards, Volume 60, 245 (1958).

8. Simpkins, P.G. and Bales, E.L., "Water-Drop Response to Sudden Accelerations," The Journal of Fluid Mechanics, Volume 55, 692 (1972).

9. Waldman, G.D., Reinecke, W.G., and Glen, D.C., "Raindrop Breakup in the Shock Layer of a High Speed Vehicle," AIAA Journal, Volume 10, 1200 (1972).

10. Hinze, J.O., "Forced Deformation of Viscous Liquid Globules," Applied Scientific Research, Volume A1, 263, (1949).

11. Gordon, G.D., "Mechanism and Speed of Breakup of Drops," The Journal of Applied Physics, Volume 30, 1759 (1959).

12. Harper, E.Y., Gruber, G.W., and Chang, I.D., "On the Breakup of Accelerating Liquid Drops," Journal of Fluid Mechanics, Volume 52, 565 (1972).

13. Dennis, S.C.R. and Walker, J.D.A., "Numerical Solutions for Time-Dependend Flow Past an Impulsively Started Shpere," The Physics of Fluids, Volume 15, 517 (1972).

14. Crum, L.A., "Acoustic Force on a Liquid Droplet in an Acoustic Stationary Wave," The Journal of the Acoustical Society of America, Volume 50, 157 (1971).

THE ROLE OF DROP DYNAMICS IN THE PHYSICS OF CLOUDS AND RAIN

Morris Neiburger, In Young Lee, Elena Lobl, and Lawrence Rodriguez, Jr.
Department of Meteorology, University of California, Los Angeles

Abstract

Condensation from water vapor onto nuclei in rising air produces clouds of numerous small drops having very small terminal velocities. One of the ways these small drops may grow to raindrop size is by collision and coalescence. Both theoretical computations and laboratory experiments show that the radii of uncharged drops must exceed 20 μm before they are effective collectors.

The methods of computation of collision efficiencies are discussed and the results compared with the results of experiments to evaluate the collection efficiencies of cloud drops with and without electric charges. The way these data enter into studies of the formation of rain is discussed.

QUALITATIVE DESCRIPTION OF PRECIPITATION PROCESSES

Broadly, the processes of formation of clouds and precipitation may be divided into the dynamic processes, concerned with the motions of air currents which give rise to the general conditions for the formation of clouds and precipitation, and the microphysical processes, concerned with the growth of the individual precipitation particles from gas phase by condensation and from smaller cloud particles by collision and coalescence. There is, of course, a strong interaction between the two kinds of processes. The upward motions determine the rate of cooling due to expansion and thus control the rate at which the microphysical processes go on. The release of latent heat in condensation and the drag of the particles formed affect the buoyant forces which determine the upward motion. While the dynamic processes are prerequisite to the microphysical ones, it is convenient to discuss the processes of particle growth first, and subsequently to turn to the larger scale setting in which it occurs.

It is a fact of common experience that clouds can remain in the sky for long periods without precipitating. Since clouds consist of water particles, liquid or solid, which are heavier than air, this phenomenon requires explanation. Usually it is that the particles are being sustained by the upward moving current of air that is causing the cloud to form. Sometimes the upward speed is not sufficient but the particles evaporate as they fall from the cloud base into unsaturated air and vanish into vapor in a short distance.

Measurements show that the radii of drops in nonprecipitating liquid clouds are in the range 2 to 20 μm with the modal radius usually between 5

and 10 μm. These drops have terminal velocities ranging from 0.05 to 5 cm s^{-1}, so that very slight upward flow of air would be required to offset their falling. Further, it has been shown that if drops of these sizes fall out of a cloud into air with 90 per cent relative humidity they evaporate before they go as much as one meter.

Rain drops, on the other hand, range in radii from 0.1 mm to 3 mm, with terminal velocities from 70 cm s^{-1} to 9 m s^{-1}. If the updrafts are not stronger drops this size will fall relative to ascending air and may reach the ground before evaporating, even when low humidities prevail below the clouds.

The key difference between cloud and precipitation is thus the particle size, and the central question in precipitation physics concerns the conditions under which the particles can grow to precipitation size.

The process of condensation by itself can be shown to be much too slow to explain the rates at which precipitation forms. For instance, the development from clear air to showers in the course of a summer day may occur in a matter of an hour or less. While condensation results in very rapid growth of drops to the size of average cloud drops, say 10 microns, continued growth is progressively slower, and with the number of drops which form there is not enough water vapor available for millimeter drops to be produced by condensation alone.

The two ways that cloud particles can grow rapidly to precipitation are (1) by collision and coalescence, and (2) by the three phase, or Bergeron process. The nature of the first process is obvious: if the cloud drops are not of uniform size the larger ones will fall relative to the smaller and tend to overtake and capture them. After collecting one small drop the large drop becomes larger, falls faster, and is more effective in collecting others. But as we shall see, because of the tendency for the air to carry drops around each other, there are limitations on the initiation of this process.

The three phase process is based on the fact that drops remain liquid at temperatures below 0°C, and ice crystals, if they form, are much fewer in number than the liquid drops. Since the equilibrium vapor pressure over ice is lower than that over water at the same (sub-zero) temperature, there is a strong gradient of vapor density away from the liquid drops toward the ice crystals, so that rapid transfer of water occurs from the drops, which evaporate, to the crystals, which quickly grow large compared to the pre-existing supercooled drops. The crystals fall relative to the remaining small drops and collect them. Process (2) thus may initiate process (1), and the two acting together can readily lead to the formation of precipitation-sized particles in subfreezing clouds. In warm clouds which precipitate, collision and coalescence alone must be the activating process. There is considerable evidence that even in clouds that extend upward into sub-zero temperatures frequently precipitation is initiated by the collection process.

Since not all drops that are brought together by their relative motion coalesce, the processes of collision and coalescence must be considered separately. The collision process involves the dynamics of the flow of the air

in which the drops are imbedded and the dynamics of the drops in response to the drag forces exerted by the air.

We shall first discuss briefly why condensation leads to the formation of clouds with numerous drops too small to fall as precipitation. Then we shall examine the conditions under which the collection process will initiate precipitation. Finally, we shall discuss the meteorological factors that may produce these conditions.

CONDENSATION AND THE FORMATION OF CLOUDS

While homogeneous nucleation requires vapor pressures several times the vapor pressure in equilibrium with a plane water surface, clouds form in the atmosphere with relative humidities very little above 100 per cent. This is because in the atmosphere particles of haze or dust are always present to serve as nuclei for heterogeneous condensation. These particles are predominantly in the size range 0.005 μm to 5 μm. The lower limit is due to the tendency for smaller particles to agglomerate rapidly because of Brownian motion. Unless there is organized upward motion, particles larger than one micron tend to settle out even though the effect of turbulence is to diffuse them upward.

Typically the number of particles is greatest in the smallest sizes and decrease rapidly with size. The larger ones and those composed of soluble or at least wettable materials are most favored as nuclei for condensation as liquid drops. Condensation on these nuclei takes the form of liquid drops even at temperatures below 0°C. Only a few of the particles are effective as nuclei for deposition of vapor directly in the form of ice or for freezing of liquid drops, and that only at temperatures considerably below 0°C. We refer to the latter as ice-forming nuclei (IFN) and the nuclei for condensation at slight supersaturations as cloud condensation nuclei (CCN). As indicated previously, the effectiveness of the three-phase precipitation process is due to the small number of IFN in comparison to the number of CCN. The possibility of the collection process producing precipitation arises from the fact that the varying size and composition of CCN lead to a dispersion in the size of drops produced by condensation.

The rate of growth of a single drop of radius a growing from a soluble nucleus of equivalent radius a_o, is to a very close approximation

$$\frac{da}{dt} = \frac{FD}{\rho R_v T a}\left(e - e_s(T)\, \exp\left[\frac{L\delta}{R_v T} + \frac{2\sigma}{\rho R_v T a} - \frac{n\phi m_w a_o^3 \rho_s}{m_s a^3 \rho} \right] \right) \qquad (1)$$

where F is the ventilation factor, D is the compensated diffusion coefficient, ρ is the density and σ the surface tension of the drop, ρ_s and m_s are the density and molecular weight of the solute, R_v the gas constant for water vapor, e and e_s (T) the ambient water vapor pressure and its value in equilibrium with a plane water surface at the ambient temperature T, m_w the molecular weight of water, $\delta = (L \rho a/\kappa T)(da/dt)$ is the increase in the temperature of the drop above T due to the release of latent heat of condensation L, κ is the coefficient of thermal conduction, n is the number of ions dissociated per molecule of solute, and ϕ is the osmotic coefficient. The argument of the

exponential is usually sufficiently small for the series expansion to be limited to the linear terms. In this case the growth rate can be expressed explicitly,

$$\frac{da}{dt} = \frac{\alpha}{a}\left[S - \frac{\beta}{a} + \frac{\gamma}{a^3}\right] \qquad (2)$$

where $S = e/e_s - 1$ is the supersaturation, $\alpha = F\,D\,R_v\,\kappa\,T^2\,e_s/\rho\,(R_v^2\kappa T^3 + F\,D\,L^2\,e_s)$, $\beta = 2\,\sigma/\rho\,R_v\,T$, and $\gamma = n\,\phi\,m_w\,a_o^3\rho_s/m_s\,\rho$. As the drop grows the third term and subsequently the second term — the solute term and the curvature term, respectively — become negligible, and for sufficiently large drops

$$\frac{da}{dt} = \frac{S\alpha}{a} \quad . \qquad (3)$$

In the early stages, condensation on nuclei will occur only if the supersaturation is sufficiently large. From equation (2) the condition is

$$S > \frac{\beta}{a} - \frac{\gamma}{a^3} \, ,$$

and since γ is proportional to the nucleus volume, the supersaturation required is lower for larger CCN than for smaller. (For insoluble but wettable nuclei the condition is $S > \beta/a_o$, and the same conclusion holds.)

If, as is always the actual case, CCN of various sizes are present, condensation on the large nuclei will keep the supersaturation from rising to the high values required for condensation on the small ones. Thus only the larger and more soluble CCN are activated and form cloud drops. Even so the number of nuclei that are effective is usually in the range 50 to 1000 per cubic centimeter.

With more than one drop present the conditions under which equation (1) is valid are not strictly met. However it has been demonstrated that even with 1000 drops per cubic centimeter the drops are sufficiently far apart relative to their size not to influence each other's growth directly, but only by affecting the degree of supersaturation.

Once the drops become large enough, the larger drops grow less rapidly than the smaller, as shown by equation (3). Thereafter the spread of cloud drop sizes becomes narrower and the rate of drop growth decreases as time goes on. Between these effects and the depletion of available water vapor the drops that are formed by condensation never are larger than a few tens of microns in radius.

As an illustration of the growth of cloud drops on a typical spectrum of CCN, Figure 1 shows the results of a computation carried out by Neiburger and Chien (1960) several years ago. The curve labeled "t = 0" shows the initial distribution assumed for the nucleus sizes. It is based on the summaries of particle size measurements reported by Junge (1963). For convenience all the nuclei were assumed to be NaCl. The air was assumed initially to have temperature 16°C and relative humidity 75 per cent at 1000 mb pressure, and to

cool adiabatically as it rose with vertical velocities approximating those measured in cumulonimbus clouds (Byers and Braham, 1949). Figure 1A shows the variation with time of the saturation ratio and of the drop sizes for the initial sizes into which the nuclei were grouped, and Figure 1B shows the drop size distributions after various elapsed times. Once the relative humidity slightly exceeded 100 per cent the drops on nuclei 0.1 μm or larger in radius grew rapidly, while those on smaller nuclei did not continue to grow. Shortly after the cloud formed, the separation between cloud drops and inactivated nuclei became evident, with modal radius of the cloud drops about 7 μm. At the end of the computation, corresponding to a rise of the air parcel to 9 km, the modal radius was 20 μm. Of the approximately 100 per cubic centimeter that were activated, about 70 had radii greater than 16 μm, but only about one per liter was greater than 22 μm.

Similar computations with various realistic assumptions about CCN spectra and cooling rates have shown that condensation of liquid drops does not produce precipitation, even for very deep clouds. It has been found, further, that turbulent fluctuation in updraft velocity and variations in nucleus composition do not lead to a broadening of the spectrum produced by condensation. However, the introduction of additional nuclei during the entrainment of environmental air into the cloudy updraft and the penetration of successive thermals through their predecessors appear to be able to explain the development of sufficiently disperse drop size distributions to initiate the collection process.

THE THEORETICAL COMPUTATION OF COLLISION EFFICIENCY

As a drop falls the air ahead of it is pushed out of the way, and if a smaller droplet is contained in that air it likewise will tend to be carried out of the path of the larger drop. Because of the inertia of the droplet, the viscous drag exerted by the air may not pull it far enough, and if the droplet is not too far from the axis of fall of the drop a collision may occur. The ratio of the number of droplets that collide to the number in the volume swept out by the drop is called the collision efficiency E_s. Similarly, the fraction of the droplets that the drop collides with that coalesce with it is called the coalescence efficiency E_ℓ, and the ratio of the number of droplets with which the drop coalesces to the number in the volume it sweeps out is called the collection efficiency E. Obviously, $E = E_s \cdot E_\ell$.

The theoretical evaluation of E_s may be treated adequately by considering the dynamics of two rigid spheres moving in a viscous medium. For the size of drops we are considering both the departures from spherical shape and the internal circulations are negligible. Similarly, the drops are generally far enough apart for the influence of the other drops on the motion of an interacting pair to be ignored. Nevertheless, because of the non-linear terms in the Navier-Stokes equations and the difficulty in satisfying the boundary conditions on the surfaces of two bodies the problem is not amenable to solution without assumptions or approximations.

The problem of computing E_s involves two phases, first to determine the flow field of the air around the two drops, regarded as rigid spheres, and from this the force exerted by the air on the drops, and second, to compute the trajectories of the drops in response to these forces. By computing the trajectories for different initial displacements of the small drop from the

vertical through the center of the large one the grazing trajectory that brings them just into contact can be determined. If the initial displacements for the grazing trajectory is Y_c and the radii of the large and small drops are A, a, respectively,

$$E_s = \frac{\pi Y_c^2}{\pi (A + a)^2} = \frac{y_c^2}{(1 + p)^2} \tag{4}$$

where $y_c = Y_c/A$ and $p = a/A$. The non-dimensional critical displacement y_c is called the linear collision efficiency.

One simplification, valid for very small p, is the assumption that the flow pattern is determined only by the large drop and is unaffected by the small one. Even with this assumption the flow field cannot be determined rigorously because of the non-linearity of the Navier-Stokes equations. Using an analog computer, Langmuir and Blodgett (1946, Langmuir 1948) carried out the computations for two limiting cases for which the equations can be linearized, very low Reynolds numbers, for which the inertia terms can be neglected, and very high Reynolds numbers, for which the viscous forces can be ignored and potential flow obtains. For the intermediate values that are of most interest in cloud physics they adopted an interpolation scheme.

Fonda and Herne (Herne 1960) repeated the computations with a digital computer. Apart from the improved computational accuracy the only change they made was to allow for the finite size of the small drop when determining whether or not there was a collision. Both they and Langmuir and Blodgett used the Stokes law for the drag exerted by the air on the small sphere.

When the size of the small drop is comparable to that of the large one the effects of both on the flow patterns must be considered. Pearcey and Hill (1957) were the first to attempt to do so. They superposed the Oseen flow due to each sphere separately to obtain the flow pattern for the two moving spheres. It can be shown that the resulting drag forces are equivalent to those that would be experienced by each sphere if it is moving with its own velocity relative to the flow induced by the other. Since the Oseen approximation is poor close to the drops, where the interaction of the drops has most influence on the collision efficiency, the values of E_s obtained by Pearcey and Hill were not reliable.

For sufficiently small drops for the Stokes linearization to hold Hocking (1959) obtained solutions that fit the boundary conditions at the surfaces of the two drops rigorously. Because the equations are linear he was able to superpose solutions for spheres moving along and perpendicular to their line of centers to obtain the solution for relative motion in an arbitrary direction. His solutions were expressed in terms of series of which he was able to determine only a few terms in evaluating the drag forces. Davis and Sartor (1967) and subsequently Hocking and Jonas (1970) obtained improved solutions for the forces in this case. They found that if the Stokes equations are valid however close together the drops come collisions cannot occur because the force opposing their approach is inversely proportional to the distance between their surfaces. Once the distance becomes commensurate with the mean free path of the molecules of air viscous theory cannot apply. Davis (1972) has considered the gas kinetic effects and found that they lead to

somewhat larger values of E_s for A < 20 μm than those found by Davis and Sartor and Hocking and Jonas. It is presumed that these results are the best evaluations of E_s for very small A.

For larger drops, for which Stokes' approximation does not hold, most of the recent evaluations of E_s have used the superposition technique with numerical solutions of the complete Navier-Stokes equations for the flow fields induced by the individual drops (Shafrir and Neiburger 1963, 1964; Neiburger 1967; Shafrir and Gal-Chen 1971; Lin and Lee 1973; Beard and Grover 1974). The exception is the work of Klett (1968) and Klett and Davis (1973), in which an attempt is made to fit the boundary conditions at the surfaces of the two spheres with a solution of Carrier's modification of Oseen equations. It is interesting and reassuring that the various procedures, while leading to some differences in the values of E_s, do not give markedly different results.

Because all the theoretical evaluations of E_s involve assumptions and approximations it is desirable to check their validity with experimental data. We shall discuss our experiments using the UCLA Cloud Tunnel later, and in the next section present a comparison of various computational values of E_s with earlier experimental results.

COMPARISON OF COMPUTED COLLISION EFFICIENCIES WITH EARLIER EXPERIMENTAL RESULTS

The set of collision efficiencies computed over the most complete range of cloud drop sizes is that of Shafrir and Neiburger (1963, 1964) and Neiburger (1967). An extended and refined version, which we shall refer to as "modified S-N" values, is used here. As we shall see, these values correspond fairly closely to the results of other computations and fit the results of experiments.

For convenience in interpolating to other drop sizes and in using the values in drop growth computations it is convenient to have an analytic expression for the collision efficiency. Berry (1967) presented a formula that fit the S-N values fairly well and Scott and Chen (1970) developed a somewhat less complicated expression. In addition to being very complicated their formulas do not include the values due to wake effects for nearly equal drops. Lee (Neiburger, Lee, Lobl and Rodriguez, 1974) has developed a simpler equation that fits closely the modified S-N values over the entire range. The S-N values shown in the following are those obtained from that equation.

Experiments give the value of the collection efficiency E rather than the collision efficiency E_s. They would be expected to be the same only if the coalescence efficiency E_ℓ is unity. Experimental evaluations of E have been carried out by Picknett (1960), Woods and Mason (1964, 1965), Beard (1968, 1970), and Beard and Pruppacher (1968, 1971). In most of these experiments the collector drops were generated by a vibrating hypodermic needle, which may have led to them having some electric charge. Usually the technique used in determining E gave a lower bound rather than a precise value. Just as the computed values of E_s, which we shall designate E_c, are subject to uncertainty because of assumptions and approximations, the experimental values of E, which we shall call E_x, are likewise uncertain because of experimental difficulties and the difference between the conditions of the

experiments and those in natural clouds. As we shall see, several computations using different approximations yield nearly the same values of E_c, and a number of experiments give values of E_s that are close to the computed values. We may thus be inclined to conclude that for those experimental conditions $E_\ell \approx 1$ and the computed E_c are good approximations of E.

Experiments using the UCLA Cloud Tunnel to evaluate E have given values of E_x considerably smaller than E_c for the same values of A and a (Neiburger, Levin and Rodriguez, 1972; Levin, Neiburger and Rodriguez, 1973). The difference between these experimental results and the earlier ones was attributed to the possibility that in the cloud tunnel, in which atmospheric conditions are more closely simulated than in earlier experiments, the coalescence efficiency E_ℓ is much smaller than one when the collector drop has no electric charge.

In this brief presentation it is impossible to review all of the results. In Figure 2 data are compared for some values of A for which the results of several computations and some experiments are available. The values of E_c and E_x are shown for fixed values of A as a function of p.

For A = 30 μm (Figure 2A) six computations are available, three in which the Stokes approximation was used, two computed with the superposition technique, and one in which the modified Oseen approximation was used. The latter three computations give generally higher values of E_c than the first three, but for the most part the shapes of the curves are similar and the values do not depart radically from each other. Only one series of experimental results (Picknett 1960) are available for this value of A. (The results of Woods and Mason [1964] for A = 33.5 μm correspond closely to Picknett's for 30 μm.) Of the computations using the Stokes approximation Hocking's earlier results agree better with Picknett's experiments over the small range of p for which they were performed than the later, more accurate, computations by Davis and Sartor and by Hocking and Jonas. Indeed, they also fit them better than the other three computational results, which take account of the nonlinear terms and should be better even for this small a value of A. However, since the experiment gives a lower bound for E rather than a precise value, it is possible that the true value of E is closer to the Klett-Davis, Lin-Lee and S-N values.

For A = 50 μm (Figure 2B) the two other computations give slightly higher values than the modified S-N ones as represented by the analytic formula, but the experimental values, which are available only for large p, are closer to the S-N. Similarly, for 70 μm (Figure 2C) the curve representing the Klett-Davis computation is everywhere above the S-N curve but the experimental points fit the S-N values. The results for 40 μm and 60 μm, not illustrated, are the same as for 70 μm. For 80 μm and 90 μm, for which other computations are not available, the experimental points also fall almost exactly on the S-N curve.

Beard and Grover (1974) carried out new computations of E_s using the superposition technique with flow fields given by Le Clair, et al (1970), and compared the results for fairly large A and small p with experiments Beard carried out using the UCLA wind tunnel. In Figure 2D their data for two values in the range that our computations apply are compared with ours. The ranges covered by the probable errors are shown by the shaded rectangles, and

it is seen that their results fall in the upper corners of the experimental error rectangles and ours in the extreme lower corners. This again suggests that for small p and large A the correct values of E may be somewhat larger than our computed values.

In summary, the results of the various computations are quite similar, and the available experimental data on the whole agree well with the modified S-N computations. It is therefore suggested provisionally that the S-N values of E_c be used for the collision efficiency of drops in the range 20 to 140 μm.

CLOUD TUNNEL EXPERIMENTS WITH COLLECTOR DROPS HAVING LITTLE OR NO ELECTRIC CHARGE

In our cloud tunnel experiments the conditions of natural collection in clouds are simulated more closely than in other experiments in several ways. The air rises through the tunnel at the speed of the terminal velocity of the collector drop, so that it remains motionless as the cloud of droplets is carried upward in the air stream. Thus, relative to the air the collector drop falls at its terminal velocity through the cloud of droplets that are also falling at their terminal velocities. The ambient relative humidity is about 100 per cent, so that evaporation or condensation plays little or no role. The cross section of the tunnel is large enough so that there is practically no influence of the walls on the flow pattern near the center. There is practically no externally induced turbulence.

To produce collector drops with essentially zero electric charge a grounded hypodermic needle was used in our first series of experiments. For later experiments a drop generator was constructed, using modifications of the design by Abbot and Cannon (1972), in which the voltage on a hood or shield determines the charge on the drop. With zero hood potential the charge is practically zero.

In Table 1 the average values of E_x for uncharged collector drops, grouped according to the range of their radii A and size ratio p, are compared with the computed collision efficiency E_c. Except for a few instances of A in the smallest size range, E_x is much smaller than E. In previous discussions of some of these data (Neiburger, Levin and Rodriguez 1972; Levin, Neiburger and Rodriguez 1973) it was suggested that the explanation of the difference was that the coalescence efficiency E_ℓ was small for the conditions of the experiments. The difference between these results and those of previous experiments was attributed to the possibility that in the earlier experiments the collector drops had sufficient charge to overcome any inhibition of coalescence.

It was reasoned that if this is true an electric charge could be applied to the collector drops that would be sufficient to raise the coalescence efficiency to unity without being so large that it would affect the motion of the drops and thereby increase the collision efficiency. The variation of E with drop charge Q would then be such that it would first increase with Q until E_ℓ reached unity, then remain constant at E_s until Q became so large that E_s would be affected. To test this hypothesis experiments were carried out in the cloud tunnel with small collector drops having various magnitudes and polarities of electric charge.

CLOUD TUNNEL EXPERIMENTS WITH CHARGED COLLECTOR DROPS

The hypothesis postulated at the end of the preceding section may be expressed as follows: For each value of A and a there exist two values of charge Q_1, Q_2 such that when the charge on the collector drop is smaller than Q_1, $E_\ell < 1$; when $Q_1 \leq Q \leq Q_2$, $E_\ell = 1$, $E_s = E_c$; and when $Q > Q_2$, $E_s > E_c$.

The effects on E_s of charge on a collector drop interacting with uncharged droplets has been evaluated previously (Semonin and Plumlee 1966) only for the case of A = 30 μm and a = 5 μm. They reported that a slight increase in E_s began when Q exceeded $6 \cdot 10^{-7}$ esu; their graph shows very little increase for Q less than $3 \cdot 10^{-6}$. For a = 10 μm, the value frequently used in our experiments, some idea of Q_2 may be obtained from the computations they carried out with charges on the collected drops as well as the collector. For charges with opposite sign the threshold charge on a 30 μm collector drop interacting with 10 μm droplets bearing charges 1/9 as large was about $2 \cdot 10^{-5}$ esu.

The influence on E_s of a charged drop collecting uncharged droplets would be due to the dipole moment of the droplet induced by the field due to the charged drop. Since the induced dipole moment is a function of the distance between the drops, it appears safe to assume that the effect will be significant only when the drops are close together, and that the charge required to affect the collision efficiency will therefore be considerably larger than that affecting it when both of the drops are charged. From this consideration we anticipate, for example, that 30 μm radius collector drops falling through a cloud of uncharged 10 μm droplets would have to bear charges of at least 10^{-4} esu in order that E_s should be affected.

For estimation of Q_1 the experiments of Jayaratne and Mason (1964) are the most informative. They studied the coalescence of drops impinging on a plane or wavy water surface. The smallest drop for which they evaluated the critical charge required to cause coalescence was 139 μm in radius; for this size the critical charge was about $6 \cdot 10^{-5}$ esu. Except for large impact velocities the critical charge increased with radius. The relation between coalescence of a charged drop with an uncharged water surface (corresponding to an uncharged much larger drop) and our case of a charged drop coalescing with an uncharged smaller droplet is not clear, but it seems safe to expect that Q_1 would have the same general order of magnitude. From this discussion we see that there is a possibility, but not a certainty, that the required condition, that $Q_1 < Q_2$, is satisfied.

We shall not discuss in detail in this paper the various experimental difficulties that were encountered in attempting to evaluate the collection efficiency of small collector drops (A ≤ 40 μm) in the cloud tunnel. They include the fact that characteristics of the cloud, such as liquid content and droplet size, may change as the air speed in the tunnel is increased to keep the growing drop stationary. The liquid content was measured continuously, but not the cloud drop size spectrum. Similarly, the charge on the collector drop was known when it was generated, but it might have changed due to collection of ions in the air stream or charges on the collected droplets, although the charges on the droplets were measured to be less than 10^{-7} esu, so that the small number of them that were collected in any one experiment would

not affect the charge on the collector drop significantly. There was a consistent decrease in the rate of collector drop growth with time for all the experiments. One possible explanation of this decrease is that the charge on the collector drop was being neutralized. Another is that the size of the droplets became smaller as the air speed increased.

When E is large and the cloud sufficiently dense the equation for continuous growth can be used to evaluate it. Solved for E this equation is

$$E = \frac{4 \rho \overline{A^2}}{\ell (A + a)^2 (V - v)} \frac{\Delta A}{\Delta t} \tag{5}$$

where ρ is the density of the liquid (one for water), ℓ the mass of liquid per unit volume of the cloud, V and v the fall velocities of the drop and droplet, and ΔA is the change in collector drop size in Δt seconds. The slope $\Delta A/\Delta t$ may be determined from an analytic expression fitted to the curve representing the variation of observed drop size with time, or an average value can be computed from the difference in radius at the beginning and end of a time interval Δt.

When the collection efficiency is so small that even with a dense cloud only a few droplets are collected during the experiment the continuous growth equation cannot be used. If n is the number of droplets collected and N is the number of droplets per unit volume of the cloud ($N = 3\ell/4 \pi \overline{a^3} \rho$), the collection efficiency is approximately

$$E \cong n/\overline{N} (V - v) \pi (A + a)^2 \Delta t . \tag{6}$$

The value of n can in some cases be determined by counting the steps in the record of the tunnel speed as it is changed when the drop grows by collection. If the steps are not sufficiently distinct and n is sufficiently large to permit assuming that the average volume of the collected droplets is representative of the entire cloud, n can be computed from the change in volume of the collector drop:

$$n = (A_f^3 - A_i^3)/\overline{a^3} = \Delta A^3/\overline{a^3}$$

where A_i, A_f are the radii of the collector drop at the beginning and end of the time interval Δt. Equation (6) becomes

$$E \cong 4 \rho \Delta A^3/3 \ell (A + a)^2 (V - v) \Delta t . \tag{7}$$

This equation is equivalent to equation (5) if the droplets are collected so frequently that Δt can be treated as an infinitesmal.

When equation (6) is used with small n, there is uncertainty in the value of E because of the variability of intervals between successive collection of droplets. If ε is the probable error in Δt, it can be shown that the probable error in E is approximately $\varepsilon E/\Delta t$.

In Figure 3A the results of one series of experiments, with A in the range 20 μm to 23 μm and $\bar{a}$ about 10 μm. For A this small the collection

efficiency with zero charge is zero. The x on the ordinate axis shows the value of E_c (the computed value of E_s). It is seen that the experiment appears to corroborate the hypothesis: E_x increases with charge Q, reaching the value of E_c at $Q = 0.7 \cdot 10^{-4}$ esu, and then remains constant until Q exceeds $1.2 \cdot 10^{-4}$ esu. Then it increases and becomes larger than the geometric collection efficiency when Q exceeds $2 \cdot 10^{-4}$ esu. This suggests that for Q smaller than $Q_1 = 0.7 \cdot 10^{-4}$ esu the coalescence efficiency E_ℓ is less than one, that it reaches unity when Q attains that value, but that the charge does not affect E_s until Q is greater than $Q_2 = 1.2 \cdot 10^{-4}$ esu.

If all the experimental data conformed to this pattern we would consider the hypothesis demonstrated. However, when all the data we have collected are considered the evidence is far from conclusive. Thus, in Figure 3B the results of all our experiments with drops in that range are shown. The same general trend is seen, with E_x smaller than E_c for small charge and increasing with Q, but for some for some of the series E_c is reached and exceeded for much smaller values of Q than in Figure 3A. We are not aware of differences in the experimental parameters that would produce the differences in the results.

Figure 3C shows results for A in the range 26 μm to 29 μm with $\bar{a} \cong 10$ μm. The data suggests that Q_1 is $1.3 \cdot 10^{-4}$ esu and Q_2 is $2 \cdot 10^{-4}$ esu. However there is some scatter in the results. In Figure 3D the data for A in the range 32-35 μm, $\bar{a} \cong 10$ μm are shown. It appears that for this size Q_1 and Q_2 are both greater than $2.5 \cdot 10^{-4}$ esu.

Figure 4 shows data for three ranges of A with $\bar{a} = 15$ μm. The behavior of the positive charge cases (solid symbols) was sufficiently different from the negative for separate lines to be drawn for them. The increase of E_x with increasing charge is more rapid for the smaller values of A, as expected, but the leveling off, insofar as it is apparent in the data, does not occur at the values of E corresponding to the computed collision efficiencies. By comparing Figure 4 with Figure 3 we see that for the same charge and range of A, E_x is considerably larger for $\bar{a} \cong 15$ μm than for $a = 10$ μm.

The data displayed here is suggestive rather than conclusive. It is clear that E_x increases with Q and that for a specified charge the effect is larger the smaller the value of A. There are indications in some of the data of the plateau that would occur if $Q_1 < Q_2$. In some instances the plateau or a leveling off occurs at another value of E_x.

Charge could affect E_ℓ in two ways, firstly by reducing the time of thinning of the air film as the drops approach each other, and secondly by changing the thickness at which surface rupture and coalescence takes place. The details of these effects cannot be studied by cloud tunnel experiments, but by careful control of the various parameters it may be possible to distinguish between the factors that affect the thinning and those that influence the surface rupture.

IMPLICATIONS OF COLLECTION EFFICIENCY ON THE PRECIPITATION PROCESS

While the information concerning the effect of charge on collection efficiency is of intrinsic interest in shedding light on the collision and coalescence processes, the data so far does not appear to clear up the initiation

of warm rain. We have seen that the charge required for influencing E is of the order of 10^{-5} or 10^{-4} esu, but the available data (e.g. Webb and Gunn, 1955; Takahashi, 1972) indicate that natural cloud drops bear much smaller charges.

There have been a number of studies to determine the circumstances under which condensation can produce sufficiently large drops to start the collection process. The collision efficiency computations suggest that there must be drops at least 20 μm in radius for it to begin, and the cloud tunnel experiments indicate that the minimum size may be as much as 30 μm or even 40 μm unless the drops carry unusually high electric charges. Among the ways that have been shown to result in the growth of large drops by condensation are (1) the presence of abnormally large soluble nuclei — giant salt praticles 5 μm or more in equivalent radius —; (2) presence of unusually few CCN, so that the water vapor is shared by relatively few drops; this is sometimes true of maritime air in contrast to continental air; and (3) occurrence of entrainment or a succession of penetrative thermals in which competition between condensed drops and newly activated CCN brought in from the environment leads to a wide drop size spectrum.

To see how sensitively cloud drop growth by collection depends on the drop size dispersion, Chin and Neiburger (1972) carried out some computations of the evolution of drop spectra with differing characteristics. The governing equation is

$$\frac{\partial n(M)}{\partial t} = \frac{1}{2} \int_0^M n(m)\, n(M-m)\, K\,(m,M-m)\, dm - n(M) \int_0^\infty n(m)\, K\,(m,M)\, dm \quad . \tag{8}$$

In this equation the first integral on the right side represents the increase in number density n(M) of drops of mass M due to collection of drops of mass m by drops of mass M-m, and the second integral is the decrease in n(M) due to collection of other drops by drops of mass M. K (m,M), the collection kernel, is given by

$$K\,(m,M) = \pi\,(A+a)^2\, E\,(V-v) \quad .$$

For the collection efficiency they used the S-N computed values of E_s, and for the droplet spectra they used both Gaussian distributions and Khrigian-Mazin (K-M) distributions, the latter given by

$$n\,(a) = (1.45\, \ell\, a^2/\overline{a}^6)\, \exp\,(-\,3\, a/\overline{a})$$

where $\overline{a}$ is average radius. Khrigian and Mazin found that this expression fits the observed distributions in a variety of types of clouds.

Chin and Neiburger's computations showed that for distributions having the liquid content, mean volume radius, and relative dispersion the K-M spectra, because of their skewness, led to more rapid development of large drops by the collection process. In the K-M expression the average radius a determines both the modal radius and the dispersion. In Figure 5A the K-M

distributions for three values of $\bar{a}$, 4.5 μm, 6.0 μm, and 7.5 μm, with ℓ = 1 gm m^{-3}, are shown. While the modal radius changes only slight with increase in a, the number of drops with radii larger than 20 μm increases markedly.

The resulting difference in the effect on collection is shown in Figures 5B, 5C, and 5D. In these diagrams the specific liquid content q, expressed in grams per cubic meter per unit of $\log_2$ a is graphed against log a, in order to show the transfer of liquid content from small to large drops. It is seen that for the case of $\bar{a}$ = 4.5 μm, in which there are very few drops with radius larger than 20 μm, there is negligible change in liquid water distribution, but for $\bar{a}$ = 7.5 μm the water accumulates on larger and larger drops, so that by 2000 seconds there is a larger mass of water in drops larger than 100 μm radius than in the more numerous smaller cloud drops. The effect of the drops initially larger than 20 μm is clearly demonstrated.

There have been a number of attempts to incorporate the microphysical processes of condensation and collection together with the larger scale dynamical processes into a complete model of the development of precipitation. As an example of these attempts we shall cite the investigation by Ogura and Takahashi (1973) of the development of warm rain in a convective cloud. They computed the development of convection in a conditionally unstable atmosphere using a "one and one-half dimensional" time-dependent model, and evaluated the distribution of drop sizes as a result of condensation, coalescence, sedimentation and drop breakup. As an indication of the result Figure 6 shows the size density as a function of height 40 minutes after the inception of convection. The water content has already developed a second peak density for drops about one millimeter in radius, and precipitation is reaching the ground.

CONCLUSION

The physics of drops remains a central problem in meteorology. While the theory of condensation on nuclei appears to be fairly well in hand, the circumstances when it leads to drops large enough to engage in the collection process are not well known. The values of collision efficiency appear to be satisfactory, but the coalescence efficiency is almost unknown. In particular, the influence of charges and fields on them, especially the very small charges and fields that occur naturally in the early stages of development of cloud and precipitation, need investigation.

ACKNOWLEDGMENT

Research supported by the Atmospheric Sciences Section, National Science Foundation, NSF Grant GA-35394X.

REFERENCES

Abbott, C. E. and T. W. Cannon, 1972: A droplet generator with electronic control of size, production rate and charge. Rev. Sci. Instr., 43, 1313-1317.

Beard, K. V., 1968: An experimental test of theoretically determined collision efficiencies of cloud drops. M.S. Thesis, UCLA, 108 pp.

Beard, K. V., 1970: A wind tunnel investigation of the terminal velocities, collection kernels and ventilation coefficients of water drops. Ph.D. Dissertation, UCLA, 125 pp.

Beard, K. V. and S. N. Grover, 1974: Numerical collision efficiencies for small raindrops colliding with micron size particles. J. Atmos. Sci., 31, 543-550.

Beard, K. V. and H. R. Pruppacher, 1968: An experimental test of the theoretically calculated collision efficiency of cloud drops. J. Geophys. Res., 73, 6407-6414.

Beard, K. V. and H. R. Pruppacher, 1971: A wind tunnel investigation of collection kernels of small water drops in air. Quart. J. Roy. Meteor. Soc., 97, 242-248.

Berry, E. X., 1967: Cloud droplet growth by collection. J. Atmos. Sci., 24, 688-701.

Byers, H. R. and R. R. Braham, 1949: The Thunderstorm. U.S. Government Printing Office, Washington, D.C.

Chin, E. H-C., and M. Neiburger, 1972: A numerical simulation of the gravitational coagulation process for cloud drops. J. Atmos. Sci., 29, 718-727.

Davis, M. H. and J. D. Sartor, 1967: Theoretical collision efficiencies for small cloud droplets in Stokes flow. Nature, 215, 1371-1372.

Davis, M. H., 1972: Collisions of small cloud droplets: Gas kinetic effects. J. Atmos. Sci., 29, 911-915.

Herne, H., 1960: The classical computations of aerodynamic capture of particles by spheres. International J. Air Pollution, 3, 26-34.

Hocking, L. M., 1959: The collision efficiency of small drops. Quart. J. Roy. Meteor. Soc., 85, 44-50.

Hocking, L. M. and P. R. Jonas, 1970: The collision efficiency of small drops. Quart. J. Roy. Meteor. Soc., 96, 722-729.

Jayaratne, O. W. and B. J. Mason, 1964: The coalescence and bouncing of water drops at an air/water surface. Proc. Roy. Soc. A, 280, 545-565.

Junge, C. E., 1963: Air Chemistry and Radioactivity. Academic Press, New York and London.

Klett, J. D., 1968: The interaction and motion of rigid spheres falling in a viscous fluid at low Reynolds numbers. Ph.D. Dissertation, UCLA, 113 pp.

Klett, J. D. and M. H. Davis, 1973: Theoretical collision efficiencies of cloud droplets at small Reynolds numbers. J. Atmos. Sci., 30, 107-117.

Langmuir, I. and K. B. Blodgett, 1946: A mathematical investigation of water droplet trajectories. U.S. Army Air Forces, Tech. Report No. 5418.40.

Langmuir, I., 1948: The production of rain by a chain reaction in cumulus clouds at temperatures above freezing. J. Meteor., 5, 175-192.

LeClair, B. P., A. E. Hamielec and H. R. Pruppacher, 1970: A numerical study of the drag on a sphere at low and intermediate Reynolds numbers. J. Atmos. Sci., 27, 308-315.

Levin, Z., M. Neiburger and L. Rodriguez, 1973: Experimental evaluation of collection and coalescence efficiencies of cloud drops. J. Atmos. Sci., 30, 944-946.

Lin, C. L. and S. C. Lee, 1973: Collision efficiency of water drops in the atmosphere. Paper presented at the AGU Fall Annual Meeting.

Neiburger, M. and C. W. Chien, 1960: Computations of the growth of cloud drops by condensation using an electronic digital computer. Monograph No. 5, American Geophysical Union, 191-209.

Neiburger, M., 1967: Collision efficiency of nearly equal cloud drops. Mon. Wea. Rev., 95, 917-920.

Neiburger, M., Z. Levin and L. Rodriguez, 1972: Experimental determination of the collection efficiency of cloud drops. J. de Rech. Atmos., VI, 391-397.

Neiburger, M., I. Y. Lee, E. Lobl and L. Rodriguez, 1974: Computed collision efficiencies and experimental collection efficiencies of cloud drops. Paper prepared for presentation at the AMS Conference on Cloud Physics, Tucson, Arizona, October 21-24, 1974.

Ogura, Y. and T. Takahashi, 1973: The development of warm rain in a cumulus model. J. Atmos. Sci., 30, 262-277.

Pearcey, T. and G. W. Hill, 1957: A theoretical estimate of the collection efficiencies of small droplets. Quart. J. Roy. Meteor. Soc., 83, 77-92.

Picknett, R. G., 1960: Collection efficiencies for water drops. Intern. J. Air Pollution, 3, 160-168.

Scott, W. T. and C-Y. Chen, 1970: Approximate formulas fitted to the Davis-Sartor-Shafrir-Neiburger droplet collision efficiency calculations. J. Atmos. Sci., 27, 698-700.

Semonin, R. G. and H. R. Plumlee, 1966: Collision efficiencies of charged cloud droplets in electric fields. J. Geophys. Res., 71, 4271-4278.

Shafrir, U. and T. Gal-Chen, 1971: A numerical study of collision efficiencies and coalescence parameters for droplet pairs with radii up to 300 microns. J. Atmos. Sci., 28, 741-751.

Shafrir, U. and M. Neiburger, 1963: Collision efficiencies of two spheres falling in a viscous medium. J. Geophys. Res., 69, 4141-4147.

Shafrir, U. and M. Neiburger, 1964: Collision efficiencies of two spheres falling in a viscous medium for Reynolds numbers up to 19.2. University of California Press, Occasional Papers No. 1, 140 pp.

Takahashi, T., 1972: Electric charge of cloud droplets and drizzle drops in warm cloud along Mauna Loa-Mauna Kea Saddle Road of Hawaii Island. J. Geophys. Res., 77, 3869-3878.

Webb, W. L. and R. Gunn, 1955: The net electrification of natural clouds at the Earth's surface. J. Meteor., 12, 211-214.

Woods, J. D. and B. J. Mason, 1964: Experimental determination of collection efficiencies for small water droplets in air. Quart. J. Roy. Meteor. Soc., 90, 373-381.

Woods, J. D. and B. J. Mason, 1965: The wake capture of drops in air. Quart. J. Roy. Meteor. Soc., 91, 35-43.

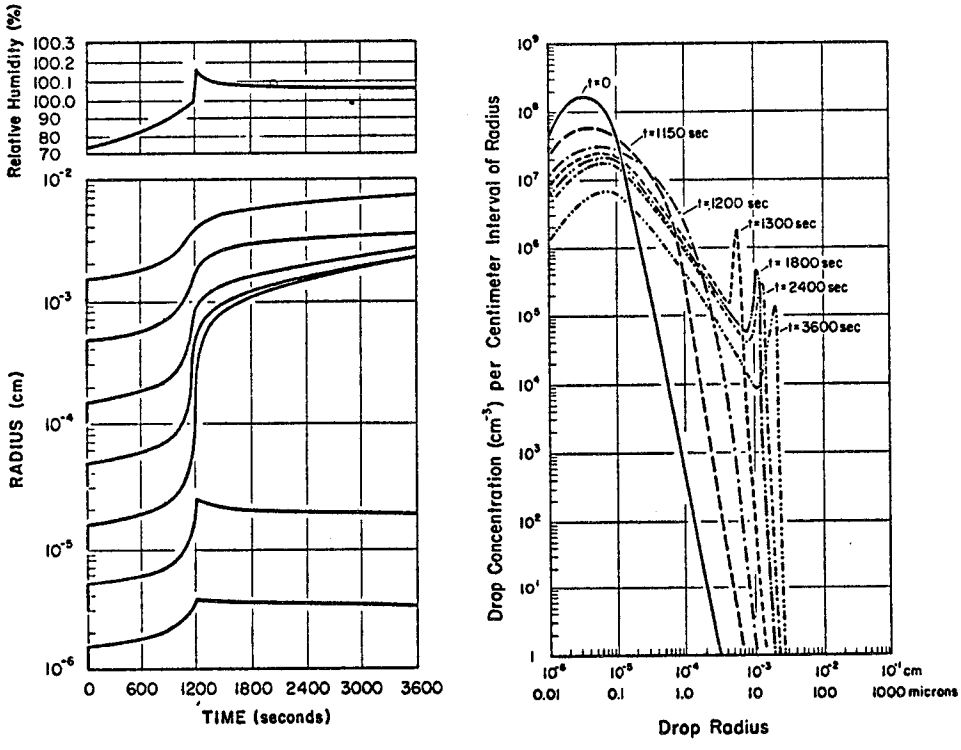

Figure 1. A (left): Variation with time of relative humidity and size of drops growing by condensation on nuclei of various sizes as air parcel rises in fashion simulating a cumulonimbus cloud. B (right): Drop size distribution at various times in air parcel containing nucleus distribution shown by curve labeled "t = 0" as it rises.

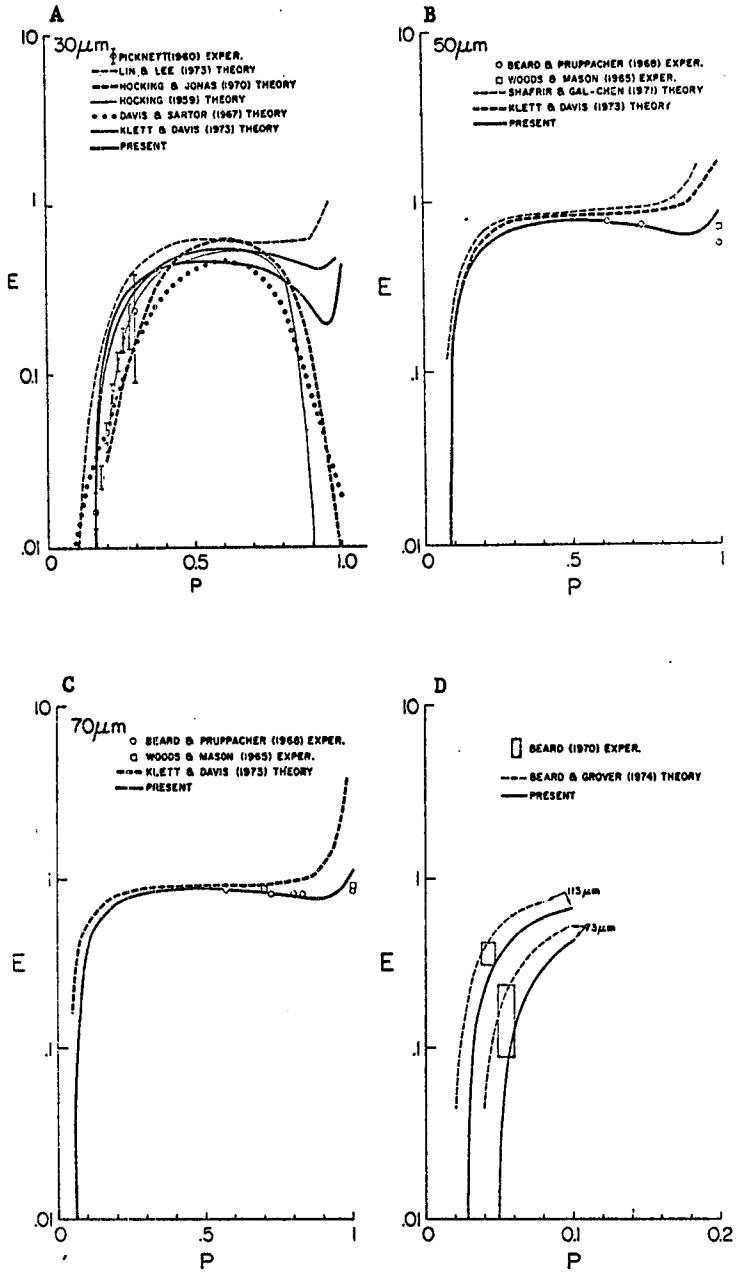

Figure 2. Comparison of results of various collision efficiency computations with experimental data. Curves labeled "Present" are based on analytic formula fitted to Shafrir-Neiburger computations.

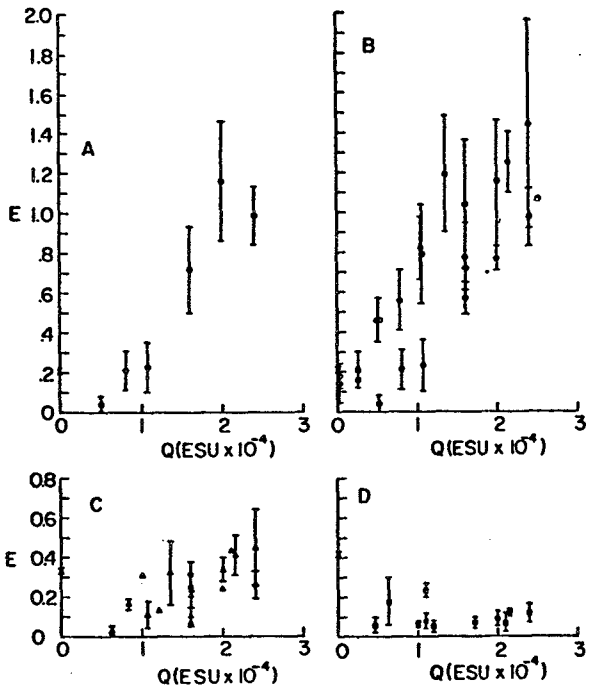

Figure 3. E_x of charged drops collecting uncharged 10 μm droplets. (A) Single series with A in range 20-23 μm; (B) All experiments with A in range 20-23 μm; (C) A in range 26-29 μm; (D) A in range 32-35 μm. Open symbols, negative charge; solid symbols, positive charge. Symbol on ordinate axis gives E_c.

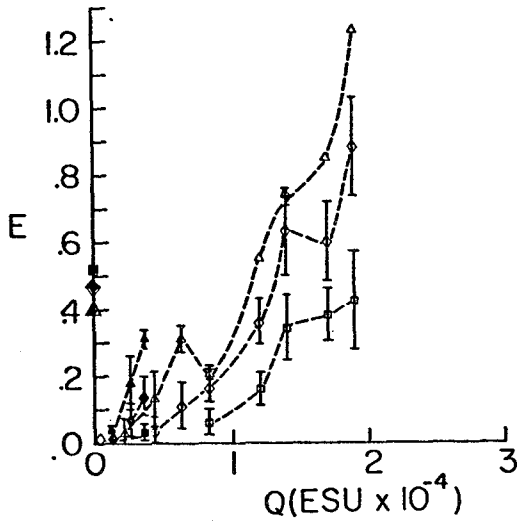

Figure 4. E_x of charged collector drops collecting uncharged 15 μm droplets. Symbols represent range of A as follows: triangles, 26-29 μm; diamonds, 29-32 μm; squares, 32-35 μm.

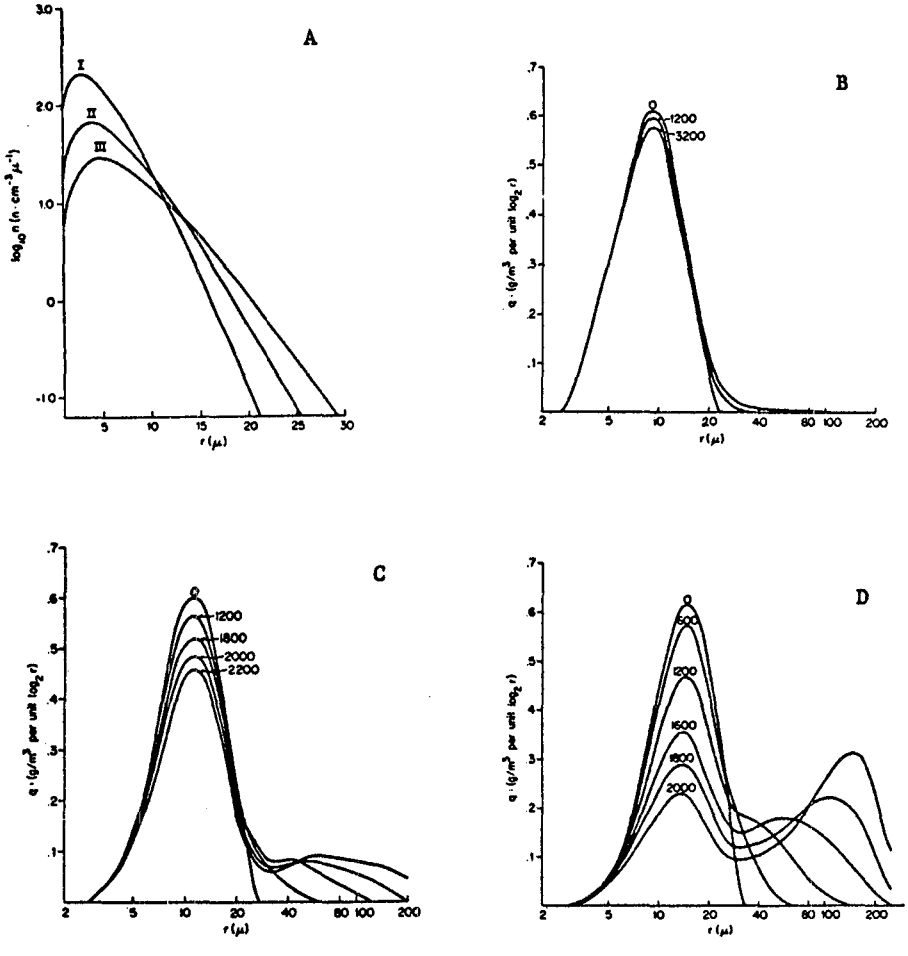

Figure 5. (A) Khrigian-Mazin drop size distributions for $\ell = 1$ gm m^{-3} and I: $\bar{a} = 4.5$ μm, II: $\bar{a} = 6.0$ μm and III: $\bar{a} = 7.5$ μm. (B) Distributions at various times, given in seconds, resulting from evolution of spectrum I due to collection. (C) Distributions resulting from evolution of spectrum II due to collection. (D) Distributions resulting from evolution of spectrum III.

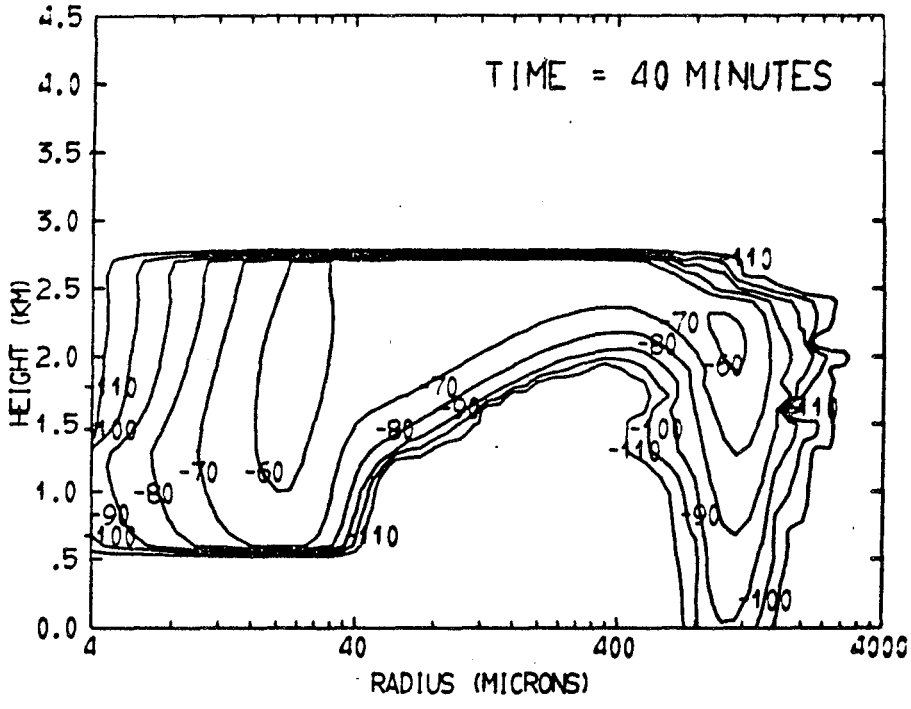

Figure 6. Size density function showing distribution of liquid content of cloud per interval of drop radius at various heights after 40 minutes of convection. Contour values range from 10^{-11} to 10^{-6} cm^{-3} gm^{-1}.

Table 1

Comparison of Experimental Collection Efficiency (E_x) and Computed Collision Efficiency (E_c) for Collector Drops of Radius A with Approximately Zero Charge

p	.18		.20		.22		.24		.42		.46		.50		.64	
A (μm)	E_x	E_c	E_x	E_c	E_x	E_c	E_x	E_c	E_x	E_c	E_x	E_c	E_x	E_c	E_x	E_c
15-24									.21	.14	.18	.15			.05	.15
25-34													.01	.46		
45-54	.26	.48			.12	.58										
55-64			.23	.65												
65-74					.07	.75	.07	.78								
85-94			.23	.81	.10	.83	.11	.85								
95-104					.11	.85										
105-114	.23	.81			.13	.86										

Table 1

Comparison of Experimental Collection Efficiency (E_x) and Computed Collision Efficiency (E_c) for Collector Drops of Radius A with Approximately Zero Charge

p	.18		.20		.22		.24		.42		.46		.50		.64	
A (μm)	E_x	E_c	E_x	E_c	E_x	E_c	E_x	E_c	E_x	E_c	E_x	E_c	E_x	E_c	E_x	E_c
15-24									.21	.14	.18	.15			.05	.15
25-34													.01	.46		
45-54	.26	.48			.12	.58										
55-64			.23	.65												
65-74					.07	.75	.07	.78								
85-94			.23	.81	.10	.83	.11	.85								
95-104					.11	.85										
105-114	.23	.81			.13	.86										

WATER DROP INTERACTIONS

C. R R. Saunders
University of Manchester
Institute of Science and Technology, Manchester
England

Abstract

Research in this department has centered on the role of the water drop in atmospheric physics. The principal interest has been in determining whether drops, either singly or by interacting with others, can modify the physical conditions inside natural clouds. By the practical modelling of water drop interactions in the laboratory in a variety of experiments, it has been shown that 1) partial coalescence is followed by satellite drop production which modifies the cloud drop-size distribution and can accelerate rainfall; 2) the freezing of supercooled drops may be accompanied by ice splinter production; 3) the vibrational frequencies of supported and freely suspended drops are modified by the presence of electric charge and electric fields; 4) interacting drops can separate charge in the weak electric field of the atmosphere in such a manner as to increase the electric field but more usually to decrease it; 5) when the ambient electric field has reached values far below that needed for breakdown of the air, two interacting drops can promote breakdown, which in natural clouds will initiate lightning.

The paper will deal with aspects of these phenomena of relevance to the Conference and in particular will present the latest results on the interaction behaviour of two water drops in an electric field.

Water drop interactions play an important role inside natural clouds; the coalescence of drops modifies the size distribution and is responsible for the growth of individual drops to precipitation drop size such that they will fall from the cloud as rain. Drop interactions within the ambient electric field of the lower atmosphere, when they result in separation, are able to separate electric charges between the two interacting particles which due to a size difference may fall at different speeds thus separating electric charge over a large volume of the cloud.

DROP COALESCENCE AND SATELLITE DROP PRODUCTION

Research in this laboratory has been closely involved with these processes and both experimental and theoretical studies have been made. Utilising the apparatus shown in Fig.1, Brazier-Smith, Jennings and Latham[1] were able to produce two controllable streams of water drops of radii R and r between 150 and 750μm with R/r in the range 1.0 to 2.5, relative velocity U from 0.3 to 3.0 m.sec^{-1} and impact parameter X, the perpendicular distance between the centre of one drop and the undeflected trajectory of the other from X = 0 to (R+r), the maximum value for contact. Water flow from the reservoir was modulated by two oscillating pumps before it passed through fine hypodermic needles. The flow

rate, frequency of modulation and size of needle controlled the size of the drops. Several types of interaction were noted:- 1) bouncing contact, with the air film preventing contact, 2) permanent coalescence and 3) temporary coalescence with and without satellite drop production. These categories are shown in Fig.2. Fig.3 indicates the collision parameters where ϕ is the angle between the streams of drops and V_R and V_r are the drop velocities, then: $U^2 = V_R^2 + V_r^2 - 2V_RV_r\cos\phi$. ϕ was measured photographically and the velocities could be determined from the modulator frequency. A critical value of X was found, X_c, above which separation of the drops occurred and below which the coalescence was permanent; thus a coalescence efficiency was defined:

$$\epsilon = \left(\frac{X_c}{R + r}\right)^2.$$

ϵ was zero when bouncing occurred for low velocity collisions with X nearly equal to $(R+r)$. At higher velocities, the other collision categories occurred and at large values of X, the angular momentum was sufficient to cause separation of the temporarily united drops and the long filament which was pulled out as they separated broke into small satellite droplets. Only at values of X close to X_c was separation not accompanied by satellite production, and because this was such a limited range of all the possible values of X which did produce satellites, it was assumed that such production is common in nature.

The criterion for separation was simply that it occurs if the rotational energy exceeds the additional surface energy required to reform the two drops from the coalesced drop-pair of radius R_o rotating with angular momentum J about its centre of gravity.

$$J = (4\pi\rho UXr^3R^3)/[(3)(R^3 + r^3)]$$

where ρ is the drop density. The rotational kinetic energy, $J^2/2I$, is given by $\text{R.E.} = 5\pi\rho U^2X^2R^6r^6/(3R_o^{11})$ where I is the moment of inertia of a sphere rotating about an axis through its centre $(I = 8\pi R_o^5\rho/15)$. The additional surface energy S.E. needed to reform two drops of surface tension σ is

$$4\pi r^2\sigma(1+\gamma^2 - [1+\gamma^3]^{\frac{2}{3}}) \quad \text{where } \gamma = R/r.$$

When $X = X_c$ at the boundary between coalescence and separation, S.E. = R.E., and

$$\epsilon = 2.4\sigma f(R/r)/(r\rho U^2) \qquad (1)$$

where $f(R/r) = [(1+\gamma^2 - (1+\gamma^3)^{\frac{2}{3}})(1+\gamma^3)^{\frac{1}{3}}]/[\gamma^6(1+\gamma)^2]$ which varies from 1.3 for $R/r = 1$ to 3.8 for $R/r = 3$. $U^2r\rho/\sigma$ is a dimensionless parameter characterizing the interaction process.

Fig.4 shows the measured variations of $\beta(= \epsilon^{\frac{1}{2}})$ and ϵ for values of r and $U^2r\rho/\sigma$ respectively for equal sized drops. The theoretical curves were obtained from the above equation. β decreases as U and r increase and ϵ decreases from 1 towards zero as $U^2r\rho/\sigma$ increases from 3 to infinity. Fig.5 is for unequal drop sizes. In all cases excellent agreement was noted between the experimental data and theory. The results showed that ϵ lies

between 0.1 and 0.4 for equal sized drops and between 0.2 and 0.6 for drops with R/r = 2.0. At larger values of R/r less angular momentum was available to pull the two drops apart.

Fig.6 shows the effect of small equal and opposite electric charges on the drops, of magnitude similar to that found in natural clouds. At the lower velocity the drops had longer to interact and hence ϵ reached a higher value than at the higher velocity. The charges were sufficient to modify the trajectories of the drops only slightly causing ϵ to reach a maximum value for charges of ± 3pC.

Brazier-Smith, Jennings and Latham[2] made use of the above data in a stochastic computation of the development of rainfall taking into account the production of satellites in an attempt to explain the rapid increase in drop size as revealed by radar which occurs in thunderclouds. The above theory predicts that drops of radii between 300μm and 500μm colliding at their terminal velocity with larger drops of radius greater by a factor of between 1.5 and 3.0 will provide the largest contribution to the rate of production of satellites which are typically of 80μm radius, a typical event producing about 3 satellites. A stochastic growth equation was generated which permitted calculations to be made of the evolution of a distribution of drops within a homogeneous cloud. The breakup of drops larger than 3mm radius was included in the computation but was found to be less important than satellites in the production of rainfall. In order to compute rainfall rates account was taken of the continuous collection of non-precipitating cloud water by the drops. The cloud water was released by condensation at a rate J mg.m^{-3}s^{-1}. The initial drop spectrum A consisted of 2,500 drops per cubic metre in the radius range 30 to 100μm with a water content of 3 mg.m^{-3}. Four types of interaction were considered: Case 1, Coalescence efficiency ϵ given by equ. 1, satellites produced; Case 2, ϵ given by equ. 1, no satellites produced; Case 3, ϵ=1, no satellites; Case 4, ϵ=0, with satellites. It was found that the time taken for the precipitation intensity to reach 10mm.hr^{-1} occurred at about 850sec for all cases; thereafter they diverged so that at an intensity of 50mm.hr^{-1} the time interval between cases 3 and 4 (the fastest and slowest respectively) was only 1 minute. Cases 1 and 2 were identical showing that the influence of satellite drops and the particular value of ϵ chosen are not important to the rainfall rate. By increasing J, the precipitation intensity increased rapidly showing that micro-physical processes involving raindrops are much less important than the rate of release of cloud water. Fig.7 shows the raindrop size-distribution after 20min in which it is seen that the rate of production of large drops is sensitive to the value of ϵ. Case 3, for ϵ=1, has developed the largest drops, and in Case 1, the satellite drops lead to a bimodal distribution with a peak around 100μm. This most realistic case is shown in more detail in Fig.8. The unrealistic depletion of smaller drop sizes is due to the cut-off of the initial size distribution at 30μm and the non-replenishment by coalescence of cloud droplets. The radar reflectivity, $\Sigma n_i r_i^6$, was determined and increased by an

order of magnitude every 2½min. Because of the r^6 dependence, the satellites produced a negligible contribution. Thus the overall conclusions of this work were that the contribution of satellite drops to the rainfall rate is insignificant.

In a development of this work Brazier-Smith, Jennings and Latham[3] computed the effects of evaporation and drop-interactions on a rainshaft. They concluded that the coalescence of raindrops acts to preserve within the rainshaft a considerable amount of liquid water that would otherwise have been lost by evaporation. Another conclusion was that the capture of small and satellite drops by larger raindrops is more efficient than evaporation in removing the smaller particles from the spectrum.

INTERACTING WATER DROPS: CHARGE TRANSFER

Sartor[4] showed that high electric fields may be rapidly generated by the interacting particles which separate charge in such a manner as to continually enhance the existing field. This process is known as the inductive process of thunderstorm electrification. Latham and Mason[5] calculated that if two contacting, conducting spheres separate in an electric field, then the amount of charge, q, which is transferred is given by:

$q = 1.1 \times 10^{-10} \gamma_1 E r^2 \cos\theta$ where θ is the angle between the electric field and the line of centers of the spheres at the moment of separation; γ_1 is a function of r/R which decreases from $\pi^2/2$ when r/R = 0 to $\pi^2/6$ when r/R = 1. In an experimental study of this effect the apparatus shown in Fig.1 was used, with the addition of a horizontal electric field and two induction cans connected to electrometers in order to catch and measure the charge on the drops after separation. The type of interaction used is shown in Fig.3(iv) in which the fine filament drawn out condenses to form satellite drops. Preliminary measurements of the charge transfer are shown in Fig.9 in which the theoretical line is calculated from the equation above. In the upper graph for equal drops there is an indication that the charge transfer is larger than that predicted by theory. Censor and Levin[6] have computed theoretically the charge transferred between two drops which have a long neck between them prior to separation. For example, for a filament of length 4R for equal drops the charge transfer is enhanced by 100% above that for the separation of undeformable drops. Without taking this enhancement into account Jennings and Latham[7] showed that the charge transfer process is capable of separating 1 Coul.$km^{-3}min^{-1}$ of charge in an existing electric field of 30kV/m typical of an embryo thunderstorm having a typical precipitation water content of 4 $gm.m^3$. Such a charge separation rate was shown by Mason[8] to be a requirement of a satisfactory thunderstorm electrification theory. However, this particular interaction studied here separates charge in a manner which reduces the electric field. Sartor envisaged a process whereby the drops do not swing around each other while in contact but separate before swinging round; such a process is more likely to occur in clouds below 0°C when solid particles interact. Thus

it seems that in all-water clouds, interactions occur which dissipate the field, and if the enhanced charge transfer due to the filaments is taken into account, this dissipation will be even faster. It seems even more difficult now to explain "warm-cloud thunderstorms", containing no ice, which have been reported in the literature. Experiments on this important subject are being continued in UMIST.

VIBRATIONAL FREQUENCIES OF DROPS

This subject is of interest because of the possibility of determining drop sizes within clouds by using a ground-based radar whose return signal is modulated by the vibrating drops. Rayleigh[9] determined the natural frequency of vibration of a drop carrying electric charge:

$$f = f_o\left(1 - \frac{Q^2}{64\pi^2 R^3 T \varepsilon_o}\right)^{\frac{1}{2}}$$

where Q is the charge on the drop, T is the surface tension and f_o is the charge-free frequency given by $(2T/\pi^2 R^3 \rho)^{\frac{1}{2}}$. Experiments were conducted by Saunders and Wong[10] using a vertical wind tunnel to freely suspend the drops and a high-speed camera to record the drop vibrations from which their frequency could be determined. The results were is excellent agreement with theory and showed that for a typical 2mm radius drop carrying 3 x 10^{-10}C the measured drop-size would suffer an error of 0.6%. Of more importance is the effect of the electric field; a field of 6 x 10^5V m^{-1} in this case leads to an error of 8.5%. Brazier-Smith, Brook, Latham, Saunders and Smith[11] investigated the behaviour of vibrating drops in an electric field and developed a theory to relate the vibrational frequency to the electric field. Experimental measurements agreed well with this theory. Thus if the vibration of raindrops is to be used to determine drop-size distributions in highly electrified clouds, the field strength will have to be measured independently.

LIGHTNING TRIGGERING BY INTERACTING WATER DROPS

The most favoured explanation for the initiation of lightning has been that positive corona is given off from the surface of a highly distorted raindrop in a high electric field. Unfortunately the electric field required for this to occur is over 550kV/m, whereas the maximum field measured in a thunderstorm is 400kV/m. A field of 400kV/m is able to extend the length of positive streamers which suggests that this value of field is required for lightning initiation. A recent study at UMIST, Crabb and Latham[12], has been made to discover whether a pair of raindrops within a thundercloud may be grossly distorted and produce corona at a lower onset field than a single drop. Fig.10 shows the apparatus in which a large drop of radius 2.7mm could be dropped while a smaller drop of radius 0.65mm could be ejected upwards so that the two collided within a vertical electric field with a realistic relative velocity of 5.8m.sec^{-1}. A storage oscilloscope was connected to the lower plate which was grounded and thus positive corona discharge given off from the underside of the drops could

be detected. Fig.11 shows several of the interactions: 'd' shows a central collision with the larger drop in the 'bag mode'; in 'e' the smaller drop has broken through the bag. The most glancing collisions (b,c,f) resulted in the formation of liquid filaments sometimes 20mm long which broke up into droplets. 70% of all interactions resulted in the emission of corona with a minimum field of 250kV/m producing corona when the filament length was a maximum. Corona occurred for central collisions in fields of around 500kV/m. Continuous corona was not observed, usually around 10^{-10}C of charge was released which is insufficient when all drop interactions are taken into account, to reduce the conductivity of the cloud and hence inhibit field growth. However, by assuming that corona is initiated in fields below 350kV/m if the two drop radii are greater than 1.8mm and 0.65mm, then in a cloud of precipitation water content 1gm/m^3 the rate of corona events is 2×10^{-2}m^{-3}s^{-1}, which is 1 per minute per cubic metre which is adequate to explain lightning initiation.

ICE PARTICLE MULTIPLICATION

One of the most puzzling problems in atmospheric physics at present is the discrepancy between the concentration of ice particles in clouds whose lowest temperature is above -12°C, compared with the concentration of ice forming nuclei. For example, Hobbs[13] found that the ratio of ice crystal concentration to ice nucleus concentration decreased sharply with decreasing temperature from about 10^4 at -5°C to unity at -25°C. In such clouds there are always observed rimed ice pellets of a few millimetres diameter together with large supercooled drops of radius greater than 250μm. The most likely mechanism of ice particle multiplication is one in which supercooled drops shatter on freezing, either in isolation or when they impact onto an ice pellet and form rime. Hallett and Mossop[14] have found that several hundred ice splinters were ejected for every milligramme of accreted rime, a result which is 3 orders of magnitude greater than other workers and has not yet been independently verified, but which is sufficiently large to explain the discrepancy. An investigation of the isolated drop freezing process has been proceeding in Manchester. Gay[15] has constructed a chamber, Fig.12, in which supercooled water droplets can be freely suspended in atmospheric conditions while their freezing behaviour is noted. The charged drop is introduced into an electrodynamic field by Blanchard's bubble bursting technique[16]. The drop is supported by a vertical d.c. field and constrained by an alternating potential applied to a metal ring surrounding the drop. Holes in this ring permit observation of the drop whose vertical position can be controlled by varying the d.c. field. The whole electrode system is surrounded by a low temperature chamber and an attempt was made to maintain the environment in a supersaturated state so that if an ice splinter were to be ejected upon freezing, it would grow and could be detected. It proved impossible, however, to achieve supersaturation due to the deposition of the vapour upon the electrode. With this limitation, the freezing of supercooled drops was studied. Below -15°C the drops often froze spontaneously;

above this temperature nucleation was induced by introducing silver iodide. The charge-to-mass ratio of the drop was determined before and after freezing; freezing resulted in the drop being displaced and it could be restored to the original position by adjusting the d.c. potential. The drop size was measured, and the initial charge on the drop was known. Table 1 shows the frequency of occurrence of the various freezing modes. In 70% of the cases freezing occurred rapidly with an increase in charge to mass ratio of 5 - 10%; no visible matter was ejected and the drop remained spherical. In 18% of the cases surface irregularities occurred but again no visible splinters were ejected. For 3% of the cases, frost-like growths on the frozen drop were seen to detach themselves from it and were swept up in the electric field. In 10% of the cases the frozen drop exhibited subsequent changes in its charge to mass ratio. 2% of freezing drops which were allowed to evaporate to the Rayleigh limit froze on disruption, the charge to mass ratio decreased but no splinters were observed. Calculations of the mass loss showed that it exceeded the theoretical evaporative mass loss on freezing and was therefore due to the ejection of either liquid or solid material. The general conclusion of this work is that drops in the radius range 25-100μm produce, typically, 40 splinters when they freeze with maximum production at -5°C, but the conclusions are based on secondary evidence only, it being impossible to capture a splinter. Such a number of splinters is adequate to explain the ice multiplication in clouds as shown by the stochastic treatment of Chisnell and Latham[17]. This multiplication process is of such importance that more effort needs to be expended in order to develop a method of permitting a droplet to freeze in a supersaturated environment so that the splinters produced will grow and may be captured.

CONCLUSION

Work in UMIST is directed towards solving some of the outstanding problems in atmospheric physics and in particular the role that water drops and water drop interactions play in the physical and electrical growth and development of clouds. To this end work is continuing into the coalescence of drops, both experimental and theoretical in order to build up a realistic picture of the development of a cloud particle spectrum through the life-time of a cloud. Laboratory simulations of charged water drop interactions in electric fields are continuing in order for us to be able to understand "warm-cloud" electrification. The study of the triggering of lightning is to be extended to a large scale laboratory cloud to learn whether the individual interactions which lead to corona discharge will occur in a more realistic environment with many more than just two particles present. It is hoped to devise a means of freely supporting a supercooled drop in a supersaturated environment in order that any fragments which may be emitted upon freezing can be captured and identified in order to resolve the most important ice multiplication problem.

REFERENCES

1 P R Brazier-Smith, S G Jennings and J Latham, "The interaction of falling water drops: coalescence" Proc.Roy.Soc.Lond.A.326, 393-408 (1972)
2 P R Brazier-Smith, S G Jennings and J Latham, "Raindrop interactions and rainfall rates within clouds" Quart.J.Roy.Met.Soc., 99,260-72 (1973)
3 P R Brazier-Smith, S G Jennings and J Latham, "The influence of evaporation and drop-interactions on a rainshaft", Quart. J. Roy.Met.Soc., 99, 704-22 (1973)
4 J D Sartor "The role of particle interactions in the distribution of electricity in thunderstorms" J.Atmosc.Sci., 24, 601-15 (1967)
5 J Latham and B J Mason "Electric charging of hail pellets in a polarizing electric field" Proc.Roy.Soc.A.266, 387-401 (1962)
6 D Censor and Z Levin "Electrostatic interaction of axisymmetric liquid and solid aerosols" Univ. Tel-Aviv,ES73-015 (1973)
7 S G Jennings and J Latham"The charging of water drops falling and colliding in an electric field" Arch.Met.Geoph.Biokl.Ser.A, 21,299-306 (1972)
8 B J Mason "Critical examination of theories of charge generation in thunderstorms" Tellus, 5, 446-60 (1953)
9 Lord Rayleigh "On the equilibrium of liquid conducting masses charged with electricity" Phil.Mag.,14,184-6 (1882)
10 C P R Saunders and B S Wong "Vibrational frequencies of freely falling charged water drops" J.Atmos.Terr.Phys.,36,707-11 (1974)
11 P R Brazier-Smith, M Brook, J Latham, C P R Saunders and M Smith "The vibration of electrified water drops" Proc.Roy.Soc.Lond.A, 322, 523-34 (1971)
12 J A Crabb and J Latham "Corona from colliding drops as a possible mechanism for the triggering of lightning" Quart.J.Roy,Met.Soc. 100, 191-202 (1974)
13 P V Hobbs "Ice multiplication in clouds" J.Atmos.Sci.,26,315-8 (1969)
14 J Hallett and S C Mossop "Production of secondary ice particles during the riming process" Nature Lond, 249, 26-8 (1974)
15 M J Gay, Ph.D. Thesis, UMIST (1974)
16 D C Blanchard "A simple method for the production of homogeneous water drops down to 1μm radius" J.Coll.Sci.9,321-8 (1954)
17 R F Chisnell and J Latham "A stochastic model of ice particle multiplication by drop splintering" Quart.J.Roy.Met.Soc.100, 296-308 (1974)

Figure 1

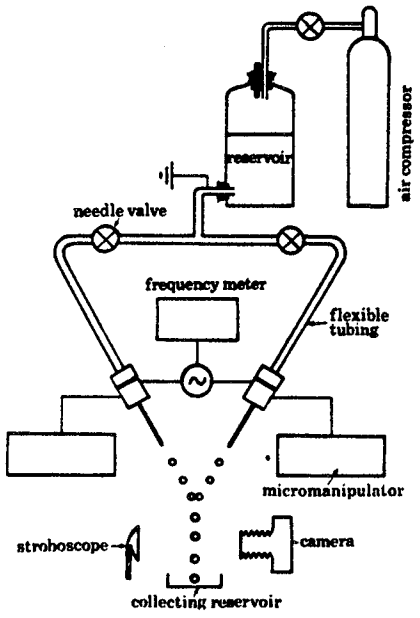

Apparatus for studying the interaction of falling drops.

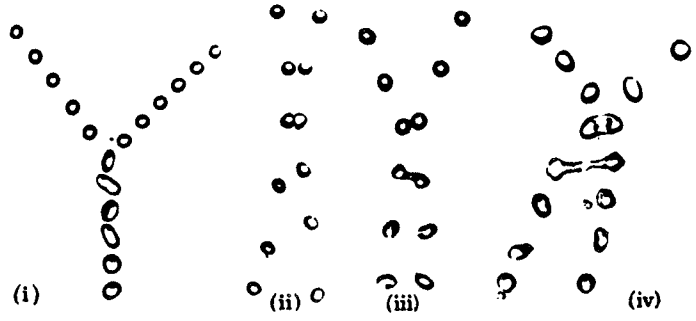

Drop collision categories: (i) permanent coalescence; (ii) bouncing; (iii) separation without satellites; (iv) separation with satellites.

Figure 2

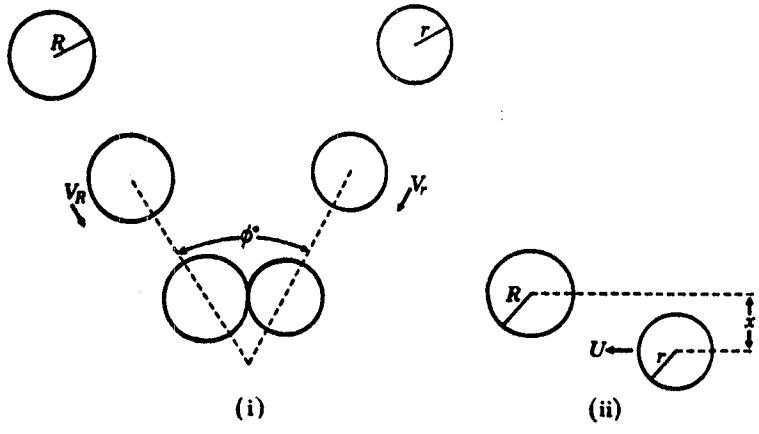

Diagram defining collision parameters. Interaction viewed from the frame of reference of (i) the laboratory, (ii) one of the drops.

Figure 3

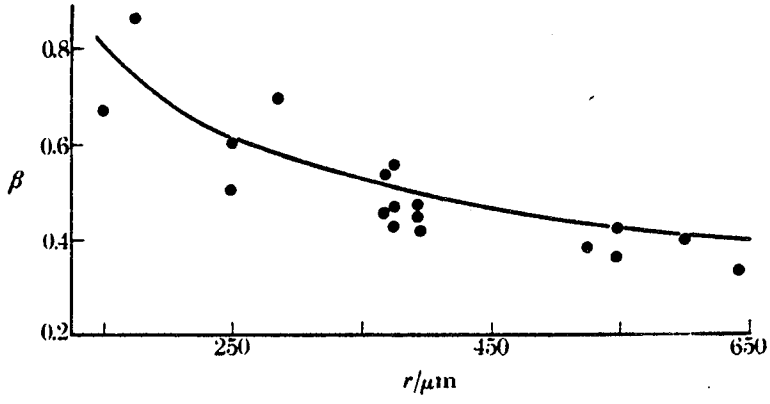

The variation of linear coalescence efficiency, β, with drop radius r. $U_t = 1.5$ m s^{-1}, $R = r$. ●, Experimental points; ———, theoretical curve.

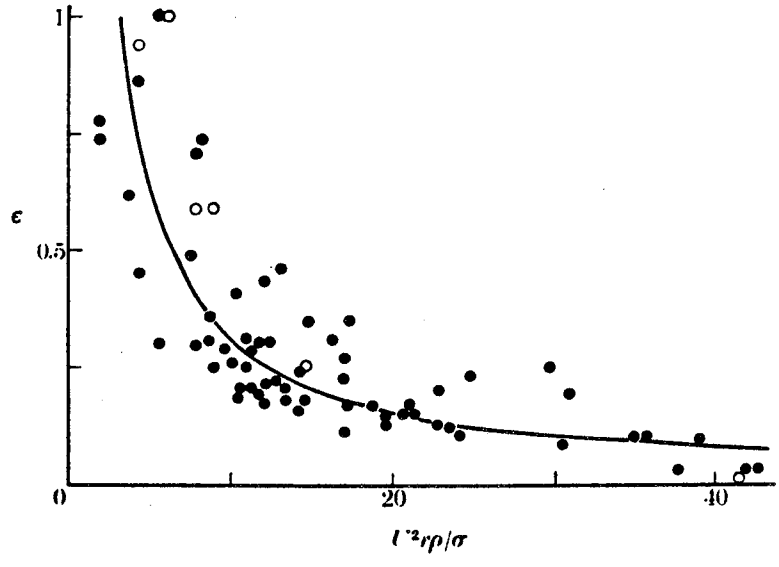

The variation of coalescence efficiency, ϵ, with the dimensionless parameter $l'^2r\rho/\sigma$ for identically sized drops. ●, Experimental points from present experiments; ○, experimental points from Adam *et al.* (1968); ———, theoretical curve.

Figure 4

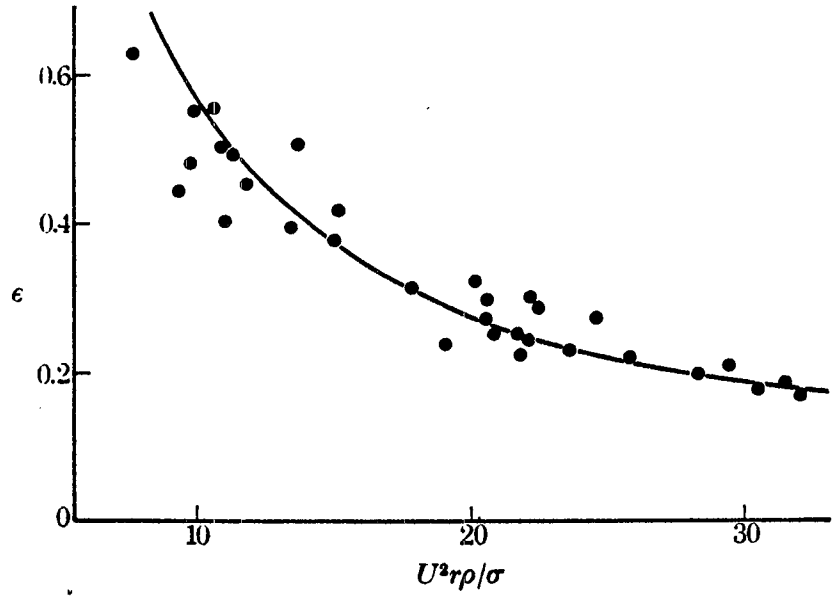

The variation of coalescence efficiency, ϵ, with the dimensionless parameter $U^2r\rho/\sigma$ for unequally sized drops. $R/r = 1.75$. ●. Experimental points; ———, theoretical curve.

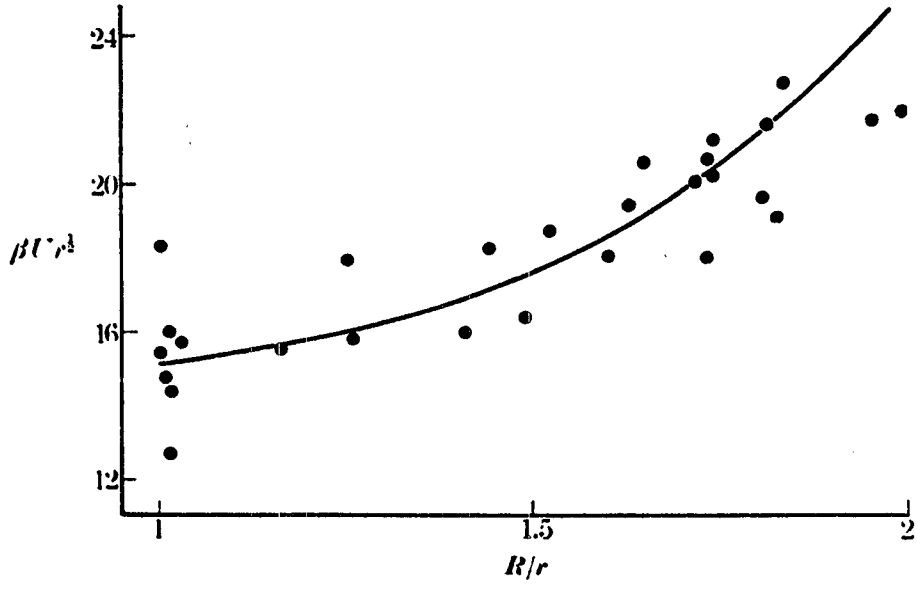

The variation of $\beta U r^{\frac{1}{2}}$ with radius ratio R/r. ●. Experimental points; ———, theoretical curve.

Figure 5

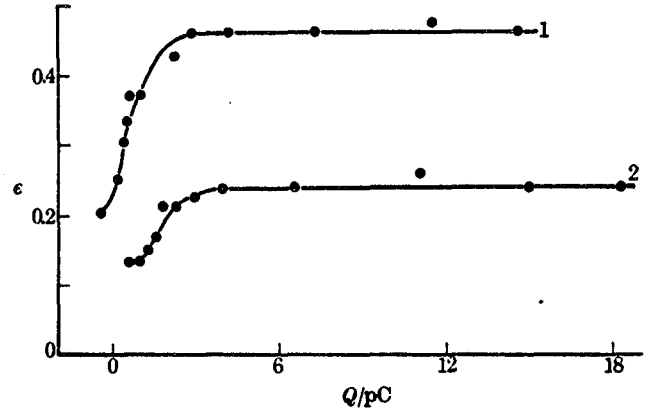

The variation of coalescence efficiency, ϵ, with drop charge Q for equally sized drops of radius 500 μm. ●, Experimental points; ———, experimental curve. 1, $U = 1.5$ m s^{-1}; 2, $U = 2.0$ m s^{-1}.

Figure 6

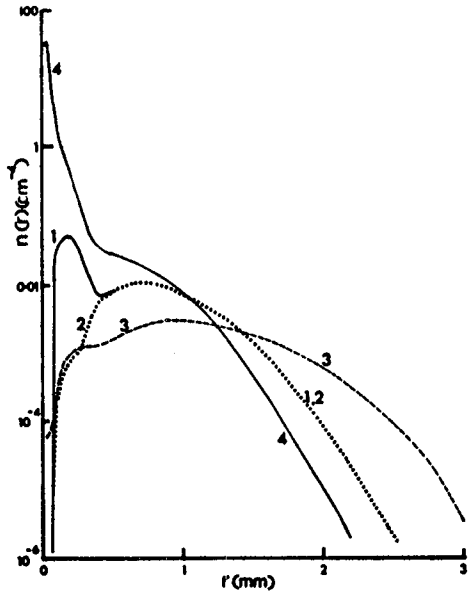

The calculated drop-size distributions after 20 min for Cases (1) to (4). Spectrum A, J_w= 2·5 mg m^{-3} s^{-1}.

Figure 7

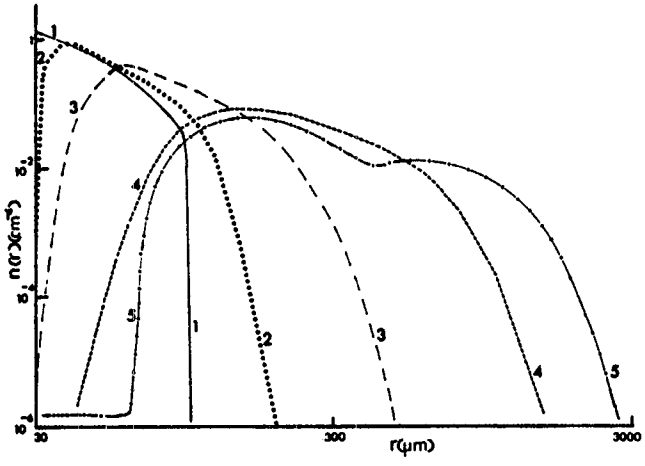

The calculated drop-size distributions at various times t. Spectrum A. Case (1). J = 2·5 mg m^{-3} s^{-1}. (1) t = 0; (2) t = 300 s; (3) t = 600 s; (4) t = 900 s; (5) t = 1,200 s.

Figure 8

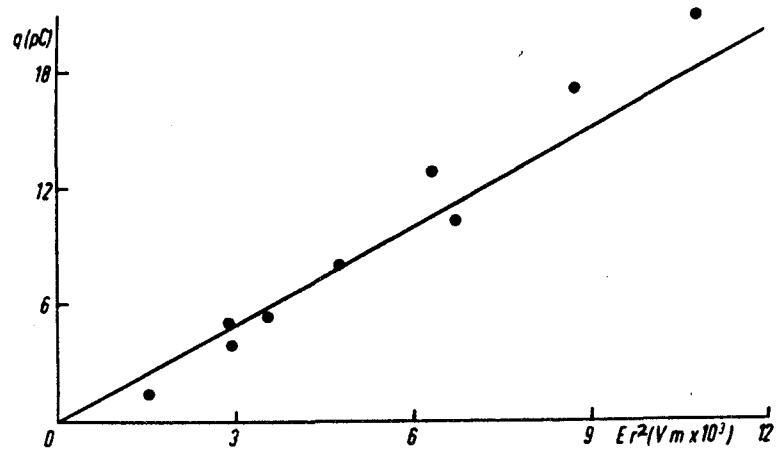

The relation between charge transfer q and Er^2 for equally sized drops. $\Theta = 0$
● experimental points; —— theoretical curve from Eq. (1)

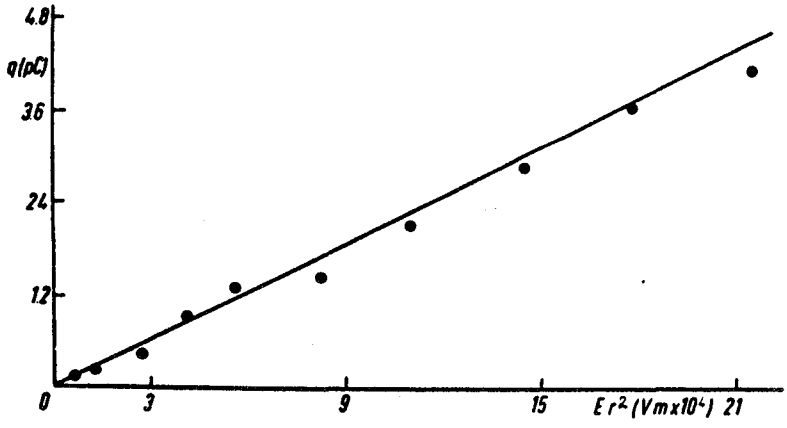

The relation between charge transfer q and Er^2 for unequally sized drops
● experimental points; —— theoretical curve from Eq. (1)

Figure 9

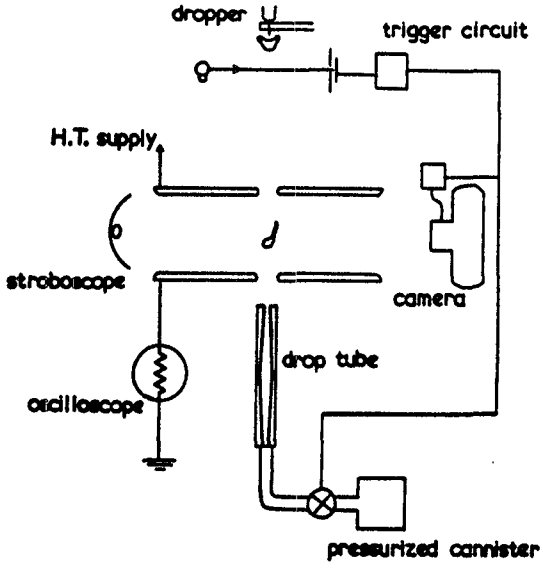

Apparatus for studying corona from colliding drops.

Figure 10

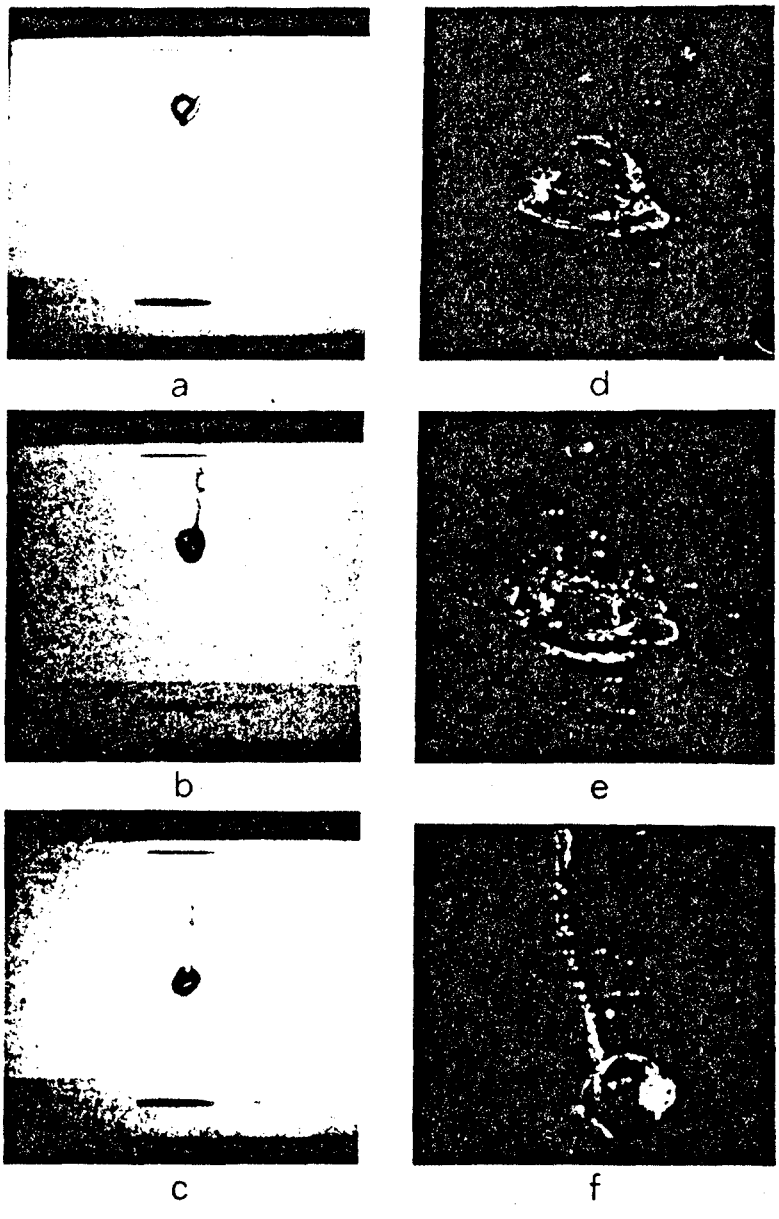

Various shapes assumed by drops of radius 2·7 mm colliding with ones of radius 0·65 mm with a relative velocity of 5·8 m s^{-1}. Photographs b, c, f: glancing collisions; e, d: head-on collisions; a: positioning at impact intermediate between the other two categories. Features on these photographs are discussed more fully in the text.

Figure 11

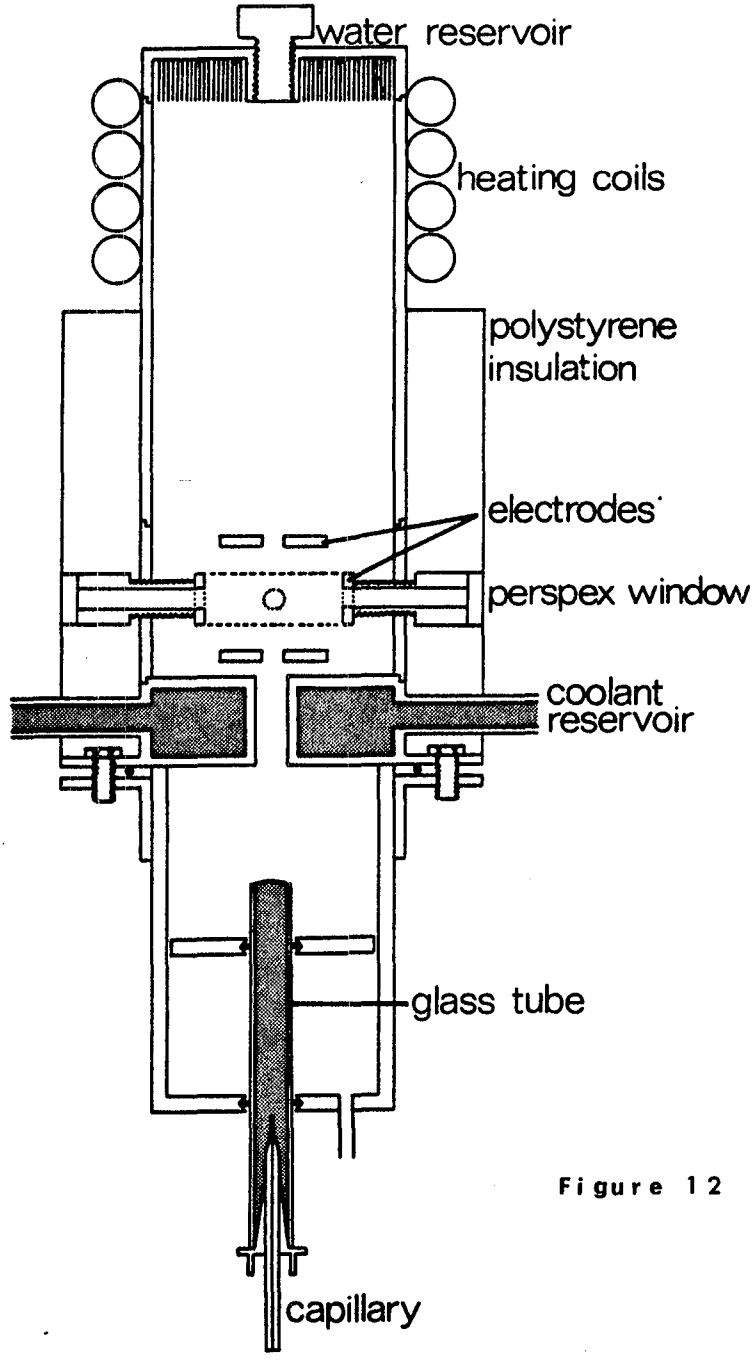
water reservoir
heating coils
polystyrene insulation
electrodes
perspex window
coolant reservoir
glass tube
capillary

Figure 12

Frequency of occurrence of various modes of freezing

Mode of freezing	Number of drops	% increase in charge-to-mass ratio	$\Delta T^{o}C$
"common"	377	5 - 10%	0 - 29
spikes & bulges	98	~ 10%	5 - 25
splinters	19	~ 10%	~ 15
secondary mass loss	53	-	1 - 15
Rayleigh freezing	2*	decrease	10
drop splitting	1	~ 5%	8
total	549		

* out of 100 drops in a separate study.

Table 1

NUCLEATION THEORY AND ITS ATMOSPHERIC APPLICATIONS

C. S. Kiang
National Center for Atmospheric Research*
Boulder, Colorado 80303

D. Stauffer
Institute of Theoretical Physics, University
66 Saarbrucken, West Germany

V. A. Mohnen
Atmospheric Sciences Research Center
State University of New York at Albany
Albany, New York 12222

Patrick Hamill
Physics Department
Clark College and Center for Environmental
and Resource Studies
Atlanta University Center
Atlanta, Georgia 30314

G. H. Walker
Physics Department
Clark College and Center for Environmental
and Resource Studies
Atlanta University Center
Atlanta, Georgia 30314

*The National Center for Atmospheric Research is sponsored by The National Science Foundation

NUCLEATION THEORY AND ITS ATMOSPHERIC APPLICATIONS

I. INTRODUCTION

In recent years, the growth of interest in the study of nucleation theory for metastable systems has greatly increased. This increased interest is due in part to the fact that nucleation in supersaturated vapors or superheated liquids is one of the most important aspects of many fields, such as the atmospheric sciences, biology, chemistry, industrial engineering, and physics. A serious communication problem and a disconcerting lack of overall direction among research efforts always exist in a field involving multiple disciplines. One of the methods of speeding up scientific progress is to bring together information from various fields relating to one common problem. The International Colloquium of Drops and Bubbles certainly will provide an opportunity to exchange information from different disciplines on the science of liquid drops and bubbles in liquids.

From the viewpoint of kinetic theory, liquid drops in a gas phase or gas bubbles in a liquid phase can be considered one of the metastable states of gas-liquid phase transition. This phase transition is initiated by nucleation. In general, the metastable states can be described by three stages: (1) the development of a supersaturated state; (2) the generation of nuclei of the new phase; (3) the growth of these nuclei to form larger drops or larger bubbles.

The supersaturated state can result from changes in physical parameters (pressure, temperature, tension, etc.) or by chemical-photochemical production of reactants which have low volatility. Nuclei of the new phase can be generated homogeneously by: (1) homogeneous homomolecular nucleation, which involves only one gaseous component; (2) homogeneous heteromolecular nucleation, which involves two or more gaseous components, i.e., H_2SO_4 and H_2O molecules can combine to form a sulfuric acid drop. They can also be generated heterogeneously by the additional force fields associated with ions, impurities, surface or structural imperfections. Each of these heterogeneous nucleations can be, of course, either homomolecular or heteromolecular. In this report, we concentrate our efforts on the studies of the nucleation phenomenon and its atmospheric applications. The growth processes are covered by other speakers in this colloquium and will not be discussed here.

We briefly discuss the present status of the homogeneous nucleation theories and experiments from the vapor to the liquid phases in section II. Section III covers some selected nucleation phenomena and their roles in the atmosphere. Problems associated with nucleation theories such as "microscopic surface tension," "contact angle," etc., are examined in detail in section IV. In the conclusion, we outline some future research problems in relation to the study of nucleation phenomena.

II. HOMOGENEOUS NUCLEATION THEORIES AND EXPERIMENTS

While homogeneous nucleation processes have little application to the real atmosphere, their study is nevertheless the basis of much other, more useful theoretical work. Here, we briefly discuss the present status of homogeneous nucleation theories and experiments.

Three theoretical approaches are most commonly used for study of homogeneous nucleation phenomena, namely, (1) the thermodynamic approach[1,2] (2) the statistical approach[3,4,5] and (3) computer simulation.[6,7,8,9] Thermodynamic theories assume the equilibrium number of clusters (per cumic centimeter) C(n), containing n molecules to be proportional to $\exp(-\Delta G_n/kT)$, where ΔG_n and the value of the proportionality factor for C(n) are controversial, most thermodynamic theories result in the general form

$$\Delta G_n = -n\cdot kT\cdot \ln(y) - n^{\sigma}\cdot kT\cdot \ln(x) + \tau kT\cdot \ln(n) + \text{const} \tag{1a}$$

$$C(n) = q_o\cdot n^{-\tau} x^{n^{\sigma}} y^{n} \tag{1b}$$

Thus C(n) = pre-exponential factor·exp[-(bulk term + surface term)/kT]. In "classical" nucleation theory[10] one has $\tau=0$ and $q_o=C(1)$=concentration of single molecules. The y-term comes from the bulk formation energy, the x-term from the surface free energy (the leading correction excess free energy, $x<1$ for positive surface tensions), and the physical interpretation of the logarithmic and constant term in Eq. (1a) are controversial[3-5]. In general the bulk term

$$y = \exp(\mu-\mu_{coex})/kT \tag{2a}$$

and for ideal gas laws

$$y = P/P_{coex} \tag{2b}$$

where μ_{coex} and P_{coex} are the chemical potential (per molecule) and the pressure of the vapor on the coexistence curve where liquid and vapor are in equilibrium; μ and P are the values in the (supersaturated) vapor. The n^{σ} term in Eq. (1a) arises from the surface area ($\propto n^{\sigma}$, $o<\sigma<<1$, for spherical cluster $\sigma=2/3$), and the surface tension:

$$-n^{\sigma}kT\cdot \ln(x) = (\text{surface tension})\cdot(\text{surface area}) \tag{3}$$

which defines the dimensionless parameter x. It is widely accepted that the surface tension of a bulk liquid is not necessarily equal to the surface tension of a droplet containing, say, only 100 molecules. With the same surface area, a difference of surface tension, say 15%, will result in a difference of nucleation rate on the order of 10^{17},

Most controversy centers on the logarithmic term and the constant contribution to the formation energy in Eq. (1a). Different values of τ and q_o are derived from the statistical approaches of various models[3-5]. The statistical approaches have focused on the evaluation of the partition function for an "embryonic liquid" droplet and the resulting prediction for nucleation theory. The correction factors due to the rotational and translational degrees of freedom for the small droplets[3] give $\tau = -4$ and $q_o >> C(1)$. Many other results for τ and q_o have been proposed[4,5] and no general agreement has been reached[11].

Previous experimental reports[12-14] (see Table I) have indicated that nucleation rates measured for H_2O, CH_3OH, and C_2H_5OH are in good agreement with the predictions of the classical theory, whereas NH_3, C_6H_6, $CHCL_3$,

and CCL_2F are found to be in remarkably good agreement with the Lothe-Pound theory.[9-13] This non-uniformity of results has furthered the controversy with respect to the treatment of rotational and translational terms in the free energy of an embryo. These terms give rise to a factor of 10^{17} in the prediction of nucleation rates. However, it should be noted that the comparison between experiment and results of the classical theory and of the comparison between experiment and results of the Lothe-Pound theory has been made using the measured bulk surface tnesion for the liquid droplet. As pointed out before, a 15% change in the surface tension of a small droplet would affect the nucleation rate by a factor of 10^{17}. Therefore, a closer examination of the calculation of the surface tension (or of the surface free energy term in the formation energy of an embryo) for small droplets is desirable. In section IV, we will examine the calculation of "microscopic" surface tension in detail.

A computer simulation of small clusters should, in principle, give an exact answer to all the controversial problems mentioned above. However, the usual microcrystalline approximations[6,7] have considered only the intermolecular binding energy and the vibrational free energy for a given configuration but neglected the anharmonic vibrational terms and the configurational entropy. (For the same number n of molecules numerous different "equilibrium" configurations exist, particluarly for liquid droplets.) From molecular dynamics and Monte Carlo simulations of argon clusters,[7,8] which take into account such necessary corrections, one observes that the droplet formation energy can differ by as much as 100 kT from the microcrystalline harmonic approximation, giving a difference of a factor 10^{43} in the nucleation rate. Recently, Binder[15] has investigated the thermodynamic properties of metastable states and nucleation process in the lattice gas model by Monte Carlo method. Although this approach provides an insight into the properties of metastable states, the lattice gas model is unrealistic.

In conclusion, the computer simulation approaches may provide accurate information on the thermodynamic properties of a small cluster and the prediction of the nucleation rate if one makes a successful choice of a suitable model. But, computer simulations are material-dependent and they are complicated for realistic intermolecular potentials. Statistical approaches are based on more fundamental principles of statistical mechanics. The controversies arise from the evaluation of the partition function which is model dependent. Further investigation of nucleation theory based on the statistical approach requires a well defined concept of "physical cluster." Thermodynamical approaches are semi-phenomenological, and thus avoid the complications of computer simulations and the controversial problems of statistical approaches. A good thermodynamic theory must be able to obtain accurate and correct parameters (such as surface tension) either from basic calculation or from experimental measurements to enable prediction of nucleation rate.

Expansion cloud chamber,[16] diffusion cloud chamber,[17] supersonic nozzle,[18] and molecular beam[19] techniques are the experimental tools most often used to check the critical supersaturation in various substances and the nucleation rate as a function of the supersaturation. An excellent critical review of various experimental measurements for different sub-

stances of critical supersaturation for nucleation of liquids from vapor was reported by Pound.[20] In this review, Pound gives brief descriptions of various experimental techniques and their limitations. Values of critical supersaturations for homogeneous nucleation of droplets from the vapor are tabulated and plotted. In addition to observing the limitations of each experimental technique pointed out by Pound, one should also examine the impurities in the substance. From the study of "binary"[21,22] and "heteromolecular"[23] nucleation theory it can be seen that the impurity factor will significantly change the values of critical supersaturation.

The authors would like to take this opportunity to inform the readers that a series of books on nucleation theory, experiment, and various applications edited by A. C. Zettlemoyer and Kiang[24] will be published in the near future. The present status of the nucleation theory and experiment will be discussed in great detail in these books.

III. ATMOSPHERIC APPLICATIONS

Selected topics of nucleation phenomena (cluster formation involving ions will not be discussed here) and their roles in the atmosphere are discussed in this section. In order to describe the roles of different nucleation processes in the atmospheric applications, we separate our discussions into two cases: relative humidity (RH) below 100% and RH above 100%.

For RH <100%, the role of nucleation theory in the atmosphere is to describe the initial stage of the atmospheric aerosol formation mechanism. The mechanism of formation and growth of aerosols in the atmosphere can be schematically illustrated by the phase transition block diagram (gas-to-particle conversion, gas-to-particle interaction, and particle-particle interaction) as shown in Fig 1. This diagram indicates all the reaction mechanisms (represented by arrows) that govern the transition of gaseous products (represented by boxes) into a solid or liquid phase.

For RH > 100%, the role of nucleation theory in the atmosphere is to describe the cloud droplet and ice crystal formation mechanism. The mechanism of formation and growth of cloud droplets and ice crystals in the atmosphere can also be schematically illustrated by the phase transition block diagram II given in Fig 2. The application of nucleation to weather modification and the mechanism for multiplication process of ice will not be discussed here.

Here we would like to discuss the most dominant nucleation processes for the aerosol formation (RH, <100%) and cloud droplet and ice crystal formation (RH > 100%).

A. Relative humidity below 100%

It is not possible to form water droplets homomolecularly under atmospheric conditions of RH <100. Relative humidity greater than 400% is required for the homogeneous homomolecular formation of water droplets, and RH > 100% for the heterogeneous homomolecular formation of water droplets

with impurities.[25] Therefore, for RH. <100%, other nucleation mechanisms are needed to form a new aerosol in the atmosphere. In a complicated system such as the atmosphere, several different gaseous molecules may come together to form an aerosol. For a completely dust-free atmosphere (or near the "source" of those different gaseous molecules) homogeneous heteromolecluar nucleation theory is required to study the initial stage of aerosol formation involving several gases. For an atmosphere containing condensation nuclei or dust particles ("surfaces") we have a situation in which heterogeneous heteromolecular nucleation theory applies.[26] This heteromolecular nucleation may be the most dominant nucleation process of droplet formation for an atmosphere with RH. <100%, since the nucleation threshold (required supersaturation) for heteromolecular nucleation can be much lower than for nucleation with pure materials (homomolecular). Other processes for the aerosol formation such as chemisorption, adsorption, and surface heterogeneous catalysis will not be discussed here.

The formation of aqueous sulfuric acid droplets is a typical example in which droplets can be formed in the atmosphere with RH far below 100% and activity $(P/P_{coex.\ H_2SO_4}$, where P_{coex,H_2SO_4} is the vapor pressure over the pure H_2SO_4) far less than one for H_2SO_4. The concentrations of the trace gases in the earth's atmosphere are measured in parts per million or parts per billion. Heteromolecular nucleation requires gaseous constituents with very low volatility; however, most of the atmospheric trace gases have high vapor pressure and their concentrations are not sufficient to allow heteromolecular nucleation out of the gas phase. Then chemical reactions, combined with radiation or other energy input, are required to produce reactants with low vapor pressure which then mix with water vapors to form new aerosols (see Fig 1). The trace gas SO_2 has very high vapor pressure (4 atm at 25°C). In the presence of water vapor and oxidants, H_2SO_4 may mix with water vapor and undergo heteromolecular nucleation to form aqueous sulfuric acid aerosol.

For binary systems, with this heteromolecular nucleation approach, we have studied the initial stage of aerosol formation for various pollutants[23,26] (H_2SO_4-H_2O, HNO_3-H_2O, etc.) and the cloud-base levels for Jupiter and Venus[4,27] (NH_3-H_2O, H_2SO_4-H_2O, HCL-H_2O, etc.).

In a ternary system, several distinct characteristics exist which a binary system does not present (for detailed discussion, see ref 28). Here we summarize those distinct characteristics as follows: (1) the nucleation rate for a ternary system is dependent not only on the relative humidity but also on the composition of the other two components at a fixed relative himidity; (2) in a ternary system, the effect of temperature on the aerosol formation is more significant,[29]; and (3) chemical reaction is more likely to occur in a ternary system. No attempt has been made to calculate the nucleation rate for a ternary system since there is not now sufficient thermodynamic data available to carry out the theoretical study.

Other problems associated with the study of heteromolecular nucleation theory will be discussed in the next section. The only experimental measurement for heteromolecular nucleation study was performed by Flood for ethyl alcohol-water mixtures;[30] the experimental results agree with

theoretical prediction.[27] Other experimental studies for H_2SO_4-H_2O and ethanol-water are in progress.[31]

B. Relative humidity greater than 100%

There are three major phase transitions which can occur in the atmosphere with RH > 100%: the condensation of water vapor to droplets; the formations of ice crystals from water droplets; and the formation of ice crystals from water vapor. The development of the supersaturated state for nucleation largely depends on the change of physical parameters such as pressure, temperature, water concentration, etc., which is not like the situation for RH <100%, where the development of the supersaturated state is largely dependent on chemical (photochemical) reactions.

Heterogeneous nucleation on soluble droplets is responsible for the condensation of water vapor to droplets. In comparison with other nucleation processes in the atmosphere, heterogeneous nucleation on soluble droplets is the least controversial since most theories and experiments for this process are in good agreement.[25] There are two effects of vapor pressure that must be considered in any treatment of the growth of droplets on a soluble particle: (1) the solution effect; and (2) the Kelvin effect. As mentioned in the previous section, vapor pressure changes over a solution as contrasted to over a pure liquid (heteromolecular effect). For example, the vapor pressure of water is less over aqueous solutions than over pure water; thus one requires less saturation than expected for pure water. Based on the thermodynamic argument, because of the Kelvin effect, one requires less saturation for the larger droplet. Therefore, from these two effects, droplets in a cloud can grow much more easily than can droplets undergoing the homogeneous nucleation process. A simple expression for the relationship between the supersaturation for water, and the solution effect and the Kelvin effect may be expressed as follows[32]

$$\ln(P/P_{coex,H_2O}) = (2M\gamma/\rho RT)\cdot(1/r) + \ln(a) \tag{4a}$$

where M is the molecular weight of water vapor, γ the surface energy of the droplet of solution, R the gas constant, r the radius of the droplet, ρ the density of the droplet of solution, and a the activity of the substance dissolved in water as defined in the last section. If one assumes that Raoult's Law governs the equilibrium vapor pressure over the solution instead of the measured activity a, then the supersaturation can be written as

$$P/P_{coex,H_2O} = \exp(2M\gamma/\rho RTr)\cdot\left[1 + \frac{im'M}{W(4/3\cdot\pi r^3\rho - m')}\right] \tag{4b}$$

where m' is the mass of solute, W the molecular weight of solute, and i the

Van't Hoff factor for the degree of dissociation of salts. This treatment was first used by Köhler,[33] modified by Wright,[34] and re-examined by McDonald[35] and Mason.[36]

Here we would like to point out that this process of heterogeneous nucleation on soluble droplets does occur in the atmosphere for RH $<100\%$ for aqueous solution droplets. For droplet growth on soluble particles involving solid phase, Eqs. (4a) and (4b) cannot be applied directly because the production of a crystalline phase may require additional supersaturation in the solution. An empirical formula was deduced by Winkler[37] to study the growth law of atmospheric aerosols involving "mixed particles"[38] of soluble and insoluble particles.

In order to form ice crystals from pure water homogeneously, the water must be supercooled to at least $-40^{o}C$.[39] Therefore, the majority of ice crystals which form in clouds with temperatures much higher than -40^{o} will be a result of heterogeneous nucleation. Depending on temperature, pressure, water content, and available surfaces, three major mechanisms are responsible for the formation of ice crystals in the atmosphere: (1) immersion nucleation (nucleation of freezing by a particle immersed in water); (2) deposition nucleation (nucleation of freezing by the deposition of water vapor on surfaces); and (3) contact nucleation (nucleation of freezing induced by a particle during first contact with supercooled water).[40]

Most studies of ice formation by heterogeneous nucleation processes derive from the basic concept of classical homogeneous nucleation theory - a macroscopic-thermydynamic approach.[25] Therefore, some weaknesses of the classical nucleation theory, e.g., the use of bulk surface tension values for microscopic nuclei, also occur in the study of heterogeneous nucleation. Furthermore, because the nucleation of foreign surfaces involves an additional degree of freedom, e.g., the nature of the nucleating surface, heterogeneous nucleation processes are more complicated to study than are homogeneous processes, and additional problems have been encountered such as the use of contact angles to describe equilibrium conditions for an embryo on a heterogeneous surface, and the difficulty associated with the treatment of the roughness of the surface. Detailed discussion of problems associated with heterogeneous nucleation processes will be presented in the following section.

IV. PROBLEMS ASSOCIATED WITH VARIOUS NUCLEATION THEORIES

In this section, selected problems associated with various nucleation theories are examined in detail. For homogeneous nucleation theory we use the Fisher droplet picture[2,41] and measured values of the second virial coefficient to determine the "microscopic" surface tension for small droplets. The estimated "microscopic" surface tension can then be used in the classical theory to calculate the nucleation rate. This approach circumvents such controversial problems as rotational, translational, configurational, and replacement partition function and gives excellent agreement between experimental measurements and our theoretical calculations of the nucleation rates for various substances. For heteromolecular nucleation theory we discuss the surface enrichment effect for a binary system,

"microscopic" surface energy and hydration effect on small droplets, and their effects on calculations of the nucleation rate. For the formation of ice crystals we present a model to study heterogeneous nucleation on a substrate. This model gives an equilibrium concentration ($\propto \exp[-\Delta G/kT]$, where ΔG is the free energy of embryo formation) without involving macroscopic thermodynamic parameters such as "contact angle," etc. A general approach for studying this heterogeneous nucleation process is qualitatively discussed.

A. Homogeneous nucleation theory

As we pointed out before, the "microscopic surface tension" is one of the most important parameters for studying nucleation theory. We adopt the Fisher droplet picture for studying "critical phenomena" to vapor-to-liquid nucleation theory of pure fields, and show how, from the static equation of state, one can determine some parameters, e.g., "microscopic surface tension," entering the theory of nucleation, a time-dependent process.

Fisher's droplet picture for the gas-to-liquid phase transition phenomenon has been applied to study gas-to-liquid nucleation processes.[2,42,43] The parameters used in this model can be determined by experimental measurement of the critical exponents.[44] The validity of extending this model from the critical point to the triple point has been examined by considering the equation of state [46] and condensation by impinging in a dense medium.[43] The agreement between this model and experimental data for the equation of state is 1% for water from the triple point to the critical point, and there is no essential difference for different treatments of the impinging rate. Here we would like to summarize the advantages of this model as follows: (1) controversial problems, such as the rotational, translational, configurational, and replacement partition function can be circumvented by use of this model; (2) this model covers a temperature range from the triple point to the critical point; (3) the "microscopic" surface tension can be estimated; and (4) the simplicity of this model means that it can be easily adapted for practical research problems.

We now outline the Fisher droplet picture and the formulation of the estimate of the microscopic surface tension for a small droplet. The free energy of a liquid drop containing n molecules can be written in the general form as Eq. (1a), and the equilibrium concentration C(n) can be expressed as Eq. (1b). With the assumption that the excluded volume effect between clusters is negligible, the equation of state for the infinite system is a generalization of the ideal gas resuls, $P/kT = C(1) = N/V$, to a mixture of ideal gases with the components being the subset of all clusters with one molecule, all clusters with two molecules, all clusters with three molecules, etc. Thus the pressure of the system is

$$P/kT = \sum_{n=1}^{\infty} C(n) = q_o \sum_{n=1}^{\infty} n^{-\tau} x^{n^{\sigma}} y^n \qquad (5a)$$

and the density of the vapor $\rho = \partial P/\partial \mu = [\partial P/\partial \ln(y)]/kT$ is given by

$$\rho = q_o \sum_{n=1}^{\infty} n^{1-\tau} x^n y^n \tag{5b}$$

Note that the critical point is defined at $x = y = 1$, where $x = 1$ defines the critical isotherm ($T = T_c$) and $y = 1$ defines the coexistence curve. With Fisher's droplet picture, the parameters τ and σ can be determined by directly measured critical indices [e.g., along the critical isotherm: $(\rho_c - \rho) \propto (\mu_c - \mu)^{\frac{\tau-2}{\sigma}} = (\mu_c - \mu)^{1/\delta}$; along the coexistence curve: $(\rho_c - \rho) \propto (T_c - T)^{\frac{\tau-2}{\sigma}} = (T_c - T)^{\beta}$, where T_c, ρ_c and μ_c are the critical temperature, critical density, and critical chemical potential respectively.] For water[45] the critical exponent δ is found experimentally to be 4.3, giving a value of $\tau = 2.23$, similarly, β has been found to be 0.35, resulting in a value of $\sigma = 2/3$. Due to the universal nature of fluid systems near the critical region,[47] all the critical exponents for fluid systems have the same value. Here we use $\tau = 2.23$ and $\sigma = 2/3$ for our calculation of the "microscopic surface tension." The extimate of the microscopic surface tension can be determined by evaluating $\ln x$ (see Eq. (3)).

From Eqs. (5a, 5b), the compressibility factor is

$$P/\rho kT = \left(\sum n^{-\tau} x^n y^n\right) / \left(\sum n^{1-\tau} x^n y^n\right) \tag{6}$$

Except near the critical region, for nearly ideal gases, $n = 1$ and $n = 2$ are the most important contributions to the compressibility factor. Thus, along the coexistence curve ($y = 1$) Eq. (6) can be approximated by

$$P/\rho kT = (x + 2^{-\tau} x^{2^\sigma}) / (x + 2^{1-\tau} x^{2^\sigma}) \tag{7}$$

Also, the compressibility factor can be expressed by the virial expansion

$$P/\rho kT = 1 + B\rho + C\rho^2 + \cdots\cdots\cdots \tag{8}$$

where B = second virial coefficient, C = third virial coefficient, etc. With $\sigma = 2/3$ and $\tau = 2.23$ determined experimentally as mentioned above, $\ln x$

can be evaluated from Eqs. (7) and (8). We obtain

$$\ln x = \frac{1}{0.5874} \ln \frac{-4.69(B\rho)}{1 + 2(B\rho)} \tag{9}$$

The nucleation rate predicted by Fisher's droplet model is derived in reference (2) and can be expressed as

$$J = P_1 S_1 q_o (2\pi m_1 kT)^{-\frac{1}{2}} |\ln x|^{(1+\tau-\sigma)/\sigma} A^{1+\tau-\sigma} \left[\sum_{\ell=0}^{\infty} A^{-\ell\sigma} \frac{\Gamma(\ell\sigma+\tau-\sigma+1)}{\ell!} \right] \tag{10}$$

$\Gamma(x)$ is the Gamma function,

where P_1, S_1, and m_1 are partial pressure, surface area and mass of single molecule, and $A = (\ln y)/[\ln x]^{1/\sigma}$ (scaled supersaturation^2). For $\sigma = 2/3$ and $\tau = 2.23$ and small A, Eq. (10) can be approximated as

$$J = 3.4 \cdot P_1 S_1 q_o (2\pi mkT)^{-\frac{1}{2}} |\ln x|^{3.85} A^{6.7} \exp(-0.148\, A^{-2}) \tag{11}$$

The results of the ratio of the nucleation rate predicted by Eq. (11) to that predicted by the "classical" theory for several substances are presented in Table II. Data for the calculations were obtained from Dawson et al.,[12] Jaeger et al.,[13] and Katz and Ostermeyer.[14] Values for the second virial coefficient were either obtained from the compilation by Dymond and Smith[48] or calculated from the tables in Hirschfelder, Curtiss and Bird.[49]

Note that for the substances listed in Table II, agreement between theory and experiment is remarkably good, particularly in view of the extreme sensitivity of the calculations to small changes in the parameters.

We might mention that the calculations for ln(x) could be greatly refined. For example, the third and higher order virial coefficients could be considered, however, the calculations which we have carried out are not intended to be more than order-of-magnitude estimates, given the lack of precise data for vapor pressures and virial coefficients.

It should also be noted that the experimentally determined nucleation rates may be imprecise due to impurities in the nucleating substance. This leads to processes such as heterogeneous or heteromolecular nucleation or both, which will greatly enhance the nucleation rate, and thus lead to experimentally measured values of required supersaturation which would be much lower than those required for pure homogeneous nucleation.

In conclusion, from our "microscopic" surface tension calculation,

it is our observation that classical nucleation theory can be considered as adequate, provided the appropriate value of the "microscopic" surface tension is used. The discrepancy between the "classical" and the "Lothe-Pound" theories may be due to the difference between the surface tension of a bulk liquid and that of a small droplet.

B. Heteromolecular nucleation theory[21,23]

To study the heteromolecular nucleation theory for a binary system, one generally expresses the formation energy of a droplet consisting of n_A water and n_B low-volatility reactant gas molecules:

$$\Delta G = (\mu_{cA}-\mu_A)n_A + (\mu_{cB}-\mu_B)n_B + S(n_A,n_B)\gamma(X) \qquad (12)$$

where μ_c = chemical potentials of the two molecular species, if gas and liquid are in equilibrium over a flat mixture surface, μ = actual chemical potentials in the supersaturated atmosphere; S = surface area of the droplet, depending on the number of molecules n_A and n_B; γ = concentration-dependent surface tension for the droplet; and $X = n_B/(n_A+n_B)$:mole fraction. Again, a closer examination of the parameter of surface tension for small droplets is most desirable. As in the study of homogeneous nucleation theory, the static thermodynamic equation of state (including the second virial coefficient) can be used to determine the "microscopic" surface parameter in sutdying heteromolecular nucleation theory for binary systems. Here the droplet consists of n_A and n_B. For a fixed mole fraction, X, there correxponds a given second virial coefficient, B(X). Thus, microscopic surface parameters for small droplets can be estimated. A preliminary study[50] shows that the calculated microscopic surface tension can be 30% lower than the measured bulk liquid surface tension.

Other problems associated with the study of heteromolecular nucleation theory for binary systems result from the chemical properties of a binary system in a small droplet, such as the surface enrichment effect and the hydration effect.

A correct heteromolecular nculeation theory for binary systems must take into account the fact that surface tension in general depends also on the composition of the liquid droplet. For example, in an ethanol-water solution, surface tension decreases with increasing ethanol concentration. Furthermore, by the Gibbs adsorption equation,[51] the concentration of the ethanol molecules is stronger on the surface than in the interior of the liquid (surface enrichment effect) and thus the surface tension is less. Recently, Stauffer et al.,[50] have introduced a material independent continuum theory to study the surface enrichment effect for the small liquid droplet. In this theory, the variation of composition is assumed to give a free energy contribution proportional to the square of the concentration gradient. For ethanol and water, this treatment of the surface enrichment for a small droplet provides a 42% smaller contribution of the surface

energy to the formation energy of a small droplet. This continuum theory has been tested by Monte Carlo methods for the lattice gas model[50] and the agreement is good. These surface enrichment effect correction calculations have included both the spatial composition variation and the curvature effect for small droplets. Taken together with the "microscopic surface tension" consideration estimated from the second virial coefficient, one may speculate that of the 42% smaller contribution, 30% may be due to the curvature effect and 12% may be arrived by the spatial composition variation. For an ideal binary system the surface enrichment effect is not important, but for systems like ethanol-water, NH_3-H_2O and H_2SO_4-H_2O the surface enrichment effect needs to be examined. An additional effect that should be considered when studying the heteromolecular nucleation process involving H_2SO_4-H_2 is the hydration effect in the liquid mixture droplet. Heist and Reiss[53] have recently constructed the free energy surface for a droplet containing n_A water molecules and n_B H_2SO_4 molecules. In their study, the surface predicts the existence of stable H_2SO_4 hydrates in the vapor phase and the number of hydrates has been calculated for different relative humidities. Shugard et al.,[54] extended this study of hydration effect to heteromolecular nucleation for the binary system H_2SO_4-H_2O and found that a finite nucleation rate is predicted with a relative humidity of 50% and H_2SO_4 vapor activity of 10^{-3}. This result gives a nucelation rate higher by a factor of 10^3 than the previous calculations made without considering the hydration effect.[21-23] No correction for surface enrichment and curvature effect were included in any of these calculations. The hydration effect for a relative humidity much greater than 100% would be more significant for the study of nucleation.

C. Heterogeneous nucleation on substrate

The simplest case for the study of heterogeneous nucleation on a substrate is to consider an ice embryo in the form of a spherical cap forming on a plane solid surface. Here we briefly review the basic approach (classical) often used to study this nucleation process and discuss the problems associated with the parameters entering into the calculation of nucleation rate. In classical nucleation theory, the nucleation rate is contributed by the product of the kinetic coefficient and the exponential function of the free energy of formation of a critical embryo on the nucleating surface (exp - $\Delta G^*/kT$). The free energy barrier (ΔG^*) for the formation of a new phase is, in general, in the order of magnitude of 40kT or more, which gives an exponential factor on the order of magnitude 10^{-18} or smaller. A 10% change of ΔG^* will give a change in the nucleation rate of two orders of magnitude. Therefore, ΔG^* is a more sensitive parameter for studying the nucleation rate, and our discussion will be largely devoted to this quantity.

The free energy of formation of an embryo on a plane solid surface is usually written as[55]

$$\Delta G = \Delta G_{12} V_2 + \gamma_{12} S_{12} + (\gamma_{23} - \gamma_{13}) S_{23} \qquad (13)$$

where ΔG_{12} is the free energy difference (per unit volume) of phase 2 between

matter in state 1 and matter in state 2, γ_{ij} is the surface free energy of the interface between phases i and j, V is the volume and S is the surface area. The cap dimensions can be specified in terms of the radius r and the contact angle θ (see Fig 3). The contact parameter $m = \cos\theta = (\gamma_{13}-\gamma_{23})/\gamma_{12}$ is used to determine the free energy of a critical embryo as follows

$$\Delta G^* = (4\pi\gamma_{12}^3/3\Delta G_{12}^2)\cdot f(m)$$
$$f(m) = (2 + m)(1 - m)^2 \qquad (14)$$

Thus the essential parameters for the free energy of a critical embryo are the surface tension γ_{12} and m. Other nucleation processes, such as deposition nucleation on insoluble particles, and contact nucleation, are based on this approach to determine the free energy of an embryo.

Most calculations of nucleation rate have used the bulk thermodynamic properties, such as the bulk liquid surface tension and the contact parameter, for the evaluation of the free energy barrier. At this point, we would like to point out a serious defect in this approach for studying heterogeneous nucleation theory. First, the use of bulk liquid surface tension for the surface free energy of a small cluster is not well justified. Again, a 10% difference in the estimation of the surface tension γ_{12} will give a 30% change in ΔG^*, which can lead to a change of the nucleation rate of seven or more orders of magnitude. Secondly, the height of a critical embryo above the nucleating surface is, in general, about 10 Å or less, which corresponds to a thickness of few molecules. Thus the concept of contact angle applied to the study of heterogeneous nucleation on substrate is ambiguous. Even though there are experiments[56] in good agreement with the theoretical predictions, one simply cannot take this theoretical interpretation too seriously before a closer examination of these parameters has been made.

Here we would like to propose a model for the study of heterogeneous nucleation on a substrate to clarify some of the ambiguities mentioned above. Binder and Hohenberg[57] recently have derived a cluster model, based on Monte Carlo calculations, to study the surface effects on magnetic phase transition. In their cluster model, the free energy for the formation of a surface cluster (a cluster that touches a free surface) can be expressed as

$$\Delta G_n = -n\cdot kT\cdot\ln(y) - n^{\sigma}\cdot kT\cdot\ln(x) + ch_1\cdot n^{\sigma_1} + \tau'\ln(n) + \text{const} \qquad (15)$$

where the first two terms are exactly the same as the first two terms in Eq. (1a) which corresponds to the first two terms in Eq. (13); the third term describes the interaction of the interface between the surface cluster and the touched surface which corresponds to the third term of Eq. (13). (h_1 is the field and c is a constant.) The logarithmic and constant terms are the correction due to the configurational entropy, vibration contribution, etc., which are analogous to the last two terms in Eq. (1a) in the bulk. Here $0 < \sigma < 1$, and $0 < \sigma_1 < 1$, for spherical cluster $\sigma = 2/3$ and

$\sigma_1 = 1/3$. The advantages of this proposed model are that (1) it is simple, semi-phenomenological and easily applied to practical research problems; (2) it is general (the model includes the entropy corrections and other possible contributions); and (3) it avoids the bulk parameters such as surface tension and contact parameter.

To determine these parameters ($\sigma,\sigma_1,\tau',x,ch_1$) used for the nucleation study, the experimental data of the correctly chosen thermodynamic properties can be used. For example, σ,σ_1, and τ' can be determined by the critical indices, and x can be determined by the second virial coefficient as demonstrated in the previous sections. The parameter c is a geometric constant and it can be approximated as $(3/4\pi)^{1/3} \cdot V_o^{1/3}$ where V_o is the volume per molecule. The determination of h_1 is relatively a new approach and we would like to discuss the background concept in the following paragraph.

Similar to the method for determination of "microscopic surface tension" by using the virial coefficients for homogeneous nucleation theory, the second gas-solid virial coefficient B_{2s} can be used to determine the interface interaction parameter h_1. B_{2s} is defined as

$$B_{2s} = \int_V \exp(-W_1/kT)\, d\tilde{r}_1 \; ; \quad W_1 = W_1(\tilde{r}_1,\{\mu_s\}, T) \tag{16}$$

where W_1 is the potential of average force for a single adsorbate molecule interacting with the adsorbent and $\{\mu_s\}$ is the set of chemical potentials of the adsorbent. Since the potential of average force constitutes the interaction energy of the adsorbate molecules as the sum of all interactions with the molecules of the adsorbent averaged over all allowable configurations of the adsorbent molecules, the second gas-solid virial coefficient B_{2s} does implicitly contain the information of the interface interaction parameter h_1 (the energy parameter generated by the interaction between the adsorbent and adsorbate molecules). To obtain more accurate information on the interface interaction h_1, higher order gas-solid virial coefficients are needed, e.g., B_{3s} which contains the average interaction between two adsorbate molecules and the adsorbent molecules. For a nearly ideal gas the interaction parameter h_1 can be obtained from the following equation

$$B_{2s} \simeq n_{ads} kT/P \tag{17}$$

where n_{ads} is the number of moles adsorbed and P is the bulk pressure. A detailed expression for h_1 can be obtained from the above equation with approximations similar to those of Eqs. (6) and (7)

$$B_{2s} = c(xz + x^{2^\sigma} z^{2^{\sigma_1}} 2^{\tau'}) \; / \; (x + x^{2^\sigma} 2^{\tau}) \tag{18}$$

where $z = \ln(ch_1)$.

Most experimental data of B_{2s} are reported for inert gases and organic gases on carbon.[58] No quantitative calculation for the determination of h_1 has been made because there is no experimental measurement of B_{2s} available for studying the heterogeneous nucleation on substrate. It is our recommendation that such experimental studies (e.g., apply gas chromatograph to obtain B_{2s} for water on AgI) should be performed for the determination of the interface interaction parameter h_1. Other approaches involving the available thermodynamic quantities (such as the isosteric heat of adsorbtion and adsorbtion isotherms) to evaluate the interface interaction parameter have been studied for the interaction between water vapor and pure silver iodide in the vicinity of saturation.[59] This new approach which applies other related thermodynamic properties to the determination of the interface interaction parameters and which avoids the usual approach by using the bulk liquid surface tension and contact parameters may provide a better insight for the study of heterogeneous nucleation.

V. CONCLUSION

There is little doubt that the nucleation processes play a significant role in the study of atmospheric sciences. For relative humidity below 100%, the heteromolecular nucleation process gives the mechanism for the initial stage of aerosol formation. If the role of aerosols in the urban air and in the stratospheric atmosphere is to be understood fully heteromolecular nucleation processes cannot be neglected. For relative humidity larger than 100%, the heterogeneous nucleation processes (either on soluble or insolbule particles) are the dominant mechanism for the formation of cloud droplets and ice crystals. While the significance of the study of nucleation phenomena in the atmosphere appears to be fairly well recognized, the basic theory for various nucleation processes is not well understood. For the study of homogeneous nucleation theory, a new approach for the determination of the parameters entering in the calculation of nucleation rate is presented and the theoretical predictions are in good agreement with the experimental measurements. Thus we suggest that classical nucleation theory can be considered as adequate, provided the appropriate value of the "microscopic" surface tension is used. This approach has been extended for the study of a heteromolecular nucleation theory for binary systems and of heterogeneous nucleation on a substrate to determine the parameters used for the study of nucleation theory. To confirm the theoretical prediction it would be desirable to obtain more experimental measurements for the necessary thermodynamic parameters and nucleation rates.

Acknowledgements:

The authors thank E. F. Danielsen, K. Binder, M. Corrin, R. A. Pierotti, C. Knight and N. Knight for suggestions, comments, and information. This investigation is partially supported by NSF Grant GA-33422 (G.H.W., D.S.), NIH Grant RR 8006(PH), EPA Grant R-801280 (GHW), NASA Grant NGR 11-010-001, (G.H.W.) and Office of Naval Research N00014-69-C-0043 (VAM).

REFERENCES

1. A. C. Zettlemoyer (ed.), Nucleation, Marcel Dekker Inc., New York, (1969).

2. C. S. Kiang, D. Stauffer, G. H. Walker, O. P. Puri, J. D. Wise, Jr., and E. M. Patterson, J. Atmos. Sci. 28, 1222 (1971); A. Eggington, C. S. Kiang, D. Stauffer, and G. H. Walker, Phys. Rev. Letters 26, 820 (1971); Patrick Hamill, D. Stauffer, and C. S. Kiang, Chem. Phys. Letters, to be published (1974).

3. J. Lothe and G. M. Pound, J. Chem. Phys. 36, 2080 (1962).

4. H. Reiss, J. Stat. Phys. 2, 83 (1970); H. Reiss, J. L. Katz, and E. R. Cohen, J. Chem. Phys. 48, 5553 (1968).

5. W. J. Dunning, in Nucleation (A. C. Zettlemoyer, ed.), Marcel Dekker Inc., New York, (1969).

6. J. J. Burton, Surface Sci. 26, 1 (1971); J. J. Burton, Acta Met. 21, 1225 (1973).

7. F. F. Abraham and J. V. Dave, J. Chem. Phys. 55, 1587 (1971); J. K. Lee, J. A. Barker and F. F. Abraham, J. Chem. Phys. 58, 3166 (1973).

8. D. J. McGinty, J. Chem. Phys. 58, 4733 (1973).

9. P. L. M. Plummer and B. N. Hale, J. Chem. Phys. 56, 4329 (1972).

10. M. Volmer and A. Weber, Z. Phys. Chem. 119, 277 (1926); R. Becker and W. Doering, Ann. Phys. (Leipzig) 24, 719 (1935); J. B. Zel'dovich, Zh. Eksp. Teor. Fiz. 12, 525 (1942); J. Frenkel, Kinetic Theory of Liquids, Oxford University Press, New York, Chap. VII, (1946); F. Kuhrt, Z. Phys. 131, 205 (1952).

11. C. S. Kiang and V. A. Mohnen (eds.), International Workshop on Nucleation Theory and Its Applications, Atlanta, Georgia, (1972).

12. D. B. Dawson, E. J. Willson, P. G. Hill, and K. C. Russell, J. Chem. Phys. 51, 5389 (1969); H. L. Jaeger, E. J. Willson, P. G. Hill, and K. C. Russell, J. Chem. Phys. 51, 5380 (1969).

13. P. P. Wegener, J. A. Clumpner, and B. J. Wu, Phys. Fluid 15, 1869 (1972).

14. J. L. Katz and B. J. Ostermier, J. Chem. Phys. 47, 478 (1967).

15. K. Binder, to be published in Nucleation II (A. C. Zettlemoyer, ed.) Marcel Dekker Inc., New York.

16. For example see J. L. Kassner et al., J. de Res. Atmos. 3, 45 (1968).

17. For example see P. P. Wegener and A. A. Pouring, Phys. Fluid 7, 352 (1964).

18. For example see J. P. Franck and H. G. Hertz, Z. Phys. 143, 559 (1956); see also ref. 14.

19. For example see J. A. Armstrong and G. D. Stein in ref. 11.

20 G. M. Pound, J. Chem. Phys. Ref. Data 1, 119 (1972).

21. K. Neumann and W. Doering, Z. Phys. Chem. A 186, 203 (1940); H. Reiss, J. Chem. Phys. 18, 840 (1950).

22. G. J. Doyle, J. Chem. Phys. 35, 795 (1961); P. Mirabel and J. L. Katz, J. Chem. Phys. 60, 1138 (1974).

23. C. S. Kiang and D. Stauffer, Faraday Symposia Chem Soc. (Fogs and Smokes) 7, 26 (1973).

24. A. C. Zettlemoyer (ed.) Nucleation II; A. C. Zettlemoyer and C. S. Kiang (eds.) Nucleation III and Nucleation IV, Marcel Dekker Inc., New York, to be published.

25. For example see N. H. Fletcher, The Physics of Rainclouds, Cambridge University Press, (1962).

26. C. S. Kiang, D. Stauffer, V. A. Mohnen, J. Bricard, and D. Vigla, Atmos. Env. 7, 1279 (1973); D. Stauffer, V. A. Mohnen, and C. S. Kiang, J. Aerosol Sci. 4, 461 (1973).

27. D. Stauffer and C. S. Kiang, Icarus 21, 129 (1974).

28. C. S. Kiang, V. A. Mohnen, and Patrick Hamill, presented at Air Pollution Control Association Annual Meeting, Denver (1974), paper no. 74-21.

29. C. S. Kiang and Patrick Hamill, Nature 250, 401 (1974); C. S. Kiang, D. Stauffer, and V. A. Mohnen, Nature (Phys. Sci.) 244, 53 (1973).

30. H. Flood, Z. Phys. Chem. A 170, 286 (1934).

31. P. P. Wegener et al. for ethanol-water, A. Birenzvige and V. A. Mohnen for H_2SO_4-H_2O, private communication.

32. P. V. N. Nair and K. G. Vohra, to be published, J. Aerosol Sci. (1974).

33. H. Köhler, Meddel. Meteorol.-Hydrogr. Anstalt, Stockholm, 3(8) (1926).

34. H. L. Wright, Proc. Phys. Soc. 48, 675 (1936).

35. J. E. McDonald, J. Met. 10, 68 (1953).

36. B. J. Mason, The Physics of Clouds, Oxford (1957).

37. P. Winkler, J. Aerosol Sci. 4, 373 (1973).

38. C. Junge, Ann. Met. 5 (Beiheft), 1 (1952).

39. V. J. Schaefer, Chem. Rev. 44, 291 (1949).

40. W. A. Cooper, J. Atmos. Sci., to be published (1974).

41. M. E. Fisher, Physics 3, 255 (1967).

42. D. Stauffer, C. S. Kiang, A. Eggington, E. M. Patterson, O. P. Puri, G. H. Walker, J. D. Wise, Jr., Chem. Phys. Letters 16, 499 (1972).

43. D. Stauffer, C. S. Kiang, A. Eggington, E. M. Patterson, O. P. Puri, G. H. Walker, J. D. Wise, Jr., Phys. Rev. B7, 2780 (1972).

44. C. S. Kiang, Phys. Rev. Letters 24, 47 (1970); C. S. Kiang and D. Stauffer, Z. Physik 235, 130 (1970).

45. J. Straub, Phys. Letters 31A, 453 (1970).

46. W. Rathjen, D. Stauffer and C. S. Kiang, Phys. Letters 40A, 345 (1972).

47. L. Kadanoff et al., Rev. Mod. Phys. 39, 395 (1967).

48. J. H. Dymond and E. B. Smith, The Virial Coefficients of Gases, Clarendon Press, Oxford, (1969).

49. J. O. Hirschfelder, C. F. Curtis, and R. B. Bird, Molecular Theory of Gases and Liquids, 2nd ed., John Wiley and Sons Inc., New York (1964).

50. G. H. Walker and C. S. Kiang, in preparation.

51. E. A. Guggenheim, Mixtures , Clarendon Press, Oxford (1952) page 166.

52. D. Stauffer, K. Binder, and V. Wildpaner, to be published in Water Air Soil Pollution, special IRCHA issue (1974).

53. R. H. Heist and H. Reiss, J. Chem. Phys., to be published (1974).

54. W. J. Shugard, R. H. Heist and H. Reiss, preprint (1974).

55. N. H. Fletcher, J. Chem. Phys. 29, 572 (1958).

56. S. Twomey, J. Chem. Phys. 30, 941 (1959).

57. K. Binder and P. C. Hohenburg, Phys. Rev. B9, 2194 (1974).

58. R. A. Pierotti and H. E. Thomas, Surface Collid Science 4, 93 (E. Matijevic, ed.), John Wiley & Sons Inc., New York (1971).

59. W. R. Barchet and M. L. Corrin, J. Phys. Chem. 76, 2280 (1972).

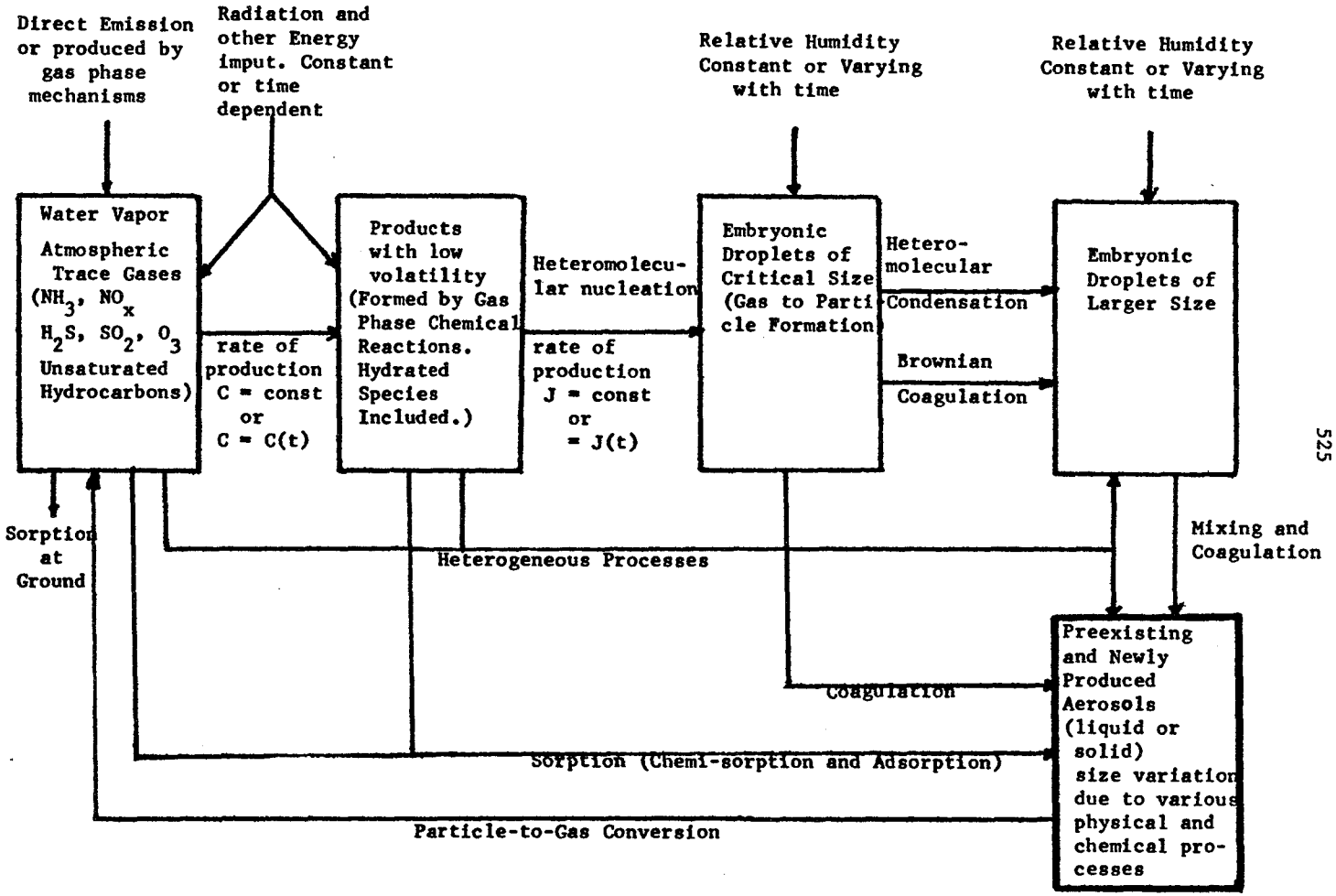

Fig. 1 Phase Transition Block Diagram I for Relative Humidity below 100%

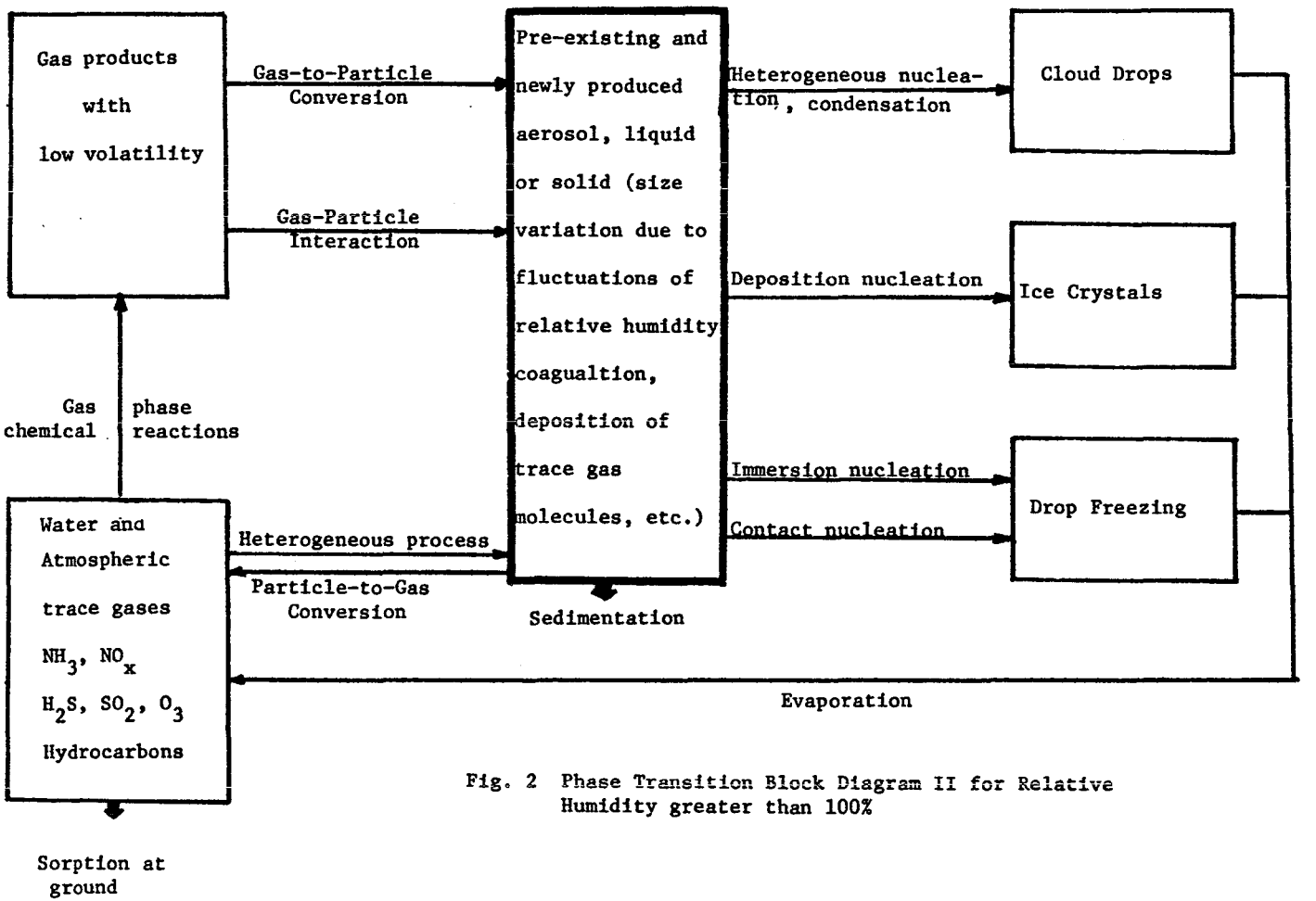

Fig. 2 Phase Transition Block Diagram II for Relative Humidity greater than 100%

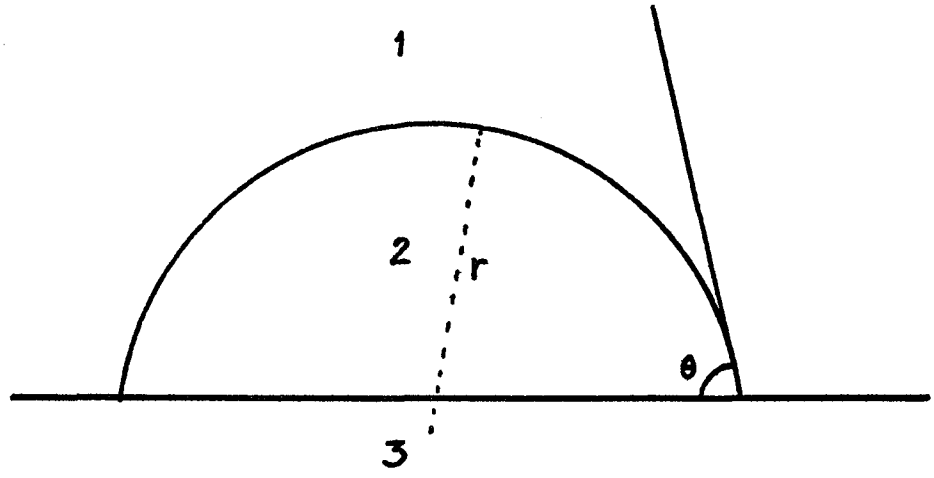

Fig. 3 Heterogeneous Nucleation on a Substrate : Embryo 2 on Nucleating Surface 3 in Parent Phase 1, where r is the radius of the embryo and θ is the contact angle.

TABLE 1

Ratio of nucleation rates measured experimentally to nucleation rates predicted by classical theory

Substance	J_{exp} / J_{class}
H_2O	10^4
C_2H_5OH	10^5
NH_3	10^{12}
C_6H_6	10^8
$CHCl_3$	10^{18}
CCl_3F	10^{14}

TABLE II

Comparison of ratios of nucleation rates

(J: calculation from "microscopic" surface tension)

Substance	Temp(^oK)	$S = P/P_o$	J/J_{class}	J_{exp}/J_{class}
H_2O	323	2.58	10^1	10^4
CH_3OH	313	1.4	10^{-6}	10^0
C_2H_5OH	313	7.39	10^4	10^5
NH_3	240	2.8	10^{11}	10^{12}
C_6H_6	230	100	10^8	10^8
$CHCl_3$	323	3	10^{12}	10^{18}
CCl_3F	240	5	10^{15}	10^{14}

CURRENT METEOROLOGICAL THEORY OF DROP GROWTH BY CONDENSATION AND SOME COMPARISONS WITH EXPERIMENT

J. C. Carstens

and

J. M. Carter

Physics Department and Graduate Center for
Cloud Physics Research
University of Missouri at Rolla

ABSTRACT

A review of the current meteorological theory of droplet growth is presented. Some comparisons with experiment are exhibited, and good agreement is found. The theory is presented so as to emphasize its logical development from basic physical ideas. It is cast into a very simple form which can be used to reveal the similarities of various other forms appearing in the literature. A few special formulas are displayed which are useful in certain practical applications. Some implications of the theory regarding size distribution broadening are discussed. The theory is compared with measurements of the growth of water drops in the one-half-to-ten micron size range which were made in Argon and air by laser scattering techniques. Scattering from a He-Ne (6328 Å) laser off of drops produced by homogeneous nucleation, and thereafter grown at supersaturation ratios ranging from about 1.2 to 3.6, was compared with the Mie theory predictions and radius vs. time curves deduced. Generally good agreement was found between the conventional theory of drop growth and experiment. The theory was fit using one parameter involving both condensation and thermal accommodation coefficients.

INTRODUCTION

The present treatment of dropwise condensation (or evaporation) is divided into two parts: (1) the theory is presented as it is normally used by atmospheric scientists, that is in application to clouds, and (2) a brief comparison with experiment is limited to cloud chamber work performed by J. Carter in the UMR Cloud Physics Center.

In (1) the emphasis has been a step-by-step exposition of the basic theory rather than on the history of its development.

It perhaps should be mentioned at the outset that the equations describing growth are subject to various simplifications peculiar to their atmospheric application. One of the most important of these resides in the fact that at any given time a cloud droplet generally experiences a very small supersaturation. "Final" equations have generally been written with this simplification in mind, and appropriate modification must be made for larger supersaturations (or undersaturations).

GOVERNING EQUATIONS

In treating cloud droplet growth it is perhaps most practical to adopt the macroscopic point of view and write down the continuum equations governing the growth or evaporation process. In doing so it is assumed that the drop diameter is rather greater than a mean free path. This regime usually covers cases of interest in cloud physics, and is amenable to extensions into the "transition" regime.

Briefly, the process of growth involves the transport of mass (vapor) toward the drop, release of latent heat at the drop surface, a subsequent heating up of the drop, and as a consequence of the latter, a thermal energy transport away from it. The continuity of water vapor concentration, n (moles/vol.), outside the drop may be written:

$$\nabla \cdot \vec{I} = -\frac{\partial n}{\partial t} \tag{1}$$

where $\vec{I}$ is the molar flux of vapor given by,

$$\vec{I} = \frac{-(n+n_g)D}{(1-x)} [\nabla x + \alpha'(x) \nabla \ln T] + \frac{x}{1-x} \vec{I}_g \tag{2}$$

Here x is the mole fraction of vapor, n the vapor molar concentration, D the diffusion coefficient of water vapor in air, T the temperature field (governed by a corresponding equation), $\vec{I}_g$ the molar flux of air, n_g the molar concentration of air, and $\alpha'(x)$ the thermal diffusion factor.

Considerable simplification of this equation is justified for normal atmospheric situations. Water vapor is a dilute solute in the atmosphere, so that the term n/n_g can be neglected compared with unity. [This corresponds to neglecting Stefan flow, (Fuchs 1959)]. Thermal diffusion and its inverse are small enough to be neglected (Neiburger and Chien, 1960). The motion of the air relative to the drop is almost always ascribable to drop fall, and v_g can be inferred from the Stoke's law velocity.

This effect is negligible up to about 10 microns (Squires, 1952). Beyond this size the effect of fall can be incorporated semi-empirically (Frossling, 1938; Squires, 1952) by a ventillation factor which multiplies the diffusion coefficient. It is usually a minor correction inasmuch as its effect on condensation drop growth is most pronounced when the latter is no longer the dominant growth mechanism. [According to Squires D or K can be multiplied by the approximate factor,

$$1 + 0.24 \sqrt{Re}, \tag{3}$$

where Re is the Reynolds number].

With the above simplifications the flux equation reduces to one of simple diffusion,

$$D\nabla^2\rho = \frac{\partial \rho}{\partial t}, \tag{4}$$

where ρ is the vapor density and D is regarded as constant. Arguments similar to the above apply to heat conduction leading to

$$k\nabla^2 T = \frac{\partial T}{\partial t}, \tag{5}$$

where k is the thermal diffusivity of the air-water vapor mixture, or simply that of air. Three of the four boundary conditions required to specify the solution can be written down immediately.

$$\rho(\infty,t) = \rho_\infty(t) \tag{6}$$

$$T(\infty,t) = T_\infty(t) \tag{7}$$

$$4\pi a^2 [K \frac{\partial T}{\partial r} + LD \frac{\partial \rho}{\partial r}]_{r=a} = Cd(a)\frac{dT_d}{dt} \tag{8}$$

where ρ_∞ and T_∞ are bulk values of the vapor density and temperature (which can be functions of time), a the drop radius, K the thermal conductivity of the gas, L the latent heat of condensation, and Cd(a) the heat capacity of the drop which is to good approximation characterized by the uniform temperature T_d. Fuchs (1959) has shown that heat loss by radiation can be neglected for the size range here contemplated. (Discussion of the third boundary condition is deferred).

The final simplification invokes the idea of quasi steady state. It is based on the assumption that the transients appropriate to the diffusion problem are small enough so that the steady state profiles "follow" the outward motion of the drop surface. The transient regime is discussed by Carstens and Zung (1970), Nix and Fukuta (1973), and the use of quasi steady state criticized by Kirkaldy (1958).

With the above simplifications the flux equations reduce to:

$$\nabla^2 \rho = 0; \tag{9}$$

and

$$\nabla^2 T = 0. \tag{10}$$

The notion of quasi steady state does not rule out the possibility that ρ_∞ and T_∞ be slowly varying functions of time in (6) and (7). Condition (8) becomes simply,

$$K \left.\frac{dT}{dr}\right|_{r=a} + LD \left.\frac{d\rho}{dr}\right|_{r=a} = 0. \tag{11}$$

The steady state solutions to (9) and (10) are:

$$\rho = \frac{a}{r} (\rho_a - \rho_\infty) + \rho_\infty, \tag{12}$$

and

$$T = \frac{a}{r} (T_a - T_\infty) + T_\infty. \tag{13}$$

These solutions, incidently, are never attained since it would take an infinite amount of mass (and heat) to establish them. The solutions are necessarily poor far away from the drop. The validity of the quasi steady state approximation resides (in part) in the fact that the "correct" solutions are achieved very quickly near the drop and, even though the drop derives the bulk of its mass from remote regions, its actual growth rate depends on the gradient at the drop surface.

Finally, the presumably slow outward motion of the drop surface reintroduces time into what would otherwise be a steady state process (hence "quasi" steady state). This "growth" equation is:

$$\frac{da}{dt} = \frac{D}{\rho_\ell} \left.\frac{d\rho}{dr}\right|_{r=a} \tag{14}$$

where ρ_ℓ is the liquid density.

Two somewhat different treatments of the growth process exist in the meteorological literature. Both are based on the above assumptions. They differ in that the most common approach assumes that the transport process is entirely controlled by the diffusion of mass and conduction of heat, while the alternate approach posits the possibility of additional control exerted at the liquid-vapor interface. This difference appears in the final boundary condition at the drop surface.

DIFFUSION CONTROLLED GROWTH

In what is perhaps the most common treatment of drop growth (Fuchs, 1959; due to Maxwell), it is assumed that to good approximation thermal equilibrium between vapor density and temperature holds at the drop surface. In addition to its dependence on temperature, the dependence of thermal equilibrium both on drop curvature and dissolved salt often must be taken into account. We can write this radial dependence formally in terms of a saturation ratio,

$$S_{sat} = \frac{\rho_{eq}(a,m_s,T)}{\rho_{eq}(\infty,0,T)}, \tag{15}$$

where $\rho_{eq}(a,m_s,T)$ is the equilibrium vapor density over a drop of radius a and dissolved salt mass m_s, and $\rho_{eq}(\infty,0,T)$ is that over a flat, pure surface. We therefore have the equilibrium condition:

$$\rho_{eq}(a,m_s,T) = S_{sat}(a,m_s)\rho_{eq}(\infty,0,T).$$

The temperature span involved in the applications is ordinarily sufficiently narrow to justify a linear relationship between $\rho_{eq}(\infty,0,T)$ and T, so that the final boundary condition can be written:

$$\rho_{eq}(a,T_a) = (bT_a+c)S_{sat}. \tag{16}$$

The constants b and c can be (and usually are) obtained by keeping linear terms in a Taylor expansion of the Clausius-Clapeyron equation about T_∞.

The condition (16) completes the problem and leads to the growth equation:

$$a\frac{da}{dt} = \frac{\rho_{eq}(\infty)[S-S_{sat}(a)]}{\frac{1}{D}+\frac{bL}{K}}, \tag{17}$$

where the liquid density is unity. Here we can identify the numerator as the "driving force" and the denominator as a "resistance" composed of mass and thermal components. For constant ambient conditions, and supersaturation ratio, S, close to unity, a solution is:

$$t(a) = \frac{1}{D_{eff}\rho_{eq}(\infty)}\int_{a_o}^{a(t)} \frac{x\,dx}{S-S_{sat}(x)} \tag{18}$$

where

$$\frac{1}{D_{eff}} = \frac{1}{D} + \frac{bL}{K}. \tag{19}$$

For temperature at about 3° C, the thermal "resistance", $\frac{bL}{K}$, begins to dominate growth. This can be seen by splitting the time in (18) into two parts, one associated with the thermal resistance. With $t=t_\rho+t_T$, we have:

$$t_T = \frac{bL}{K} \frac{1}{\rho_{eq(\infty)}} \int_{a_o}^{a(t)} \frac{x\,dx}{S-S_{sat}} \tag{20}$$

$$t_\rho = \frac{1}{D} \frac{1}{\rho_{eq(\infty)}} \int_{a_o}^{a(t)} \frac{x\,dx}{S-S_{sat}} \tag{21}$$

At 3°C the ratio t_T/t_ρ is about 1, at 30°C nearly 4.

Finally it should be pointed out that $S_{sat}(a)$ is usually identified with the Kohler curve:

$$S_{sat}(a) = 1 + \frac{r^*}{a} - \frac{Am_s}{a^3} \tag{22}$$

where r^* is a constant obtained from the Kelvin-Thompson equation (curvature effect) and $m_s(A/a^3)$ from Raolt's law. Derivation and discussion of the Kohler curve may be found, for example, in Fleagle and Businger (1963).

GROWTH CONTROLLED BY DIFFUSION AND SURFACE KINETICS: DIFFUSION-KINETIC APPROACH

In the previous development it was assumed that drop growth is controlled both by the rate at which vapor molecules are transported to the surface by diffusion, and the rate at which thermal energy is removed from the surface by conduction. This transport process can obviously be affected if, in the first case, vapor molecules do not always stick to the surface upon striking it (or are inhibited from evaporating), and, in the second case, if the gas molecules on the average acquire some reduced fraction of the surface energy upon collision. These possibilities naturally lead to a consideration of coefficients of condensation, evaporation, and thermal accommodation.

The thermal accommodation coefficient, α, can be defined as:

$$\alpha = \frac{E_i - E_r}{E_i - E_w} \tag{23}$$

where according to Kennard (1938) E_i denotes the energy brought up to unit area per second by the incident molecular stream, E_r that carried away by these molecules as they leave the wall after reflection from it, and E_w the energy that this latter stream would carry away if it carried the same mean energy per molecule as does a stream issuing from a gas in equilibrium at the wall temperature T_w.

It is perhaps timely to discuss the evaporation and condensation coefficient in the context of water drops that may possess impurities, especially as such considerations may be important in cloud physics (Bartlett and Jonas, 1972). The condensation coefficient can be taken to be the fraction of incoming vapor molecules that strike the surface and stick to it. The evaporation coefficient may be defined relative to the condensation coefficient as the fraction of molecular flux that would emanate from a pure surface at the same temperature (this being the condensation flux under equilibrium conditions at that temperature). A relative condensation coefficient may be similarly defined. The following simplified illustrative model may serve to fix these ideas. Consider a water surface upon which condensation (or evaporation) occurs. Let us for the sake of argument evaluate the fluxes involved from uniform (ideal) gas kinetics. For pure water (superscript zero) the flux is

$$I^{(o)} = \frac{1}{4}\,\bar{v}\,\beta_c{}^{(o)}(n-n_{eq}{}^{(o)}) + \frac{1}{2}\,I^{(o)}\beta_c{}^{(o)}$$

or

$$I^{(o)}\left(1-\frac{\beta_c{}^{(o)}}{2}\right) = \frac{1}{4}\,\bar{v}\,\beta_c{}^{(o)}[n-n_{eq}{}^{(o)}]. \qquad (24)$$

Here $\beta_c{}^{(o)}$ is the condensation coefficient for pure water, $\bar{v}$ the average molecular speed, n the actual water vapor molecular concentration, and $n_{eq}{}^{(o)}$ the equilibrium concentration at the surface temperature. The factor $I^{(o)}/2$ accounts for the fact that the condensation process itself establishes a net flow of vapor toward the surface which is not accounted for by kinetic term alone. Next, consider the surface of "contaminated" water. From a purely phenomenological point of view the condensation and/or the evaporation flux could be altered. The condensation term may be changed to

$$\beta_c{}'\,[\tfrac{1}{4}\,n\,\bar{v}\,\beta_c{}^{(o)}],$$

where $\beta_c{}'$ is the relative condensation coefficient, $o<\beta_c{}' \leq 1/\beta_c{}^{(o)}$. Likewise the evaporation flux can be affected; that is the flux that would ordinarily evaporate off a pure surface is changed by a factor $\beta_e{}'$ (evaporation coefficient), i.e.,

$$\beta_e' \left[\frac{1}{4} n_{eq}^{(o)} \bar{v} \beta_c^{(o)}\right].$$

Hence:

$$I\left(1-\frac{\beta_c^{(o)}\beta_c'}{2}\right) = \frac{\beta_c^{(o)}\beta_c' \bar{v}}{4}\left[n-\frac{\beta_e'}{\beta_c'} n_{eq}^{(o)}\right]$$

The new equilibrium "position" is,

$$n_{eq} = \frac{\beta_e'}{\beta_c'} n_{eq}^{(o)}, \tag{25}$$

and the shift in equilibrium,

$$\frac{n_{eq}-n_{eq}^{(o)}}{n_{eq}^{(o)}} = \frac{\beta_e'-\beta_c'}{\beta_c'}. \tag{26}$$

In terms of the displaced equilibrium,

$$I\left(1-\frac{\beta_c' \beta_c^{(o)}}{2}\right) = \frac{\bar{v}}{4}\beta_c' \beta_c^{(o)}(n-n_{eq}) \tag{27}$$

with $\beta_c' \beta_c^{(o)}$ the condensation coefficient for the contaminated surface. This illustration is only meant to define these coefficients in such a way as to correspond with common sense. Clearly the kinetics of the process, that is the rate at which equilibrium approached, is affected by the condensation coefficient ($\beta_c = \beta_c' \beta_c^{(o)}$) alone, while the shift in equilibrium obviously requires a difference in β_c' and β_e'.

In the case of drop growth the introduction of possible surface control requires that the thermal equilibrium boundary condition (16) be replaced by mass and heat fluxes. The simplest technique, and that usually found in the meteorological literature (Langmiur, 1944; Fuchs, 1959; Carstens and Kassner, 1968; Fitzgerald, 1970; Fukuta and Walter, 1970) consists of equating the molecular and energy flux determined from uniform gas kinetics to that calculated directly from Fick's and Fourier's law. This flux matching is done at the drop surface, or in the vicinity of a mean free path of it (Fuchs, 1959). This approach has been dubbed the "diffusion kinetic" by Smirnov (1971). A very thorough exposition of it is that of Fukuta and Walter (1970).

Using this approach, the mass flux equation around the drop is given by:

$$D\frac{d\rho}{dr}\Big|_{r=a} = \frac{1}{4}\rho_a\,\bar{v}(T_a)\beta_c(T_a) + \frac{D}{2}\frac{d\rho}{dr}\Big|_{r=a}\beta_c(T_a)$$

$$-\frac{1}{4}\rho_{eq}(T_d)\bar{v}(T_d)\beta_c(T_d)$$

Here β_c is the condensation coefficient, T_a is the temperature of the gas adjacent to the drop, T_d that of the drop itself, and $\bar{v}$ the average molecular speed at the temperatures indicated. The addition of half of the Fickian flux on the right hand side rests on reasoning similar to that given in connection with equation (24). (The consistency of adding such a term is perhaps more easily seen away from the surface. In a uniform gas the number of molecules traversing an imaginary plane is $\frac{1}{4}n\bar{v}$ in one direction and $\frac{1}{4}n\bar{v}$ in the other; the net flux is of course zero. If there is known to be a flux $-D\frac{\partial n}{\partial x}$ in the gas then the uniform flux calculation can be made to produce it if, to $\frac{1}{4}n\bar{v}$, one simply adds $-\frac{1}{2}D\,\partial n/\partial x$.) We next neglect the intrinsic temperature dependence of β_c to get

$$D\frac{d\rho}{dr}\Big|_{r=a} = \frac{\bar{v}(T_\infty)}{4}\left(\frac{\beta_c}{1-\frac{\beta_c}{2}}\right)\left[\rho_a\sqrt{\frac{T_a}{T_\infty}} - \rho_{eq}(T_d)\sqrt{\frac{T_d}{T_\infty}}\right].$$

The narrow range of temperatures also justifies the simplifying approximation,

$$\sqrt{\frac{T_d}{T_\infty}} \simeq \sqrt{\frac{T_a}{T_\infty}} \simeq 1.$$

The approximate "connection" equation is:

$$D\frac{d\rho}{dr}\Big|_{r=a} = \frac{1}{4}\,\bar{v}\,\frac{\beta_c}{1-\frac{\beta_c}{2}}\,[\rho_a - \rho_{eq}(T_d)]. \qquad (28)$$

From the solution (12) it follows that,

$$\rho_a = \frac{\rho_\infty + \frac{a}{\ell_\beta}\,\rho_{eq}(T_d)}{1+a/\ell_\beta}, \qquad (29)$$

where, following Fukuta and Walter (1970) we have introduced the length ℓ_β,

$$\ell_\beta = \frac{4D}{\bar{v}\beta}, \tag{30}$$

and where

$$\beta = \beta_c\left(1-\frac{\beta_c}{2}\right)^{-1}. \tag{31}$$

The departure from equilibrium is,

$$\rho_{eq}(T_d)-\rho_a = \frac{\rho_{eq}(T_d)-\rho_\infty}{1+a/\ell_\beta}, \tag{32}$$

and its magnitude is determined by the value of a/ℓ_β relative to unity.

As exemplified by eq. (32), the diffusion-kinetic model is constructed so that it is valid in the opposite limits of free molecular flow (Kn>>1) and continuum flow (Kn<<1). It may thus be regarded as an "interpolation" covering the intermediate regime bounded by these two extremes. Smirnov (1971) (see also Shankar, 1970) discusses the degree of approximation achieved by this interpolation through the regime of intermediate Knudsen number. However, the chief merit of the model, at least in most cloud physics applications (Rooth, 1957), lies in its incorporation of surface effects via the condensation and thermal accommodation coefficients. If β (and/or α) is sufficiently small compared with unity, significant surface control can extend well into the continuum regime -- a regime where the theory purports validity. The smaller either or both of these coefficients, the more important it is to ascertain their values, since they represent a tendency for surface control to be the rate determining process. Kn/β and Kn/α are the important numbers here, and as implied by eq. (32) they have to do with the validity of assuming the thermal equilibrium; Kn itself of course pertains to the validity of using Fick's and Fourier's laws. If α and β are near unity the distinction is unnecessary, but in this case growth through the regime of intermediate Knudsen number is sufficiently fast that one is usually justified in using the simpler approach [that is, eq. (17)].

The actual magnitude of the sticking coefficient appears to be the subject of some controversy (see for example Mills and Seban, 1967; Jamieson, 1965; or Amelin, 1966). Values have been measured (Alty and Mackay, 1935; Vietti and Schuster, 1973; Carter and Carstens, 1974;) that would not be insignificant in cloud physics applications (Fitzgerald, 1970; Warner, 1969).

In evaluating the energy flux around the drop we will follow the analysis of Kennard (1938), appealing to the same sort of assumptions invoked in evaluating the mass flux (the calculation is done for air):

$$-K\frac{dT}{dr}\Big|_{r=a} \simeq \alpha[-\frac{\bar{v}_g}{4}n_g(T_a)(E_{tr}+E_i)-\frac{K}{2}\frac{dT}{dr}\Big|_{r=a}$$

$$+\frac{\bar{v}_g}{4}n_g(T_a)(E'_{tr}+E'_i)].$$

E_{tr} is the translational energy of the incoming molecules and E_i is their energy other than translational; E'_{tr} and E'_i are these quantities for the outgoing flux. The average translational energy of the molecules in a molecular stream is given by:

$$<\frac{1}{2}mv^2> = \frac{4}{3}(\frac{3}{2}kT).$$

The following identifications are made:

$$E_{tr} = 2RT_a \text{ and } E'_{tr} = 2RT_d.$$

This puts n_g in moles/cm^3, and $(1/4)n_g\bar{v}$ in the moles/cm^2/sec, so that the energy flux is in cal/cm^2/sec (R is in cal/^{o}K mole). Then,

$$-K\frac{dT}{dr}\Big|_{r=a}(1-\frac{\alpha}{2}) = \frac{\bar{v}_g n_g(T_a)\alpha}{4}[2R(T_d-T_a)+E'_i-E_i].$$

Now for an ideal gas

$$C_v = \frac{\Delta U}{\Delta T} = \frac{3}{2}R + \frac{\Delta E}{\Delta T}$$

where C_v is the molar specific heat at constant volume. Putting $\Delta T=T_d-T_a$ and $\Delta E=E'_i-E_i$ gives:

$$E'_i-E_i = (C_v-\frac{3}{2}R)(T_d-T_a).$$

This leads to:

$$-K\frac{dT}{dr}\Big|_{r=a} = \left(\frac{\alpha}{1-\frac{\alpha}{2}}\right)\frac{n_g(T_a)\bar{v}_g}{4}\ \frac{R}{2}\left(\frac{\gamma+1}{\gamma-1}\right)(T_d-T_a) \qquad (33)$$

where γ is the ratio of specific heat at constant pressure to that at constant volume. Using the solution (13) a result analogous to (29) is obtained:

$$T_a = (T_\infty + \frac{a}{\ell_\alpha} T_d)/(1+a/\ell_\alpha) \tag{34}$$

where, again following Fukuta and Walter (1970), we introduce the length ℓ_α:

$$\ell_\alpha = 8K(\frac{\gamma-1}{\gamma+1})(\frac{1-\alpha/2}{\alpha})/\bar{v}_g Rn_g$$

The well-known phenomena of "temperature jump" (Kennard, 1938) is given by,

$$T_d - T_a = (T_d - T_\infty)/(1+a/\ell_\alpha), \tag{35}$$

which is analogous to eq. (32).

Now equations (34), (29), and the condition for thermal equilibrium, along with the usual boundary conditions (11) (6), and (7) comprise the required six conditions to solve for the six "constants" T_a, T_d, ρ_a, $\rho_{eq}(T_d)$, ρ_∞, and T_∞. It is quicker, however, to exploit the idea of "compensated" coefficients (Fitzgerald, 1970; see also Carstens, 1972). Here the formalism of the simpler theory is retrieved by "compensating" the coefficients as they appear in eq. (17) in such a way that the growth law includes the above surface effects. In what follows the simpler theory is referred to as the Maxwell Theory with subscript "M".

The flux computed from the diffusion-kinetic theory is,

$$I_{DK} = D(\rho_a - \rho_\infty)\frac{a}{r^2}. \tag{36}$$

We write the Maxwellian flux as,

$$I_M = D^*(a)[\rho_{eq}(T_a) - \rho_\infty]\frac{a}{r^2}, \tag{37}$$

where, if I_{DK} and I_M are to be equal,

$$\frac{D^*}{D} = \frac{\rho_a - \rho_\infty}{\rho_{eq}(T_a) - \rho_\infty}.$$

It is easily shown directly from eq. (29) that,

$$\frac{D^*}{D} = \frac{\rho_a - \rho_\infty}{\rho_{eq}(T_a) - \rho_\infty} = (1+\ell_\beta/a)^{-1}$$

This, as Fukuta and Walter demonstrate clearly, is the key manipulation that causes the linear theory [i.e. based on a linearization of the thermal equilibrium condition, eq. (16)] to have such a simple form.

Clearly,

$$D^*(a) = \frac{D}{1+\ell_\beta/a} \tag{38}$$

and, analogously,

$$K^*(a) = \frac{K}{1+\ell_\alpha/a}. \tag{39}$$

Now the compensation of K and D insures that the flux is calculated so as to satisfy conditions (28) and (33). But the power balance, eq. (11), and growth eq. (14), in fact involve only flux terms. Therefore the Maxwellian approach gives the growth law, eq. (17), "correctly" with D and K compensated, i.e.

$$a\frac{da}{dt} = D^*_{eff}(a)\rho^{(o)}_{eq}(\infty)[S-S_{sat}(a)] \tag{40}$$

where

$$\frac{1}{D^*_{eff}} = \frac{1}{D^*(a)} + \frac{bL}{K^*(a)}. \tag{41}$$

($S_{sat}(a)$ has here been assumed sufficiently close to unity to justify putting $b\,S_{sat} \tilde{=} b$ in D_{eff}). It is easy to establish an equivalent form, resembling that of Rooth (1957),

$$(a+\ell)\frac{da}{dt} = D_{eff}\rho^{(o)}_{eq}(\infty)[S-S_{sat}(a)], \tag{42}$$

where ℓ is a weighted average of ℓ_α and ℓ_β:

$$\ell = (\frac{bL}{K}\ell_\alpha + \frac{\ell_\beta}{D})/(\frac{bL}{K} + \frac{1}{D}). \tag{43}$$

It is also clear that, $D^*_{eff} = D_{eff}(1+\ell/a)^{-1}$.

Four contributions to the "resistance" may be identified [refer to discussion in connection with equation (19)],

$$R = \frac{1}{D} + \frac{bL}{K} + \frac{1}{D}\frac{\ell_\beta}{a} + \frac{bL}{K}\frac{\ell_\alpha}{a}. \tag{44}$$

The last two represent the mass and thermal contribution to the surface resistance. At a given temperature the single parameter ℓ suffices to account for surface effects. The slope b, however, is responsible for an increasing thermal weighting toward ℓ_α as temperature increases. (From the Clausius-Clayperon equation;

$$b \approx \rho_{eq}^{(o)}(\infty)ML/RT_\infty^2).$$

Thus a low value of β, for example, will have more of an effect at lower temperatures than at high. This effect exists aside from any intrinsic dependence of β or α on temperature. As mentioned in connection with equations (20) and (21) the weighting is about equal at 3°C and nearly fourfold toward ℓ_α at 30°C.

SOME SOLUTIONS

Although (40) or (42) is usually solved numerically (e.g. Brown and Arnason, 1973), a few solutions may be helpful. For constant ambient conditions,

$$t(a) = \frac{1}{\rho_{eq}(\infty)D_{eff}} \int_{a_o}^{a} \frac{(x+\ell)dx}{S-S_{sat}(x)}, \tag{45}$$

which with $S_{sat}(x)$ given by eq. (22) can be solved by conventional integration (Carstens, et al, 1974).

If the maximum value of S_{sat}, that is the critical supersaturation S_c, exceeds the applied supersaturation, S, then growth is inhibited, and the radius approaches a stable-equilibrium value, a_s, corresponding to the smallest positive root of $S-S_{sat}(a)=0$. If S is not too close to S_c, a rough idea of the relaxation time corresponding to the approach of a to a_s can be obtained by linearizing S_{sat} around a_s (Sedunov, 1972), the argument being that if the drop attains a radius near a_s the bulk of its growth time is spent in this vicinity. Substituting

$$S_{sat}(a) = S_{sat}(a_s) + \left.\frac{dS_{sat}}{da}\right|_{a_s}(a-a_s) \qquad (46)$$

into eq. (45) gives,

$$a(t) = a_s+(a_o-a_s)\exp(t/\tau),$$

with

$$\tau(S) = \frac{-(a_s+\ell)}{D_{eff}\rho_{eq}^{(o)}(\infty)}\left[\left.\frac{dS_{sat}}{da}\right|_{a_s}\right]^{-1}. \qquad (47)$$

At S=1, using the Kohler curve, eq. (22):

$$\tau(1) = \frac{-Am_s}{2D_{eff}\rho_{eq}^{(o)}(\infty)}\cdot\frac{(\ell+\sqrt{\frac{Am_s}{r^*}})}{(r^*)^2}. \qquad (48)$$

At 17°C with α=1, β=.036 we have $\ell\tilde{=}1.65\mu$; then for $m_s=10^{-15}$ gms, $\tau(1)\sim 1$ sec, and for $m_s=5.8\times10^{-13}$ gms, $\tau(1)\sim10^3$.

For large drops where $S_{sat}(a)\tilde{\sim}1$ and $a>>\ell$,

$$a \tilde{=} [a_o^2+2D_{eff}(S-1)\rho_{eq}^{(o)}(\infty)t]^{\frac{1}{2}}. \qquad (49)$$

From eq. (42) it is clear that surface effects alone ($S_{sat}\tilde{=}1$) can be taken into account by rescaling the radius:

$$a+\ell = [(a_o+\ell)^2+2D_{eff}(S-1)\rho_{eq}^{(o)}(\infty)t]^{\frac{1}{2}}. \qquad (50)$$

If curvature and surface effects are small perturbations they can both be included by replacing ℓ by $\ell+r^*/(S-1)$.

DROP SIZE DISTRIBUTIONS

It is safe to say that interactions between growing drops exist by virtue of their combined effect on ambient vapor density and temperature. Otherwise they can be regarded as isolated (Williams and Carstens, 1971). Therefore the above theory can be used in infer certain trends in the evolution of drop size spectra. This can be done using a simple two drop model.

Consider two noninteracting drops of radius a_1 and a_2, where $a_1 > a_2$, growing under identical ambient conditions. In

addition, consider activated (free growing) drops where curvature dominates the effect of dissolved salts. Substituting a_1 and a_2 into eq. (42) and dividing yields:

$$\frac{\dot{a}_1}{\dot{a}_2} = \frac{a_2}{a_1}\,\frac{1+\ell/a_2}{1+\ell/a_1}\,\frac{1-\dfrac{r^*/a_1}{S-1}}{1-\dfrac{r^*/a_2}{S-1}} \tag{51}$$

The first factor on the right implies a narrowing of the spectrum, and is associated with the basic geometry of the process; this term is responsible for the well known narrowing tendency of diffusive growth of drops. The second term implies a broadening tendency and is associated with surface kinetic effects; its effect diminishes as the drops grow larger. The first two factors together, $(a_2+\ell)/(a_1+\ell)$, imply a narrowing, but at a slower rate than that given by a_2/a_1. The last factor implies a broadening, and is ascribable to curvature effects. There is also a dependence on the applied supersaturation via the "radius", $R=r^*(S-1)^{-1}$. The first and last factors will lead to a broadening if $a_1^{-1} + a_2^{-1} > R^{-1}$. But one would only expect significant broadening if S is such as to cause a_1 to increase (growth) and a_2 to decrease (evaporation), that is if S intersects (due, for example, to depletion) S_{sat} at the unstable equilibrium radius, a_u, where $a_2<a_u<a_1$. Elton et al (1957) nevertheless argue that this process is too slow to be of much importance in cumulus spectra. If the size distribution is localized around a_u sufficiently to justify the expansion of eq. (46) (around a_u instead of a_s) the broadening,

$$a_1 - a_2 = [a_1(o)-a_2(o)]\exp(t/\tau),$$

is characterized by a (positive) relaxation time,

$$\tau = \frac{[r^*/(S-1)+\ell]r^*}{D_{eff}\rho_{eq}^{(\infty)}(S-1)^2}.$$

The magnitude of τ depends strongly on the value of S-1 where it "cuts" the distribution. At S-1 $\sim 10^{-4}$ (17^oC) for example $\tau \sim 10^4$ sec. At S-1 $\sim 10^{-3}$, on the other hand $\tau \sim 10$ sec.

While there is a tendency for the radial size distribution to narrow, no such tendency is implied for areal size distributions, at least under growth conditions:

$$\frac{\frac{d}{dt}(4\pi a_1^2)}{\frac{d}{dt}(4\pi a_2^2)} = \frac{1+\ell/a_2}{1+\ell/a_1} \quad \frac{1-r^*/(S-1)a_1}{1-r^*/(S-1)a_2} \qquad (52)$$

In this case there is a broadening tendency which diminishes as the radii become larger. As fall velocity is directly proportional to area (up to about 30 μ), there is no diminution of relative fall velocities, but rather the possibility of an early increase. (Such a trend may enter into consideration of the "next stage" in the growth process, collision-coalescence, especially in light of the pronounced increase in collision efficiencies displayed by Klett and Davis (1973) in the region of closely spaced radii.) The divergence of the mass distribution may be similarly argued.

The remarks made here are confined to direct consequences of diffusive growth on size distributions. The spectra of nuclei upon which droplets grow can play an important role. Spectra are also affected by larger scale dynamics as found in clouds (Warner, 1970; Bartlett and Jonas, 1972). Mason and Jonas (1974) predicted drop size distributions agreeing with those of Warner (1969) on the basis of simple diffusive growth (ℓ=0) applied to drops growing (and evaporating) inside spherical thermals which ascend through the residue of their predecessors. Fitzgerald, on the other hand, predicted drop spectra in continental clouds on the basis of eq. (40), with measured nuclei distribution using a closed parcel model.

COMPARISON WITH EXPERIMENT

The experiments herein reported are a direct outgrowth of the work of Vietti and Schuster (1973a, b). Some preliminary results have already been discussed by Carter and Carstens (1974). It should be mentioned that measurements reported here do not apply directly to the atmosphere because the supersaturations produced in a Wilson cloud chamber are much larger than those produced in clouds. Nevertheless the present analysis argues for the general validity of the conventional growth theory since one would expect the basic physical mechanism, and hence the theory describing it, to be the same at the low as at the high supersaturations, and moreover (with changes in constants) independent of the non-condensible gas employed.

It is common to put the thermal accommodation coefficient equal to unity (Alty and Mackay, 1935), and we have done so here for both gases. Other pairs of these constants will fit as well; even though we have some temperature spread we have not as yet been able to separate the two parameters.

The experimental apparatus, laser, cloud chamber, etc., are the same as were used by Vietti and Schuster (1973a, b) and we refer to their articles for a full description. The droplets were generated by homogeneous nucleation in a Wilson expansion chamber and allowed to grow, after nucleation, at supersaturation ratios ranging from about 1.3 to 3.5. Scattering from a 6328 Å He-Ne laser at 30° (off of the incoming beam) provided part of the experimental data. A continuous pressure measurement within the chamberprovided the data needed to relate growth rate to bulk thermodynamic conditions. Details of the pressure and scattering intensity measurements are discussed by Vietti and Schuster. Also, these authors discuss the drop size distribution (which is narrow, due to the abruptness of the generation technique) as well as its influence on the sharpness of the Mie peaks.

From the analysis of Vietti and Schuster, it may be concluded that there is a fair agreement between their data and the standard growth theory (Fukuta and Walter, 1970). Furthermore, it is clear that such agreement can be secured with values of either sticking or thermal accommodation coefficients considerably less than unity. Our reason for looking again at these experiments and the analysis is to uncover reasons for what discrepancy exists between theory and experiment and attempt to improve the agreement. As will be seen, the agreement can be substantially improved, leading not only to more confidence in the theory but to a more precise estimate of the sticking and accommodation coefficients.

The growth in Argon was measured under supersaturation ratios ranging from about 1.3 to 3.5. (Appropriate physical constants, diffusion coefficient, thermal conductivity, etc., were taken from Vietti and Schuster's work where the various sources can be found.) Seventeen runs were analyzed, two of which are displayed in figures 1 and 2. In fig. 1 the total pressure after nucleation runs from 1.37×10^6 dynes/cm^2 at .3 sec. about linearly to 1.39×10^6 dynes/cm^2 at 1.0 sec; the corresponding temperatures are 6.4°C and 7.8°C. In fig. 2 these values are 1.43×10^6 and 1.44×10^6 dynes/cm^2 at 11.2°C and 12°C. The dashed line denotes the theoretical prediction of growth without depletion of vapor and addition of heat due to growth. The solid line follows the data and the lower solid line denotes the course of the supersaturation ratio during the growth process. It is felt that the two runs shown are typical of all our Argon runs. While we did not investigate the matter in statistical detail, it would appear that there is no systematic difference between the agreements at low and high growing supersaturations.

The air runs are shown in figures 3 and 4. In figure 3 the pressure and temperature at .4 sec are 1.26 x 10^6 dynes/cm^2 and 2.8°C, and at 1. sec 1.28 x 10^6 dynes/cm^2 and 4°C. These numbers for figure 4 are 1.5 x 10^6 dynes/cm^2, 19 °C and 1.5 x 10^6 dynes/cm^2, 19°C.

The data of all runs can be fit, to the degree indicated in figures 1 through 4, by $\alpha = 1$ and $\beta = .022$; they appear to be equally well fitted, for example, with $\alpha = .1$ and $\beta = .11$.

The problem of "initial conditions" is important in using this technique. There is no guarantee that the first observed peak is actually the first Mie peak. This may be due to the possibility that the first peak, which is weak anyway, is not resolved. It may also be that the size distribution is just broad enough at the first peak (.45 microns) that it is washed out. In systematically decreasing the growing supersaturation, we have continuously scrutinized the data for the earliest peak. In Argon we have identified the earliest peak as the first Mie peak on the grounds that the extrapolation of the growth curves through radius "zero" (embryonic size) always passes through the nucleation event, i.e. that very narrow portion of the supersaturation pulse during which the supersaturation is critical. Shifting the data by one peak, that is assuming that the first observed peak is really the second Mie peak, leads to an extrapolation which clearly precedes the nucleation event. Thus in Argon our identification of the first peak depends upon the validity of the above extrapolation (i.e. that the growth does not drastically depart from the theory below 0.45 microns), as well as the fact that we simply never observe an earlier peak. In air, on the other hand, the Mie peaks had to be shifted in order to cause the curve to pass through the nucleation event. The data for the air runs are not as clean cut as in Argon due to the difficulty of generating drops by homogeneous nucleation in air. Also, while the fits at higher growing supersaturations are about as good in air as in Argon, there seems to be a systematic worsening, in air only, of the overall fit toward lower growing supersaturations. Further work on air is continuing.

The analysis of error, especially in the data, is a difficult problem, and we have accepted Vietti and Schuster's values on this (1973a). They give about 4% on the evaluation of the theoretical curve. On the data, time resolution was within 5% on placement of the first few data peaks and tends to decrease to .5% toward the end of the run. Uncertainty in pressure measurement led to negligible error. Placement of the maxima and minima from the theoretical curves, we feel, led to a negligible error, especially since this error was non-systematic. Estimated drop counts were small enough to neglect vapor depletion and heat addition.

CONCLUDING REMARKS

The comparison between the theory herein presented and data is good, and indicates that the condensation and/or thermal accommodation coefficient should be small. We have chosen .022 and 1. for air and Argon. Work on air is continuing.

ACKNOWLEDGEMENTS

This work was funded by the Army Research Office (grant DA-ARO-31-124-72-G188) to whom we tender our thanks. Thanks go to Drs. Schuster and Vietti for their encouragement, and useful discussion. Thanks also to Dr. J. L. Kassner, Jr., and Dr. D. White for their invaluable assistance, and to Mrs. S. Shults for typing and proofing the manuscript.

REFERENCES

1. T. Alty and C. A. Mackay, 1935: The accommodation coefficient and the evaporation coefficient of water. Proc. Roy. Soc., London, A199, 104-116.
2. A. G. Amelin, 1966: Theory of Fog Condensation. Israel Program for Scientific Translations, Jerusalem.
3. P. S. Brown and G. Arnason, 1973: Efficient numerical integration of the equations governing droplet growth by condensation. J. Atmos. Sci., 30, 245-248.
4. J. T. Bartlett, and P. R. Jonas, 1972: On the dispersion of the sizes of droplets growing by condensation in turbulent clouds. Quart. J. R. Met. Soc., 98, 150.
5. J. C. Carstens, J. Podzimek, and A. Saad, 1974: On the analysis of the condensational growth of a stationary cloud droplet in the vicinity of activation. J. Atmos. Sci. 31, 592.
6. _____, 1972: Comments on "Kinetics of hydrometeor growth from a vapor spherical model." J. Atmos. Sci., 29, 588-591.
7. _____ and J. T. Zung, 1970: Theory of droplet growth in clouds I. J. Coll. Interf. Sci., 33, 299.
8. _____ and J. L. Kassner, Jr., 1968: Some aspects of droplet growth theory applicable to nuclei measurements. J. Rech. Atmos., 3, 33-39.
9. J. M. Carter and J. C. Carstens, 1974: Experimental corroboration of the conventional theory of drop growth by laser scattering. Trans. AGU (abstr.), 55, 268.
10. G. A. H. Elton, B. J. Mason, and R. G. Picknett, 1958: The relative importance of condensation and coalescence processes on the stability of a water fog, Trans. Faraday Soc. 54, 1724.
11. J. W. Fitzgerald, 1970: A reexamination of the classical theory of the growth of a population of cloud droplets by condensation. Preprints Conf. Cloud Physics, Ft. Collins, Colo., Amer. Meteor. Soc., 111-112.

12. R.G. Fleagle and J. A. Businger, 1963: An Introduction to Atmospheric Physics. New York, Academic Press.
13. N. Frossling, 1938: On the evaporation of falling drops. Beitr. Geophys. 52, 170.
14. N. A. Fuchs, 1959: Evaporation and Droplet Growth in Gaseous Media (English translation). New York, Pergamon Press, 72 pp.
15. N. Fukuta and L. A. Walter, 1970: Kinetics of hydrometeor growth from a vapor spherical model. J. Atmos. Sci., 27, 1160-1172.
16. D. T. Jamieson, 1965: The condensation coefficient of water, Advances in Thermophysical Properties at Extreme Temperatures and Pressures (3rd Symp. on Thermophys. Properties, ASME), Ed. S. Gratch, p. 230.
17. E. H. Kennard, 1938: Kinetic Theory of Gases. New York, McGraw-Hill, 438 pp.
18. J. S. Kirkaldy, 1958: The time dependent diffusion theory for condensation on spherical and plane surfaces. Can. J. Phys., 36, 446.
19. J. D. Klett and M. H. Davis, 1973: Theoretical collision efficiencies of cloud droplets at small Reynolds numbers. J. Atmos. Sci., 30, 107.
20. I. Langmuir, 1944: Supercooled water drops in rising currents of cold saturated air. Gen. Elec. Res. Lab., p. 2984 (6).
21. B. J. Mason and P. R. Jonas, 1974: The evolution of droplet spectra and large droplets by condensation in cumulus clouds. Quart. J. R. Met. Soc., 100, 23.
22. A. F. Mills and R. A. Seban, 1967: The condensation coefficient of water. Int. J. Heat Mass Transfer, 10, 1815.
23. M. Neiburger and Chien, 1960: Computations of the growth of cloud drops by condensation using an electronic digital computer. Geophysical Monograph No. 5, NAS-NRC (746), p. 191.
24. N. Nix and N. Fukuta, 1973: Nonsteady state theory of droplet growth. J. Chem. Phys., 58, 1735.
25. C. Rooth, 1957: On a special aspect of the condensation process and its importance in the treatment of cloud particle growth. Tellus, 9, 372-377.
26. U. S. Sedunov, 1972: The Physics of Liquid Phase Formation in the Atmosphere (in Russian). Leningrad, Gidrometeoizdat, 206 pp.
27. P. N. Shankar, 1970: A kinetic theory of steady condensation. J. Fluid Mech., 40, 385-400.
28. V. I. Smirnov, 1971: The rate of quasi-steady state and evaporation of small drops in a gaseous medium. Pure Appl. Geophys., 86, 184-194.
29. P. Squires, 1952: The growth of cloud drops by condensation, I. Aust. J. Sci. Res., A5, 59-86.
30. M. A. Vietti and B. G. Schuster, 1973a: Laser scattering measurements of droplet growth in binary mixtures I. H_2O and air. J. Chem. Phys. 58 434.

31. _____, 1973b: II. H_2O and Argon, H_2O and Helium, J. Chem. Phys., 59, 1499.
32. J. Warner, 1970: The microstructure of cumulus cloud. Part III. The nature of the updraft. J. Atmos. Sci., 27, 682.
33. _____, 1969: II. The effect of droplet size distribution of the cloud nucleus spectrum and updraft velocity. J. Atmos. Sci., 26, 1272.
34. A. Williams and J. C. Carstens, 1971: A note concerning the interaction of two growing water droplets, J. Atmos. Sci., 28, 1298.

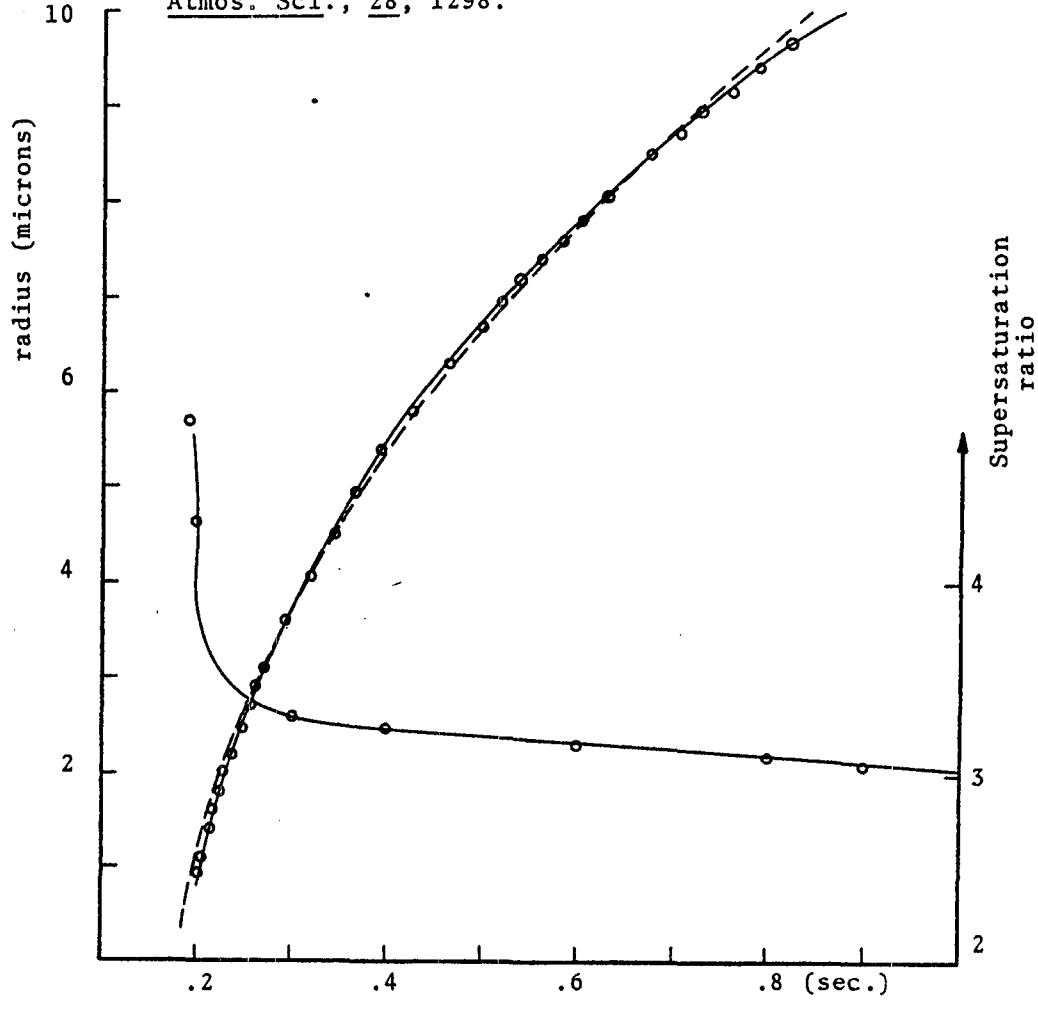

Fig. 1. Radius (μ) vs. time (sec.). Argon

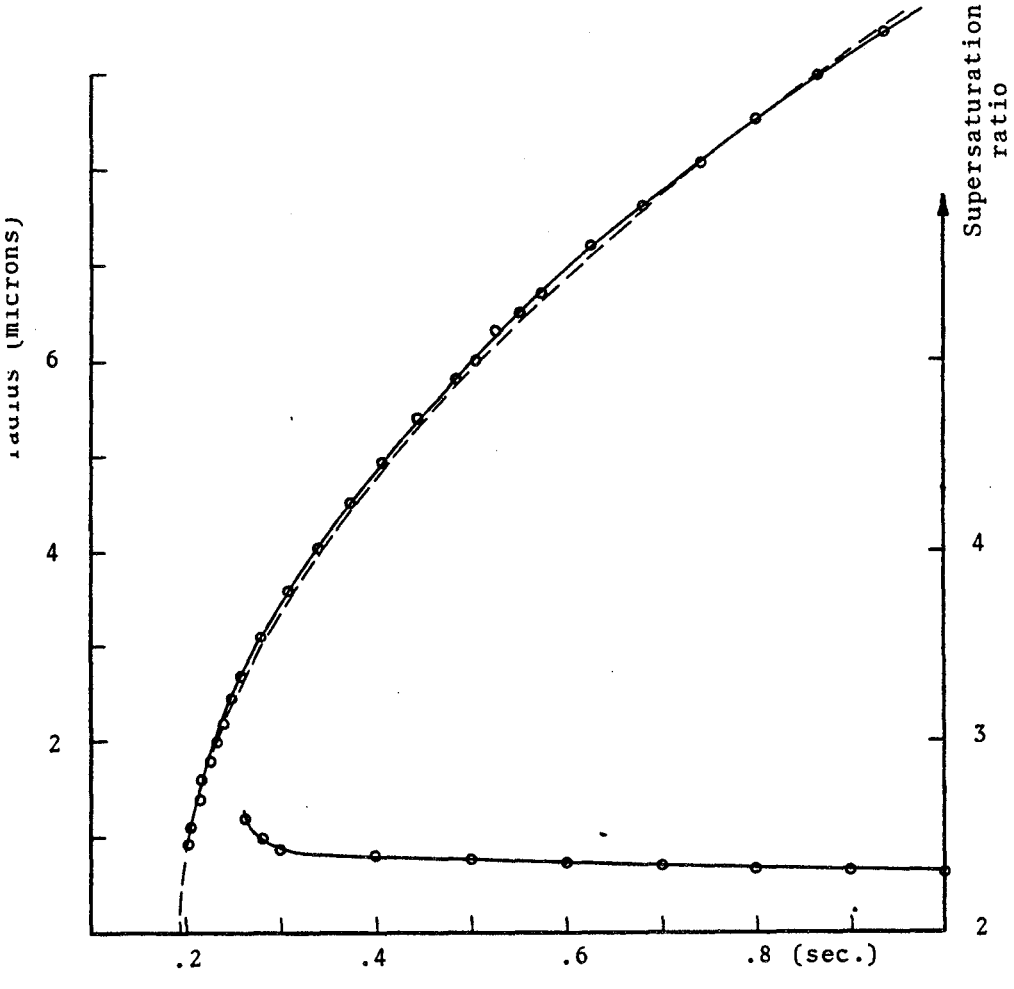

Fig. 2. Radius (μ) vs. time (sec.). Argon

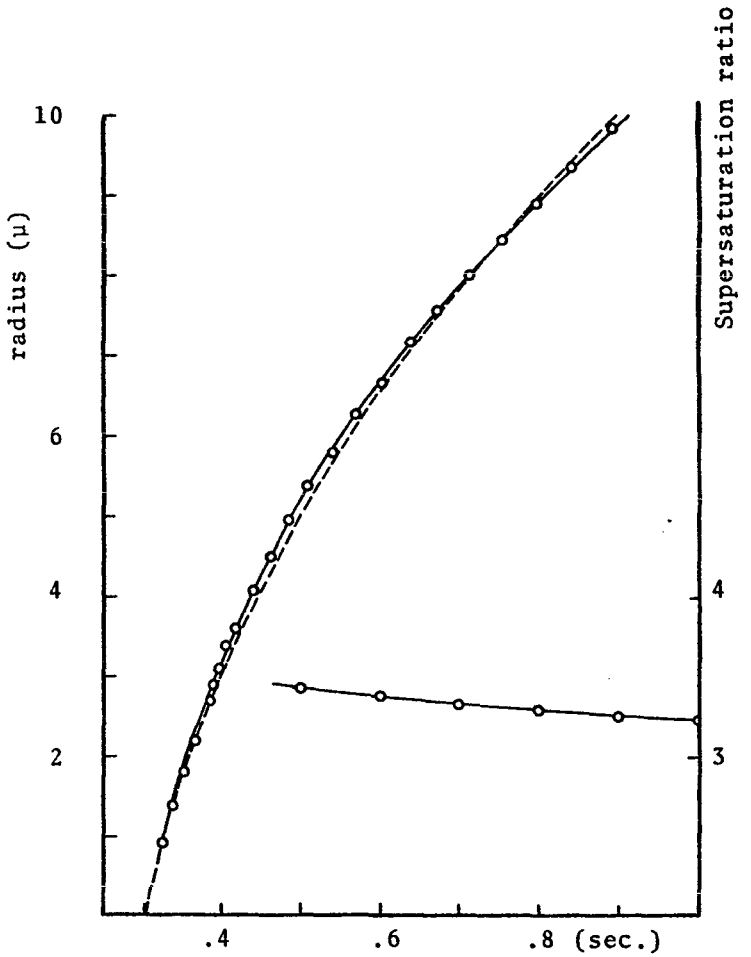

Fig. 3. Radius (μ) vs. time. Air

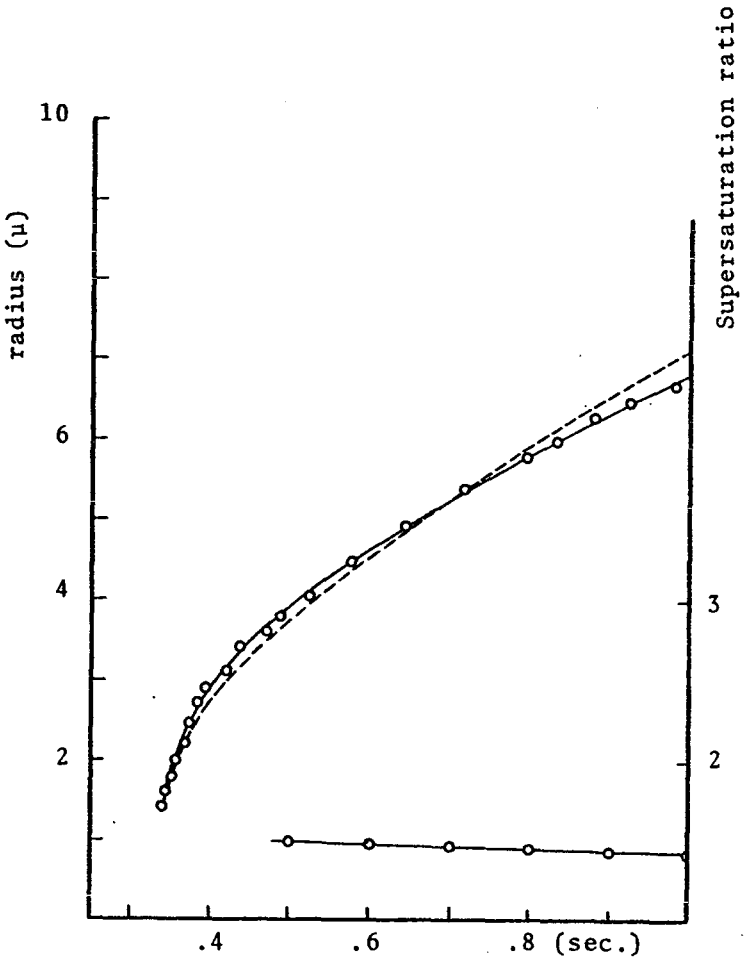

Fig. 4. Radius (μ) vs. time. Air

GROWTH MECHANISMS FOR URBAN AEROSOL PARTICLES

S. L. Heisler and S. K. Friedlander
California Institute of Technology
Pasadena, California

ABSTRACT

The general equation describing the dynamics of a cloud of small particles includes a term for growth from the continuous phase. This process is of controlling importance in the dynamics of urban aerosols and is closely related to the visibility problem.

An experimental program has been initiated to determine the form of the growth law under conditions simulating the Los Angeles atmosphere. Experiments have been conducted in which hydrocarbons, sulfur dioxide and oxides of nitrogen were added to ambient Pasadena aerosol in a 60 m^3 Teflon bag exposed to natural solar radiation. The ensuing photochemical reactions caused growth of the aerosol particles. An optical particle counter was used to measure the size distributions of the aerosol as a function of time for particles larger than 0.30μm diameter.

The changes in the size distributions with time were used to determine particle growth rates as a function of size and time. The results indicate that the gas-to-particle conversion process consists of the formation of supersaturated chemical species in the gas phase followed by condensation of these species on preexisting particles. In the condensation process, the variation of vapor pressure of the condensing species above the droplet with size (Kelvin relation) must be taken into account; this effect leads to sizes below which condensation does not occur.

INTRODUCTION

Reliable methods for relating the urban smog aerosol to its sources are needed for the control of visibility and of human exposure to trace metals, organic substances, sulfates and nitrates. Visibility reduction by light scattering and health effects by deposition of particles in the lungs are complex functions of the aerosol size distribution. It is necessary to be able to determine the manner in which the aerosol is modified by various processes.

Particulate sources can be classified as either primary or secondary. Primary sources are those which emit particles directly into the atmos-

phere. Secondary sources are those which lead to the formation of particulate material in the atmosphere through gas-to-particle conversion. Much of the organic material, sulfates and nitrates in urban aerosols results from secondary processes and accounts for about one-half of the aerosol mass during periods of moderate to heavy smog in Los Angeles (1). It is the goal of this research to determine the manners in which the size distribution is affected by these secondary sources.

AEROSOL DYNAMICS

The dynamics of a cloud of small particles can be described by a partial integro-differential equation:

$$\frac{\partial n(d_p, \vec{r}, t)}{\partial t} + \nabla\cdot[(\vec{v}(\vec{r}, t) + \vec{v}_s(d_p))n(d_p, \vec{r}, t)] + \frac{\partial}{\partial d_p}[I(d_p, \vec{r}, t)n(d_p, \vec{r}, t)]$$

$$= \nabla\cdot D(d_p)\nabla n(d_p, \vec{r}, t) + \tfrac{1}{2}\int_0^{d_p} \beta(d_p', \tilde{d_p}, \vec{r}, t)\, n(d_p', \vec{r}, t)\, n(\tilde{d_p}, \vec{r}, t)\, dd_p' - \qquad (1)$$

$$n(d_p, \vec{r}, t)\int_0^{\infty} \beta(d_p, d_p', \vec{r}, t)\, n(d_p', \vec{r}, t)\, dd_p'$$

$n(d_p, \vec{r}, t)$ is the size distribution function and is defined such that dN, the number of particles per unit volume with sizes in the range d_p to $d_p + dd_p$ is given by:

$$dN(d_p, \vec{r}, t) = n(d_p, \vec{r}, t)dd_p \qquad (2)$$

where d_p is particle diameter, $\vec{r}$ is the position vector and t is the time. $\vec{v}(\vec{r}, t)$ is the velocity of the suspending fluid and $\vec{v}_s(d_p)$ is the particle settling velocity. $I(d_p, \vec{r}, t)$ is the rate of change of particle diameter by gas-to-particle conversion and growth of preexisting particles:

$$\frac{dd_p}{dt} = I(d_p, \vec{r}, t) \qquad (3)$$

$D(d_p)$ is the particle diffusion coefficient. $\beta(d_{pi}, d_{pj})$ is the coagulation constant for particles of sizes d_{pi} and d_{pj} so that $\beta(d_{pi}, d_{pj})n(d_{pi}, \vec{r}, t)$ $n(d_{pj}, \vec{r}, t)dd_{pi}dd_{pj}$ is the collision rate per unit volume of fluid between particles of sizes d_{pi} to $d_{pi} + dd_{pi}$ and d_{pj} to $d_{pj} + dd_{pj}$. $\tilde{d}_p$ is defined by

$$\tilde{d_p} = (d_p^3 - d_p^{3'})^{1/3} \tag{4}$$

Eq. (1) results from an analysis of the rate of change of the number of particles with sizes between d_p and $d_p + dd_p$ in an infinitesimal volume, as a result of convection, diffusion, sedimentation, coagulation and gas-to-particle conversion. Differences between the velocities of the fluid and the particles due to inertial effects have not been considered. The second term on the left side of Eq. (1) results from convection and settling. The third term arises from growth through gas-to-particle conversion. The first term on the right side results from particle diffusion, and the second and third terms from coagulation. The growth term can be interpreted to include homogeneous nucleation provided suitable constraints are placed on β, the collision frequency function. Primary aerosol sources appear in the boundary conditions for the equation, while the secondary sources are in the equation itself.

If the motion of the suspending fluid is turbulent, short time fluctuations must be taken into account. The Reynolds hypothesis can be applied where $\vec{v}$, n and I are assumed to be sums of slowly and rapidly varying terms such that the averages of the rapidly varying terms vanish over short times

$$\begin{aligned} \vec{v} &= \bar{\vec{v}} + \vec{v}' \\ n &= \bar{n} + n' \\ I &= \bar{I} + I' \end{aligned} \tag{5}$$

Turbulent coagulation is neglected, and β is not considered to be a fluctuating variable. The over-lines represent short time averages and the prime denote rapid fluctuations. The fluctuating term in I is due to variations in gas phase concentrations. Eq. (5) can be substituted into (1) and the equation averaged over short times to give:

$$\frac{\partial \bar{n}}{\partial t} + \nabla\cdot(\bar{\vec{v}} + \vec{v}_s)\bar{n} + \nabla\cdot\overline{(\vec{v}'n')} + \frac{\partial}{\partial d_p}\overline{(In)} + \frac{\partial}{\partial d_p}\overline{(I'n')} = \nabla\cdot D\nabla\bar{n}$$

$$+ \tfrac{1}{2}\int_0^{d_p} \beta(d_p', \tilde{d_p})\bar{n}(d_p')\bar{n}(\tilde{d_p})\,dd_p' + \tfrac{1}{2}\int_0^{d_p} \beta(d_p', \tilde{d_p})\overline{n'(d_p')n'(\tilde{d_p})}\,dd_p' \tag{6}$$

$$- \bar{n} \int_o^\infty \beta (d_p', d_p) \bar{n}(d_p') dd_p'$$
$$- \int_o^\infty \beta (d_p, d_p') \overline{n'(d_p) n'(d_p')} dd_p' \quad (6)$$

Various terms in Eq. (6) dominate in different particle size ranges. Convection and eddy diffusion are independent of particle size in the absence of inertial effects. Sedimentation is significant only for large particles ($d_p > 1\mu m$). Gas to particle conversion causes an increase in particle size and, for certain forms of I, leads to accumulation of particles in certain size ranges. Brownian diffusion affects very small particles ($d_p < 0.1\mu m$). Brownian coagulation causes a drop in the number of very small particles and transfers them to larger sizes. However, the effect on these larger sizes is generally small since only a small amount of material is transferred. Coagulation by laminar shear can affect all sizes. Coagulation by differential sedimentation is important for coagulation between large particles of differing sizes and can, under certain circumstances, sweep large numbers of smaller particles from the atmosphere.

Visibility reduction by smog aerosols results primarily from light scattering by particles with diameters between 0.1 and 1.0μm (2). Primary aerosols as they are emitted cannot account for the observed visibility reduction (1). Analysis of chemical composition shows that the products of secondary conversion processes account for a major portion of the aerosol on days of poor visibility (1, 4). This is consistent with the results of Husar, et al. (3) who have shown that gas-to-particle conversion can account for the accumulation in the 0.1 to 1.0μm size range. Hence particle growth plays a key role in the dynamics of the urban aerosol; the purpose of this study was to evaluate growth mechanisms experimentally and theoretically.

GROWTH LAWS

The form of the growth law depends on the mechanism which controls the rate of transfer to the individual particles (4). If diffusion of gas phase material to the particles controls, the growth law is given by Fuchs and Sutugin (5) based on the work of Sahni (6):

$$\frac{dv}{dt} = \sum_i \frac{2\pi D_i M_i}{\rho_i R T} \frac{d_p}{1 + \ell \frac{2\lambda}{d_p}} (p_i - p_{io}) \quad (7)$$

where v is the particle volume, t is time, D_i the diffusion coefficient of the i^{th} species, p_i and p_{io} its partial pressure far from and near the particle, ρ_i its particulate phase density and M_i its molecular weight. R is the gas law constant, T the absolute temperature, and λ the mean free path in air. The factor ℓ is given by:

$$\ell = \frac{1.333 + 0.71\ Kn^{-1}}{1 + Kn^{-1}} \tag{8}$$

where $Kn = 2\lambda/d_p$ is the Knudsen number. Equation (7) assumes that (1) the diffusion is a quasi-stationary process, so that the flux of material to the particle can be considered constant with time, (2) the concentration of diffusing molecules in the gas phase is small enough that collisions between diffusing molecules can be neglected and (3) the masses of the diffusing molecules are much less than those of the bulk phase (air) so that diffusing molecules assume the velocity distribution of the bulk phase molecules following collisions. The first two assumptions are probably valid in urban smog while the last is not. However, the problem for which the last assumption does not hold has not been solved.

When the diffusing species is adsorbed or absorbed by the particles, p_{io} vanishes. When droplet curvature and solution composition have a significant effect on vapor pressure, the Gibbs-Duhem equation can be used to calculate the equilibrium partial pressure of the i^{th} species over the solution droplet:

$$p_{io} = p_{vi}\, \gamma_i x_i \exp(4\sigma M_i/\rho_i RTd_p) \tag{9}$$

where p_{vi} is the vapor pressure of the species, x_i its particulate mole fraction, σ the surface tension of the particle and γ_i is the activity coefficient of the species in the particle defined such that γ_i approaches one as x_i approaches one. It is assumed that the gas phase is ideal. The growth rate is then given by:

$$\frac{dv}{dt} = \sum_i \frac{2\pi D_i M_i p_{vi}}{p_i RT} \frac{d_p}{1 + \ell \frac{2\lambda}{d_p}} \left[S_i - \gamma_i x_i \exp\left(\frac{4\sigma M_i}{\rho_i RTd_p}\right)\right] \tag{10}$$

where $S_i = p_i/p_{vi}$ is the saturation ratio for the i^{th} species. If all the saturation ratios are near one and $\gamma_i x_i$ is independent of particle size, the

exponentials can be expanded and only the linear terms retained to give:

$$\frac{dv}{dt} = \frac{1}{1 + \ell \frac{2\lambda}{d_p}} \sum_i A_i (d_p - d_{pi}^*) \tag{11}$$

where

$$d_{pi}^* = 4\sigma M_i / \rho_i RT \ln(S_i / \gamma_i x_i) \tag{12}$$

and

$$A_i = \frac{2\pi D_i M_i p_{vi}}{\rho_i RT} \gamma_i x_i S_i \ln S_i \tag{13}$$

Equation (5) can be written as:

$$\frac{dv}{dt} = \frac{A}{1 + \ell \frac{2\lambda}{d_p}} (d_p - d_p^*) \tag{14}$$

where

$$A = \sum_i A_i \tag{15}$$

and

$$d_p^* = \frac{\sum_i A_i d_{pi}^*}{\sum_i A_i} \tag{16}$$

d_p^* is the critical size below which growth does not occur.

If the rate of particle growth is limited by a chemical reaction which occurs on the surface of the particle, the growth law is:

$$\frac{dv}{dt} = K_1(t) \pi d_p^2 \tag{17}$$

where the factor $K_1(t)$ is equal to the rate of production of particulate material per unit surface area and is assumed to be independent of size.

If reactions occurring within the particle control the growth, the rate is:

$$\frac{dv}{dt} = K_2(t)\pi d_p^{\,3}/6 \qquad (18)$$

where $K_2(t)$ is the rate of production of particulate material per unit particle volume and, like K_1, is assumed to be independent of size.

EXPERIMENTAL PROCEDURE

Experiments are being conducted to measure the growth rate as a function of particle size using a $60m^3$ bas constructed of 1 mil Teflon^R sheets as a reaction vessel. The sheets are heat sealed together and the seams reenforced with mylar tape. Teflon^R was chosen because of its transparency to ultra-violet radiation and its inert chemical nature; ozone losses to the walls are small. Experiments are conducted on the roof of the Keck Laboratory using natural solar radiation.

In a typical experiment, atmospheric air with its ambient aerosol burden is introduced into the bag, and an organic vapor, NO, and NO_2 are added. In some cases, SO_2 is also added. Precautions are taken to assure adequate mixing of the additives with the air. The quantity of NO added is sufficient to reduce the initial ozone concentration to zero. The bag is flushed with ambient air a minimum of three times before the introduction of the additives in order to remove residual products from previous experiments. Particle size distributions are measured as a function of time in the size range above $0.30\mu m$ particle diameter with a modified Climet Instruments Model CI-201 optical particle counter in conjunction with a multichannel analyzer. Concentrations of NO, NO_2, SO_2 and ozone are also monitored as well as total aerosol number concentration, light scattering and solar radiation. The size distribution measurements are made over a 100 to 150 sec time period. An additional 100 sec. is required between measurements for output of the data to a Teletype.^{R}

The Mie theory of light scattering in conjunction with monodisperse polystyrene latex spheres has been used to determine theoretical calibrations for the optical counter system for various particle refractive indices. The particles in the bag have been assumed to be spherical with an index of refraction of 1.5 (2).

EXPERIMENTAL RESULTS

To calculate particle growth rates, the following assumptions are made: (1) coagulation does not affect the number or size of particles measured by the optical particle counter ($d_p > 0.3\mu m$), (2) all particles of a given size grow at the same rate and (3) the growth rate is a monotonic function of size. Calculations of coagulation rates based on Brownian diffusion and measured total number concentrations support the first assumption, and the experimental results are consistent with the second and third. Then, as a given size particle grows, the number concentration of larger particles will remain the same. Let $NGT(d_p, t)$ be the number concentration of particles with diameters greater than or equal to d_p. If a particle of size d_{po} at t_o grows to d_{pl} at t_1:

$$NGT(d_{pl}, t_1) = NGT(d_{po}, t_o) \tag{19}$$

Hence, measurements of NGT at two different times can be used to calculate values of d_{pl} for various values of d_{po}. Particle growth rates as a function of size are then approximated by:

$$\frac{dv}{dt} = \frac{\pi}{6\Delta t}\left(d_{pl}^3 - d_{po}^3\right) \tag{20}$$

where Δt is the time between measurements. The value of the growth rate is assumed to be for the mean size d_p:

$$d_p = (d_{pl} + d_{po})/2 \tag{21}$$

Three experiments have been conducted. In each, 1 ppm of 1,7-octadiene, 0.33 ppm of NO and 0.33 ppm of NO_2 were added. In one, F91, 0.05 ppm of SO_2 were also added. The times, initial and final total number concentrations, light scattering coefficient (b_{scat}) and maximum ozone concentrations are listed in Table I. Local visibility is inversely proportional to b_{scat}. Figure 1 shows NGT vs. d_p for various times in experiment FO5.

Schuetzle, et al. (7) have identified difunctional organic compounds, such as adipic acid in smog aerosol. Such compounds result from the photochemical oxidation of diolefins or cyclic olefins. Octadiene was chosen as representative of such aerosol precursors.

If the growth is described by either Equation (7) or by (14), both of which result from diffusion, $dv/dt\ (1 + \ell Kn)$ should be a linear function of particle size. Values of $dv/dt\ (1 + \ell Kn)$ from experiment FO4

are shown in Figures 2-6. The lines in the figures are least-squares best fit straight lines to the data. The fits are seen to be good with positive intercepts on the particle size axis. Since Eq. (7) predicts that this intercept should be zero and Eq. (14) predicts a positive value, the results indicate that Eq. (14) can be used to describe the growth and that the growth is therefore due to condensation on the particles and that the variation of vapor above the droplet with radius must be taken into account.

The best-fit values of A varied from 3.89×10^{-5} to $1.03 \times 10^{-4} \mu m^2$/sec in experiment FO4 with an average of $7.05 \times 10^{-5} \mu m^2$/sec and a standard deviation of 1.97×10^{-5}. The values of d_p^* varied from 0.259 to 0.274μm with an average of 0.268μm and a standard deviation of 0.005μm. For experiment FO5, the values of A varied from 4.83×10^{-5} to $1.48 \times 10^{-4} \mu m^2$/sec, with an average of 8.25×10^{-5} and a standard deviation of 3.31×10^{-5}. d_p^* varied from 0.270 to 0.310μm with an average and standard deviation of 0.285 and 0.011μm. For experiment F91, A varied from 3.84×10^{-5} to $1.44 \times 10^{-4} \mu m^2$/sec with an average and standard deviation of 9.78×10^{-5} and $2.95 \times 10^{-5} \mu m^2$/sec. d_p^* varied from 0.257 to 0.423μm with an average and standard deviation of 0.281 μm and 0.056μm. The uncertainties in the individual estimates of A and d_p^* were on the order of 5% and 8%, respectively, for all three experiments.

A series of calculations have been carried out to see whether Eq. (14) can predict the changes in the measured size distributions. The calculations consisted of using a measured size distribution and applying the fitted growth laws over the intervening time period to a later measured distribution. The results of such calculations are shown in Figures 7 and 8. Fig. 7 resulted from using the third measured distribution in experiment FO5 as an initial condition and applying the growth law over the 460 sec. to the fourth measured distribution. Figure 8 shows the results of using the first measured distribution in FO5 as an initial condition and integrating over 2719 sec. to the time of the last measured distribution. The function plotted is $dV/d \log (d_p)$ where V is total aerosol volume concentration and the logarithm is to base 10. The agreement is seen to be good in Fig. 7. Similar agreement between predicted and measured distributions were found for all other calculations between consecutively measured distributions. The agreement in Fig. 8 is not as good, small deviations having propogated over the long integration time involved.

CONCLUSIONS

Three experiments have been conducted in which the growth of aerosols due to gas-to-particle conversion was studied. The system used was naturally irradiated, ambient, unfiltered urban air to which 1,7-octadiene, NO, NO_2 and, in one case, SO_2 were added. The growth rates of the particles larger than 0.3μm diameter were measured as functions

of time and particle size. The observed variations of growth rate with particle size can be described by a growth law resulting from a multi-component supersaturated vapor phase, where the supersaturations are on the order of a few percent and the particulate chemical composition is fairly constant with size. The variation of the vapor pressure of the condensing substances above the particles with radius must be taken into account. Critical diameters on the order of 0.28μm were found.

REFERENCES

1. G. Gartrell, Jr. and S. K. Friedlander, "Relating Particulate Pollution to Sources: the 1972 California Aerosol Characterization Study," to be published in Atmospheric Environment.

2. D. S. Ensor, et al., "Multiwavelength Nephelometer Measurements in Los Angeles Smog Aerosol (I: Comparison of Calculated and Measured Light Scattering)," J. Colloid Interface Sci. 39, 242-251 (1972).

3. R. B. Husar, K. T. Whitby and B. Y. H. Liu, "Physical Mechanisms Governing the Dynamics of Los Angeles Smog Aerosol," J. Colloid Interface Sci. 39, 211-224 (1972).

4. S. L. Heisler, S. K. Friedlander and R. B. Husar, "The Relationship of Smog Aerosol Size and Chemical Element Distributions to Source Characteristics," Atmos. Environment 7, 633-649 (1973).

5. N. A. Fuchs and A. G. Sutugin, "High-Dispersed Aerosols," Topics in Current Aerosol Research, v. 2, Ed. G. M. Hidy and J. R. Brock, Pergamon, Oxford (1971).

6. D. Sahni, J. Nucl. Energy 20, 915 (1966).

7. D. Schuetzle, A. L. Crittenden and R. J. Charlson, "Applications of Computer Controlled High Resolution Mass Spectrometry to the Analysis of Air Pollutants," J. Air Poll. Control Assoc. 23, 704-709 (1973).

Table I

Summary of Experimental Results

Experiment	Date	Time (PDT)	Total Number x 10^{-3} (cm^{-3})		b_{scat} x 10^{4} (m^{-1})		Maximum O_3 (ppm)
			Initial	Maximum	Initial	Maximum	
FO4	6/21/74	1050-1320	13.8	86.1	3.2	24.7	1.16
FO5	6/25/74	1057-1334	18.5	97.5	2.2	>27 (off scale)	1.39
F91	6/26/74	1220-1438	22.5	219	3.5	>27 (off scale)	1.38

Initial gas concentrations: 1 ppm 1,7-octadiene, 0.33 ppm NO, 0.33 ppm NO_2. F91 - 0.05 ppm SO_2. FO4 and FO5 no SO_2. Temperatures ranged from 35 to 45°C in all experiments and were not constant due to variable convective cooling of the bag by winds. Relative humidities ranged from 15 to 30% as temperature varied.

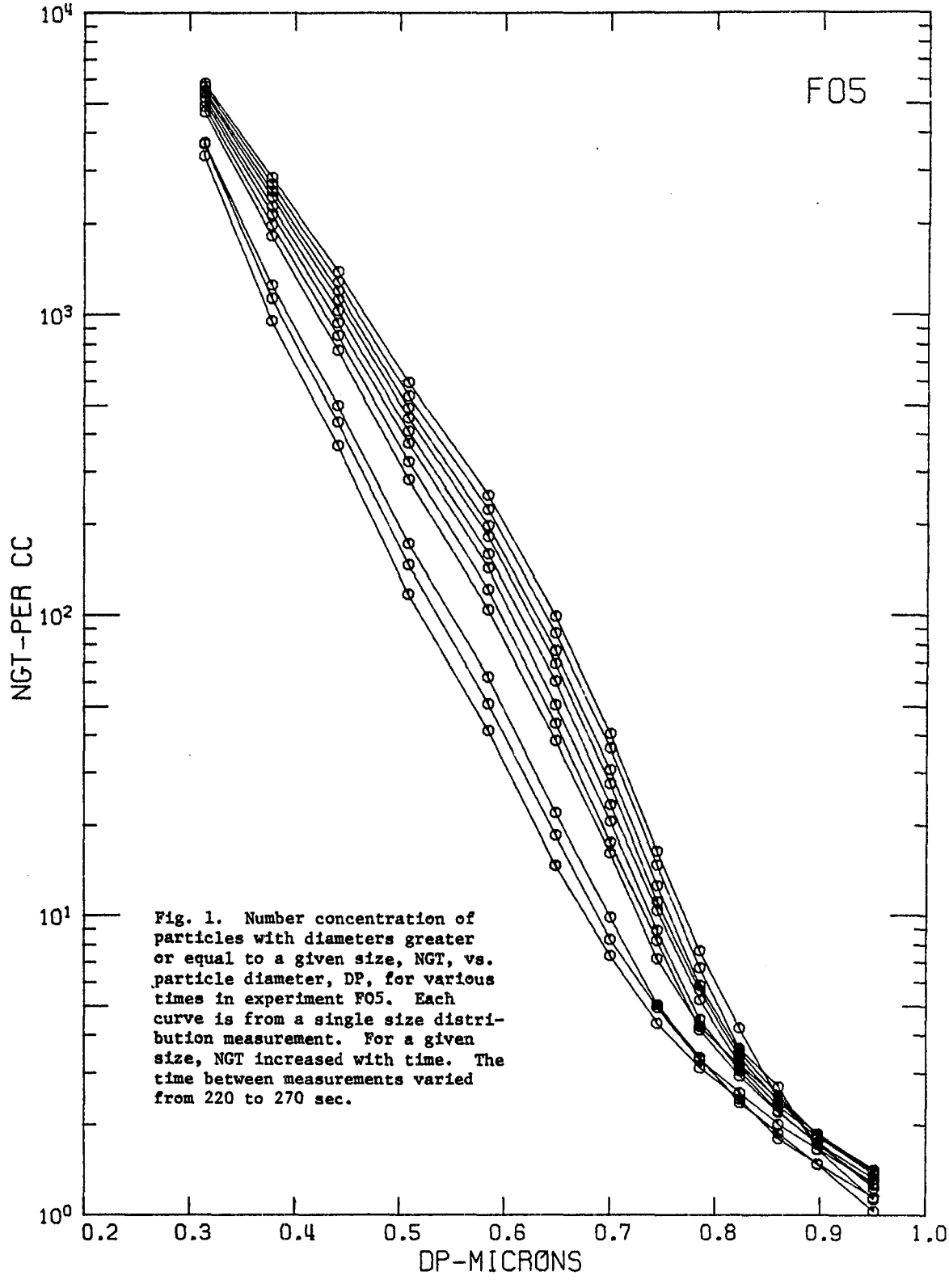

Fig. 1. Number concentration of particles with diameters greater or equal to a given size, NGT, vs. particle diameter, DP, for various times in experiment F05. Each curve is from a single size distribution measurement. For a given size, NGT increased with time. The time between measurements varied from 220 to 270 sec.

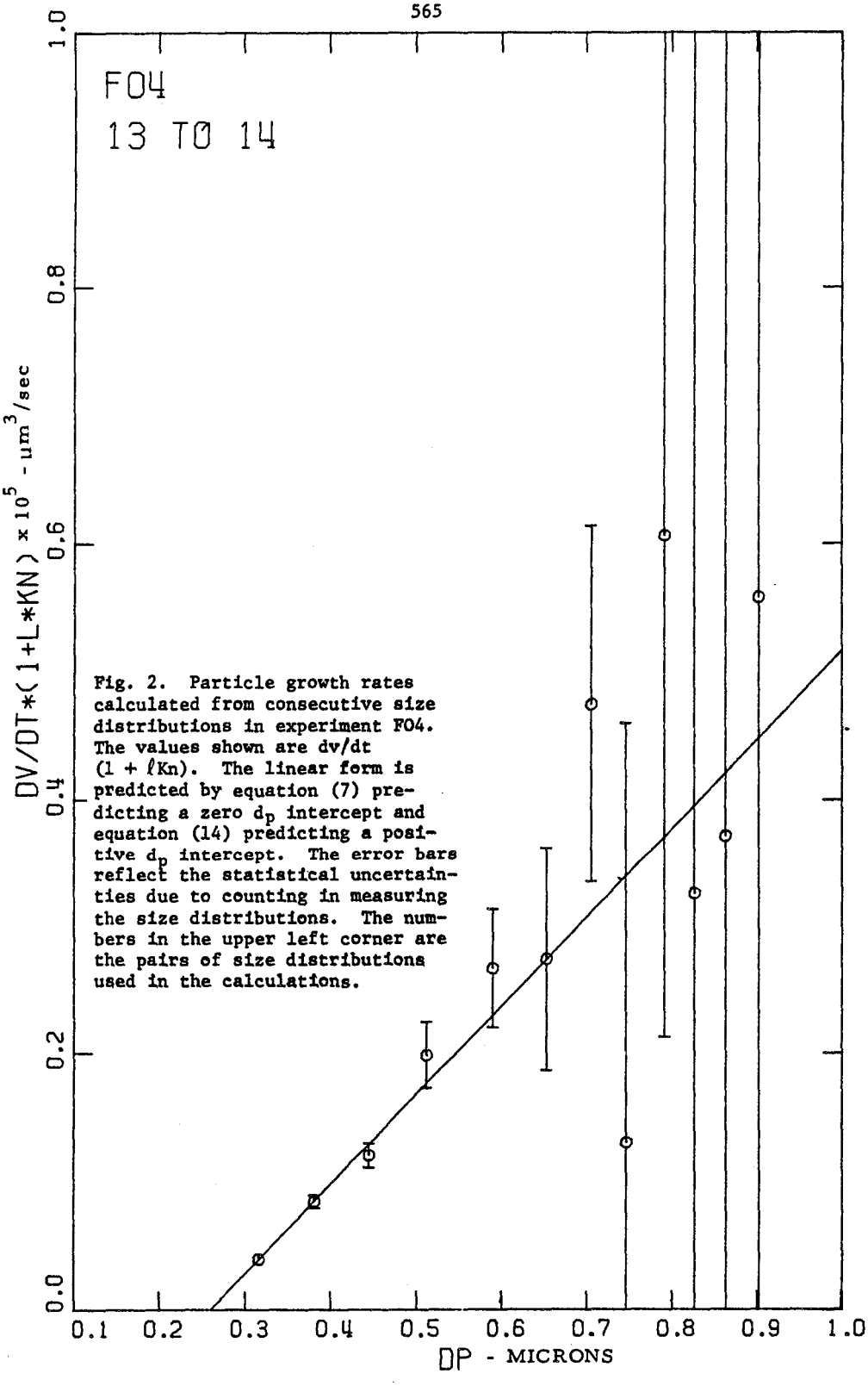

Fig. 2. Particle growth rates calculated from consecutive size distributions in experiment F04. The values shown are dv/dt $(1 + \ell Kn)$. The linear form is predicted by equation (7) predicting a zero d_p intercept and equation (14) predicting a positive d_p intercept. The error bars reflect the statistical uncertainties due to counting in measuring the size distributions. The numbers in the upper left corner are the pairs of size distributions used in the calculations.

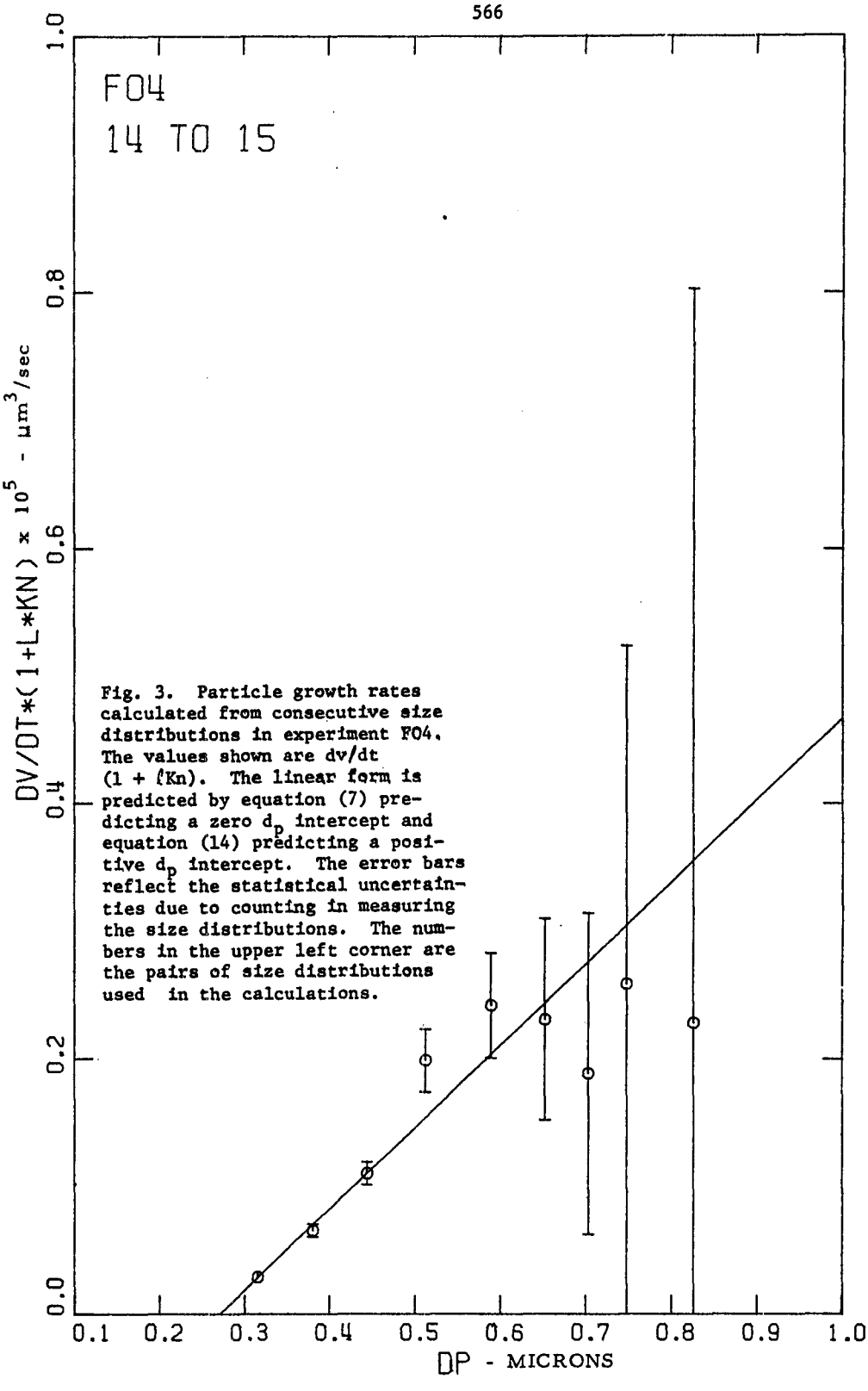

Fig. 3. Particle growth rates calculated from consecutive size distributions in experiment F04. The values shown are dv/dt (1 + ℓKn). The linear form is predicted by equation (7) predicting a zero d_p intercept and equation (14) predicting a positive d_p intercept. The error bars reflect the statistical uncertainties due to counting in measuring the size distributions. The numbers in the upper left corner are the pairs of size distributions used in the calculations.

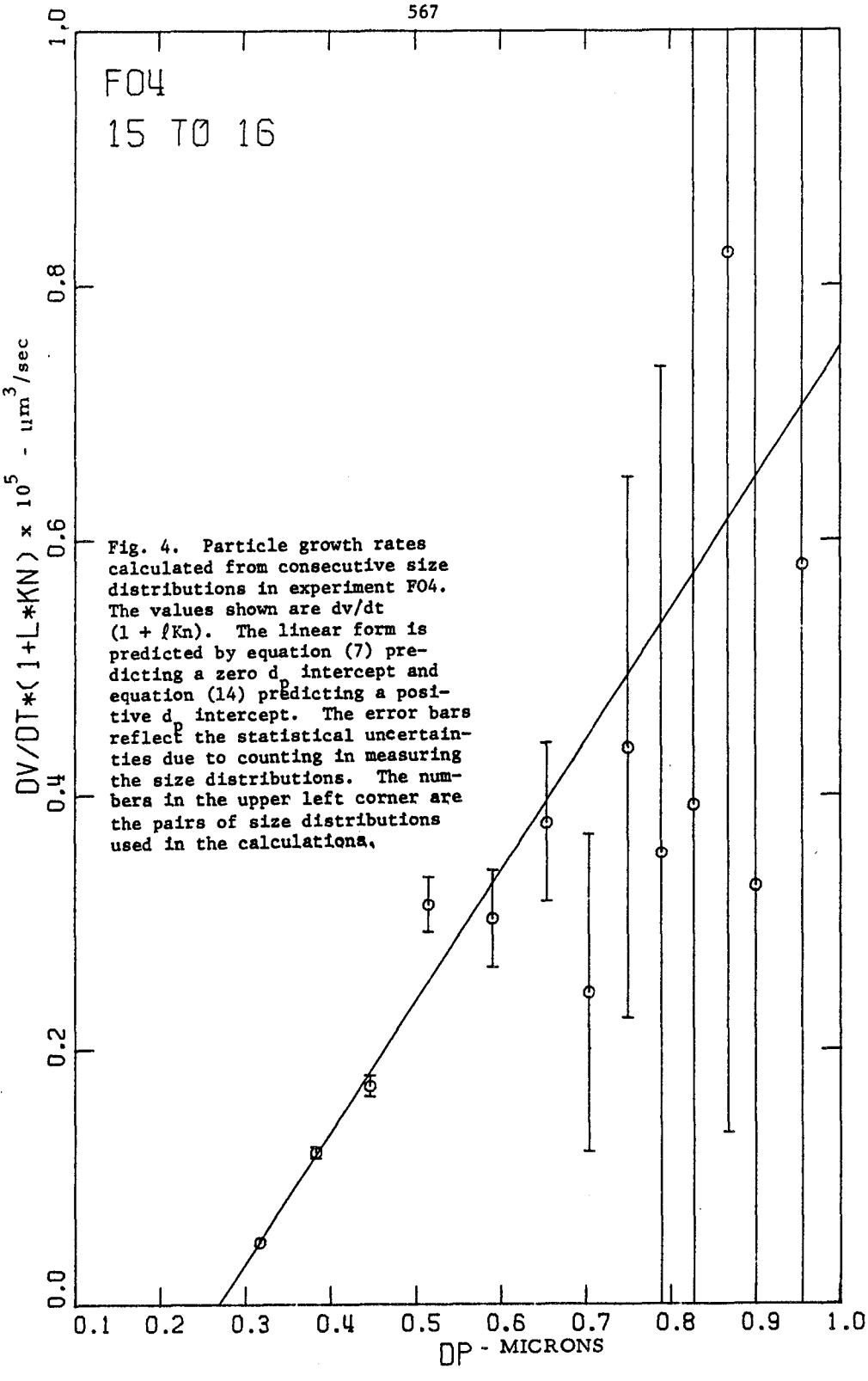

Fig. 4. Particle growth rates calculated from consecutive size distributions in experiment F04. The values shown are dv/dt $(1 + \ell Kn)$. The linear form is predicted by equation (7) predicting a zero d_p intercept and equation (14) predicting a positive d_p intercept. The error bars reflect the statistical uncertainties due to counting in measuring the size distributions. The numbers in the upper left corner are the pairs of size distributions used in the calculations.

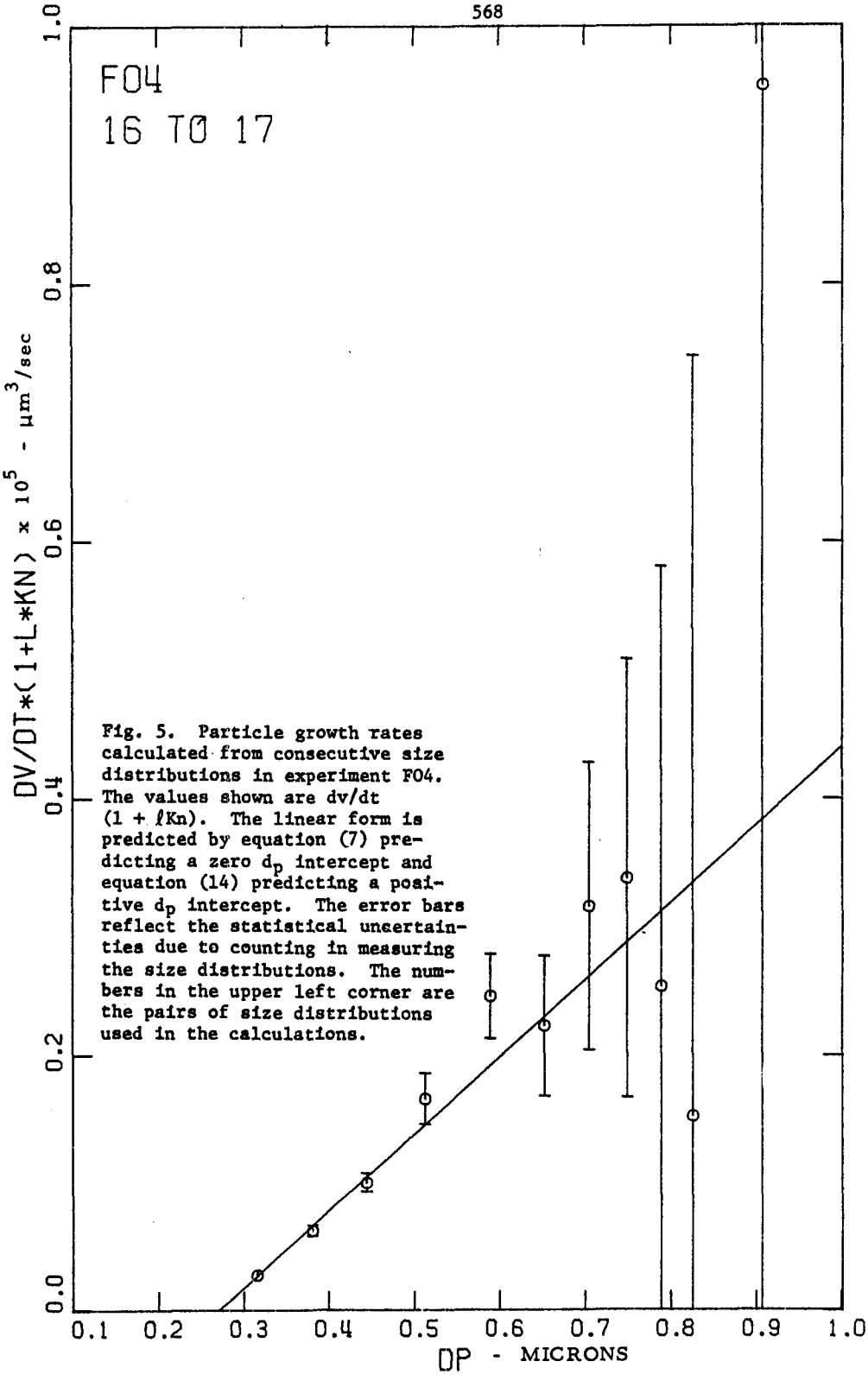

Fig. 5. Particle growth rates calculated from consecutive size distributions in experiment F04. The values shown are dv/dt $(1 + \ell Kn)$. The linear form is predicted by equation (7) predicting a zero d_p intercept and equation (14) predicting a positive d_p intercept. The error bars reflect the statistical uncertainties due to counting in measuring the size distributions. The numbers in the upper left corner are the pairs of size distributions used in the calculations.

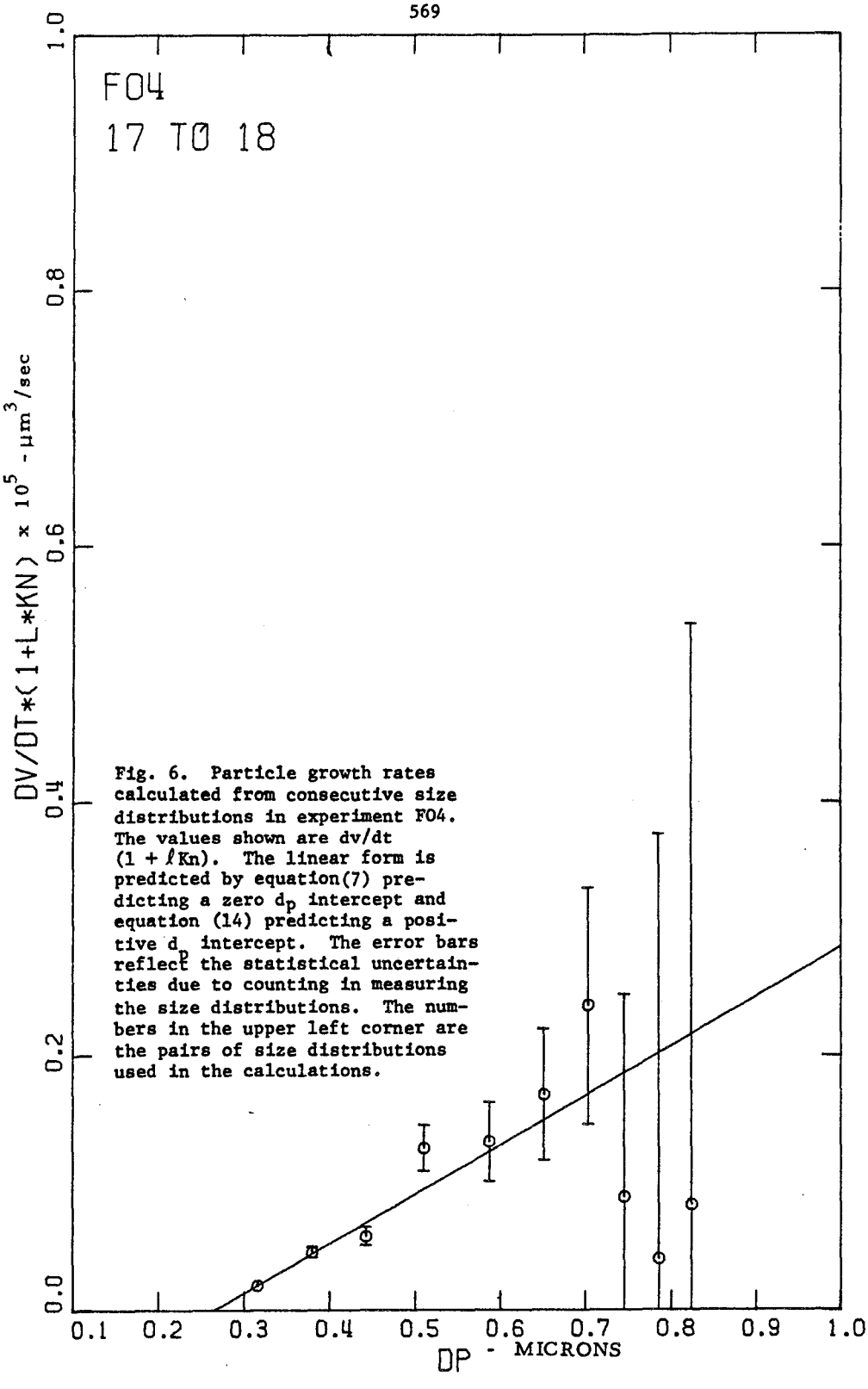

Fig. 6. Particle growth rates calculated from consecutive size distributions in experiment F04. The values shown are dv/dt $(1 + \ell Kn)$. The linear form is predicted by equation(7) predicting a zero d_p intercept and equation (14) predicting a positive d_p intercept. The error bars reflect the statistical uncertainties due to counting in measuring the size distributions. The numbers in the upper left corner are the pairs of size distributions used in the calculations.

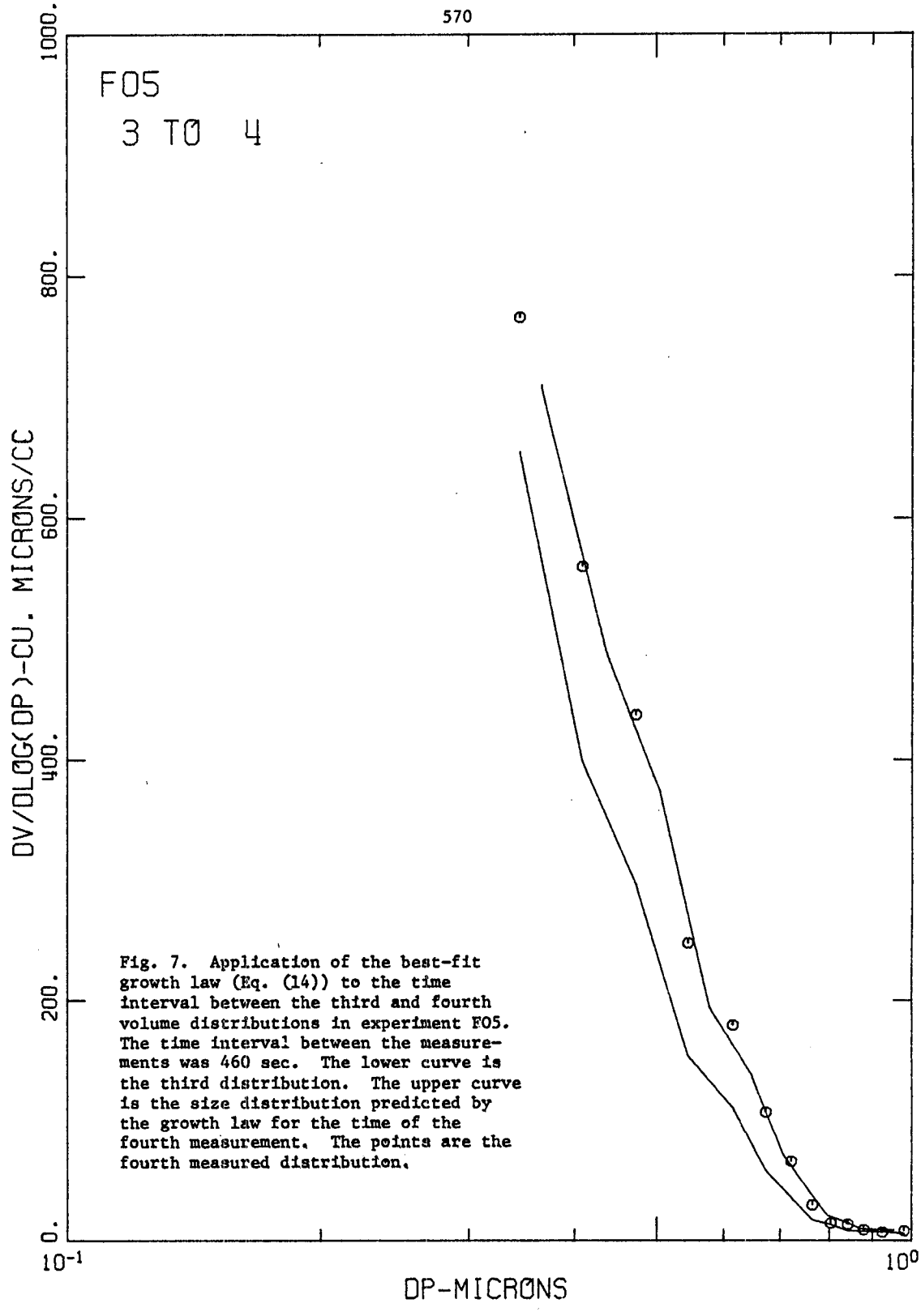

Fig. 7. Application of the best-fit growth law (Eq. (14)) to the time interval between the third and fourth volume distributions in experiment F05. The time interval between the measurements was 460 sec. The lower curve is the third distribution. The upper curve is the size distribution predicted by the growth law for the time of the fourth measurement. The points are the fourth measured distribution.

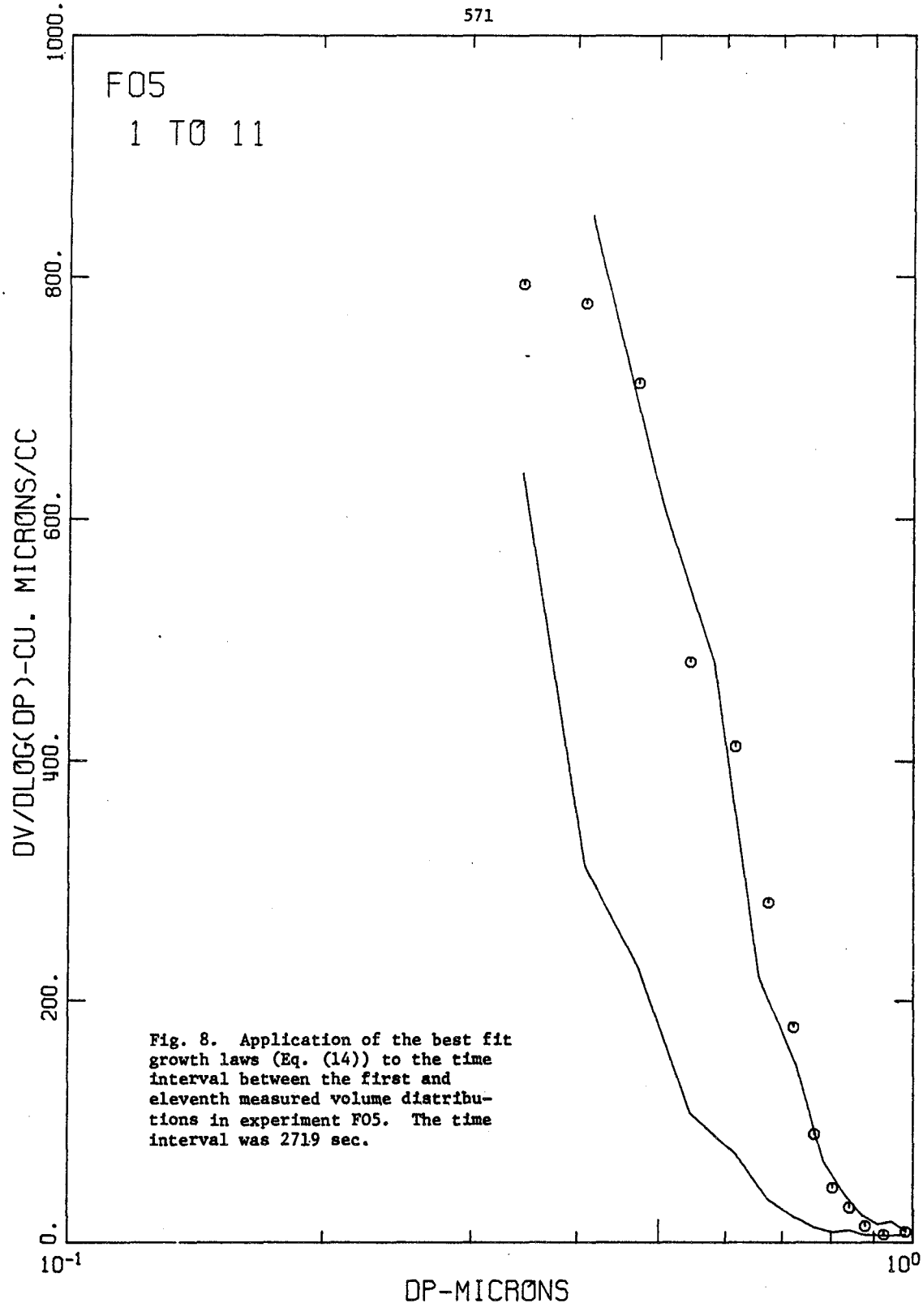

Fig. 8. Application of the best fit growth laws (Eq. (14)) to the time interval between the first and eleventh measured volume distributions in experiment F05. The time interval was 2719 sec.

MICROSTRUCTURE, COMPOSITION AND DYNAMICAL EVOLUTION OF SCATTERING PARTICULATES DETERMINED FROM OPTICAL DATA

Alain L. Fymat
Jet Propulsion Laboratory,
California Institute of Technology
Pasadena, California 91103

ABSTRACT

A method is described for determining the microstructure and composition of scattering particulates from optical data. In a first step, angular measurements of light scattered in a forward cone of approximate half-width 7.5° are performed with an angular resolution of 15 min, or finer, at a near IR wavelength longer than approximately 0.7 μm but not exceeding the expected minimum particle radius. Data obtained in this manner are used to reconstruct the particle size distribution beyond 0.7 μm from a closed form, analytical inverse solution to the angular diffraction integral generalized to a polydispersion. This solution is essentially independent of the refractive index, and is unconstrained relatively to any analytical distribution model. It applies to any arbitrary mixture of j different species of particles, each species eventually exhibiting a different refractive index, imbedded in i different species of gases. An effective gaseous depolarization factor can be determined separately from the measurement at a single near-forward scattering angle of the degree of polarization of the diffracted light. The effect of gases on light scattered by larger particles can thus be effectively eliminated. In a second step, the identical measurement are carried out at a set of additional wavelengths substantially different from the first one. With the size distribution determined in the first step, the latter data are employed to retrieve the complex refractive index at these other wavelengths using a nonlinear minimization search routine we developed earlier. The method can be implemented for real-time operation, thus also providing a means for monitoring the dynamical evolution of the particles.

I. INTRODUCTION

Clouds, radiation and dynamics form the closed system which determines our weather and climate. Each of these three elements is affected, either directly or indirectly, by the scattering

particulates present in the atmosphere in the form of aerosols (natural and anthropogenic), hydrosols (fog, sea sprays) and larger particles (water drops and ice crystals). The effect of these particulates depends on their physical characteristics (geometrical shape, size and distribution, complex refractive index), and on their residence time in the atmosphere. Great interest is therefore attached to the determination of these characteristics and this residence time. Current concern about the quality of our environment has added tremendously to this interest. Several experimental and theoretical techniques dealing with this problem are therefore being revived, improved or newly developed. These techniques transcend the field of meteorology and may be of direct applicability in other fields of science and engineering.

Conventional experimental techniques are based on in situ sampling during which the particles are thermally precipitated, impacted or otherwise mechanically collected. Analysis of their sizes is effected in the bulk range (0.01 - 1,000 μm) covering aerosols, non-precipitating clouds and some rain drops. As is well known, however, several problems are associated with these techniques. While it is not our purpose to discuss here these problems, let us at least indicate that, because the medium is disturbed by the sampling process, it is generally thought that the sample so obtained is not representative. Imaging techniques are also being developed. However, because the measurements are still performed within the medium, it is difficult to assess whether the problem just indicated has been overcome and to what extent. Remote sensing techniques, on the other hand, can by definition overcome this fundamental problem. They are, however, encumbered with analytical and numerical difficulties. These are discussed systematically elsewhere [1]. In the latter techniques, the main efforts have concentrated on only the determination of the size distribution of spherical particles of known composition. In this paper, we wish to present a method we have recently developed for retrieving the size distribution as well as the refractive index and its spectrum. This method involves a two-step process. The first step provides the size distribution independently of the refractive index, a feature of particular interest in the study of drops and bubbles. Using this knowledge, the second step of the process then yields the refractive index spectrum.

II. SOME BACKGROUND REMARKS

Consider an arbitrary mixture of gases and particulates, either contained in a laboratory cell or freely suspended in air or in weightlessness. This medium is illuminated by shortwave radiation (solar light or artificial light source) of known brightness and state of polarization. On interaction, this incident light is partly absorbed and scattered by both gases and particles in the medium. The radiation emerging after interaction can be conveniently separated, both analytically and experimentally, into a direct and a diffuse component. The former component is that part of the incident radiation that has been reduced by absorption and first-order scattering

processes. It propagates in the exact forward direction and is in the same state of polarization as the incoming light. The latter component, the remaining fraction of the incident light, has suffered the same two processes of absorption and scattering but has, in counterpart, been augmented by second- and higher-order scattering (i.e., virtual medium emission) into any viewing direction of interest. It propagates in all directions between and including the exact forward and the exact backward directions. With the exception of the exact forward direction, it is generally in a different state of polarization than the light source. Its intensity in this forward direction is negligible compared to that of the direct beam but, nevertheless, amounts to half the total scattered light, the remaining half being distributed among all other directions.

Both the direct and the diffuse light beams contain information about the absorbing and scattering medium. While it is difficult to quantify the relative information content of these two beams, it is immediately clear that the diffuse beam affords many more possibilities for retrieving this information than the direct beam. To be sure, the diffuse beam will be described by four observables, so called Stokes's parameters (I, Q, U, V) which give, respectively, the light intensity, its degree of polarization, the orientation of its plane of polarization, and the ellipticity of its polarization ellipse. Each observable exhibits variations with both angle and frequency. On the other hand, the direct beam, characterized only by its intensity, presents solely frequency variations. This statement, however, should not be construed to imply that the direct beam is in any way of lesser importance, or contains less information than the diffuse beam. Only a detailed and systematic investigation of both situations will provide a reasonable conclusion as to their relative merits and disadvantages. A concerted use of both beams, when experimentally feasible, may indeed provide a powerful approach since the two determinations of particle parameters resulting from use of the two beams must necessarily be consistent.

The basic problem, in any event, is the following: given, with all required details, the lights incident on, and emerging from, the medium under consideration, determine the medium composition and microstructure. More specifically, determine for each gas present its absorption cross-section, refractive index, anisotropy parameter (for nonspherical atoms and molecules), and number density. (The scattering cross-section is expressed in terms of the latter three parameters by the well-known Rayleigh-Cabannes formula [2]). Likewise, for each particulate, determine its shape, number density, size distribution, and refractive index (both real and imaginary parts). Lastly, determine the medium total optical thickness and, if the medium is bounded by a reflecting surface, such as for the Earth's atmosphere, also determine the surface characteristics. This is a formidable task! Excluding for the moment the surface reflection, the number of unknowns is $5(N + M) + 1$ in the case of N gases and M particulates, assuming that each particulate type can be described by a single characteristic dimension. If the detailed size distribution must be determined, this number becomes

$5N + (4 + P) M + 1$, where P is the number of parameters describing adequately the distribution. Although analytical distributions may not, in many cases, provide adequate representations, let us at least mention that for the most widely used distributions in meteorology, $P = 1$ (power, exponential and lognormal distributions) or $P = 2$ (modified gamma distribution). The spatial variations of these unknowns must also be determined. The corresponding formulation, considering only variations in the vertical, has been provided in our earlier work [1] for the direct beam, and the diffuse beam either reflected by, or transmitted through, the medium after an arbitrary number of scattering events. If the surface, composed of Q different materials, is assimilated to an optically infinite atmosphere, the above cited numbers of unknowns become $5(N + M + Q) + 1$ and $5N + (4 + P)(M + Q) + 1$, respectively. No solution has yet been obtained to this general problem. In the meantime, workers in the field are concentrating their efforts on specialized cases in the hope that the experience and understanding thus acquired will lend a helpful hand for tackling the realistic problem. It is clear from the start that reductions in the problem dimensionality, when justified by either a theoretical analysis or the experimental conditions will be critical to the success of the enterprise. If the actual inhomogeneous medium exhibiting spatial variations can be mimicked by an equivalent homogeneous medium with no such variations, that is if two such media can be found that result in the same emergent radiation field, then, obviously, the true physical parameters of the particles cannot be determined. Instead, "effective" parameters will be obtained which may depart from the true ones. Such effective parameters may nevertheless be useful for a study, not of the properties, but of the effects of the particulates on radiation field observables. We have provided [1] a critical, although not exhaustive, analysis of the various methods thus developed. In this paper, we will limit ourselves to that method developed by the author that seems more appropriate to the purposes of the present volume. Additional material can be found in our earlier publications [1, 3, 4].

III. STATEMENT OF PROBLEM

The following problem will be considered: unpolarized light of wavelength, λ, forming a parallel beam of intensity, I_0, is incident along the direction $\theta_0 = \cos^{-1} \mu_0$ on a plane-parallel stratified medium consisting of an arbitrary mixture of i different species of gases and j different species of particulates. The direction of incidence is referred to the normal to the plane of stratification of the medium, and the particles, which may present a distribution in their refractive indices, are assumed to be homogeneous, spherical, and their sizes described by some arbitrary distribution, n(r), where r is the particle radius. It must be noted that this distribution is not restricted to any particular analytical model and may describe a monodispersion or any arbitrary polydispersion having one or several modes.

The total optical thickness, τ_1, of the medium at wavelength λ will be assumed to be small, $\tau_1 \ll 1$, so that only single scattering need be studied. No reflecting boundary will be considered.

The diffuse light transmitted along the direction $\theta = \cos^{-1}\mu$, referred as earlier to the normal to the plane of stratification, is polarized with components $I \equiv I_1$ and $Q \equiv I_2$, only. They are [1]:

$$I_k(\tau_1; \theta, \lambda) = \tilde{\omega} f I_0 \int_0^\infty P_{k1}[m(\lambda), r]\, n(r)\, dr, \quad k = 1, 2, \tag{1}$$

where

$$f \equiv f(\tau_1; \mu, \mu_0) = \frac{\mu_0}{4(\mu_0 - \mu)} \left(e^{-\tau_1/\mu_0} - e^{-\tau_1/\mu} \right), \tag{2}$$

$\tilde{\omega}$ is the single scattering albedo:

$$\tilde{\omega} = \frac{\sigma_g^i + \sigma_p^j}{\left(\alpha_g^i + \alpha_p^j\right) + \left(\sigma_g^i + \sigma_p^j\right)} \equiv \frac{\sigma}{\epsilon}, \tag{3}$$

and P_{k1} are elements of the scattering phase-matrix:

$$\underset{\sim}{P} \equiv \left\{P_{mn}\right\} = \left[(\sigma_g \underset{\sim}{P}_g)^i + (\sigma_p \underset{\sim}{P}_p)^j \right] / \sigma$$

$$= \left(\underset{\sim}{F}_g^i + \underset{\sim}{F}_p^j \right) / \sigma, \qquad m, n = 1 \text{ to } 4. \tag{4}$$

In deriving Eq. (1) it was assumed that the medium is optically homogeneous, i.e., $\tilde{\omega}$ and $\underset{\sim}{P}$ do not vary in the medium. This is a reasonable assumption in view of the hypothesis $\tau_1 \ll 1$. However, if the medium were inhomogeneous, then, $\tilde{\omega}$ and $\tilde{P}$ would apply to an equivalent homogeneous medium that yields the same transmitted light, as discussed earlier. The quantity $m(\lambda)$ is the medium complex refractive index at wavelength λ; σ and α are volume scattering and absorption coefficients, respectively, with subscripts g for gases and p for particles; and ϵ is a volume extinction coefficient. The superscripts i and j denote, respectively, summations over all i species of gases and j species of particles, i.e.,

$$(\ldots)^{\ell} \equiv \sum_{\ell} (\ldots)_{\ell}, \qquad \ell = \text{i or j}$$

(Einstein's convention). In Eq. (3), σ_p^j and α_p^j must be interpreted as applying to a polydispersion, i.e.,

$$\gamma \equiv \int_0^\infty \gamma(r)\, n(r)\, dr, \qquad \gamma \equiv \sigma_p^j,\ \alpha_p^j, \tag{5}$$

where $\gamma(r)$ is for a single particle radius. Lastly, the matrices $\underset{\sim}{P}_g$ and $\underset{\sim}{P}_p$ are the Rayleigh-Cabannes [2] and the Mie [5] phase-matrices, respectively. For any $m(\lambda)$ and $n(r)$, $\underset{\sim}{P}_p$ can be computed from Mie's theory.

Inserting Eqs. (3), (4) and (5) in Eq. (1), the latter equation becomes:

$$\frac{\epsilon}{f}\left(\frac{I_k}{I_0}\right) - F^i_{k1,g} = \int_0^\infty F^j_{k1,p}\,[m(\lambda), r]\, n(r)\, dr. \tag{6}$$

Now, for any arbitrary θ, we have:

$$\left.\begin{aligned} F^i_{11,g} &= \frac{3}{4} \sum_i \frac{2(\gamma_i + 1) + \sin^2\theta\,(\gamma_i - 1)}{1 + 2\gamma_i}, \\ F^i_{21,g} &= \frac{3}{4} \sum_i \frac{\sin^2\theta\,(\gamma_i - 1)}{1 + 2\gamma_i}, \end{aligned}\right\} \tag{7}$$

where $\gamma_i = \rho_i/(2 - \rho_i)$, ρ_i being the depolarization factor of the ith gas species (e.g., $\rho_n = 0$ for isotropic molecules, $\rho_n = 0.031$ for air), and

$$\left.\begin{aligned} F^j_{11,p} &= \frac{1}{2k^2} \sum_j \left\{ |S_{2,j}|^2 + |S_{1,j}|^2 \right\} , \\ F^j_{21,p} &= \frac{1}{2k^2} \sum_j \left\{ |S_{2,j}|^2 - |S_{1,j}|^2 \right\} , \end{aligned}\right\} \tag{8}$$

where $k = 2\pi/\lambda$ is the wavenumber, and $S_{k,j} \equiv S_{k,j}(\theta, \lambda; r)$, $k = 1, 2$, are Mie functions for a single particle of the j^{th} species and of radius r. For given λ and r, the latter functions will depend only on the refractive index of the jth particle species. However, for forward scattering ($\theta = 0°$), they reduce to (Kirchkoff approximation to Fraunhoffer diffraction; see, for example, Ref. 5):

$$S_{1,j} \equiv S_{2,j} = \frac{kr\, J_1(x)}{\sin\theta} , \quad x = kr \sin\theta , \tag{9}$$

where J_1 is Bessel function of the first kind and order unity. Equation (9) shows that $S_{k,j}$ is remarkably independent of the refractive index, i.e.

$$S_{k,j} \equiv S_k . \tag{10}$$

It follows in this case that Eqs. (8) reduce to

$$\left.\begin{aligned} F^j_{11,p} &= j\, \frac{r^2 J_1^2(x)}{\sin^2\theta} , \\ F^j_{21,p} &= 0 . \end{aligned}\right\} \tag{11}$$

With this result, Eqs. (6) become:

$$\left.\begin{aligned} \frac{1}{j}\left[\frac{\epsilon}{f}\left(\frac{I_1}{I_0}\right) - F^i_{11,g}\right] &= \frac{1}{\sin^2\theta}\int_0^\infty r^2 J_1^2(x)\, n(r)\, dr\,, \\ \frac{\epsilon}{f}\left(\frac{I_2}{I_0}\right) - F^i_{21,g} &= 0\,. \end{aligned}\right\} \quad (12)$$

Under the present conditions of single scattering, we also have by expanding the exponentials in Eq. (2);

$$\lim_{\tau_1 \ll 1} f = \frac{\tau_1}{4\mu} = \frac{\epsilon}{4\cos\theta}\,; \quad (13)$$

and, when this last result is substituted in Eqs. (12), we get the final expressions:

$$Z_1(\theta, \lambda) \equiv \frac{1}{j}\left[4\cos\theta\left(\frac{I_1}{I_0}\right) - F^i_{11,g}\right]$$

$$= \frac{1}{\sin^2\theta}\int_0^\infty r^2\, J_1^2(x)\, n(r)\, dr\,, \quad (14)$$

and

$$Z_2(\theta,\lambda) \equiv 4\cos\theta\left(\frac{I_2}{I_0}\right) - F^i_{21,g} = 0\,. \quad (15)$$

These two expressions provide the required formulation of the problem of interest. Equation (14) is the angular diffraction integral generalized to the case of a polydispersion of scattering particles. Equation (15) can be used to infer information on gaseous depolarization [see Eqs. (7)]. Our main problem will now lie in the following two-step procedure:

1. Assuming $F^{i}_{11,g}$ is known or can be determined separately, to invert Eq. (14) so as to reconstruct the size distribution n(r).

2. Using step No. 1, to infer from Mie's theory the only remaining unknown, namely the complex refractive index, and its spectrum.

The exact manner in which these two steps are carried out explicitly is described in the following sections.

IV. DETERMINATION OF SIZE DISTRIBUTION

Consider again Eq. (14). The left-hand side of this equation is a measured quantity which must be used to reconstruct the size distribution n(r). The ratio (I_1/I_0) is directly provided by angular measurements of light (radiance) scattered in near forward directions contained within a narrow cone whose half-width will later be prescribed. The quantity $F^{i}_{11,g}$ is assumed to be either known a priori or simultaneously measurable. For example, if $\bar{\gamma}$ is an "effective" parameter describing the combined effect of all gaseous species present, $\bar{\gamma} = \bar{\rho}/(2 - \bar{\rho})$, where $\bar{\rho}$ is an effective depolarization factor for the assembly of gases, or in the simple case of i = 1 (single gas species), then, Eqs. (7) become:

$$\left.\begin{aligned} \bar{F}_{11,g} &= \frac{3}{4}\,\frac{2(\bar{\gamma}+1)+\sin^2\theta\,(\bar{\gamma}-1)}{1+2\bar{\gamma}}\ , \\ \bar{F}_{21,g} &= \frac{3}{4}\,\frac{\sin^2\theta\,(\bar{\gamma}-1)}{1+2\bar{\gamma}}\ , \end{aligned}\right\} \tag{16}$$

where $\bar{F}_{kl,g}$ are effective values of $F_{kl,g}$. A simultaneous measurement of the degree of polarization of forwardly scattered light in any direction $\theta \approx 0°$ will provide the quantity $\bar{F}_{21,g}$, that is $\bar{\gamma}$ and, hence, also $\bar{F}_{11,g}$. With the above expressions, the quantity Z_1 becomes:

$$\bar{Z}_1 = \frac{1}{j}\left\{\frac{4\cos\theta}{I_0}\,(I_1 - I_2) - \frac{3}{2}\cdot\frac{1+\bar{\gamma}}{1+2\bar{\gamma}}\right\}\ , \tag{17}$$

which is obtained immediately for any given cone angle θ, measured values of (I_1/I_0) and (I_2/I_0), and depolarization factor $\bar{\gamma}$.

It has been shown [6] that Eq. (14) with J_ν substituted in place of J_1 and $\nu = 1/2, 1, 3/2$ applies to a whole class of scattering particles: Rayleigh-Gans particles, Fraunhoffer particles, and those particles covering the intermediate cases between Rayleigh-Gans and anomalous diffraction [see Ref. 5 for a description of these various particles]. With this substitution in mind, the following will cover all these cases. Using the Bateman-Titchmarsh formula [7, 8], Eq. (14) can be inverted analytically [3, 4, 6] to yield the closed form solution:

$$n(r) = -\frac{2\pi k}{r^2} \int_0^\infty J_1(x)\, Y_1(x)\, x \frac{d}{d(\sin\theta)} (\sin^3\theta\, Z_1)\, d(\sin\theta), \tag{18}$$

where Y_1 is a Bessel function of the second kind of order unity. For the class above listed of particles, Y_ν should be substituted in place of this last function. It must be noted that the result in Eq. (18) makes no assumption regarding the form of n(r); in particular, it does not assume, as is generally done, that n(r) follows any of the analytical distributions derived empirically in the literature. Thus, it is emphasized, n(r) is unbiased and can be any distribution: isolated spike (monodispersion), unimodal, polymodal. For the restricted case of a single species of particles and no gases present, the corresponding result to Eq. (18) is quoted in the Russian literature [see, e.g., Ref. 9], but no explicit demonstration of it could be found.

From Titchmarsh's conditions [8], it follows that Eq. (18) is valid for $\nu \geq 0$ if $k^2 r^2 n(r)$ is integrable over $(0, \infty)$. This will always be true since physical distributions always decay, and vanish beyond a certain maximal radius value. [The validity for $-1/2 < \nu < 0$ requires that $(kr)^{2\nu+2}\, n(r)$ be integrable over $(0, \delta)$, $\delta < \infty$. For $\nu = \pm 1/2$, Equation (18) reduces to Fourier's sine formula.] The solution n(r) given is exactly true for the function Z_1 defined by Eq. (14). In reality, however, θ must remain contained within a narrow cone of angles; in any event, it cannot exceed 180°. Hence, it cannot become unbounded as implied by the above solution, and it therefore becomes conceivable that the distribution n(r) may not be reproduced exactly or, in some extreme cases, not at all.

We have performed a considerable amount of numerical experiments aimed at assessing the effects of this limitation, and at delimiting the domain of applicability of the solution. Some results of the study have been discussed elsewhere [3]. Here, we should like to present some additional new results which should prove to be helpful in the system design of a particle size spectrometer based on the method.

The "measurements", $Z_1(\theta, \lambda)$, were generated in the computer from Eq. (14) using a number of different forms of n(r): monodispersions, and polymodal distributions constructed from a linear combination of a number of expressions like the modified gamma distribution [10]:

$$n(r) = a\, r^{\alpha} e^{-br^{\gamma}} , \tag{19}$$

where

$$a = \frac{N\gamma b^{\delta}}{\Gamma(\delta)} , \qquad \delta = \frac{\alpha + 1}{\gamma} ,$$

N is the number density of particles, b is related to the mode radius (maximum concentration size), r_c, of the distribution:

$$b = \frac{\alpha}{\gamma\, r_c^{\gamma}} ,$$

and α and γ are constants whose values, as well as those of N and b, depend on the type of cloud or haze studied. For simplicity, we shall present here some of the results for $a = b = \gamma = 1$ and various α and λ values. Typical CPU times were approximately 5 sec per case studied.

A. Effect of Operating Wavelength

The effect of the initial wavelength $\lambda = \lambda_1$ selected for this first part of the method is illustrated in Fig. 1 which shows a true plot of particle size distribution, labeled "n(TRUE)", for comparison with distribution curves determined with a wavelength of 0.05 μm, 0.1 μm and 1.0 μm. The ordinate scales on the left and on the right apply respectively to the solid-line and dashed-line curves. Clearly, the curves for $\lambda = 0.05$ μm and $\lambda = 0.1$ μm are absurd and must be discarded for the present case where the minimum radius is $r_0 = 1$ μm. On the other hand, the curve for $\lambda = 1$ μm is excellent in locating accurately the position of the mode radius and in reconstructing the entire distribution except in the region between 1 and 2 μm where a small negative tail has developed. This tail, which is related to an improper selection of the smallest opening of the forward light cone [9], can be "regularized" for all practical purposes. The result of this regularization for the case under study is illustrated by the dotted curve. We have determined that λ_1 and r_0 are intimately connected by the relation:

$$0.7\ \mu m \lesssim \lambda_1 \lesssim r_0 \,. \tag{20}$$

In other words, we must operate with near IR wavelengths which must be approximately equal to or smaller than, the expected minimum radius. Alternatively, the method will not be able to sample particle sizes smaller than approximately 0.7 μm.

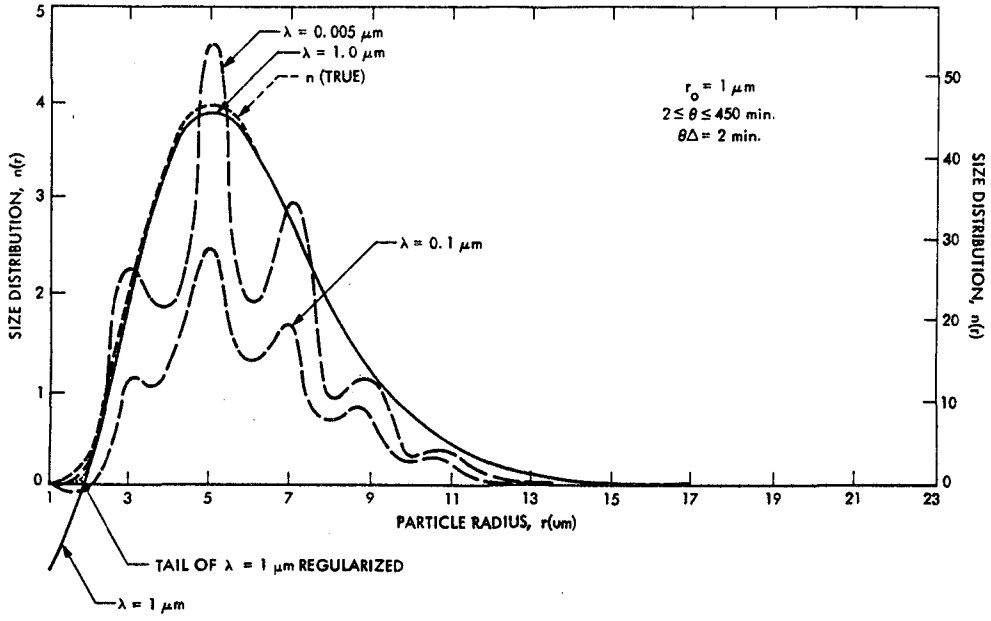

Fig. 1. Effect of Operating Wavelength

B. Effect of Angular Range

This effect is illustrated in Fig. 2 which shows a set of curves reconstructed from data obtained within the angular ranges of 100 min, 200 min, 300 min, 450 min, 500 min and 750 min. The curve for 100 min is clearly absurd. The range of 200 min is not much better although the mode radius is located approximately correctly (its magnitude however is substantially underestimated by approximately 25%), and the sizes beyond 9 μm are sampled correctly. The range of 300 min is close to being acceptable, and may be for some applications, particularly if the tail at the smallest sizes is regularized. At a range of 500 min, the result coincides with the true curve except in the region where $n(r) < 0.5$ which is the only region where the curve labeled "θ_{max} = 500 min" departs from the true curve, and even then only slightly. The results for θ_{max} = 450 min would be even better

than those at 500 min. Further departures from this optimum result in progressive degradation as shown by the curve at 750 min. Note that the range is here indicated by a positive maximum angle, θ_{max}. In practice, one would want to scan between $+\theta_{max}$ and $-\theta_{max}$ in order to detect inhomogeneities in the scattering medium.

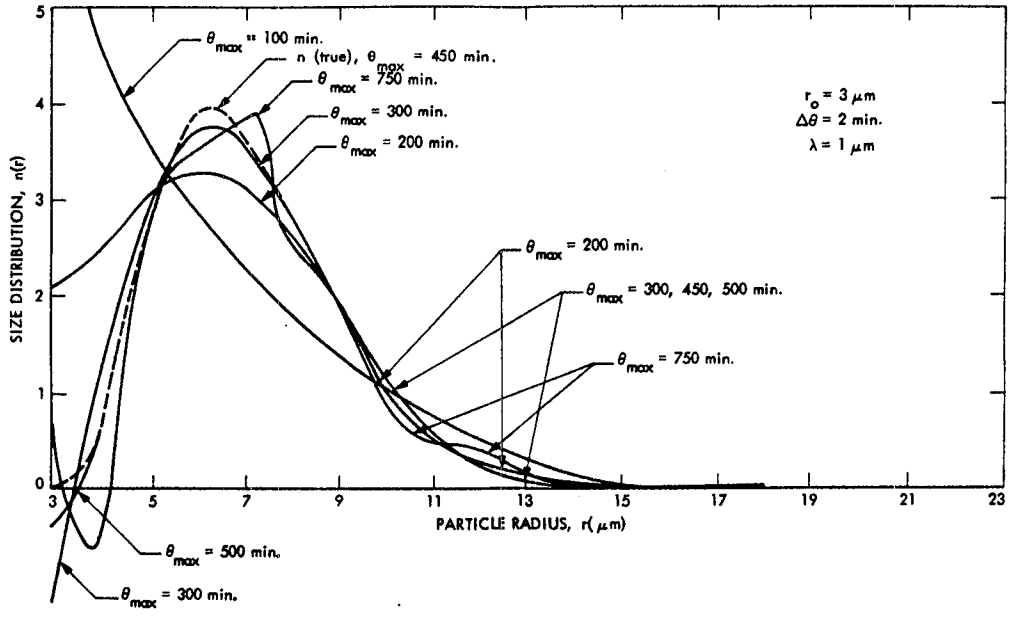

Fig. 2. Effect of Angular Range

C. Effect of Angular Resolution

It is illustrated in Fig. 3 for various values of the angular resolution: $\Delta\theta$ = 10 min, 15 min, 25 min, 30 min, 45 min and 75 min. At all these resolutions, the mode radius is always accurately located. The curve for 75 min is clearly unsatisfactory, while for progressively finer resolutions the corresponding curves are constantly improved. This graph illustrates an important point regarding the uniqueness of the solution. It is seen that as $\Delta\theta$ becomes smaller, there is uniform convergence to the true curve, and the solution is unique and identical to the true one only if the resolution is very small. Theoretically, $\Delta\theta$ should be infinitesimally small. In practice, however, because of inherent noise in both experimental data and computations it is only necessary that $\Delta\theta$ be approximately less than 15 min. Little improvement would be achieved by using smaller $\Delta\theta$'s.

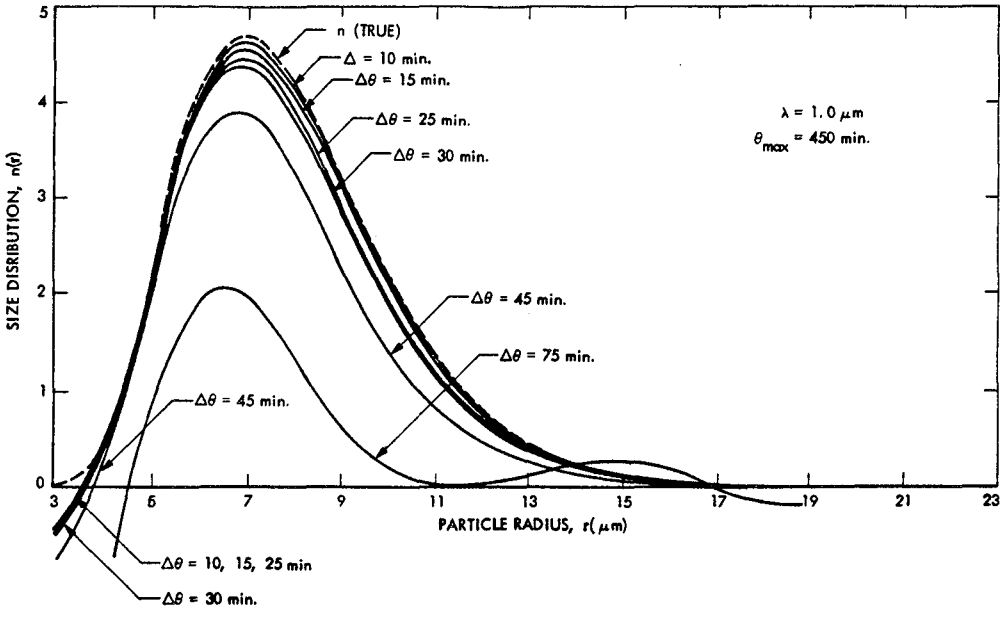

Fig. 3. Effect of Angular Resolution

V. DETERMINATION OF COMPLEX REFRACTIVE INDEX SPECTRUM

The second part of the method will now be described. The selection of the first wavelength λ_1 according to Eq. (20) has enabled us to work within the Fraunhoffer approximation to scattering theory and to retrieve the particle size distribution, independent of the refractive index, through a closed form analytical solution of the angular diffraction integral for a scattering polydispersion. On selecting a second wavelength λ_2 departing substantially from λ_1, (this is clearly required in order that the data obtained separately with these two wavelengths be independent), the above approximation can no longer be used. Instead, one is forced to resort to the more general Mie's theory. This is a rather interesting situation for, then, the size distribution determined from λ_1 (which is evidently wavelength-independent) can be substituted in Mie's solution leaving only $m(\lambda = \lambda_2)$, the complex refractive index at the second wavelength, as the only remaining unknown. The way in which $m(\lambda_2)$ is retrieved will now be discussed.

Let $I_i \equiv I(\theta_i; m_r, m_i)$ denote the forwardly scattered intensities computed from Mie's solution at λ_2 with the known n(r). The forward

angle θ, taking the values θ_i, is the independent variable. The dependent variables are m_r and m_i, that is respectively the real and imaginary parts of the refractive index. The dependence of m_r and m_i on λ_2 is implicit. The measurements obtained by repeating with the second wavelength λ_2 the procedure described in the previous section, according to the prescribed optimal angular range and resolution, will similarly be denoted $\tilde{I}_i \equiv \tilde{I}(\theta_i;\ m_r,\ m_i)$. The purpose would be to solve the equation

$$\left|\tilde{I}_i - I_i\right| \leq \epsilon_i \ , \tag{21}$$

where ϵ_i is an upper bound for the accuracy with which we require the computations I_i to approximate the measurements $\tilde{I}_i$; ϵ_i is fixed in particular from values of the noise in both the data and the computations since the evaluation of I_i will involve the use of finite word length arithmetic and quadrature rules of finite accuracy. We then define the function (independent of θ)

$$S(m_r,\ m_i) = \sum_i \left(\frac{\tilde{I}_i - I_i}{d_i \tilde{I}_i} \right)^2 \ , \tag{22}$$

where d_i is a statistical factor related to the distributions of the measurements within the observed angular interval, and to their relative weights. We say that an "inverse solution" of the original problem, i.e., a set of "best" values of the unknown parameters, m_r and m_i, would have been obtained, if the weighted sum of squares of relative deviations appearing on the right-hand side of Eq. (22) is a minimum, say

$$S(m_r,\ m_i) = S_{min}(m_r,\ m_i) \ . \tag{23}$$

The function S can be considered as the equation of a curved surface, the minimum of which (if it exists) it is required to find. If the problem is well-conditioned and possesses a unique solution, then, the surface S will be smooth and will exhibit a unique minimum. The pair of values of m_r and m_i corresponding to this minimum, or in other words the coordinates of the minimum in the parameter space of dimensions m_r and m_i, represents "the solution".

We have developed a nonlinear search routine (called Minimization Search Method) for accomplishing such minimizations [11, 12]. The algorithm is able to find the minimum of any arbitrary function, not necessarily S-functions like in Eq. (22). It can handle any

arbitrary number of unknowns, and is independent of the physical or mathematical assumptions made in evaluating the quantities I_i. Complete details as well as flow charts can be found in our earlier published work.

Sample results for a water (fair weather cumulus) cloud and a sulphuric acid cloud are illustrated in Table 1. The parameters of the size distributions for these two cases are respectively: (i) $\alpha = 6$, $\gamma = 1$, $b = 1.5$; and (ii) $\alpha = 9.5$, $\gamma = 1.0$, $b = 12.5$.

Table 1. Illustrating applications of the Minimization Search Method in retrieving complex refractive index values of clouds.

	Real Part, m_r		Imaginary part, m_i		Maximal CPU Time
	True	Computed	True	Computed	
H_2O cloud (λ_2 = 2.27 μm)	1.290	1.290	0.000304	0.00029	48 sec
H_2SO_4 cloud (λ_2 = 0.55 μm)	1.440	1.440	0.0001	0.0001	68 sec

The total CPU times vary with the type of cloud considered and with the initial guess used for initiating the search algorithm. For the present cases, their maximal values are indicated in the Table.

The same procedure can of course be applied to a set of second wavelengths. In this manner the spectrum of the refractive index could be obtained.

VI. DISCUSSION AND CONCLUSIONS

We have described a two-step approach for retrieving simultaneously and separately the size distribution, and the complex refractive index and its spectrum of atmospheric particulates from angular measurements of light they scatter in a narrow forward cone. In the first step, the problem of determining the size distribution only was considered within the framework of Fraunhoffer diffraction theory. The same treatment holds however in the Rayleigh-Gans approximation as well as in all intermediary cases between this approximation and anomalous diffraction. In the Fraunhoffer case, we have limited our study to homogeneous spheres. We are not able to distinguish this case from that of homogeneous ellipsoids since the corresponding diffraction patterns differ only by a constant factor [13]. These particles can however be distinguished from ice needles. The same

situation exists in the Rayleigh-Gans case. The interest of working in the forward scattering region is multiple: (i) independence from the particle refractive index (Babinet's principle). This results in a particularly interesting situation where size distribution can be determined without regard to refractive index; (ii) availability of a high level of scattered energy, half of the total (Huygens' principle), which can be separated out from the much weaker energy reflected by, and refracted in, the particles; (iii) independence from polarization which thus does not affect the diffracted field since the incident polarization state persists after diffraction. Such particles, in a number j of species, each species having eventually a different refractive index, but all species together following a certain size distribution, can be imbedded in a host gaseous mixture consisting of i different species of gases. The optical thickness of this medium was assumed to be sufficiently small in order that single scattering effects only be considered. For coherent light, Zuev et al [14] have determined that this thickness can take values up to approximately 25. For incoherent light, van de Hulst [5] has stated that it should not exceed 0.1; for larger values up to 0.3 a correction may be needed for double scattering while for still larger values of the thickness the complete multiple scattering must be considered. This statement was taken too literally in the past. However, detailed computations by Weinman et al [15] for a mixture of volcanic dust (thickness = 0.5) and gases (thickness = 0.145) have shown that near the zenith ($\mu = \mu_0 = 0.966$), the contribution of multiple scattering to the observed transmitted light is less than approximately 5% for the scattering angles of interest here ($\lesssim 8°$)! A similar conclusion has been reached by Deepak [16] who has found that the double scattering correction is within 4% up to angles of 20°. These results support earlier conclusions of Piaskowska-Fesenkova [17] and de Bary [18] that multiple scattering is negligible at small scattering angle under reasonably clear sky conditions. Clearly, single scattering theory has its usefulness for determining particle size distribution. It can certainly be retained as the basis for a particle size spectrometer either in the laboratory or in an airborne instrument. The use of laser light considerably extends the domain of applicability of such an instrument. The present approach is nevertheless being extended to include multiple scattering effects in order to cover all possible cases.

The effect of the gases can be determined separately if the degree of polarization of the transmitted light at any single, near-forward scattering angle is also measured. Otherwise, it must be assumed to be known.

The proposed method, then, consists in effecting an angular scan of the near-forward scattering region at a set of wavelengths. The scan must be performed with a resolution of approximately 15 min, or less, and the forward cone half-width must not exceed approximately 8 deg. The first wavelength is accurately prescribed by Eq. (20). Data obtained with this wavelength can then be used to reconstruct the size distribution for radius values larger than approximately 0.7 μm from the closed form, analytical solution in Eq. (18).

This solution, it is emphasized, is not constrained by any analytical distribution model (as is usually done). No fitting of distribution parameters is performed. Ample illustrations have been provided here, and in our earlier work, of the working of this first step of the method, the uniqueness of the solution, and its stability with regard to experimental and numerical noise.

The other wavelengths, which must be substantially different from the one used above for reasons of statistical independence of information content, are employed in the second step of the method. Here, Mie's theory is used, and the effects on the corresponding solution by particle sizes smaller than approximately 0.7 μm are implicitly considered to be negligible. With the size distribution previously determined, this solution will only depend on the complex refractive index. Accurate values of this quantity can be recovered using the nonlinear search routine we developed earlier. It may be noted that his routine is independent of the assumption of single scattering and can be coupled with the multiple scattering solution with equal success.

The CPU times quoted for determining both size distribution and refractive index spectrum are considerably shorter than the time scales of the physical processes considered. Hence, the approach can be implemented for real-time operation to monitor the dynamical evolution of the particulates. The principle of the method proposed (called Angular Forward Scattering Method) has been retained for the system design of a particle size spectrometer and refractometer [12], and is being implemented at the Jet Propulsion Laboratory. Results of the corresponding experiments will be reported elsewhere.

ACKNOWLEDGEMENT

This paper presents the results of one phase of research carried out at the Jet Propulsion Laboratory, California Institute of Technology, under Contract NAS 7-100 sponsored by the U. S. National Aeronautics and Space Administration.

REFERENCES

1. Fymat, A. L., 1975, Remote Monitoring of Environmental Particulate Pollution: A Problem in Inversion of First Kind Integral Equations, Appl. Math. and Comp. (in press).

2. Chandrasekhar, S., 1950, Radiative Transfer, Oxford University Press (reproduced by Dover Publications, New York, 1960).

3. Fymat, A. L., 1973, Determination of Atmospheric Particle Size Distribution from Forward Scattering Data, in Monitoring of Terrestrial Environment from Space, Ed. Rassegna Internazionale Elettronica, Nucleare Ed Aerospaziale, Rome, pp. 183-195.

4. Fymat, A. L., 1974, Satellite Determination of Nature and Microstructure of Atmospheric Aerosols, in Satellites for Meteorology and Terrestrial Resources, Ed. Rassegna Internazionale Elettronica, Nucleare Ed Aerospaziale, Rome, pp. 325-345.

5. Hulst, H. C. van de, 1957, Light Scattering by Small Particles, Wiley, New York.

6. Fymat, A. L., 1975, Appl. Math. and Comp. (in press).

7. Bateman, H., 1906, On the Inversion of a Definite Integral, Proc. London Math. Soc., II, 4, 461.

8. Titchmarsh, E. C., 1924, Extensions of Fourier's Integral Formula to Formulae Involving Bessel Functions, Proc. London Math. Soc., II, 23, xxii.

9. Shifrin, K. S. and I. B. Kolmakov, 1966, Effect of Limitation of the Range of Measurement of the Indicatrix on the Accuracy of the Small-Angle Method, Izv. Atm. and Ocean. Phys., 2, No. 8, 851.

10. Deirmendjian, S., 1969, Electromagnetic Scattering on Spherical Polydispersions, American Elsevier, New York.

11. Fymat, A. L. and R. E. Kalaba, 1974, Inverse Multiple Scattering Problems: II. Limited Information Content of Partially Fitted Planetary Curves with Application to the Venusian Visual Phase Curve, J. Quant. Spec. and Rad. Transf., 14, 919.

12. Fymat, A. L., 1975, Particle Size Spectrometer and Refractometer, U. S. Patent (pending). NASA Case No. NPO-13614.

13. Born, M. and E. Wolf, 1959, Principles of Optics, Pergamon Press, New York.

14. Zuev, V. Ye, 1970, Propagation of Visible and Infrared Waves in the Atmosphere, Engl. Translation, NASA TT F-707 (available from National Technical Information Service, Springfield, Virginia, 22151).

15. Weinman, J. A., J. T. Twitty, S. R. Browning and B. M. Herman, 1975, Derivation of Phase Functions from Multiply Scattered Sunlight Transmitted Through a Hazy Atmosphere, J. Atm. Sci. (in press).

16. Deepak, A., 1973, Double Scattering Corrections for the Theory of the Sun's Aureole, NASA Technical Memorandum TM-X-64800.

17. Piaskowska-Fesenkova, E. V., Investigations of Light Scattering in the Earth's Atmosphere, Akad. Nauk., Moscow.

18. Bary, E. de, 1973, Beitrage zur Physik der Atmosphäre, 46, 213.

SURFACE INSTABILITY OF STATIONARY AIR BUBBLES*

Carl J. Remenyik**

ABSTRACT

This study was prompted by observations that pulsations of stationary bubbles accumulating in the fuel lines of the Saturn missile resulted in intense structural oscillations.

High speed motion pictures were taken of bubbles oscillating with fixed mean positions in vertically oscillated containers. It was observed that the degree of instability of the bubble surface increases with the value of $\omega a^2/\nu$, where ω = angular frequency, a = a characteristic linear bubble dimension, and ν = kinematic viscosity.

EXPERIMENTAL APPARATUS

Experiments were performed on a magnetic Vibration Exciter, Model C25H of the MB Manufacturing Company (Fig. 1). For the first five bubbles described below, a transparent, cubical plastic container (Fig. 2) was mounted on the vibration table. Its edges are 14 in., and the hole at the top is 12 in. deep and 2 in. in diameter. The wall was constructed unusually thick to eliminate wall vibrations. When thinner walled containers were used, wall vibrations significantly affected the fluctuating pressure field in the liquid.

The liquid in the container was glycerol, whose high viscosity prevented large bubbles from disintegrating into clusters of small bubbles. Large bubbles were required for study of their surface motions using available equipment.

The photographs shown here are frames of motion pictures taken with a HYCAM K20S4E high-speed camera. During filming, the container was between the camera and a flood lamp. The light beam was aligned with the axis of the camera lens, allowing the beam to pass through the container into the lens. A translucent plastic sheet placed before the flood lamp dispersed its light, producing an even photographic background.

EXPERIMENTAL PROCEDURES

Before each experiment, the camera was focused on a selected point inside the liquid to which the bubble was later steered.

---

* This project was supported in part by the Propulsion and Vehicle Engineering Laboratory, George C. Marshall Space Flight Center, Huntsville, Ala., under Contract NAS 8-20152.

** Department of Engineering Science and Mechanics, The University of Tennessee, Knoxville, Tennessee 37916

After activating the vibration exciter, oscillation frequency was set as desired. To ensure that the subsequently injected bubble would not rise to the surface, the amplitude was set sufficiently high to drive any size bubble to the container bottom. Subsequently, a measured volume of air was injected with a hypodermic needle, and the amplitude readjusted until the bubble hovered within camera focus in a stationary mean position.

Wherever the bubbles were released inside the container, they drifted to the wall. The final position was very near the container wall, but far enough away to prevent contact. The explanation for the tendency to move towards the wall probably is that two effects are combined in the process. The presence of the wall generates a "mirror image" of the bubble, i.e., the flow field set up by the wall is nearly the same as if there were a bubble on the opposite side of the plane of the wall, pulsating in phase; Bjerknes (1909) demonstrated that two submerged objects pulsating in phase exhibit mutual attraction.

DESCRIPTION OF THE BUBBLES AND THEIR SURFACE MOTIONS

Bubbles shown in the illustrations were viewed by the camera from several directions. For the following discussions, a frontal view of the bubble is defined as one in which the region of the container's inside wall nearest to the bubble is behind the bubble as seen by the camera. In a right side view, the direction of sight is turned 90 degrees relative to the direction of the previous view, in such a way that the nearest point of the wall is to the right in the picture. A view from the opposite direction will be called a left side view, and the opposite of the frontal view, i.e., a view in which the bubble clings to the wall region nearest to the camera, will be a rear view.

The motion picture frames shown in the sequences were selected so that elapsed time between them is 1/8 of the oscillation period. Thus, the first and ninth pictures in any sequence show the same motion phase.

On one-half of the inside container surface, horizontal semi-circles were inscribed at 1/4 in. vertical intervals to serve as reference lines fixed in the container. Locations of bubbles shown in the figures were on or near an imaginary line connecting the middle points of these semi-circles. Thus, segments of reference lines visible in the pictures were in the immediate vicinity of the bubbles. In most figures, cross hairs provide a reference system fixed in the camera lens.

These bubbles hovered at fixed mean positions three to four inches above the container bottom; total depth of the glycerol column was between 10 and 11 in.

Some bubbles are surrounded by small specks. Most of these are approximately neutrally buoyant, plastic filings or ion exchange beads which were added to the glycerol to trace steady streaming (Remenyik 1970). Around those large bubbles which are distorted by large instabilities, part of the specks are small bubblets which have been shed by the large bubble.

Observations indicate that instability of the bubble's surface is controlled by the parameter $St \equiv \omega a^2/\nu$, in which ω represents the angular frequency, ν the kinematic viscosity, and "a" a characteristic linear dimension associated with the top of the bubble's surface. A radius of curvature of the bubble top is such

a linear dimension, but its determination is frequently difficult or even impossible. Since it was observed on several oblate bubbles that the bubble's height had about the same magnitude as the radii of curvature at the top, the height was used as characteristic length "a" for such bubbles.

The figures are arranged in order of increasing $\omega a^2/\nu$, and thus of increasing bubble size.

1. The smallest bubble is shown in Fig. 3. It oscillated with a frequency of 50 cps and maintained a nearly spherical shape throughout the oscillation cycle. Its periodic, asymmetric distortion was undoubtedly caused by strong shear stresses which resulted from the proximity of the wall. Its diameter was about 0.2 cm., and $\omega R^2/\nu \approx 0.5$, where R is half the diameter. The bubble is shown in a right side view.

2. The flattened bubble in Fig. 4 had a height of about 0.47 cm., oscillated with a frequency of 54 cps, and $\omega a^2/\nu \approx 10$. Its entire surface was smooth at all times during the oscillation cycle. The bubble is shown in frontal view.

3. Figure 5 shows a bubble of 1.46 cm. approximate height, oscillating with 51 cps; $\omega a^2/\nu \approx 50$. The intended view was frontal; however, the bubble drifted unexpectedly to the left, and the view became intermediate between frontal and left lateral. As a consequence, the curving wall optically distorted the left side of the bubble more than the right side. The mottled background of the bubble was accidentally caused by the wrong material having been placed in front of the flood lamp to diffuse its light.*

In a frame-by-frame examination of the film, shot at 6000 frames per second, the following observations were made. At about the time when the bubble top is in its highest position, a short, thin, faint white line appears along the upper edge of the silhouette (←Fig. 5f). This line lengthens rapidly (Fig. 5g and h); when it reaches the edge of the silhouette at the point of interception a small break appears in the smooth line of the edge. This break runs downward along the edge of the silhouette as the white line curves downward and continues to lengthen and eventually disappears (←Fig. 5i, a and b).

A second, much wider and brighter streak begins to develop above the first one when the top assumes its lowest position and the bubble its smallest size (Fig. 5a and i). It seems to be a wave interrupting the bubble surface. It grows in width and depth while the top accelerates upward (Fig. 5b and c), and diminishes until it disappears when the top accelerates downward (Fig. 5d and e). One can conjecture that it is an instability feature that grows out of a periodic initial deformation of the surface caused by the shear field of the wall. Following its disappearance (between Fig. 5e and f), the faint line reappears after an interval of about 0.09 of the oscillation period, i.e., in about 0.0018 seconds. Scant available evidence indicates that this interval decreases and the maximum amplitude of the wave increases with increasing $\omega a^2/\nu$, and when this parameter surpasses a certain value, this feature no longer disappears, but periodically varies in magnitude. Plotting locations of various points on the bubble against time indicates that the surface motion contains a significant second harmonic component.

---

* In an effort to eliminate these shortcomings, the experiment was repeated; however, the new film was subsequently destroyed by yet another accident.

4. If $\omega a^2/\nu$ is increased, the wave-like surface distortion eventually becomes irregular. This is shown in Fig. 6, where the bubble appears in rear view.

The bubble's oscillation frequency was 53 cps, the average height was about 1.6 cm., and $\omega a^2/\nu \approx 75$.

The protrusion at the bottom is a characteristic feature of this bubble, appearing and disappearing with each cycle, and developing to varying sizes, apparently randomly. It was observed, however, that an unusually large protrusion is always followed during the next cycle by one that is smaller than average. The protrusion in Fig. 6 is larger than average. Although it is not typical due to its large size, it was chosen for reproduction here because it exhibits exceptionally well certain details that are observable on nearly all protrusions. One such typical feature is the shape of the protrusion at the very beginning of its development. Photographs indicate that it is cylindrical and its tip terminates flat in a plane perpendicular to the cylinder axis (Fig. 6d).

Large protrusions persist longer than smaller ones and, as a result, a small remnant of a large protrusion may still be present after the next protrusion had already appeared (Fig. 6l and m; the new protrusion is at right←). The bubble is surrounded by a cloud of small bubblets which had broken off from it, and these steadily stream as they oscillate and pulsate. Since the amount of light scattered by the bubblets varies with size, overall darkness of the photographs varies accordingly (Fig 6n). This offers a convenient method to determine the pulsation phase of the bubblets relative to that of the main bubble. This method leads to the conclusion that bubblets oscillate very nearly in phase with the main bubble, at least in its neighborhood, extending to a distance of one or two bubble diameters. Also, both main bubble and bubblets pulsate with a very large second harmonic component which in turn indicates that the fluctuating pressure field contains a very intense component having twice the fundamental frequency.

5. The bubble in Fig. 7 is only slightly larger than the previous one, and motions of both are essentially equal. The view in Fig. 7 is from the right side, and outlines of the inner wall surface can be seen near the bubble and to the right. The photographs show the upper portion of the bubble surface. The surface of this bubble is distorted during each cycle by deep instability waves. The maximum distortion that developed during the cycle shown appears in Fig. 7g. This instability feature is possibly the same kind seen in Fig. 5, but extremely amplified.

On some frames of the film, one can see that a bubblet is being pinched off by a local instability. In a few other frames, bubblets coalesce with the large bubble. Apparently, this process establishes a different equilibrium bubblet concentration for each value of $\omega a^2/\nu$. The bubblets drift steadily to and from the main bubble along looped paths (Remenyik 1970).

The local states of strain in the liquid affect bubblet shape (compare, e.g., the shapes of bubblet indicated in Fig. 7h and i), and one may observe that the second harmonic is even more pronounced than before in the pulsations of both main bubble and bubblets.

6. When $\omega a^2/\nu$ was substantially increased, surface instability brought about the final state (Fig. 8). The bubble disintegrated completely into a

turbulent cluster of bubblets. The container used was of Plexiglas, had a 6.5 in. inside diameter and a 1/2 in. wall thickness, and is shown in Fig. 1 mounted on the vibration exciter. The liquid was methyl alcohol, 20 in. deep.

The cluster is shown in rear view, and the flood lamp illuminated it from the side of the camera. It oscillated 126 times per second and it had an approximate mean diameter of 5.6 cm. If R is half the cluster diameter, $\omega R^2/\nu \simeq 6.42 \times 10^5$.

A cloud of bubblets surrounding the cluster extended about a cluster-diameter beyond the apparent limits visible in Fig. 8. The less-densely populated region of the cloud did not show up on film because of applied illumination.

Bubblets forming the cloud were being expelled at the bottom of the cluster in a steady but violently turbulent stream. They then circulated the cluster along paths resembling dipole flow, and plunged back into the cluster's top.

Two intersecting straight lines visible in the photographs were threads. One was attached to the outside container surface, and the other was stationary a short distance in front of the first.

ACKNOWLEDGEMENT

I wish to thank Robert F. Braswell for editing the manuscript, and the staff of the Photographic Services of the University of Tennessee for photographic reproduction of the film frames.

REFERENCES

Bjerknes, V. Die Kraftfelder, Braunschweig: Friedrich Vieweg & Sohn, 1909.

Remenyik, C. J. Bubbles, Steady Streaming and Surface Instability in Vibrated Liquid Columns, Proceedings of the 1970 Heat Transfer and Fluid Mechanics Institute, 1970, Stanford University Press.

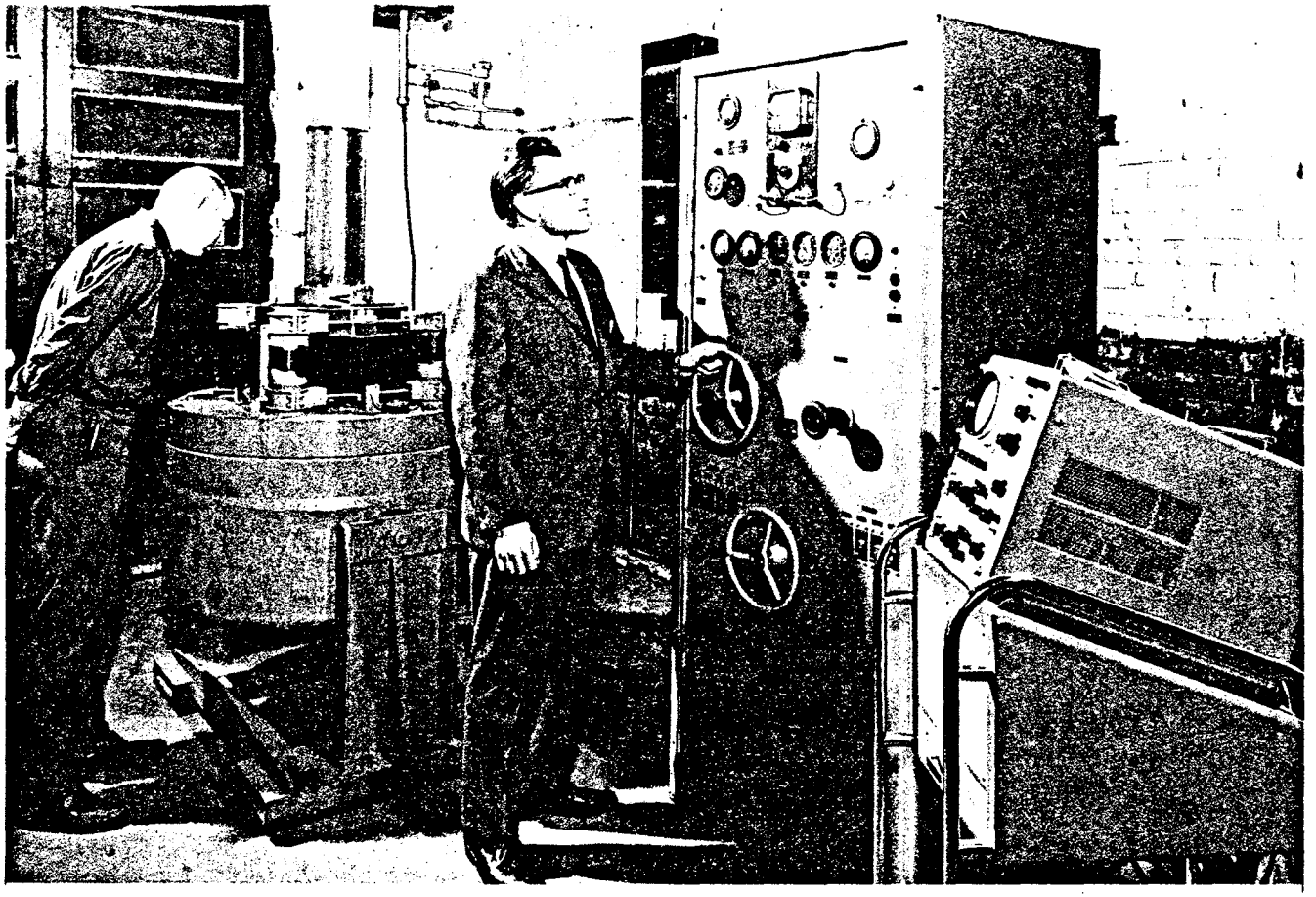

Fig. 1 Vibration exciter and circular container mounted on vibration table

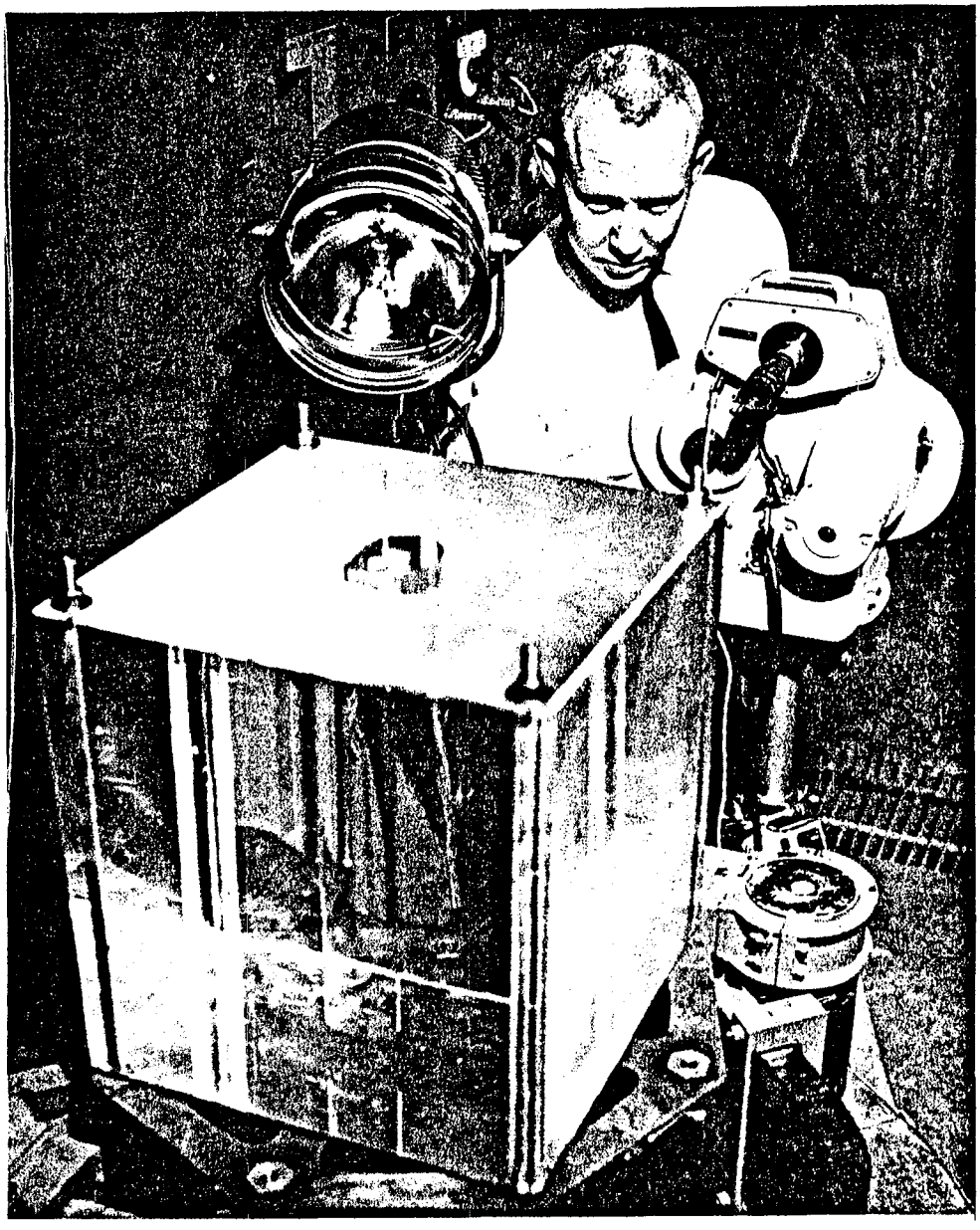

Fig. 2 Cubical container

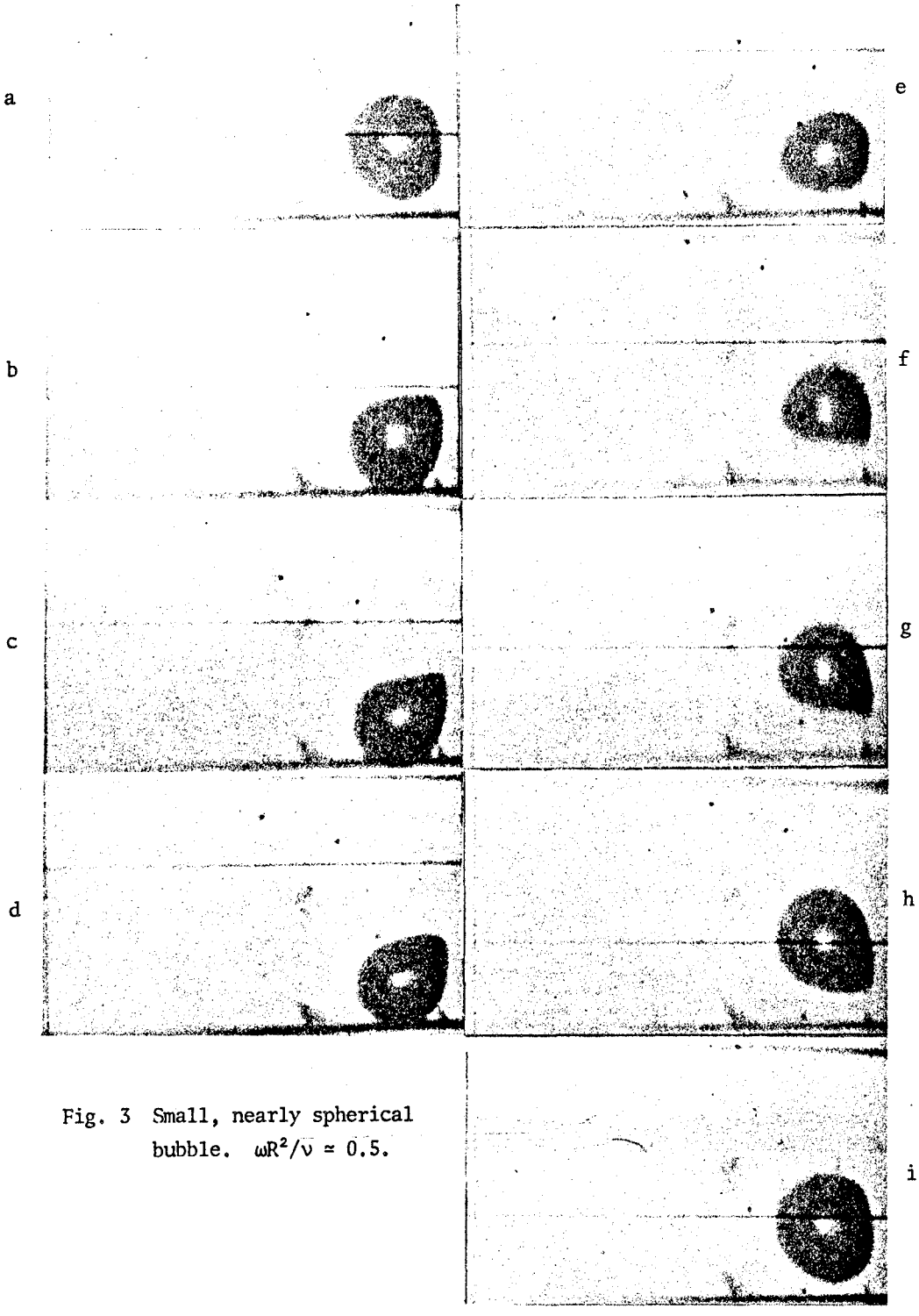

Fig. 3 Small, nearly spherical bubble. $\omega R^2/\nu \simeq 0.5$.

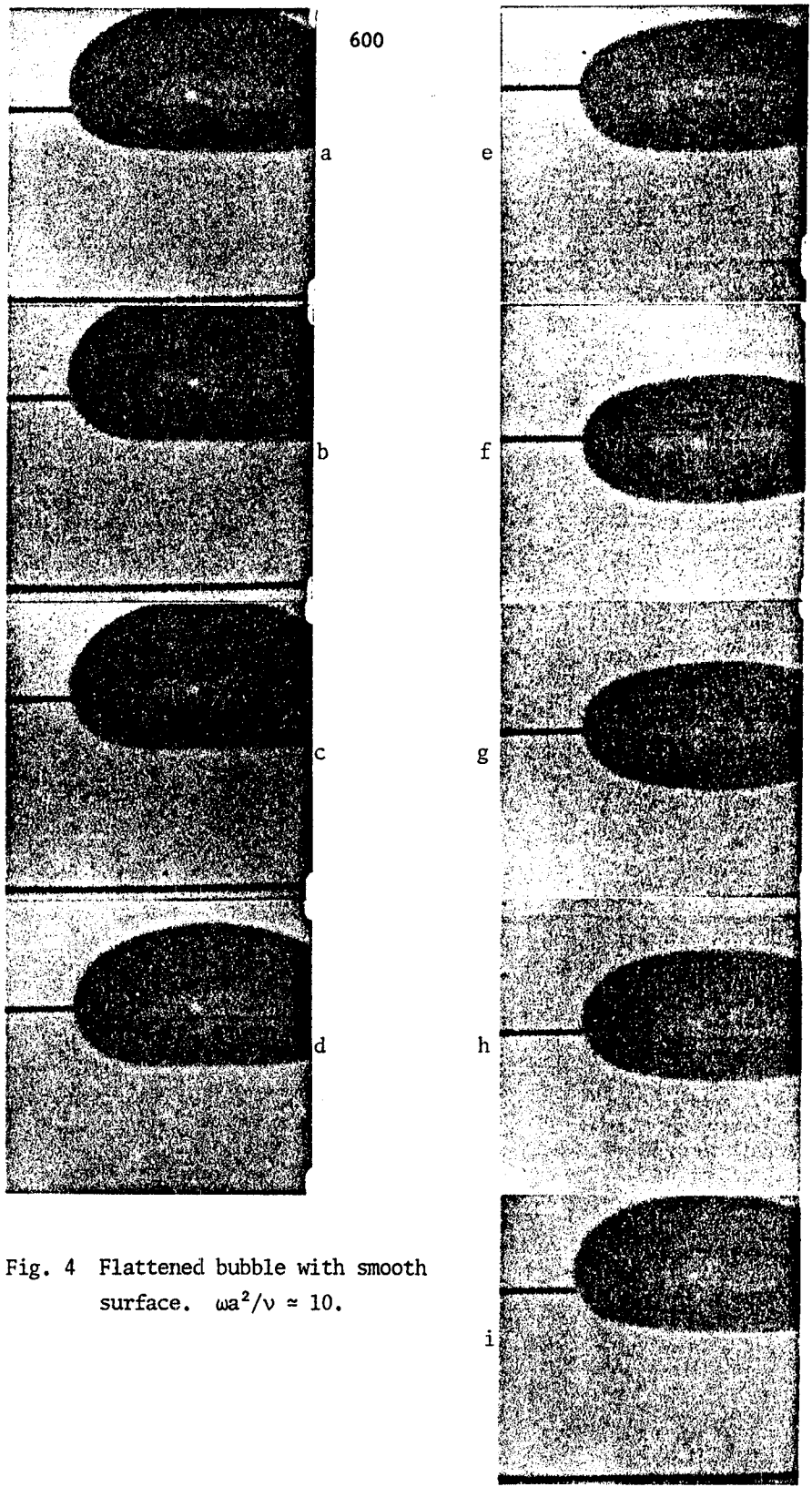

Fig. 4 Flattened bubble with smooth surface. $\omega a^2/\nu \approx 10$.

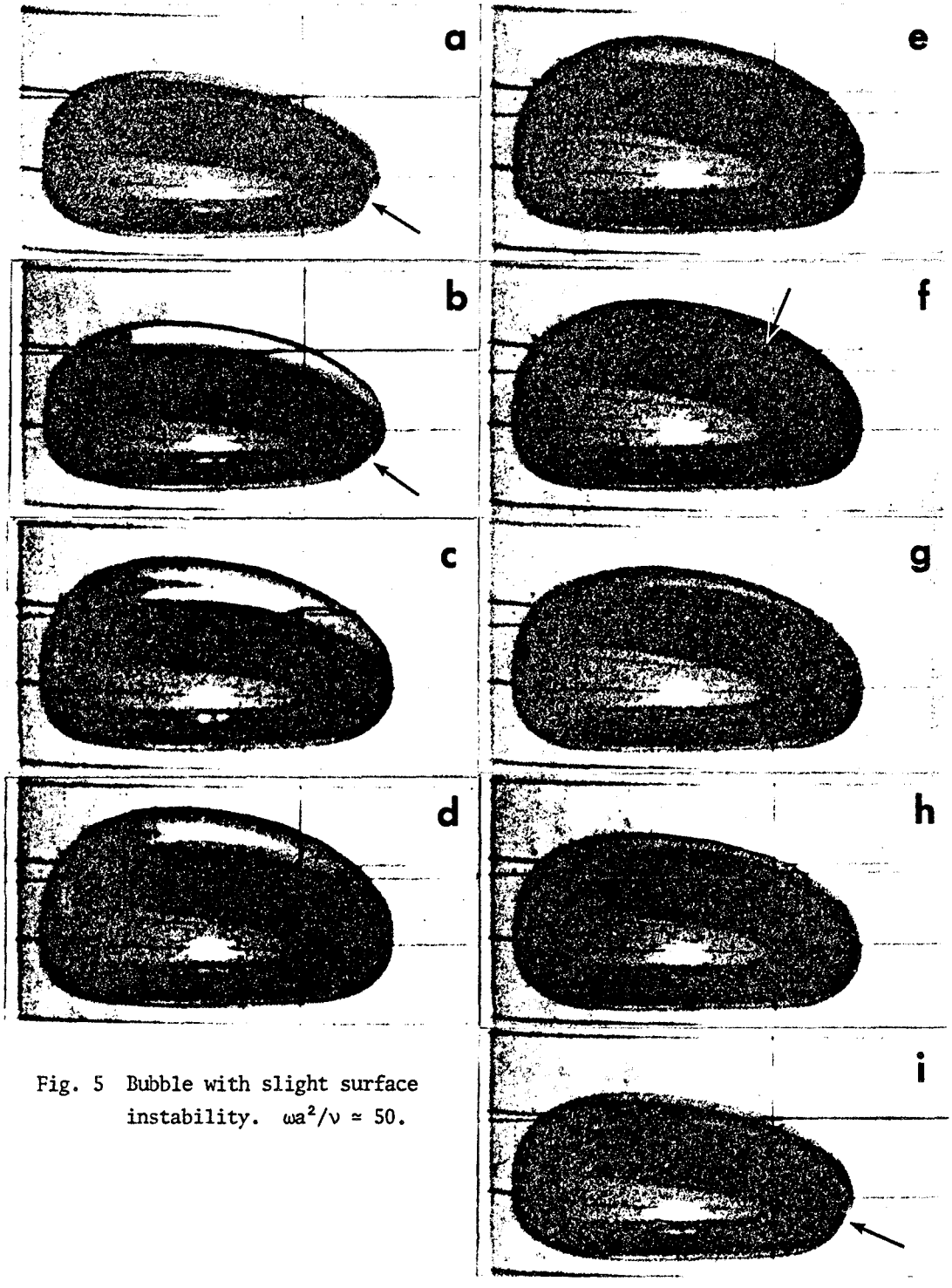

Fig. 5 Bubble with slight surface instability. $\omega a^2/\nu \simeq 50$.

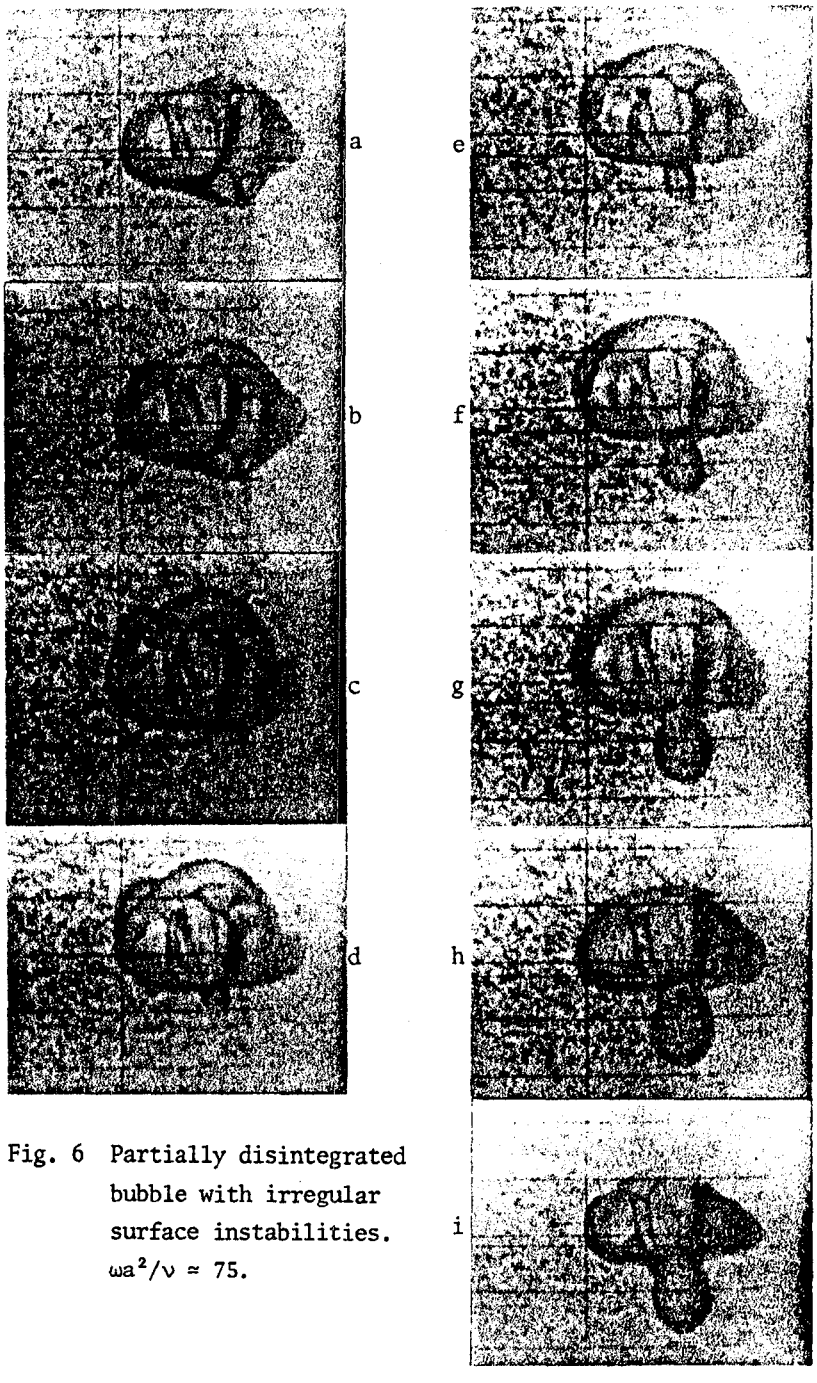

Fig. 6 Partially disintegrated bubble with irregular surface instabilities. $\omega a^2/\nu \simeq 75$.

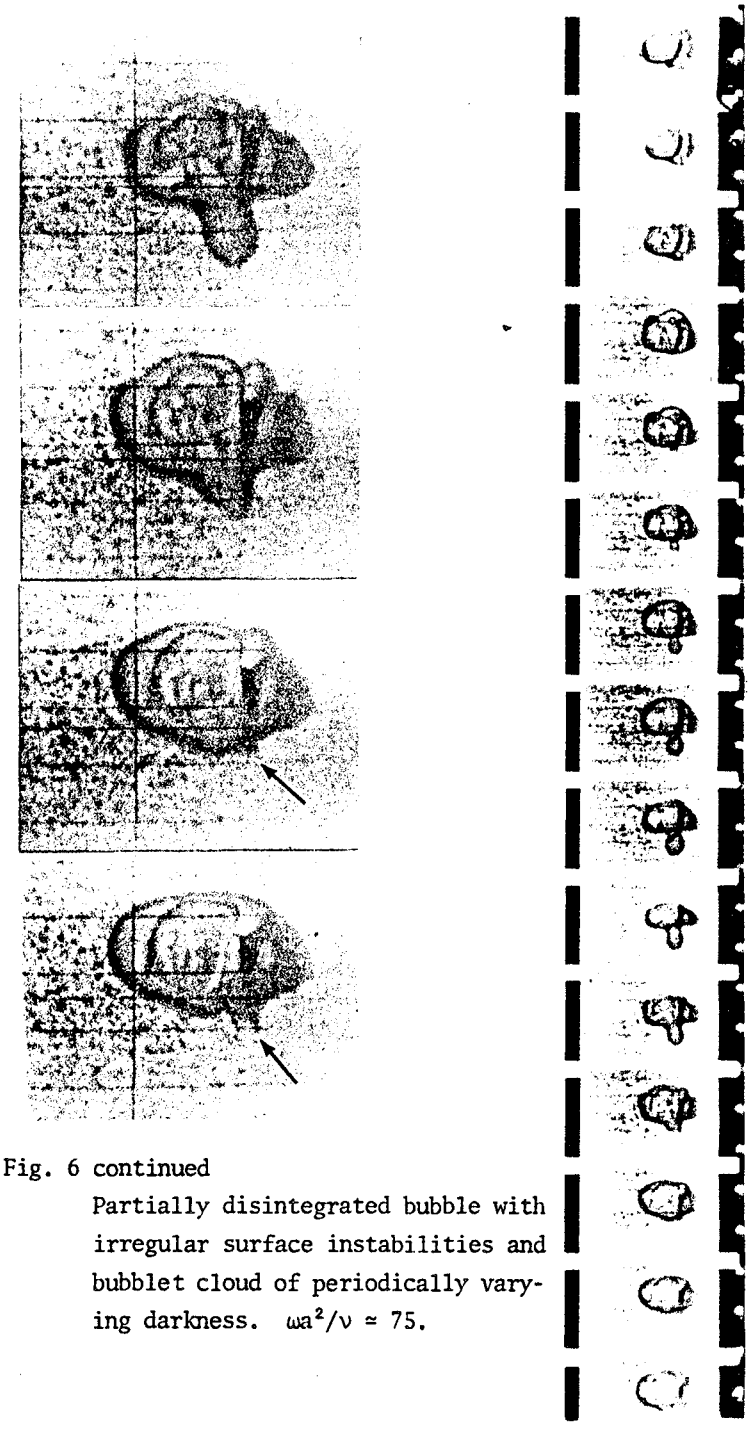

Fig. 6 continued

Partially disintegrated bubble with irregular surface instabilities and bubblet cloud of periodically varying darkness. $\omega a^2/\nu \simeq 75$.

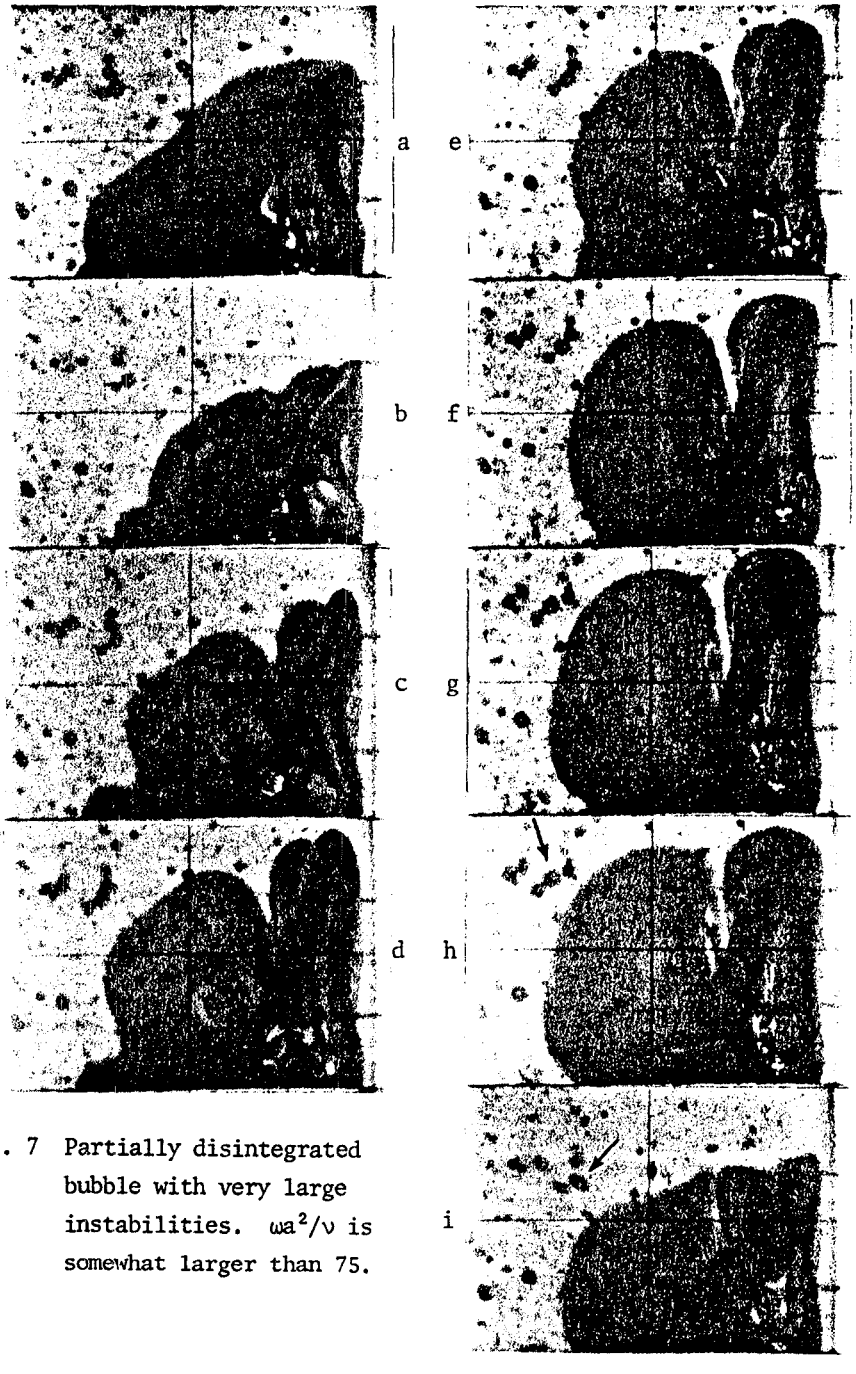

Fig. 7 Partially disintegrated bubble with very large instabilities. $\omega a^2/\nu$ is somewhat larger than 75.

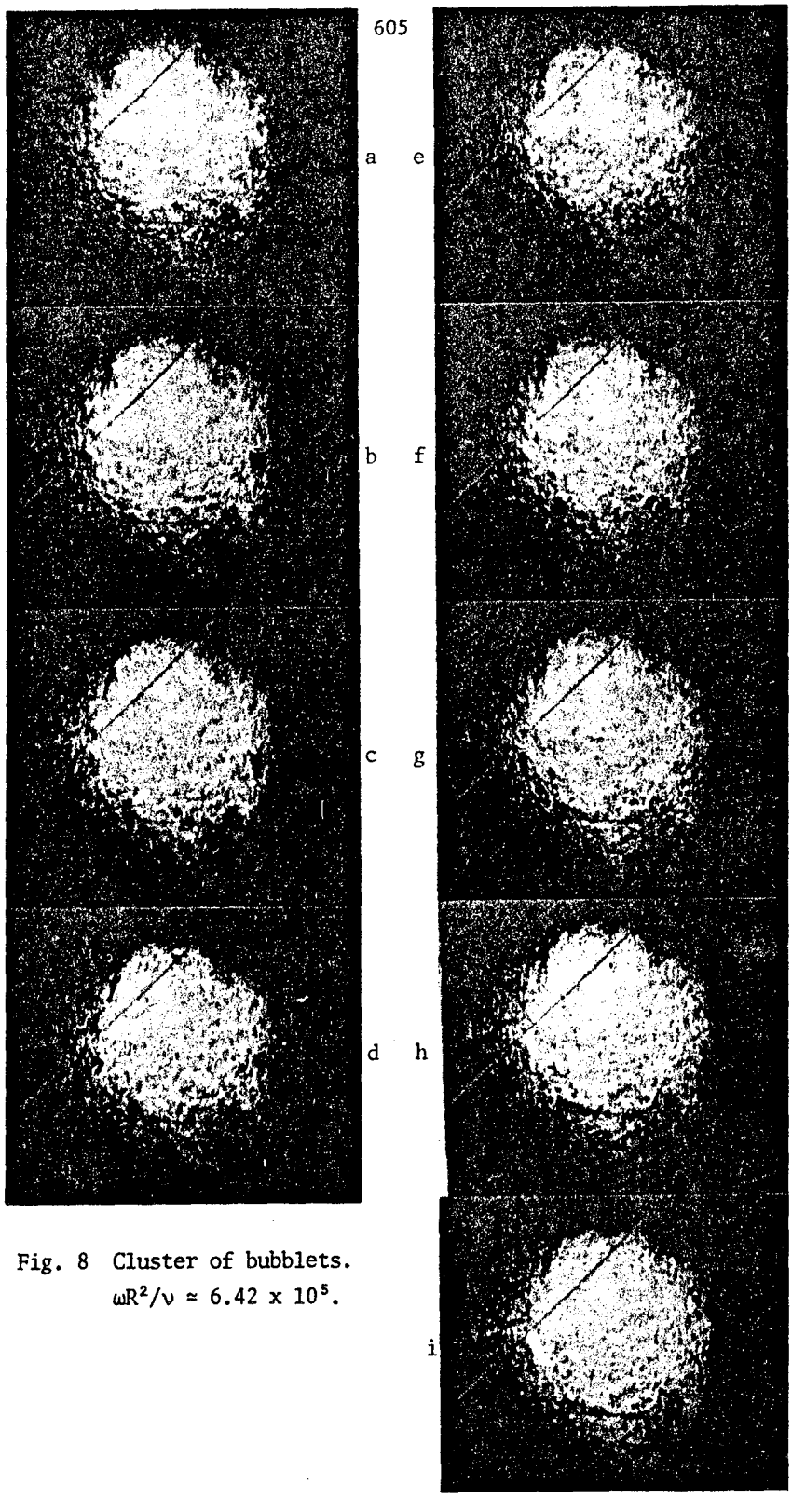

Fig. 8 Cluster of bubblets.
$\omega R^2/\nu \simeq 6.42 \times 10^5$.

ON THE GROWTH AND COLLAPSE OF VAPOR BUBBLES AT LIQUID/LIQUID INTERFACES

William E. Kastenberg
Ivan Catton
Energy and Kinetics Department
School of Engineering and Applied Science
University of California, Los Angeles

I. INTRODUCTION

The study of the thermal interaction initiated by quenching a hot liquid in a cooler one has recently received a great deal of attention. The subsequent behavior is important in the metal foundry industry, the liquid natural gas industry and the nuclear reactor industry. For the latter, the primary problem is the thermal interaction between molten fuel (usually uranium oxide) or stainless steel and the coolant (water or sodium). This thermal interaction is characterized by 1) high pressures and significant vapor production for the case of molten metal and water, 2) low pressures and efficiencies for the case of molten uranium and sodium, and 3) significant surface enhancement or fragmentation of the hot material for both.

The parametric models (computer simulation) of Wright et al. [1] and Caldarola [2] can be made to match the pressure/time histories for each case with a suitable adjustment of heat transfer coefficients. However, these adjustments are made with little physical basis. In addition, Fauske [3] has proposed a criterion for which a full scale vapor explosion can be predicted. As mentioned above, surface enhancement or fragmentation occurs in any case.

At the present time, the phenomena of fragmentation is not well understood. Several theories have been proposed and are reviewed by Caldarola

and Kastenberg [4]. In that paper, a model, based upon bubble vapor growth and collapse, was presented to describe the fragmentation process. The basic hypothesis is that microjets formed during the collapse of vapor film at the liquid/liquid interface, contain enough kinetic energy to penetrate and fragment the molten material.

The objective of this paper is to describe a set of experiments which are being conducted to study the fragmentation process. Results of these experiments, presented as a set of still photos, duplicated from high-speed motion picture films are discussed. Some preliminary conclusions, based upon these experiments are also given.

II. DESCRIPTION OF EXPERIMENTS

A series of experiments with simulant metals (tin, aluminum and lead) and water were run. Typically, the metals were heated above their melting point in a graphite crucible. They were then dropped through an argon atmosphere into water at various degrees of subcooling. High speed motion pictures (3,000-5,000 frames per second) were employed to reveal the thermal interaction.

The general results can be summarized as follows. For water below 70°C (30°C subcooled) a vapor film formed at the liquid/liquid interface. This was followed by apparent collapse and then violent mixing, distortion, high pressure and the spewing out of debris. Post mortem inspection showed that 90% of the molten material had formed a fibrous material. For water above 70°C, stable film boiling was observed, with little or no interaction. Post mortem inspection yielded large, smooth pieces of solid metal in the form of drops.

To simulate the low conductivity oxide fuels, a series of experiments with molten salt were conducted. These experiments yielded extremely violent interactions, indicating that some sort of chemical interaction had taken place. This is atypical of the UO_2/sodium experiments conducted at Argonne [5].

III. EXPERIMENTAL RESULTS

In Figure 1, a reproduction of one frame of a high speed motion picture is shown. In this case, molten tin, at 580°C is being dropped into 80°C water. The molten tin is completely encapsulated in vapor. This vapor film is stable, during the descent and when the metal comes to rest on the bottom container. The sample loses heat by radiation through the film and conduction through the catcher on the bottom. The post mortem inspection yielded three pieces of smooth debris of roughly equal mass.

Figure 2 shows a strip taken sequentially from a run with the molten tin at 580°C and the water at 20°C (80° subcooled). As shown in the larger photos, an unstable vapor film is formed about the molten sample as it makes its descent. In frame number two of the second strip (smaller pictures) the film has partially collapsed. An unstable microjet has appeared. This is also shown in the following frame. By frame 4 of the second set, there is rapid production of vapor with a large pressure pulse. The mottled appearance of the vapor liquid interface indicates that the driving mechanism for the interaction is of a scale much smaller than the molten metal drop size. When the frames are viewed in motion, the surface appears to be pushed out by jets of vapor originating inside the interaction region. This could be postulated to be the result of collapsing bubbles and the resulting microjet of water penetrating the molten material and vapor production.

An interesting phenomena is observed in the third column of Figure 2. The pressure wave created by the rapid expansion is reflected off the container wall and interacts with the vapor zone. The effect of the reflected pressure wave is seen in the several frames following the first frame. The vapor zone is seen to decrease in size. The remainder of the sequence indicates further vapor production, violent mixing and fragmentation.

This film strip is typical for metal/water reactions where the water is highly subcooled.

The next sequence, depicted in Figures 3 and 4, is for molten salt (NaCl) and water. Inspecting the strip, it is seen that an interaction takes place as soon as the sample hits the surface. A full scale vapor explosion takes place, with rapid mixing, high pressure, and water being forced up into the furnace area. Five distinct pressure pulses are observed when running the movie at reduced speed. These are difficult to visualize in the movie strip. Because of the violent nature of this run, it was concluded that some chemical interaction may have taken place.

IV. CONCLUSIONS

As a result of these experiments the following conclusions can be made. First, for the case of molten metals (tin, aluminum and lead) and subcooled water (below 70°C), collapse of the vapor film triggers the fragmentation process. Second, above 70°C, the stable vapor film inhibits fragmentation. Third, that while the vapor collapse triggers the event, the film speed is too slow to observe the action of the microjet on the surface. Fourth and finally, nothing can be concluded for the low conductivity case (i.e., extrapolation of UO_2) because of the apparent chemical interaction present in the salt system. This is not expected to occur for a molten UO_2 coolant, sodium or water interaction.

References

1. Cho, D. H., Ivins, R. O. and Wright, R. W., "Pressure Generation by Molten Fuel-Coolant Interactions Under LMFBR Conditions", Proceedings of Conference on New Developments in Reactor Mathematics and Applications, USAEC CØNF-710302 (Vol. 1), 1971, pp. 1-24.

2. Caldarola, L., "A Theoretical Model for the Molten Fuel-Sodium Interaction in a Nuclear Fast Reactor", Nucl. Engr. and Design, Vol. 22, No. 2, 1972, pp. 175-211.

3. Fauske, H. K., "On the Mechanism of Uranium Dioxide-Sodium Explosive Interactions", Nucl. Sci. and Engr., Vol. 51, 1973, pp. 95-101.

4. Caldarola, L. and Kastenberg, W. E., "On the Mechanism of Fragmentation During Molten Fuel/Coolant Interactions", Proceedings of the Fast Reactor Safety Conference, USAEC CØNF-440401-P2, 1974, pp. 937-954.

5. Armstrong, D. R., Testa, F. J. and Rariden, D., "Interaction of Sodium with Molten UO_2 and Stainless Steel using a Dropping Mode of Contact", ANL-7890, Argonne National Laboratory, 1971.

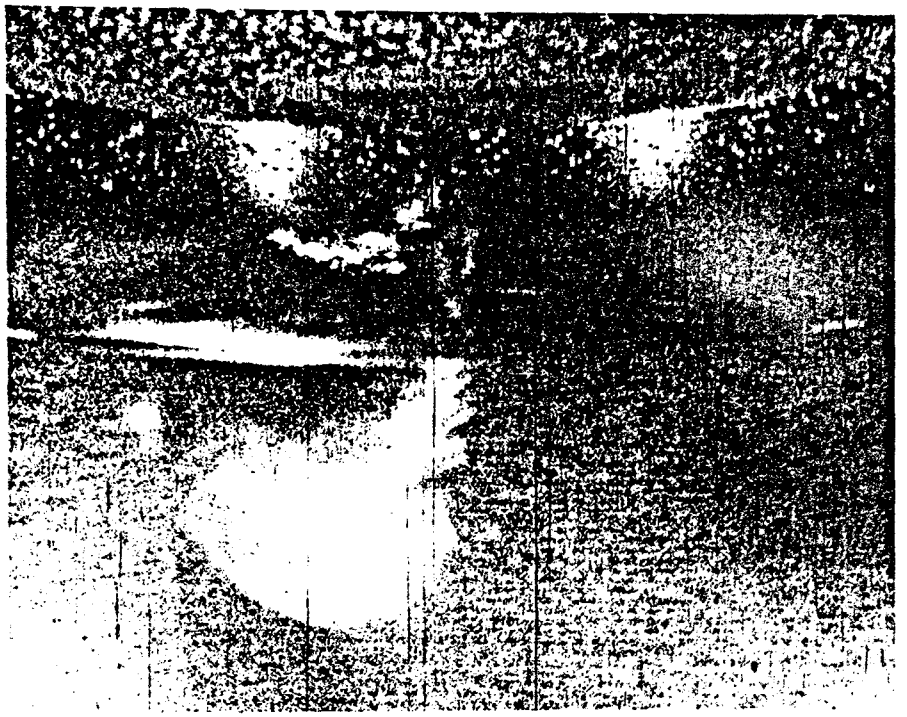

Fig. 1. Molten tin at 580°C into H_2O at 80°C yielding stable film boiling.

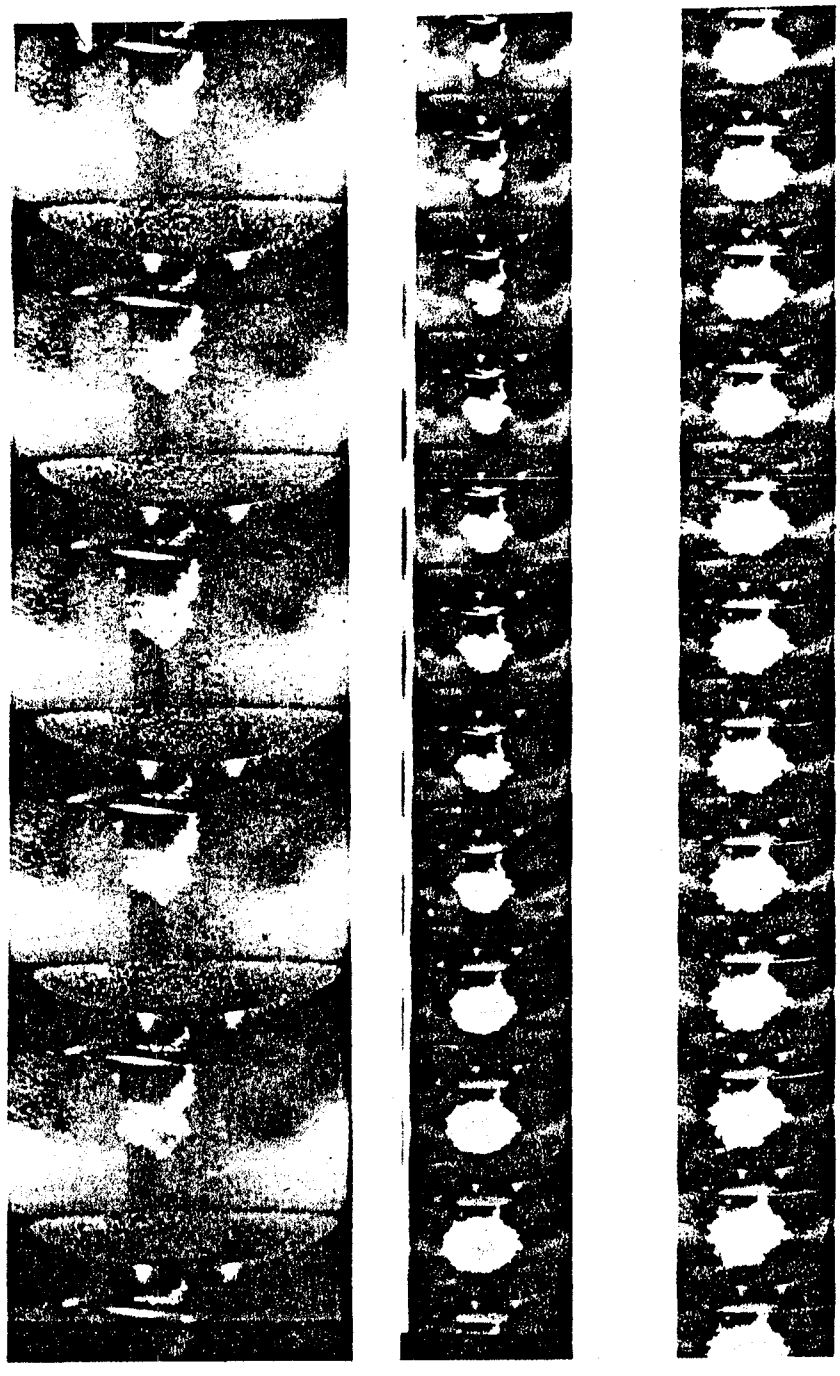

Fig. 2. Molten tin at 580°C into H_2O at 20°C yielding unstable vapor film with subsequent fragmentation.

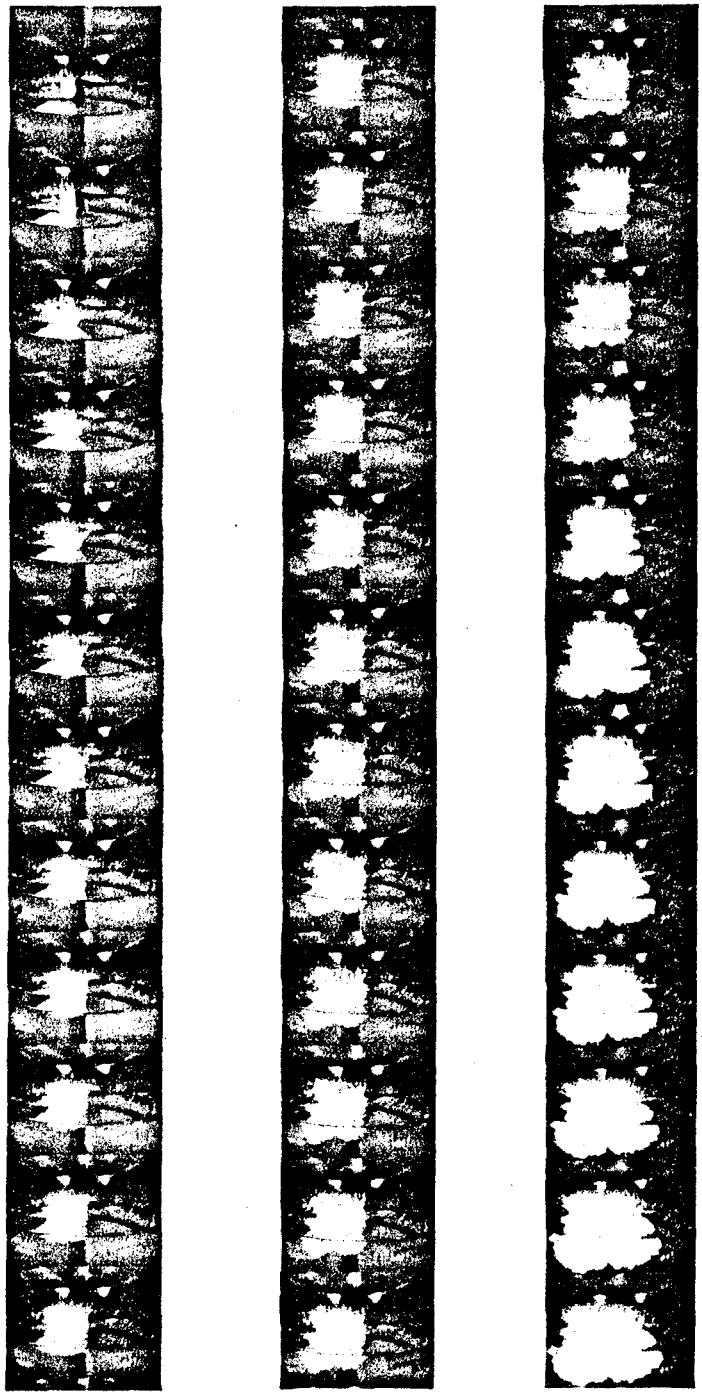

Fig. 3. Initial stages of molten salt into water yielding chemical reactions.

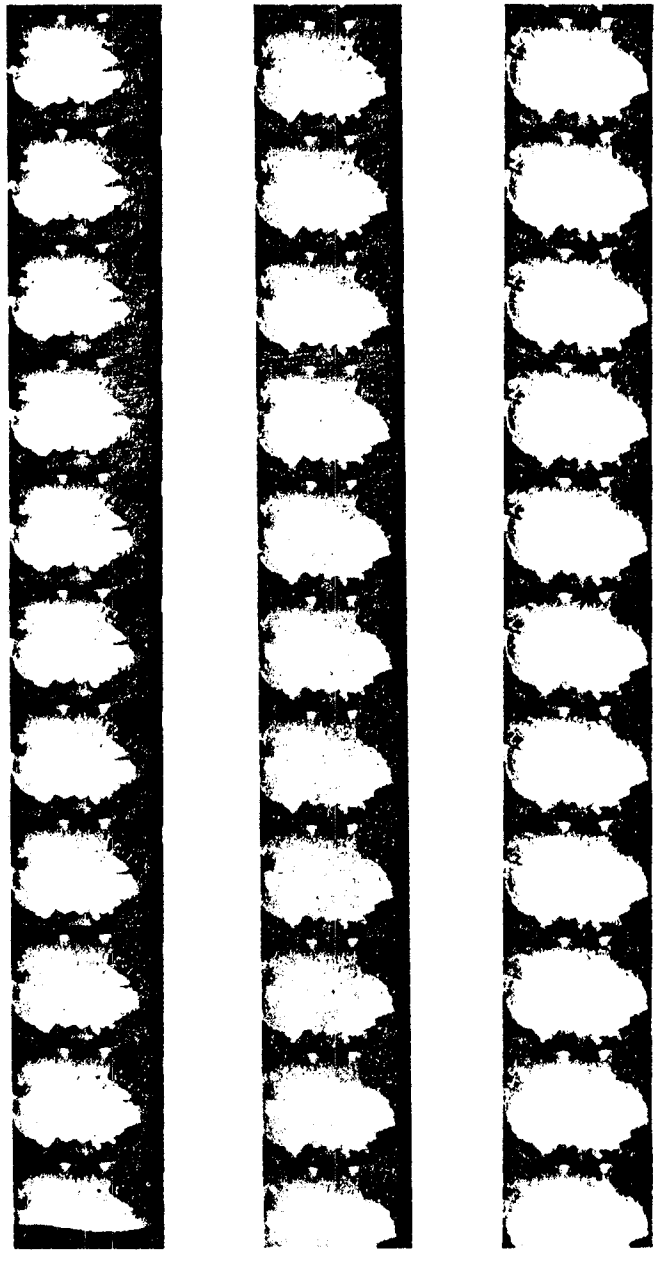

Fig. 4. Final stages of molten salt into water with chemical reaction.

AN ANALYSIS OF OSCILLATIONS OF A WATER DROPLET UNDER LOW GRAVITY CONDITIONS

by

O. H. Vaughan and R. E. Smith
Aerospace Environment Division/Space Sciences Laboratory
NASA/Marshall Space Flight Center
Huntsville, Alabama 35812

and

R. J. Hung and S. T. Wu
The University of Alabama in Huntsville
Huntsville, Alabama 35807

ABSTRACT

Astronaut William R. Pogue conducted some water droplet oscillation demonstrations on the Skylab 4 mission in low earth orbit. In one of the demonstrations he used a soda straw to cause the droplet, attached to a flat plate, to oscillate. Marker pen ink was added to the droplet to enhance photography using an on-board TV camera. The drop, which was 2.54 cm high and 3.52 cm wide, was observed to have a natural oscillation frequency of 1.3 Hz. The demonstration was photographed with an on-board TV camera to record the oscillation of the droplet and dissipation. We were able to obtain excellent data on the change in amplitude with time from the observations. An analysis was performed using these photographic data and a theoretical model was developed for determining the oscillation frequency, wavelength, surface tension and damping characteristics of the water droplet when attached to a flat plate. The theoretical model and these observation data are in good agreement.

I. INTRODUCTION

Experiments performed in an orbiting spacecraft under low gravity conditions allow observations of phenomena which normally cannot be done in a terrestrial laboratory. An example of such an observation is that of the impact of two spheres of water which are not supported by either an aerodynamic force due to a flowing column of air or held in position with an encumbering supporting apparatus. Either of these two techniques tends to dampen the oscillations of the spheres of water and to mask other types of phenoma. The natural or free oscillations of water drops and other phonema are of special interest to the cloud physicist and other fluid mechanics researchers.

Atmospheric microphysics deals with droplet and droplet-droplet interactions. Particularly, the mechanisms which occur during the creation of rain, such as the rebound of drops, coalescence of drops, splintering after impacts, oscillation breakup, electrical effects, etc., are all of special interest. To study these mechanisms, the Skylab 4 crew was requested to do some fluid mechanics type science demonstrations during their long duration mission so that natural oscillations and other phenomena of water droplets could be observed.

This paper presents results of a demonstration conducted by astronaut William R. Pogue to study water droplet oscillations in low earth orbit. In this demonstration he perturbed a droplet, attached to a flat surface, and caused it to oscillate. The droplet had been contaminated with marker pen ink to enhance it for photography using an on-board TV camera. An analysis was performed using this photographic data and a theoretical model was developed to determine the oscillation frequency, wavelength, surface tension and damping characteristics of the water droplet attached to a flat plate. A comparison between laboratory surface tension and experiment and the value calculated from this experimental observation was made with good agreement.

II. EXPERIMENTAL ARRANGEMENTS

The hardware used for this demonstration consisted of on-board medical type syringes, pieces of tape attached to drinking straws, a pad of ruled paper, marker pen writing ink, the teflon coated flat surface of the ED 52 "Web formation in zero gravity" spider cage, and the on-board TV camera. The water used in this demonstration was colored, to enhance the photography, by adding a small amount of the marker pen ink. During the demonstration a water droplet, attached to a flat surface, was caused to oscillate by motion of a soda straw. By observing the change in amplitude with time we were able to obtain the data required to verify the applicability of a proposed theoretical model.

In the present investigation, the film, taken with the on-board TV camera, was studied and measurements of the characteristics of the drop oscillations were made using a Vanguard film analyzer. The amplitude and wavelength of the oscillations were determined directly from the film using appropriate scale factors. The frequency of oscillations was

determined by counting the number of frames that were observed during the time interval between the time that the water drop underwent deformation and returned to its original shape and then dividing this count number by the TV camera framing rate (30 frames/sec).

Some selected frames of the various modes of the oscillating water droplet attached to the flat surface are presented in Figure 1. The numbers on the pictures in the figure show the sequence of TV camera frames taken in the Skylab demonstration. Picture number 1 is at the moment when a drinking straw was inserted into the center of the water drop attached to the flat surface. Picture numbers 4, 6, 9 and 12 show the soda straw being pulled out of the water drop, and picture number 13 shows the moment when the soda straw left the surface of the water drop. Picture number 14 shows the oscillation of the water drop at its maximum amplitude right after the soda straw completely left the surface of the drop while picture number 28 shows the drop at its minimum amplitude. Picture numbers 30, 33, 34, 35, 36, 37 and 38 show how the water drop increased its amplitude again and picture number 40 shows the moment when the water drop just completed one cycle of oscillation and returned to its maximum amplitude.

Analysis of these pictures frame by frame give us an opportunity to measure the frequency and wavelength of the oscillations and how these oscillations decay with time.

III, THEORETICAL MODEL

A theoretical calculation for the oscillation of free floating liquid droplet was given by Lord Rayleigh (1879) almost a hundred years ago. Recently, Nelson and Gokhale (1972) reported an experimental study of small amplitude natural droplet oscillations with droplet sizes from a few hundred micrometers to millimeters in a vertical wind tunnel study, and concluded that the agreement between experimental results and theoretical calculation given by Rayleigh was good. The present study concerns oscillations of a water droplet attached to a flat plate rather than oscillations of a free floating droplet, and the size of the droplet is several cm rather than a hundred μm. It is interesting to study the present experiment to see how well the data agrees with theoretical models.

The theoretical model is based on the concept that fluid surfaces tend to be in equilibrium when the surface tension forces are balanced by the fluid pressure. If we assume that the amplitude of the oscillations is small compared to the wavelength, then the boundary conditions on the velocity potential ψ for the rectangular coordinates can be written (Landau and Lifshitz, 1959)

$$\rho \frac{\partial^2 \psi}{\partial t^2} - \alpha \frac{\partial}{\partial z}\left(\frac{\partial^2 \psi}{\partial x^2} \quad \frac{\partial^2 \psi}{\partial y^2}\right) = 0 \quad \text{at } z = 0 \qquad (3.1)$$

where ρ is the density of the fluid and α is the surface tension coefficient. If we consider a plane wave propagated along the x-axis, then the solution of the system can be assumed to be in the form

$$\psi = \mathrm{Re}\left[Ae^{-kz}\, e^{-i(\omega t - kx)}\right] \tag{3.2}$$

where A is the amplitude, k is the wave number, and ω is the circular frequency of the wave. The relation between k and ω which is called the dispersion relation can be obtained by substituting Equation (3.2) into the boundary condition (3.1)

$$\omega^2 = \frac{\alpha k^3}{\rho} \tag{3.3}$$

Since $\omega = 2\pi f$ where f is the oscillation wave frequency in Hz, we have

$$f^2 = \frac{\alpha k^3}{4\pi^2 \rho} \tag{3.4}$$

It is important to point out that a plane wave solution as we have shown in equation (3.2) may not be true when the radius of curvature of the oscillating fluid is on the order of the wavelength of the oscillations. In this case, spherical harmonics rather than a plane wave solution is more suitable for describing the oscillation of the droplet. For the case of a spherical droplet oscillation of an incompressible fluid under the action of surface tension force, the boundary condition shown in equation (3.1) in rectangular coordinates can be written into spherical coordinated as follows:

$$\rho \frac{\partial^2 \psi}{\partial t^2} - \frac{\alpha}{R^2}\left\{2\frac{\partial \psi}{\partial r} + \frac{\partial}{\partial r}\left[\frac{1}{\sin\theta}\frac{\partial}{\partial \theta}\left(\sin\theta \frac{\partial \psi}{\partial \theta}\right) + \frac{1}{\sin^2\theta}\frac{\partial^2 \psi}{\partial \phi^2}\right]\right\} = 0 \quad \text{at } r = R \tag{3.5}$$

If we prostulate a solution in the form of a spherical wave which satisfies the spherical harmonic function of the form:

$$\psi = \mathrm{Re}\left[Ae^{-i\omega t}\, r^{\ell}\, Y_{\ell m}(\theta,\phi)\right] \tag{3.6}$$

with $\ell = 0, 1, 2, \cdots$, and m, $\pm 1, \pm 2, \pm 3, \cdots \pm \ell$ and using the spherical harmonic function

$$Y_{\ell m}(\theta, \phi) = P_{\ell}^{m}(\text{Cos } \theta)\, e^{im\phi} \tag{3.7}$$

where $P_{\ell}^{m}(\cos \theta)$ is an associated Legendre function. Then knowing that the spherical harmonics $Y_{\ell m}$ satisfies

$$\frac{1}{\text{Sin}} \frac{\partial}{\partial \theta}\left(\text{Sin } \theta \frac{\partial Y_{\ell m}}{\partial \theta}\right) + \frac{1}{\text{Sin}^2 \theta}\left(\frac{\partial^2 Y_{\ell m}}{\partial \phi^2}\right) + \ell\,(\ell+1)\, Y_{\ell m} = 0 \tag{3.8}$$

we now have the relation

$$\omega^2 = \frac{\alpha\, \ell\, (\ell-1)\, (\ell+2)}{\rho\, R^3} \tag{3.9}$$

Substituting the relations $\omega = 2\pi f$, and $R = d/2$, where d is the diameter of the spherical droplet, equation (3.9) becomes

$$f^2 = \frac{2\, \alpha\, \ell\, (\ell-1)\, (\ell+2)}{\pi^2\, \rho\, d^3} \tag{3.10}$$

which agrees with the formula obtained by Rayleigh (1879).

It is clear that the fundamental mode of the spherical harmonic oscillations is $\ell = 2$. In the present study, the wave mode of oscillation observed for the water droplet attached to the flat surface is a single mode which is equivalent to $\ell = 2$ for the spherical harmonic case. By making a comparison between equations (3.4) and (3.10) and substituting $k = 2\pi/\lambda$ and $\lambda = \pi d/2$ in equation (3.4), we find that the plane wave solution and the spherical harmonic solution are equivalent for $\ell = 2$. For the case of multi-modes oscillations derivations between the plane wave solution and spherical harmonic solution becomes apparent. Table I shows the percentage deviation between these two solutions. The maximum deviation shown is 11% when $\ell = 4$ with the deviation gradually decreasing as ℓ increases.

In the present study, the contact angle between the water droplet and the flat surface is close to $\pi/2$, and there is no indication shown in the film obtained from Skylab that the contact line between the fluid and solid surface moved as the water droplet oscillated. This is the fundamental assumption we have made for boundary conditions in which we assume that the velocity potential vanishes on the contact line. If the contact line moves, a special justification is necessary (West, 1911; Huh and Scriven, 1971).

Physically, the surface tension α is a measure of the work done per unit area to balance the pressure difference between the two sides of the fluid. This implies that α increases when the pressure difference increases, and α decreases when the fluid is contaminated with impurities.

Furthermore, let us now calculate the energy dissipation of droplet oscillations. In this case the mechanical energy, E_{mech}, includes both the kinetic and the potential energy. Thus, the energy dissipated per unit time in the droplet is

$$\dot{E}_{mech} = - \int \sigma'_{ij} \frac{\partial v_i}{\partial x_j} dV \tag{3.11}$$

where σ'_{ij} is the viscous stress tensor which is defined

$$\sigma'_{ij} = \eta\left(\frac{\partial v_i}{\partial x_j} + \frac{\partial v_j}{\partial x_i} - \frac{2}{3}\delta_{ij}\frac{\partial v_\ell}{\partial x_\ell}\right) + \zeta\delta_{ij}\frac{\partial v_\ell}{\partial x_\ell} \tag{3.12}$$

and v is the velocity and V is the volume of the fluid. Here η and ζ are called coefficients of first and second viscosity, respectively. Under the condition of an incompressible fluid (water droplet), equation (3.11) becomes

$$\dot{E}_{mech} = - \frac{1}{2}\eta \int \left(\frac{\partial v_i}{\partial x_j} + \frac{\partial v_j}{\partial x_i}\right)^2 dV \tag{3.13}$$

If we assume that during the oscillation of the liquid droplet the volume of the surface region of the rotational flow is small and that the velocity gradient is not large, then the existence of the region of rotational flow may be ignored. If the integration is taken over the whole volume of the fluid which moves as if it were an ideal fluid, then we have potential flow,

$$\frac{\partial v_i}{\partial x_j} = \frac{\partial^2 \psi}{\partial x_i \partial x_j} = \frac{\partial v_j}{\partial x_i} \tag{3.14}$$

so that

$$\dot{E}_{mech} = -2\eta \int \left(\frac{\partial^2 \psi}{\partial x_i \partial x_j}\right)^2 dV. \tag{3.15}$$

In the present analysis we are not interested in the instantaneous value of energy dissipation, but the mean value of energy dissipation with respect to time. By using the definition of mean value with respect to time for periodic motion

$$\langle \psi \rangle = \frac{\omega}{2\pi} \int_0^{\frac{2\pi}{\omega}} \psi(\omega t)\, dt \tag{3.16}$$

and the wave form shown in equation (3.2), we have the mean value of mechanical energy

$$\langle \dot{E}_{mech} \rangle = -8\eta k^4 \int \langle \psi^2 \rangle \, dV \, . \tag{3.17}$$

Now, the mean value of mechanical energy is

$$\langle E_{mech} \rangle = \rho \int \langle v_i^2 \rangle \, dV$$

$$= \rho \int \langle \left(\frac{\partial \psi}{\partial x_i}\right)^2 \rangle \, dV$$

whence

$$\langle E_{mech} \rangle = 2 \rho k^2 \int \langle \psi^2 \rangle \, dV. \tag{3.18}$$

It is known that the energy of the wave decreases according to the low

$$\langle E_{mech} \rangle \propto e^{-2\gamma t} \tag{3.19}$$

since the energy is proportional to the square of the amplitude where the amplitude decreases with time as

$$A = A_o \, e^{-\gamma t} \tag{3.20}$$

Here A_o is the initial value of the amplitude and γ is the damping rate of the wave. Thus, the damping rate obtained from equations (3.17) and (3.18) is

$$\gamma = \frac{|\langle \dot{E}_{mech} \rangle|}{2\langle E_{mech} \rangle} = \frac{2\eta k^2}{\rho} \tag{3.21}$$

IV. RESULTS AND DISCUSSIONS

We were able to obtain measurements of the natural frequency of the oscillations of the droplet attached to a flat surface, and the size of the droplet from the film. As we have stated earlier, the phenomena of fluid-solid contact line is always a problem when contact line moves (Huh and Scriven, 1971). This is because the movement of fluid-solid

contact line violates the basic boundary conditions. Fortunately, after careful examination of Skylab films, we found that there is no indication that the contact line between the fluid and solid surface moved when the water droplet oscillated in the present case. The natural frequency of the oscillations as measured was 1.3 Hz for the contaminated water droplet (2.54 cm in height and 3.52 cm in width) attached to a flat surface. By using the observed natural frequency and wavelength, λ ($\equiv 2\pi/k$) = 6.1 cm, determined from the Skylab demonstration film, the surface tension of the droplet oscillation can be obtained from the following relation based on equation (3.4) or equation (3.10) with $\ell = 2$

$$\alpha = \frac{f^2 \lambda^3 \rho}{2\pi} = 61 \text{ dynes/cm.} \tag{4.1}$$

This value is for the surface tension for water contaminated with marker pen ink while the surface tension for pure water at 20° C is 72 dynes/cm.

A laboratory measurement of the surface tension of a reproduction of the Skylab water which is contaminated with marker pen ink was made at the NASA/Marshall Space Flight Center and gave a value of α = 60 dynes/cm which is in good agreement with Skylab demonstration value.

Calculation of the dissipation rate of the droplet oscillation is rather straightforward by substituting the observed wave number in equation (3.21). It is

$$\gamma = 2.05 \times 10^{-2} \text{ rad/sec} = 3.26 \times 10^{-3} \text{ Hz} \tag{4.2}$$

when the viscosity coefficient of pure water at 20° C is used (η = 0.01 cm^2/sec). This damping rate of the droplet oscillation corresponds to a dissipation time of 306 seconds.

Using the initial amplitude of the droplet oscillations as measured on the film and equation (3.20), we attempted to compare the actual damping rate curve with a theoretical curve, and our results are shown in the Figure 2. Although we were only able to observe the oscillations of the droplet for 22 seconds, there is good agreement between the actual dissipation rate and the theoretical curve.

In the present analysis, the theoretical model is based on the assumption that the wave amplitude is small compared with the wavelength. The maximum amplitude of the droplet oscillation is 7% of the wavelength which substantiates the validity of the assumptions used in the development of the theoretical model.

ACKNOWLEDGEMENT

RJH and STW wish to acknowledge the support of NASA/Marshall Space Flight Center through Contract No. NAS8-30247.

REFERENCES

Huh, C. and L. E. Scriven, J. Coll. and Interf. Sci. 35, 85, 1971.

Landau, L. D. and E. M. Lifshitz, Fluid Mechanics, Pergamon Press, London, 1959.

Nelson, A. R., and N. R. Gokhale, J. Geophys. Res. 77, 2724, 1972.

Rayleigh, L., Proc. Roy. Soc. London 29, 71, 1879, or The Theory of Sound, by Lord Rayleigh (J. W. Strutt), Vol. 2, Dover, New York, 1945.

West, G. D., Proc. Roy. Soc., Ser. A 86, 28, 1911.

TABLE 1

COMPARISON OF THE PLANE WAVE SOLUTION AND SPHERICAL HARMONIC SOLUTION

Mode (ℓ)	Deviation*
2	0.0
4	0.11
6	0.10
8	0.085
10	0.080
12	0.065
15	0.055
20	0.043
30	0.030
50	0.018
80	0.012
100	0.009

$$*\text{Deviation} = \frac{f^2]_{\text{plane wave}} - f^2]_{\text{spherical harmonic}}}{f^2]_{\text{plane wave}}}$$

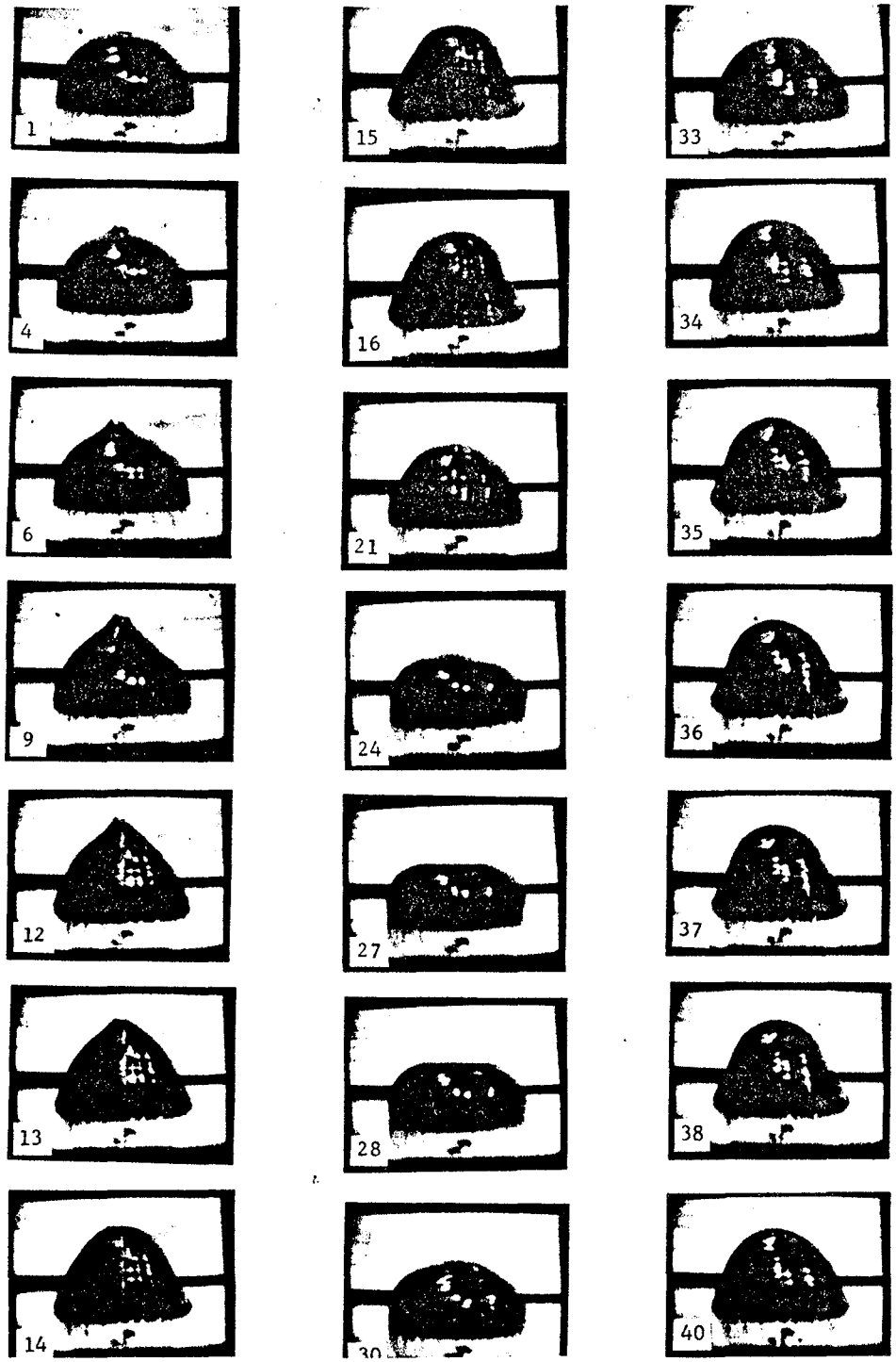

Fig. 1. Skylab 4 Science Demonstrations of Selected Sequences of the Oscillating Water Droplet Attached to the Flat Surfaces in a Low Gravity Environment.

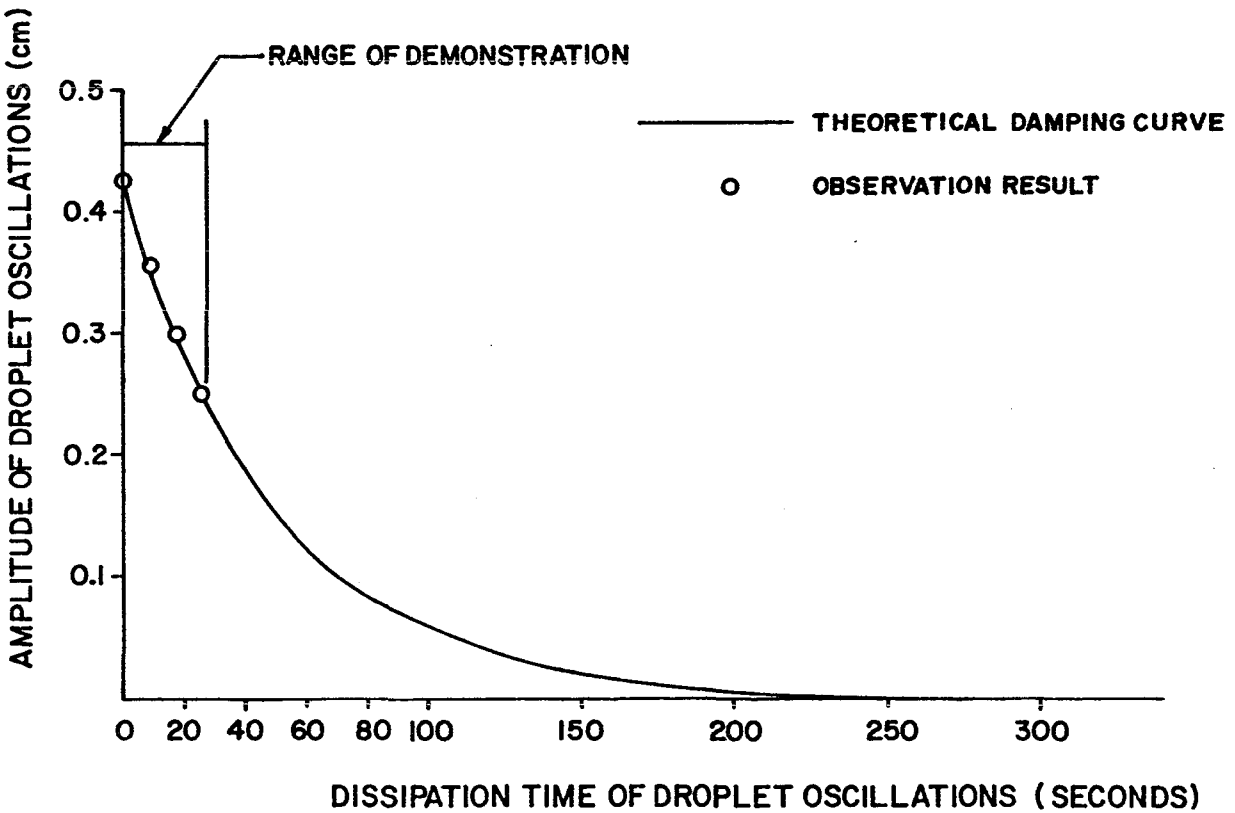

Fig. 2. Dissipation of the Amplitude of Droplet Oscillations Against Dissipation Time of Droplet Oscillations,

LIQUID DROP BEHAVIOR IN WEIGHTLESSNESS FROM SKYLAB*

Tommy C. Bannister
NASA-Marshall Space Flight Center, Huntsville, Alabama 35812

and

Sidney V. Bourgeois
Lockheed Missiles & Space Company, Inc , Huntsville, Alabama 35807

ABSTRACT

Several science demonstrations were performed on the Skylab IV mission on the behavior of typically ~ 100 ml drops of a water and water/soap solution. Symmetric and antisymmetric oscillations were observed. Also, other phenomena were observed, including drop collisions, rotational instability and dampening of oscillations. A total in excess of two hours of data was obtained. The film shown was a seventeen minute composite of selected sequences.

DISCUSSION

A 17-minute film was shown which consisted of selected sequences from Skylab IV science demonstrations TV-101, Liquid Floating Zone, and TV-107, Fluid Mechanics Series. Over two hours of TV video tape were obtained on these demonstrations by the Skylab IV crew of Ed Gibson, Bill Pogue and Gerald Carr. The film contained the following five segments:

- Oscillation and damping of a free-floating, 100 cc spherical drop of marker ink-doped water which was initially perturbed into an ellipsoid.
- Same as preceding with a soap-water solution.
- Impact and coalescence of two Tang-water globules each 30 cc in size.
- Rotation and breakup of a 100 cc water drop.
- Rotational and longitudinal stability of Tang-water and soapy water cylindrical floating zones.

Each of these sequences exhibit liquid dynamics in an environment of 10^{-4} g_{Earth}, 5 psi, 70°F, and 70% N_2-30% O_2. The film had sound and contained comments from the astrounauts as they performed the experiments in Skylab.

---

* Film presented at International Colloquium on Drops and Bubbles, California Institute of Technology, Pasadena, California, 29 August 1974.

Demonstration TV-101, Liquid Floating Zone, was proposed by Dr. John Carruthers of Bell Research Laboratories, Murray Hill, New Jersey. It was performed and recorded on TV video by Science Pilot Ed Gibson. This demonstration simulates an important method of growing crystals and was done to define the stability of the liquid zone under a steady rotation rate of about 30 rpm as well as to obtain data on the instability modes and convection patterns. This information is important in the utilization of this technique for growing crystals both on the ground and in space in the planned Space Laboratory. Specifically, the demonstration consisted of rotating water zones of varying lengths. The effect of viscosity on the zone was studied by using foams of water, soap solution and air for the zone. In addition the longitudinal vibration characteristics of the floating zones were also investigated. Measurements from the flight film are being made for thirty-nine different rotation sequences of which twenty-four were stable and fifteen were unstable and broke. The measurements include the rotation rate versus time and the zone deformation versus time for each sequence. Data are also being taken from the film of several longitudinal vibration sequences. The preferred stable mode which was exhibited in the film sequence by the rotating zone was a nonsymmetric "C" shape, whereas previous Plateau experiments and theoretical analyses lead to axisymmetric shapes (Ref. 1). Rayleigh's criteria for the maximum stable zone length (Ref. 1) seems to be valid for the zones shown in the film sequence.

Demonstration TV-107, Fluid Mechanics Series, consisted of several fluid demonstrations grouped under one heading. The investigators were Ms. Barbara Facemire and Mr. O. Vaughan of MSFC; Dr. Sid Bourgeois of Lockheed Missiles and Space Company, Huntsville, Alabama; and Dr. T. Frost of the General Electric Company, Valley Forge, Pennsylvania. Both Science Pilot Ed Gibson and Pilot Pogue recorded this demonstration on TV video. It was essentially a series of tests to obtain data on fluid oscillation times, dampening times, rotational instability, wetting characteristics, internal vortices and fluid flow patterns in liquid drops under microgravity. Over two hours of excellent data were obtained.

Quantitative measurements are in the process of being made from the film of these Skylab IV fluid mechanic science demonstrations. These include the frequency and damping of oscillations of different size liquid droplets, the approach velocity and frequency of oscillation for the droplet coalescence demonstrations and the deformation of drops during the rotation and breakup demonstration. Other demonstrations are not amenable to quantitative measurements and are being analyzed qualitatively.

The drop oscillation sequences shown in the film indicate that Lord Rayleigh's classical analysis (Ref. 1) of the problem accurately predicts the effect of surface tension on the vibration frequency of free-floating water drops. The damping factor for these oscillations on Skylab IV, however, do not seem to agree with Lamb's analysis (Ref. 2) of the viscous damping of free-floating, spherical drops undergoing ellipsoidal oscillations. This is probably due to the rather large exictations to which the drops were exposed.

The impact demonstrations indicate that a minimum velocity is necessary to overcome surface forces and affect a coalescence. There is also an indication that electrostatic effects may occur in some coalescences. Since quantitative data can not be obtained in many of the impact demonstrations, especially when impacts occur without coalescence, criteria for the coalescence of liquids in low-g will be difficult to determine.

The slow mixing of the liquids after impact and the dogbone shape of a droplet upon rotation demonstrate a small amount of internal circulation of a freely floating fluid in a low-gravity environment. This is an important observation which had not been predicted and could prove very significant for space processing applications.

The injection of air into liquid globules demonstrates the effect of compressible air in damping oscillations. This technique also demonstrates the feasibility of forming hollow thin-walled liquid spheres. Several syringes of air were injected into a water globule forming a single sphere of air inside the liquid globule.

The difficulty of handling freely floating liquids and the complexity of the fluid motion becomes clear while viewing these demonstrations and listening to the comments of the astronauts. In the post-flight debriefing the astronauts mentioned that a lot of time was necessary for learning how to handle fluids and recommended that non-wetting surfaces be used to handle fluids since on a wetting surface the fluid spreads, preventing the release of free floating globules. They also noted that air currents had a significant effect on free-floating globules, making it difficult to position them. However, even with these difficulties the astronauts, after an initial learning period, became proficient at maneuvering the liquids and performing demonstrations.

These demonstrations were used to fill extra time during the Skylab flights and were limited to on-board hardware. Data from the fluid mechanic demonstrations consisted only of the astronaut's voice transmission and television transmission. Even with these constraints, a great deal of basic and practical information was obtained on fluid motion and handling in low-g environments. This type of information will be beneficial to the design and development of many future space processing, cloud physics, and other related fluids handling programs.

REFERECNES

1. Carruthers, J. R., and M. Grasso, "The Stabilities of Floating Liquid Zones in Simulated Zero Gravity," Journal of Crystal Growth, Vol. 13/14, 1972.

2. Lamb, Horace, Hydrodynamics, 6th ed., Dover, New York, 1945.

PARTICIPANTS

Acrivos, Andreas
Dept. Chemical Eng.
Stanford Univ.
Stanford, CA 94305

Alonso, C. T.
Bldg. 71
Lawrence Berkeley Labs
Berkeley, CA 94720

Apfel, Robert E.
Dept. Eng. Appl. Sci.
Yale Univ.
New Haven, CT 06520

Ashkenas, Harry I.
M/S 183-601
J.P.L.
Pasadena, CA 91103

Ashkin, A.
Rm 4E-426
Bell Telephone Labs
Holmdel, NJ 07733

Bencala, Ken
M/S 208-41
Calif. Inst. Tech.
Pasadena, CA 91109

Berger, Melvyn S.
362 Blanvelt Rd.
Pearl River, NY 10965

Bertram, L. A.
Division 2642
Sandia Laboratories
Albuquerque, NM 87115

Billet, Michael L.
Applied Research Lab
Box 30
State College, PA 16801

Boulanger, Marc
Meteorologie Nationale
73-77 Rue De Sevres
92100 Boulogne, France

Bourgeois, S. V.
Lockheed Missiles/Space
Huntsville Res. Ctr.
Huntsville, AL 35807

Brennen, Christopher
M/S 301/46
Calif. Inst. Tech.
Pasadena, CA 91109

Buckholtz, Thomas J.
Lawrence Radiation Lab
P. O. Box 808 L-71
Livermore, CA 94550

Busse, F. H.
Dept. Planetary Sci.
U.C.L.A.
Los Angeles, CA 90024

Cagliostro, Dominic J.
Q - 297
Stanford Research Inst.
Menlo Park, CA 94025

Carrigan, C. R.
Dept. Planetary/Sp. Sci.
U.C.L.A.
Los Angeles, CA 90024

Carruthers, John R.
1B-315
Bell Telephone Labs.
Murray Hill, NJ 07974

Carstens, John C.
109 Norwood Hall
Univ. Missouri-Rolla
Rolla, MO 65401

Cass, Glen R.
M/S 138-78
Calif. Inst. Tech.
Pasadena, CA 91109

Catton, Ivan
Boelter Hall 5531
U.C.L.A.
Los Angeles, CA 90024

Chahine, M. T.
M/S 183-301
J.P.L.
Pasadena, CA 91103

Chan, Paul
M/S 208-41
Calif. Inst. Tech.
Pasadena, CA 91109

Chang, Chong E.
Dept. Chem. Eng./Mat.
Univ. So. Calif.
Los Angeles, CA 90007

Chen, Kuo-Hung
3760 S. McClintock 310A
Los Angeles, CA 90007

Chu, Helen
50A-3115
Lawrence Berkeley Lab
Berkeley, CA 94720

Collins, Donald J.
M/S 183-601
J.P.L.
Pasadena, CA 91103

Collins, Roy
Dept. Mech. Eng.
University College
London WC1E 7 JE England

Concus, P.
Lawrence Berkeley Labs
90-3108
Berkeley, CA 94720

Dauber, Philip M.
Lawrence Berkeley Labs
Bldg. 50
Berkeley, CA 94720

Davidson, Cliff I.
M/S 138-78
Calif. Inst. Tech.
Pasadena, CA 91109

Donnelly, Russell J.
Dept. Physics
Univ. Oregon
Eugene, OR 97403

Dragoo, Alan L.
Inst. Metals Research
National Bur. Stds.
Washington, DC 20234

Drummond, Alastair M.
Flight Research Lab
N R C Canada
Ottawa, Canada K1AOR6

Eaton, Larry R.
A3-253 AJEO M/S-28
McDonnell Douglas Astr.
Huntington Bch. 92647

Eichhorn, Roger
Dept. Mech. Eng.
Univ. Kentucky
Lexington, KY 40506

Eisner, Melvin
Dept. Physics
Univ. Houston
Houston, TX 77004

Elleman, D. D.
M/S 183-401
J.P.L.
Pasadena, CA 91103

Elliott, David G.
M/S 122-123
J.P.L.
Pasadena, CA 91103

Estabrook, Frank B.
M/S 183-601
J.P.L.
Pasadena, CA 91103

Foote, G. B.
N.C.A.R.
P. O. Box 3000
Boulder, CO 80303

Franz, Gerald J.
Silencing Tech. Div. 194
Naval Ship R/D Ctr.
Bethesda, MD 20034

Friedlander, Sheldon K.
M/S 138-78
Calif. Inst. Tech.
Pasadena, CA 91109

Fymat, Alain L.
M/S 183-301
J.P.L.
Pasadena, CA 91103

Gabris, Edward A.
Code RS
NASA Headquarters
Washington, DC 20546

Garg, S. K.
Systems/Science/Software
P. O. Box 1620
La Jolla, CA 92037

Gibson, Edward G.
Code CB
Johnson Space Ctr.
Houston, TX 77058

Goddard, Frank E.
M/S 180-700
J.P.L.
Pasadena, CA 91103

Gough, D.
Inst. Astronomy
Cambridge Univ.
Cambridge, England

Griffin, James J.
Dept. Physics/Astronomy
Univ. Maryland
College Park, MD 20742

Grosjean, Daniel M.
M/S 138-78
Calif. Inst. Tech.
Pasadena, CA 91109

Happe, Ralph A.
Rockwell Int. D/193-600
12214 Lakewood Blvd.
Downey, CA 90241

Harper, Ed
4C-224B
Bell Telephone Labs
Whippany, NJ 07981

Harper, J. F.
Dept. Mathematics
Victoria Univ. Wellington
Wellington, New Zealand

Harvey, D. W.
2039 Port Weybridge Pl.
Newport Beach, CA 92660

Hashimoto, Lewis K.
Blacker House
Calif. Inst. Tech.
Pasadena, CA 91109

Heisler, S. L.
M/S 138-78
Calif. Inst. Tech.
Pasadena, CA 91109

Hilton, Howard T.
IBM E73/025
Montery - Cottle Rd.
San Jose, CA 95193

Ho, Bosco
M/S 208-41
Calif. Inst. Tech.
Pasadena, CA 91109

Hocking, L. M.
Dept. Mathematics
University College
London, England

Hsieh, Din-Yu
Div. Appl. Math.
Brown Univ.
Providence, RI 02912

Huff, Charles F.
Division 5718
Sandia Laboratories
Albuquerque, NM 87115

Hung, R. J.
Dept. Mech. Eng.
Univ. Alabama
Huntsville, AL 35807

Jameson, G. J.
Dept. Chem. Eng.
Imperial College
London, S. W. 7
England

Janik, Gary
287 E. California
Pasadena, CA 91106

Johnson, Robert E.
359 S. Wilson
Pasadena, CA 91106

Keller, Stu
M/S 104-44
Calif. Inst. Tech.
Pasadena, CA 91109

Kelly, Arnold J.
Exxon Research Labs
P. O. Box 45
Linden, NJ 07036

Kiang, C. S.
N.C.A.R.
P. O. Box 3000
Boulder, CO 80302

Kikuchi, Ryoichi
Hughes Research Labs
3011 Malibu Canyon
Malibu, CA 90265

Kistler, Alan
Dept. Mech. Eng.
Northwestern Univ.
Evanston, IL 60201

Kotsovinos, Nikos E.
M/S 138-78
Calif. Inst. Tech.
Pasadena, CA 91109

Kovitz, Arthur A.
Dept. Mech. Eng.
Northwestern Univ.
Evanston, IL 60201

Kumar, S.
M/S 208-41
Calif. Inst. Tech.
Pasadena, CA 91109

Larson, David J.
Research Plant 26
Grumman Aerospace Corp.
Bethpage, NY 11714

Lauterborn, W.
Third Physical Inst.
Univ. Gottingen D-34/FRG
Gottingen, W. Germany

Leal, Gary L.
M/S 208-41
Calif. Inst. Tech.
Pasadena, CA 91109

Lebovitz, Norman R.
Dept. Mathematics
Univ. Chicago
Chicago, IL 60637

Lee, In-Young
Dept. Meteorology
U.C.L.A.
Los Angeles, CA 90024

Liu, V. C.
Dept. Aerospace Eng.
Univ. Michigan
Ann Arbor, MI 48104

Lobl, Elena
Dept. Meteorology
U.C.L.A.
Los Angeles, CA 90024

Mackin, Robert J.
M/S 186-133
J.P.L.
Pasadena, CA 91103

Mason, Peter V.
M/S 183-401
J.P.L.
Pasadena, CA 91103

McMurry, Peter H.
M/S 138-78
Calif. Inst. Tech.
Pasadena, CA 91109

Moore, D. W.
Dept. Mathematics
Imperial College
London SW7, England

Myers, William D.
Nuclear Chemistry Dept.
Lawrence Radiation Labs
Berkeley, CA 94720

Neiburger, Morris
Dept. Meteorology
U.C.L.A.
Los Angeles, CA 90024

O'Brien, Vivian
Appl. Physics Lab.
Johns Hopkins Univ.
Silver Spring, MD 20910

Pena, J.
Dept. Meteorology
Pennsylvania St. Univ.
University Park, PA 16802

Peterson, Tom
M/S 208-41
Calif. Inst. Tech.
Pasadena, CA 91109

Pickering, William H.
M/S 180-904
J.P.L.
Pasadena, CA 91103

Plesset, Milton S.
Dept. Eng. Science
Calif. Inst. Tech.
Pasadena, CA 91109

Pompa, M. F.
M/S 125-224
J.P.L.
Pasadena, CA 91103

Prosperetti, Andrea
M/S 104-44
Calif. Inst. Tech.
Pasadena, CA 91109

Reichman, James M.
Lawrence Livermore Lab.
P. O. Box 808 L-301
Livermore, CA 94550

Remenyik, Carl J.
Dept. Eng. Science
Univ. Tennessee
Knoxville, TN 37916

Rhomberg, Albin A.
M/S 183-401
J.P.L.
Pasadena, CA 91103

Roberts, Paul H.
Dept. Physics
Univ. Oregon
Eugene, OR 97403

Rosenkilde, Carl E.
Dept. Physics
Kansas State Univ.
Manhattan, KS 66506

Saffren, M. M.
M/S 186-118
J.P.L.
Pasadena, CA 91103

Sarma, Kalluri R.
1107 W. 41st Place
Los Angeles, CA 90007

Saunders, C. P. R.
Dept. Physics Umist
Manchester M60 1QD
England

Saville, Dudley A.
Dept. Chem. Eng.
Princeton Univ.
Princeton, NJ 08540

Scriven, L. E.
Dept. Chemical Eng.
Univ. Minnesota
Minneapolis, MN 55455

Simpkins, P. G.
M/S 1A-109
Bell Telephone Labs
Murray Hill, NJ 07974

Smyth, Joseph M.
M/S 183-601
J.P.L.
Pasadena, CA 91103

Somerscales, E. F. C.
Dept. Mechanical Eng.
Rensselaer Poly. Inst.
Troy, NY 12181

Stephens, James B.
M/S 11-14A
J.P.L.
Pasadena, CA 91103

Suo-Anttila, Ahti J.
11607 Sunshine Terrace
Studio City, CA 91604

Swiatecki, W. J.
Lawrence Berkeley Labs
Berkeley, CA 94720

Tegart, James
5439 S. Huron Way
Littleton, CO 80120

Tiefenbruck, Grant
M/S 208-41
Calif. Inst. Tech.
Pasadena, CA 91109

Trefethen, Lloyd M.
Dept. Mech. Eng.
Tufts University
Medford, MA 02155

Tsang, C. F.
Lawrence Berkeley Labs
Berkeley, CA 94720

Tsang, Leslie
Ames
Univ. Calif. San Diego
La Jolla, CA 92037

Tu, Yih-O
IBM Research Labs
D-K43
San Jose, CA 95193

Tulin, Marshall
Hydronautics, Inc.
7210 Pindell School Rd.
Laurel, MD 20810

Turnbull, Robert
Dept. Electrical Eng.
Univ. Illinois
Urbana, IL 61801

Van Wijngaarden, L.
Tech. Hogeschool Twente
Postbus 127
Enschede, Netherlands

Vrebalovich, Thomas
New Delhi
Department of State
Washington, DC 20520

Wahlquist, Hugo
M/S 183-601
J.P.L.
Pasadena, CA 91103

Wake, S.
Dept. Chem. Eng.
Calif. Inst. Tech.
Pasadena, CA 91109

Wang, Taylor
M/S 183-401
J.P.L.
Pasadena, CA 91103

Webbon, Bruce
M/S 239-4
Ames Research Ctr.
Moffett Fld., CA 94035

Westervelt, Peter J.
Dept. Physics
Brown Univ.
Providence, RI 02912

Whatley, Gary E.
M/S 208-41
Calif. Inst. Tech.
Pasadena, CA 91109

Wilcox, William R.
SSC 302
Univ. So. Calif.
Los Angeles, CA 90007

Willson, Richard C.
2845 Windfall Ave.
Altadena, CA 91001

Wong, C. Y.
Oak Ridge Nat. Lab.
P. O. Box X
Oak Ridge, TN 37830

Wright, F. H.
1250 S. Orange Grove
Pasadena, CA 91105

Wu, Theodore Y.
M/S 104-44
Calif. Inst. Tech.
Pasadena, CA 91109

Yankura, G.
M/S 125-224
J.P.L.
Pasadena, CA 91103

Yates, George
M/S 104-44
Calif. Inst. Tech.
Pasadena, CA 91109

Zahn, Markus
Dept. Electrical Eng.
Univ. Florida
Gainesville, FL 32611

Zana, E.
M/S 208-41
Calif. Inst. Tech.
Pasadena, CA 91109

Zieg, Kenneth F.
Time Zero Corp.
1488 W. 178th St.
Gardena, CA 90247

1	A.M. SHANAHAN	17	K. CHEN	33	I. CATTON	49	L.G. LEAL	65	P.J. WESTERVELT	81	P.H. ROBERTS
2	D.J. COLLINS	18	T.S. CHEN	34	A.L. DRAGOO	50	E. ZANA	66	C.E. ROSENKILDE	82	M.L. BILLET
3	L.E. SCRIVEN	19	C.S. KIANG	35	S.K. GARG	51	J.M. REICHMAN	67	R. TURNBULL	83	G.J. FRANZ
4	D.D. ELLEMAN	20	R. KIKUCHI	36	H.T. HILTON	52	D.J. CAGLIOSTRO	68	M.T. CHAHINE	84	F.H. WRIGHT
5	J.R. CARRUTHERS	21	C.T. ALONSO	37	A.L. FYMAT	53	R.J. HUNG	69	A. KISTLER	85	L.M. HOCKING
6	R.J. DONNELLY	22	A.A. KOVITZ	38	E.F.C. SOMERSCALES	54	J.A. PANA	70	L.A. BERTRAM	86	A.A. RHOMBERG
7	M.S. PLESSET	23	K.R. SARMA	39	C.J. REMENYIK	55	D.Y. HSIEH	71	H. CHU	87	J.J. GRIFFIN
8	M.M. SAFFREN	24	A. PROSPERETTI	40	D.G. ELLIOTT	56	L. VAN WIJNGAARDEN	72	T.J. BUCKHOLTZ	88	W.D. MYERS
9	M. NEIBURGER	25	W. LAUTERBORN	41	M. ZAHN	57	T.Y. WU	73	B. WEBBON	89	T. VREBALOVICH
10	E.A. GABRIS	26	R.E. APFEL	42	P.M. DAUBER	58	M. BOULANGER	74	G.J. JAMESON	90	S.V. BOURGEOIS
11	F.H. BUSSE	27	C.F. TSANG	43	C.P.R. SAUNDERS	59	R.A. HAPPE	75	A.M. DRUMMOND	91	D.J. LARSON
12	W.J. SWIATECKI	28	P.G. SIMPKINS	44	R. COLLINS	60	M.S. BERGER	76	C.F. HUFF		
13	J.F. HARPER	29	C. WONG	45	Y.O. TU	61	J.C. CARSTENS	77	E.Y. HARPER		
14	D.O. GOUGH	30	A. ASHKIN	46	T. WANG	62	P. CONCUS	78	R. EICHORN		
15	A. ACRIVOS	31	W.R. WILCOX	47	V. O'BRIEN	63	G.B. FOOTE	79	D.W. HARVEY		
16	N.R. LEBOVITZ	32	L.M. TREFETHEN	48	D.A. SAVILLE	64	A.J. KELLY	80	J. TEGART		

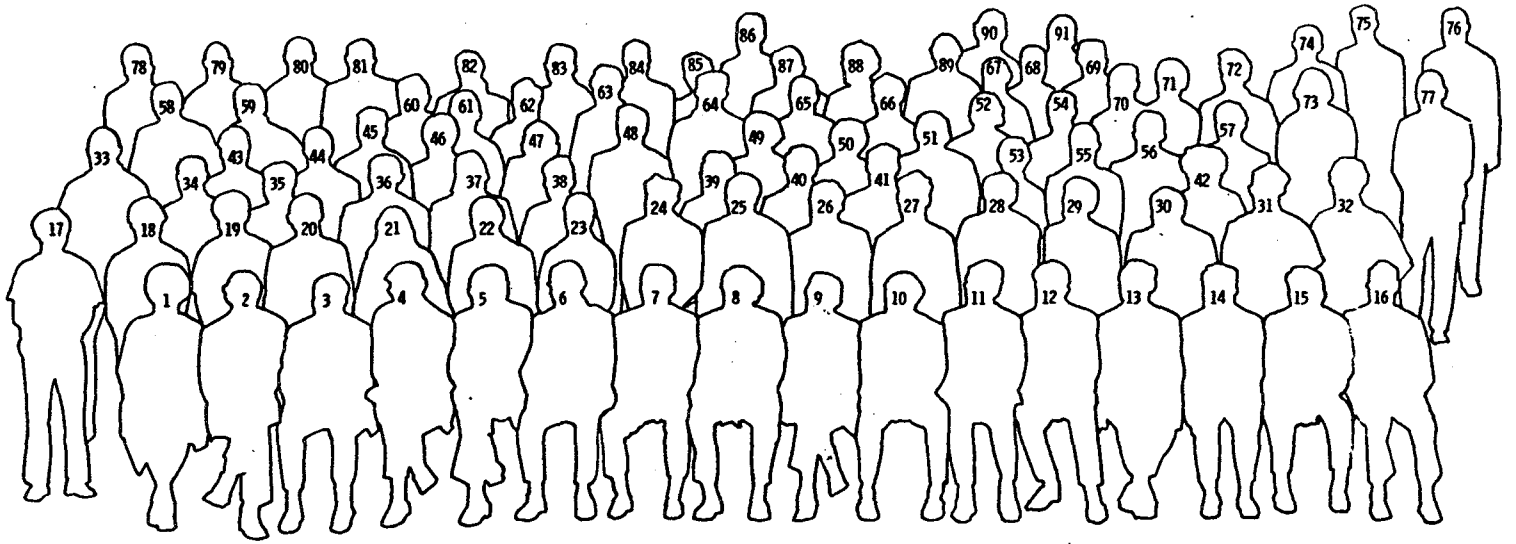

End of Document